Towards High-Throughput Characterization of Protein Biophysical Properties using Native Mass Spectrometry

by

Jacob Smith Jordan

A dissertation submitted in partial satisfaction of the

requirements for the degree of

Doctor of Philosophy

in

Biophysics

in the

Graduate Division

of the

University of California, Berkeley

Committee in charge:

Professor Evan R. Williams, Chair
Professor Susan M. Marqusee
Professor Kristie A. Boering
Dr. Kevin R. Wilson

Fall 2024

Towards High-Throughput
Characterization of Protein Biophysical Properties using Native Mass Spectrometry

by

Jacob Smith Jordan

Abstract

Towards High-Throughput
Characterization of Protein Biophysical Properties using Native Mass Spectrometry

by

Jacob Smith Jordan

Doctor of Philosophy in Biophysics

University of California, Berkeley

Professor Evan R. Williams, Chair

Native mass spectrometry (MS) is a powerful tool for the characterization of protein structure, stoichiometry, and stability, made possible by the use of electrospray ionization (ESI) to gently transfer proteins from solution to the gas phase. However, nonspecific aggregation can occur during ESI, which may lead to inaccurate determinations of biomolecular complex stoichiometry and adds ambiguity towards the existence of small molecule clusters in solution. This work resolves a long standing debate in the MS community by using submicron diameter emitters to investigate the abundance of small serine clusters *in solution* and to compare the physical properties of these clusters when formed from solution or by dissociation of even larger clusters in the gas-phase, demonstrating that the homochiral serine octamer exists in solution and that the unusually high abundance of the octamer observed in prior ESI-MS experiments is due to activation/dissociation of larger clusters in the MS instrument. Submicron diameter emitters also enable the measurement of protein charge-state distributions from nonvolatile buffers, but there are no standardized protocols for their fabrication or use. This work contains a detailed protocol for fabricating nanoelectrospray (nESI) emitters with diameters between 200 nm – 2.5 μm and guidelines for their use. To date, this is the only systematic characterization of the effect of instrument parameters on electrospray emitter diameter and morphology. This work also investigates the effect of electrospray voltage and emitter tip size on ESI droplet sizes and describes unique ionization phenomena that result from corona discharge at the tip of submicron diameter nESI emitters.

In native MS, compact protein structures exhibit low extents of charging whereas highly elongated conformations, such as denatured forms, exhibit higher extents of charging. Protein thermal denaturation curves can be obtained from MS data by plotting the average charge state as a function of solution temperature. Protein melting temperatures (T_m) can be extracted from these data by fitting with a two-state model. However, thermal equilibration of typical "variable-temperature ESI" sources requires 1 – 3 minutes at each temperature. These long thermal equilibration times are not compatible with solution-phase separations and can result in protein aggregation that clogs ESI emitters. Using an infrared laser to directly heat only ~200 pL of solution at the tip of nESI emitters, this work describes an apparatus to circumvent these issues

termed laser heated ESI (LH-ESI). LH-ESI can be used to obtain melting curves and T_m values for individual proteins in a mixture in less than 45 seconds. Protein molecules are directly exposed to heat from the laser beam for only ~140 ms, enabling the simultaneous measurement of melting curves for the apo- and ligand-bound forms of bovine carbonic anhydrase II, an aggregation-prone protein, and the first observation of a ~6.4 °C stabilizing effect on the T_m due to bicarbonate ligand binding. LH-ESI shows significant promise for the high-throughput characterization of protein thermal stabilities and protein-ligand interactions through fast melting curve measurements that enable a higher number of samples to be analyzed per day.

Biotherapeutics, as well as proteins involved in neurodegenerative disease, can undergo aggregation that results in the formation of oligomers that may be conformationally heterogeneous and spread across a wide range of mass and size. These aggregates are difficult to characterize using conventional mass spectrometry due to the limited transmission and loss of charge state resolution for large biomolecules, as well as extensive *m/z* overlap of elongated species. Charge detection mass spectrometry (CDMS) circumvents these issues by separately measuring the mass and charge of individual ions. This work describes the development of CDMS methods to characterize the oligomers formed from biotherapeutic monoclonal antibodies during purification, freeze/thaw cycles, or heat stress. Similar experiments performed on a model protein, bovine serum albumin (BSA), investigate how protein monomer concentration and the presence of aggregation inhibitors affects the oligomer size and shape after heat stress. These experiments show, for the first time, the conformational heterogeneity of small protein oligomers, how aggregation inhibitors or protein concentration affects the aggregation pathway and kinetics at the individual oligomer level, and demonstrate the promise of CDMS as a high-throughput technique for characterizing the effect of drugs or additives on the aggregation of proteins related to neurodegenerative disease and biotherapies.

Table of Contents

Acknowledgements

Firstly, I would like to thank my mentor Professor Evan Williams for his support and guidance. Evan has been a consistent source of career mentorship, scientific guidance, and inspiration. I think it is rare to find an advisor who cares so much about the success of their students and is willing to provide so much for their success. I owe much of the work presented here, and surely much of the work I hope to accomplish in my future career, to his mentorship and guidance during my Ph.D.

I would also like to thank the current and former members of the Williams lab for all of their help and friendship over the years. In particular, many insightful discussions and fruitful collaborations with Dr. Conner Harper have helped me to understand so much about mass spectrometry instrumentation and applications. He has been a consistent source of enjoyable conversation. I also owe special thanks to Dr. Zijie Xia, who taught me how to fabricate nanoelectrospray emitters, and Prof. James S. Prell, whose continued support has helped in earning several awards and fellowships. Thanks are also owed to Casey Chen, Matt McPartlan, Zachary Miller, and Veena Avadhani, whose discussion and friendship made times in the Williams lab brighter and to Katherine Lee for being a fantastic undergraduate researcher. These individuals, through our daily interactions and occasional outings, have made my time in the Williams lab full of special memories and their companionship will be sorely missed. I would also like to thank the scientists at Merck & Co., Inc., in particular Dr. Fan Zhang, whose continued collaboration and generous sample provisions have helped me to learn much about the analysis of biopharmaceuticals. Without the support of her and other scientists at Merck, much of the laser-heating and CDMS experiments described in this work would not have been possible.

I would also like to thank many individuals who have welcomed me into the mass spectrometry community at conferences, seminars, and other events. Fruitful discussions at posters, coffee breaks, and lunches have sparked many ideas that will continue to influence me in my future endeavors. I would also like to thank the ASMS hospitality suites for being a particularly potent catalyst for scientific conversation and friendship.

I would also like to thank all those who supported me in achieving my dream of pursuing a Ph.D., in particular Prof. Jeffrey Yarger, who generously welcomed me into his lab as a naïve high school student, Dr. Bennett Addison, who taught me to think critically as an undergraduate researcher, Prof. Timothy Steimle and Dr. Anh T. Le, who taught me the basics of instrumentation and strongly encouraged my application to UC Berkeley, and Dr. Trent Northen, who took a chance on someone with no practical knowledge of mass spectrometry and introduced me to the field that is now my passion.

I would also like to thank the many friends I met at Berkeley who helped me to enjoy life outside of the lab. In particular, I have greatly treasured my friendships with Darren Kahan, Erin Katz, Jon Kruppe, Daniel Mamane, Ulrike Warzok, Garrett Schmelzel, Virginia Lenander, and many in the Bay Area musician community. Thank you all for reminding me that science can take the backseat every once in a while to enjoy life.

I would also like to thank my family for their continued support of me throughout the many years of my academic journey. In particular, my mother who worked hard to give me the chance to even begin in higher education. Finally, I would like to thank Hanneke Leegwater, whose continued support, encouragement, and conversation has provided a beacon of light to navigate the muddied waters of COVID, my Ph.D., and life.

Chapter 1

Introduction

1.1 Overview

Modern analytical instrumentation has enabled the characterization and quantification of many different types of biochemically relevant molecules. This revolution has resulted in the establishment of many different so-called "-omics" fields: proteomics, metabolomics, lipidomics, and glycomics to name just a few. The ability to characterize these molecules enhances our understanding of the connections between different classes of macromolecules in biology, which has proven important towards understanding the underlying causes of several human diseases. Modern methods for performing these analyses can distinguish tens to tens of thousands of different compounds or sequences using high-throughput workflows that often require just a few hours - days of measurement time compared to the months – years of the previous century. New techniques are continuously being developed with the promise of faster measurement times, lower overall costs, and increased portability that will expand the use of these -omics methodologies in the field, in the clinic, and at the research bench.

Mass spectrometry (MS), which separates ions based on differences in the mass-to-charge ratio (m/z), is an excellent method for the separation of complex mixtures.[1] Advances in mass spectrometry technology have been a critical component of advances in the -omics fields. Modern MS instruments are capable of identifying compounds at attomolar concentrations and resolving species with mass differences of less than 0.001 Da in less than 1 second.[2] MS experiments as early as the 1970s reported some success in ionizing large biomolecules using fast atom bombardment,[3] secondary ion MS,[4] and ^{252}Cf plasma desorption,[5,6] but these techniques were generally disruptive to protein tertiary structure. In the late 1980s, developments in electrospray ionization (ESI)[7] and matrix assisted laser desorption ionization (MALDI)[8] enabled the gentle transfer of biomolecular species into the gas-phase and preservation of their structure. Continued developments in ionization technologies, separations methods, detector designs, and ion transfer optics have followed suit that have enabled MS experiments that provide significant insight into biochemical and biological problems relevant to human health and the environment.[2,9,10]

Proteins typically have a well-regulated 3D structure that is dependent on the primary sequence and is critical for correct biochemical function.[11] The biophysical properties of these protein structures can be studied using native MS. In native MS, intact, folded forms of biomacromolecules and their complexes are transferred into the gas-phase using ESI and "native" structures from solution are preserved in the gas-phase by kinetic trapping.[9,12,13] Native MS has become a well-established technique for the characterization of the mass, stoichiometry, shape, ligand binding affinities, and stability of proteins, protein complexes, DNA/RNA structures, monoclonal antibody therapeutics (mAbs) and drug-antibody complexes.[9,14,15] Although native MS typically requires the use of volatile salts such as ammonium acetate to provide ionic strength and prevent extensive salt adduction and chemical noise caused by salt clusters from obscuring protein signal in mass spectra,[16] developments in ionization apparatus have made it possible to obtain quantitative information about ligand-binding affinities and to measure native mass spectra directly from biochemically relevant buffers, which is the topic of section 1.3. Orthogonal

experiments performed in tandem, such as ion mobility spectrometry[17,18] or collisional activation,[19,20] can be used with MS to obtain additional information about the abundances of individual protein conformers or the composition and connections between subunits of protein complexes, respectively. These methods have also been combined with developments in ionization apparatus to measure thermochemical values of proteins and their ligand-bound complexes as a function of temperature,[21] which is discussed in more detail in section 1.4. Native MS methods are continuing to become faster, more sensitive, and higher resolution with the aim to obtain more information about the biophysical properties of biomolecules in states that mimic those present in living organisms.

Native mass spectrometry has significant advantages for characterizing the smaller oligomeric states of proteins including high sensitivity and speed, the ability to distinguish species based on differences in mass, and the ability to kinetically trap what can be transient structures via ESI.[22–24] These advantages are described in more detail and compared to other conventional analytical characterization techniques for protein aggregates in section 1.5. However, characterizing full length proteins or higher order aggregates using native MS is hampered by the mass range of conventional MS instrumentation that measures ensembles of ions. Complex mixtures of high molecular mass species can lead to charge-state distributions with overlapping *m/z* values that prevents information about ion charge and hence mass from being obtained.[25] Charge detection mass spectrometry (CDMS), which separately measures the *m/z* and charge (*z*) of ions, is a promising method to overcome these analytical challenges and is discussed further in section 1.6.

The work described herein focuses on the development of higher-throughput, native MS methods for obtaining detailed information about biomolecules and their aggregates. High-throughput measurements are achieved by overall faster measurement times, which enables more samples to be analyzed within a given time period, and the ability to obtain information in a single measurement that previously would have required the use of multiple techniques, shortening the overall time required to analyze a single sample. These advantages enable a larger number of measurements to be made per day without sacrificing the quality of information obtained from each measurement. In chapters 2, 3, and 4, submicron diameter electrospray emitters are used to provide evidence for the existence of homochiral serine clusters at low abundance in solution, to compare the stability of heterochiral and homochiral species formed from solution versus from fragmentation of larger structures in the gas-phase, and to provide an explanation for observations by many in the MS community of a "magic" high abundance serine octamer. In chapter 5, a protocol for manufacturing and using these emitters is given with the intent to increase their use in the native MS community. Chapter 6 investigates the relationship between emitter diameter and ESI voltage on ESI droplet sizes, while also investigating a unique ionization mechanism that only occurs from submicron diameter emitters at high voltage. In chapters 7 and 8, a new method and apparatus is developed that uses an infrared laser to rapidly obtain protein melting curves by MS and to investigate the stabilizing effect of a protein-ligand interaction on the thermal denaturation of an aggregation-prone protein. In chapter 9, temperature-dependent ion mobility-mass spectrometry measurements indicate both elongated and compact conformers of the model protein cytochrome *c* are formed at high temperatures *from the same solution*. In chapters 10, 11, and 12, CDMS is applied to investigate the size and conformation of protein and antibody oligomers after heat and freeze-thaw cycle stress in the absence and presence of aggregation inhibitors, providing detailed insight into the kinetics and mechanism of aggregation at the level of individual conformational families for individual oligomers.

1.2 Electrospray Ionization (ESI)

1.2.1 Ionization Mechanisms

Electrospray ionization is performed by applying a high potential between solutions containing the analytes of interest and the mass spectrometer inlet or ground.[26] Competition between the electrostatic force and the surface tension of the solution results in the formation of a Taylor cone at the emitter tip.[26–28] When the electric field becomes strong enough to overcome the surface tension of the solution, a spray is formed from the Taylor cone that, depending on the emitter diameter,[29] flow rate of the solution,[30] surface tension of the solvent,[29,30] and electrospray voltage,[29–33] produces droplets between a few nm to microns in size. This process has been well characterized and documented by photography- and microscopy-based methods since initial observations by Sir Geoffrey Taylor in the 1960s.[29,32,34]

The mechanism for how gas-phase protein ions are formed from these droplets is still a subject of debate, but there are two dominant models for ion formation. The charge residue model proposes that after formation droplets undergo evaporation, gradually concentrating charge at the surface until the droplet reaches the Rayleigh limit, where coulombic repulsion overcomes the cohesive force of surface tension, resulting in a fission event.[35–37] The progeny droplets of this fission event continue the cycle of evaporation and fission until bare ions are formed. In the final stages of solvent evaporation, charge is deposited onto charge retaining sites on the protein.[38] A wide body of literature on ESI of globular proteins and dendrimers with masses between 6 kDa and 1400 kDa reports typical charging to ~80% of the Rayleigh limit, indicating that these are likely formed by the charge residue mechanism.[37,38]

In contrast, proteins produced from denaturing solutions exhibit charging well above the Rayleigh limit, which has prompted the search for a different model to describe the ionization of unfolded proteins. Another potential model for ionization is the ion evaporation model originally developed by Iribarne and Thomson to describe the transfer of salts into the gas-phase.[39,40] This model describes droplet evaporation until the electric field at the surface is large enough to directly expel solvated ions. This process is only postulated to occur for small droplets with diameters less than 20 – 40 nm and the rate constant for ion evaporation is analyte specific, depending on the atomic size, extent of hydration, and solvation free energy.[39,41–43] A derivative of this mechanism specifically invoked for unfolded proteins is the chain ejection model, whereby a combination of electrostatic and hydrophobic forces drives unfolded protein molecules to the surface of the droplet where they are gradually extruded as electrostatically stretched structures via charge-charge repulsion that detach from the droplet as highly charged ions.[44–46] All currently available evidence that can be directly attributed to ionization by the chain ejection model is from molecular dynamics simulations. The ongoing debate over which of the mechanisms occur and their prevalence reflects the difficulty in characterizing the ESI process at nanometer size-scales experimentally.

1.2.2 ESI Methods

From a practical perspective, ESI methods are often distinguished based on the solvent flow rate. Microflow methods, which utilize microliter per minute flow rates, are commonly employed for experiments coupling liquid-phase separations methods, such as high-performance liquid chromatography, to MS-based characterization methods.[7,36,47] Microflow experiments are typically performed using metal ESI emitters with diameters of ~50 μm or more, which can produce relatively large droplets (>1 μm in diameter) that are difficult to desolvate.[48] This necessitates the use of organic solvents, heated sheath gas flows, or specific source orientations, such as the Z-Spray source from waters, to assist in the droplet desolvation process. Both online and offline nanoflow methods, which use nanoliter per minute flow rates, are routinely used for proteomics and native MS measurements.[49–51] These experiments use metal, quartz, or borosilicate glass emitters with diameter ranging from 200 nm to 30 μm.[51,52] Emitters with diameters smaller than ~2 μm produce smaller droplets (<100 nm in diameter) that are easier to desolvate.[53–55] Emitters with submicron diameters exhibit several unique advantages for protein ESI, which are discussed in the next section. Separating analyte molecules into individual ESI droplets results in less charge competition. This combined with more efficient desolvation of smaller droplets enhances the ionization efficiency and sensitivity of nanoESI compared to microflow ESI.[49,56,57] In addition, the easier desolvation of these smaller droplets enables the use of 100% aqueous solutions, which represent a more native environment for native MS measurements of folded proteins and protein complexes. Chapters 5 and 6 of this work investigate the use and manufacture of nanospray emitters with inner diameters between 200 nm - 2.5 μm for protein measurements. Nanoflow columns are being developed to take advantage of these benefits of lower ESI flow rates during separations which show significant promise for higher throughput, higher sensitivity proteomics and native MS experiments.

The beneficial aspects of nanoelectrospray have prompted the development of even lower flow rate ESI methods. Both pico- and femtoflow regimes have been actively explored.[58–62] These measurements are typically performed from glass emitters with diameters between 50 nm and 450 nm. Picoflow experiments have demonstrated sensitivities and limits of detection in the zeptomolar range and appear to be very promising for the characterization of samples with limited volume.[62] Native mass spectra of peptides and proteins in the femtoflow regime have different average charge states (both higher and lower have been observed) and adduct peak abundances compared to nanoflow experiments on the same solutions.[58,60] The ESI mechanisms underlying these observations, and the analytical properties of these ultra-low flow rate sources, are not well understood yet, but the benefits of low flow rate ESI surely warrant further investigation.

1.3 Submicron Diameter Electrospray Ionization Emitters

The size of nanodroplets produced from ESI emitters depends on the emitter diameter, the electrospray voltage, and other physical properties of the solvent. The droplets produced during nanoESI have been reported to be ~$1/14^{th}$ – $1/20^{th}$ the diameter of the emitter across a range of different solvent conditions and emitter tip sizes.[53–55,58] Therefore, smaller emitter tips produce corresponding smaller initial ESI droplets, which contain fewer analyte molecules on average. By adjusting the analyte concentration and emitter tip diameter, there can be fewer than one analyte molecule, on average, per initial ESI droplet.[55,63] NanoESI performed under these conditions has

several advantages to that performed from higher concentrations or diameter tips, namely (1) the ability to resolve protein charge state distributions from solutions containing high concentrations of nonvolatile salts and (2) the ability to prevent non-specific aggregation from occurring inside electrospray droplets.

1.3.1 Submicron Emitters for Protein Ion Desalting

Under conditions where there is significantly less than one analyte molecule per initial ESI droplet, a majority of droplets contain no analyte molecules of interest. When there are high concentrations of nonvolatile salts in solution, these salts are distributed evenly among the ESI droplets that are formed. This effectively "dilutes" the salt concentration inside of droplets that contain protein analytes of interest, which results in fewer salt adducts to protein ions and resolved protein charge state distributions. This was first demonstrated by the Williams group,[16,55,64–66] and subsequently adopted by others,[67–69] to characterize protein and protein complex,[16,55,64–68,70,71] as well as DNA and RNA strand conformations and stoichiometries[72] directly from biochemically relevant buffers containing high concentrations of NaCl, KCl, HEPES, Tris, PIPES, as well as from ionic and nonionic detergents that mimic the membrane environment. Protein solubilities have been observed to change based on the presence of different salt ions in solution,[65,73] making comparisons between native MS measurements performed in ammonium acetate and other biophysical techniques performed in nonvolatile buffers ambiguous. Submicron emitters are promising for resolving this ambiguity and investigating the effect of different ions on the conformation and stability of biomolecules using native MS methods.

1.3.2 Submicron Emitters Prevent Nonspecific Aggregation

When multiple analyte molecules are present in the same ESI droplet, nonspecific aggregation can occur during solvent evaporation that results in stoichiometries observed in mass spectra that do not match values observed by other solution-phase measurements.[74] Using submicron diameter emitters under conditions that limit the number of analyte molecules per droplet to less than one, nonspecific aggregation can be prevented and the observed complexes must have entered the ESI droplet from solution. This principle has been used for the high-throughput investigation of ligand- and drug-protein binding,[75–79] to determine the number of specifically coordinated salt ions to DNA, RNA, and proteins,[55,68,69,72] and to screen substances of significant environmental concern such as PFAS compounds, for specific interactions with human proteins.[80] Approaches developed by Klassen and coworkers have enabled the characterization of protein-ligand interaction affinities with high accuracy compared to alternative techniques like isothermal titration calorimetry.[75,79] Methods developed by the Donald group for natural products screening have enabled the simultaneous measurement of thousands of small molecules for binding to a target protein.[76,77,81] The rapid measurements of MS as a readout method show significant promise for the use of submicron diameter emitters and nanoESI as a tool for drug development and screening.

1.3.3 The Current Disadvantages of Submicron Emitters

Despite the advantages of submicron diameter nanoESI emitters, widespread use has been limited due to difficulties in reproducible manufacturing and use, as well as experimental artifacts that can affect the observed abundances and charging of proteins in native mass spectra.[16,52,58,77,78,82,83] Different laboratories often use different tip pulling instruments, methods for separating the pulled capillaries, and characterization methods for the resulting diameters.[52] In some cases, the capillaries are separated during the pull, but others manually clip capillaries using dissection scissors and a microscope, which can lead to significant differences in the diameter of tips under the same instrument conditions. Chapter 5 of this work addresses problems in manufacturing and use of these emitters by providing a protocol adaptable to most conventional tip pulling instruments and providing guidelines for use of submicron diameter emitters for native MS measurements.

Due to the small size of submicron diameter emitters, particulates or bubbles in solution can result in clogging that stops the electrospray process.[75,78,84] Several methods have been developed to address this issue, including filtering all buffers through a 0.22 μm filter before use and using capillary action or centrifugation to ensure that sample reaches the end of the emitter without trapping air bubbles.[52,72] Hydroxyl groups on the surface of borosilicate glass emitters are deprotonated at neutral pH.[85,86] Interactions between proteins that have a net positive charge or positively charged regions and the negatively charged glass surface can result in adsorption.[66,87] Proteins with a high isoelectric point can require up to 30 minutes to "elute" from the tip due to surface interactions.[66] In addition, these protein-glass interactions can also result in protein unfolding, as evidenced by significantly higher protein charge states that those observed from larger diameter tips.[87] These issues can be circumvented by coating the interior of the emitters with inert polyethylene glycol or silane-derived coatings.[88,89]

1.4 Native MS for Measuring Protein Conformational Changes

Protein conformation has a significant effect on the charge states observed in native mass spectra.[90] Compact structures exhibit charging below the Rayleigh limit and a narrow charge-state distribution spanning just a few charge states. In contrast, unfolded or elongated structures exhibit charging well above the Rayleigh limit and have broad charge-state distributions that can span a wide range of *m/z* values.[90,91] Thus, the abundance-weighted average charge state and width of the charge-state distribution in protein mass spectra are reflective of the extent of unfolding and conformational heterogeneity of protein molecules in solution.[92,93] Each charge state can result from a single or multiple protein conformers and, conversely, a single conformer can be ionized to form several different charge states.[92] Ion mobility spectrometry is useful for deconvolving these possibilities. In ion mobility measurements, ions drift through a tube filled with low pressure gas (typically He or Ar) under the influence of a weak electric field.[94] The time required for ions to drift through the tube is related to the frequency of collisions with buffer gas molecules and thus the size and shape of the ion. Ions with the same charge state, but different drift times, correspond to different conformations. Drift times can also be converted to rotationally averaged collision

cross sections (in $Å^2$) that are independent of the charge state, providing insight into the effect of various solution conditions on the overall protein conformational ensemble.[95–102] Individual protein conformers can be identified by fitting the collision cross section distribution of each charge state with the minimum number of Gaussian curves required to obtain an overall R^2 value of >0.9.[102–105]

1.4.1 Variable-Temperature Electrospray Ionization (vT-ESI)

Variable-temperature electrospray ionization (vT-ESI), in which mass spectra are acquired as a function of solution temperature, has been used to construct protein,[101,106–113] protein complex,[97,104,111,114–116] and RNA/DNA[117–119] thermal denaturation (melting) curves from mass spectrometry data. Melting curves are obtained using the average charge state, the collision-cross section, or the abundance of individual conformers identified by ion mobility spectrometry as a function of solution temperature. Melting temperatures (T_m), defined in many vT-ESI studies as the inflection point of a two-state model, can be obtained by fitting average charge state versus temperature data and have found to be comparable to T_m values determined from other biophysical characterization methods.[101,104,110,111,120,121] These experiments have been performed on mixtures containing up to 7 proteins, demonstrating the multiplexing capacity of this technique.[108] Relative thermochemical values ($\Delta\Delta G$, $\Delta\Delta H$, $\Delta\Delta S$ to an arbitrary reference state) can also be obtained from vT-ESI measurements using the abundances of individual protein conformations at different temperatures.[97,102,103,122–124] The thermochemistry of individual protein conformers, as well as ligand binding to protein- and DNA-ligand complexes, has been determined using vT-ESI in combination with ion mobility-mass spectrometry measurements.[97,102,103,122–126] Chapter 9 of this work investigates the conformational changes of the model protein cytochrome *c* using vT-ESI, finding evidence for both compaction and unfolding of the native structure at temperatures near the T_m value.

The methods used to heat solutions during ESI differ from laboratory to laboratory and have undergone significant changes since the earliest source designs in the 1990s.[106] Most modern implementations use a design involving resistive heating wire or a heating element wrapped around or placed inside of a thermally conductive metal block containing the electrospray emitter. Temperature measurements are typically performed using a thermocouple placed inside of the metal block close to the emitter, but thermal gradients can still occur due to differences between thermocouple positioning and the position of the emitter. Calibrations can be performed that measure the temperature in the metal block and the temperature inside of the capillary to account for this difference.[110,121] The use of proportional-integral-derivative temperature controllers enables precise control of the temperature of the solution, but the large thermal mass of these sources typically requires between 1 to 3 minutes for thermal equilibration at each temperature, limiting experiment throughput.[106,107,109,110,114,122,125,126] However, recent promising results demonstrate the acquisition of full melting curves for model proteins in <1 minute.[127] Typical vT-ESI sources heat a significant portion of solution in the electrospray emitter, which can result in aggregation and loss of signal at temperatures above the T_m of aggregation-prone proteins. These difficulties in overcoming aggregation have limited the application of vT-ESI to relatively well-behaved proteins that undergo reversible unfolding.

1.4.2 Laser-Based Methods of Protein Thermal Stability Measurements by MS

A promising alternative method of measuring heat-induced protein conformational changes by MS is to heat solutions using an infrared laser. Protein thermal stabilities have been investigated using laser heating either by irradiating the end of electrospray emitters or by heating the electrospray droplets directly. Initial "laser spray" experiments by Hiraoka and coworkers in the 1990s used a focused 10.6 μm infrared laser aligned coaxially with a 100 μm diameter metal electrospray emitter.[128–134] Increases in the applied laser power resulted in an increase in the average charge state of cytochrome *c*.[130] A sigmoidal curve fit to the average charge state versus laser power data was used to obtain a melting power (P_m), which decreased with decreasing pH in a similar trend to the T_m value of cytochrome *c* measured by circular dichroism.[130] Similar experiments were performed to investigate the effects of laser irradiation and laser power on the thermal stabilities of proteins,[130,131,134] as well as protein-DNA and DNA-drug complexes.[128,132] Subsequent investigations found that laser spray can be performed such that no degradation of thermally labile molecules occurs, showing promise as a novel liquid chromatography/mass spectrometry interface for ionizing small molecules.[133,135] Hiraoka and coworkers also reported that laser spray enhanced ion evaporation for salts and surface-active molecules, making this a promising method for ionizing analytes challenging to investigate using conventional electrospray.[136] Building on this early body of literature, chapters 7 and 8 of this work report the development of novel laser heating methods for the rapid measurement of melting curves for model proteins, as well as aggregation-prone proteins and their ligand bound forms.

A focused infrared laser has also been used to directly heat nanodroplets produced from electrospray emitters during ESI. El-Baba *et al.* reported an increase in the weighted average charge state of ubiquitin while heating ESI droplets at high laser power similar to that obtained from vT-ESI experiments at high temperature, suggesting that proteins could be thermally denatured inside of the electrospray droplets.[137] Changing the diameter of the emitter, and thus the size and lifetime of droplets produced during ESI, resulted in different extents of unfolding at constant laser power. Fast conformational rearrangements, including the *cis-trans* isomerization of ubiquitin Pro^{19} could be monitored as a function of emitter size and droplet lifetime. In a similar experiment, Woodall *et al.* investigated the different extents of myoglobin unfolding by vT-ESI and nanodroplet heating.[101] The weighted average charge state of myoglobin increases by +4 charges in vT-ESI experiments, whereas an increase in the average charge state of only +1.5 and +2.5 was observed when heating droplets produced from 4 μm and 24 μm emitters, respectively. The thermal equilibration of the vT-ESI source ensures that conformational changes that occur with increases in temperature reflect equilibrium conditions. In contrast, heating of the nanodroplet, where the droplet lifetime limits the time for protein conformational changes to occur, limits the extent of unfolding that can occur. The droplet lifetime can be readily varied from ~1 μs to ~50 μs,[74,138,139] making droplet heating a promising method for obtaining "kinetic snapshots" of short-lived unfolding intermediates. By tuning solution concentrations and emitter diameters such that there is only a single analyte molecule per droplet, these experiments have the potential to investigate the thermal denaturation of the monomeric form of proteins that aggregate rapidly in the complete absence of further aggregation. These types of experiments show the analytical potential of native mass spectrometry and novel developments in ambient ionization for the

characterization of protein aggregation processes and products, which is explored further in chapters 8, 10, 11, and 12 of this work.

1.5 Methods for Characterizing Protein Aggregation

Protein aggregation is involved in many devastating human diseases including Alzheimers', Parkinsons', and Huntington's disease, as well as in dementia, amyotrophic lateral sclerosis (ALS), and transmissible spongiform encephalopathy.[140,141] Protein-based biotherapeutics can also undergo aggregation during development, shipment, and storage, which can result in inefficacy and toxicity *in vivo*.[142–144] A critical step in the production of biotherapeutics is the optimization of a "formulation buffer" that promotes tolerance of stress and prevents the formation of aggregates. Both neurodegenerative disease research and formulation buffer development require the characterization of protein aggregates formed under a wide range of conditions.

1.5.1 Separative Methods of Measuring Protein Aggregation

Small protein oligomers are routinely characterized using separative methods such as size-exclusion chromatography and analytical ultracentrifugation.[145,146] SEC methods, which separates proteins and oligomers based on differences in their hydrodynamic radii, have demonstrated excellent separation of small aggregates of peptides, proteins, and biotherapeutic antibodies.[147–150] SEC columns typically have a limited mass range over which optimal separation occurs, making it challenging to simultaneously resolve monomers, small oligomers, and higher order aggregates. Protein or oligomer conformations with different hydrodynamic radii can result in additional peaks in an SEC trace, making it challenging to quantify the extent of aggregation for proteins that are conformationally heterogeneous. Analytical ultracentrifugation (AUC) relies on the separation of molecules with different molecular weights under the influence of radial acceleration.[145,146,151,152] AUC has been used to separate disease relevant protein aggregates,[153] including α-synuclein.[154] However, AUC is time-consuming, typically requiring days per experiment, and the precision is dependent on a number of factors including the hardware, sample characteristics, and data analysis approach.[146]

1.5.2 Spectroscopic Methods of Measuring Protein Aggregation

Spectroscopic approaches, including light scattering, turbidity measurements, and fluorescence assays, can also be used to quantify the formation of much larger protein aggregates.[146] Fluorescence assays can be performed using hydrophobic dyes, such as Thioflavin T, that exhibit increased fluorescence and a characteristic red shift upon binding to β-sheet rich amyloid structures.[155,156] Thioflavin T assays are commonly used in both the biopharmaceutical industry and in academic research for characterizing the formation of protein aggregates, but some

reports have indicated that the presence of the dye can alter the biophysical properties of non-amyloid protein analytes and may affect aggregation kinetics.[155,157–159] Light scattering measurements report on the average size of complexes in solution. These measurements are routinely used to provide information about the kinetics of large aggregation formation for a number of proteins in both biopharmaceutical and academic research.[160–163] Similarly, turbidity measurements provide information about the formation of large insoluble aggregates that scatter sufficient light to produce noticeable changes in light transmission.[145,164,165] These techniques have the benefit that they are simple to perform, widely available, and provide reliable information about the formation of large insoluble aggregates, but they are relatively insensitive to protein conformation, require the use of pure samples as they cannot distinguish between individual components in mixtures, and cannot be used to quantify the individual abundances of small oligomers.

A recently developed alternative spectroscopic technique for measuring protein aggregation is mass photometry.[166] Mass photometry measures the scattering of light as molecules interact with a glass surface.[166] A comparison against standard calibrants is then used to determine the mass of molecules based on the amount of scattered light. To date, mass photometry has been used to investigate the formation of small protein oligomers,[167] to separate protein and antibody complexes with different stoichiometries,[168–170] to characterize the polymerization process of actin,[171] and even to characterize droplets formed from liquid-liquid phase separation of α-synuclein.[172] Oligomers can be effectively resolved across a mass range spanning from a few kDa to several MDa, which appears promising for characterizing protein aggregation.[25] However, mass photometry does not provide any information about oligomer conformations. Inaccurate masses have been reported for proteins that deviate from globular shapes, indicating that mass photometry may not be effective for the analysis of conformationally heterogenous samples.

1.5.3 Native Mass Spectrometry for Measuring Protein Aggregation

Native MS is a promising technique for characterizing the formation, structure, and gas-phase stability of smaller protein oligomers. In combination with ion mobility spectrometry, abundance and shape information have been obtained for several small proteins and peptides relevant to human disease, including Aβ,[24,173–175] Tau,[176–178] TDP-43,[179,180] α-synuclein,[93,181,182] SOD1,[183] prion protein,[184,185] and insulin.[186–189] Information about oligomer secondary structure has also been obtained using a combination of gas-phase infrared spectroscopy and IMS-MS.[190–192] Antibody complexes as large as ~1.4 MDa containing up to 7 components have been well-resolved using native MS,[170,193] but the presence of heterogenous components can result in unresolved charge state distributions and no information about the mass of higher order complexes.[170] Characterizing the aggregates formed from the full-length forms of disease relevant proteins remains challenging due to detection and resolution limitations of conventional MS instruments for high *m/z* ions and the intrinsic heterogeneity of large protein oligomers, which can result in significant overlap in *m/z* that prevents any information from being obtained from *m/z*-only native mass spectra.[25]

1.6 Charge Detection Mass Spectrometry

An alternative approach to characterizing large, conformationally heterogeneous protein aggregates is charge detection mass spectrometry (CDMS). In CDMS, the *m/z* and charge (*z*) of individual ions are measured separately, preventing the need for resolved charge states to obtain mass information, as in conventional native MS. This approach has two main advantages: 1) mass information can be obtained for very high mass ions, for which charge states cannot typically be resolved in *m/z,* and 2) the mass of ions that have the same *m/z* but different mass or charge can be individually measured. These advantages make CDMS a promising technique for the characterization of protein oligomers and the protein aggregation process.

1.6.1 Homemade CDMS Instrumentation

"Single tube" CDMS instruments originated in the 1960s and were developed to characterize micron-sized dust particles in order to study the effects of their collisions with spacecraft.[194] This detector geometry consisted of a single conductive tube upon which a charge pulse is induced as ions pass through it. The *m/z* can be determined based on the velocity of the ion (determined from the width of the charge pulse) and the *z* is proportional to the amplitude of the charge pulse. Detector electronics innovations by Benner and coworkers in the 1990s resulted in significantly lower noise and charge thresholds and compatibility with electrospray ionization sources.[195–197] This was subsequently used to characterize the mass of high molecular weight biomolecules, including large DNA assemblies and intact viruses with masses between 1 – 31 MDa and 6 – 41 MDa, respectively.[195,197] Later implementations of similar single tube CDMS instruments by Jarrold, Dugourd, and Antoine, were used to measure the mass and charge of electrospray droplets,[198] nanoparticles with sizes between ~0.1 – 30 GDa,[199–201] and even intact amyloid fibrils.[202,203] While measurements using single tube CDMS instruments are fast, requiring only up to ~100 μs per measurement, and thus beneficial for measuring large numbers of ions quickly, the high noise levels and corresponding error in the charge measurement associated with a single measurement lead to large errors in the determined mass and relatively low resolution. Gamero-Castaño developed "array detector" CDMS to remedy this problem by using multiple detector tubes aligned in series.[204] The addition of multiple detector tubes increases the signal-to-noise in the time domain, which reduces the uncertainty in charge by √N, where N is the number of detectors. Designs with up to 22 tubes were implemented with charge thresholds of ~10 *e* and detection thresholds of ~100 *e*.[205] While this was effective for reducing uncertainty, gains in precision were ultimately limited by the maximum number of detector tubes that could be aligned in series.

An alternative method to obtain higher charge precision is to measure ions multiple times as they move back and forth in a trap. This has the advantage that the number of measurements is then limited only by how long ions can be trapped. The first "Benner Trap" consisted of electrostatic ion mirrors that passed ions back and forth through a field free region containing a charge conductive tube.[206] This apparatus was used to measure the mass of a ~3 MDa DNA plasmid ion to high precision with a charge uncertainty of ~2 *e*. Jarrold and coworkers first demonstrated that FT analysis could be applied to trapped CDMS by relating the *m/z* of the ion to the measured frequency and a calibration constant that depends on trap geometry, ion energy, and ion velocity.[207]

Subsequent technical developments, including cryogenically cooling the detector and selecting the energy of ions entering the trap, resulted in charge uncertainties and charge detection thresholds of <0.2 *e* and 1 *e*, respectively.[208–211] Measuring single ions at a time can result in long experiment times, but the presence of multiple ions in the trap can result in ion-ion interactions that alter their energy and result in higher charge uncertainties. To resolve this issue, the Williams group demonstrated dynamic measurements of ion energy, enabling the measurement of multiple ions simultaneously.[212–215] Dynamic ion energy measurements have shown to be critical for the analysis of ion-ion interactions, as well as characterizing the evaporation and fission behavior of trapped nanodroplets.[216,217]

1.6.2 Commercial CDMS Instrumentation

In collaboration with Thermofisher Scientific, several research groups have also established the use of commercial instruments for CDMS.[180,218–221] Heck and coworkers pioneered the use of Orbitrap instruments for characterizing the heterogeneity and stoichiometry of monoclonal antibodies[170,222,223] and biopharmaceutically relevant virus capsids.[224,225] Comparisons with other conventional techniques often used for characterizing these samples, such as SEC or mass photometry, demonstrated the analytical capacity of Orbitrap CDMS for providing insight into the higher molecular weight species in these samples.[170] Top-down proteomics workflows developed in the Kelleher group have provided insight into large protein complexes involved in disease response.[180,218,226] The thermal stability of capsids from different AAV serotypes was compared as a function of pH using a vT-ESI source and Orbitrap CDMS.[116] CDMS on products formed by surface-induced dissociation, a method of rapid, high-energy activation in the gas phase, has been used to characterize the dissociation energy and pathways of intact AAV capsids of different serotypes.[227] The ease of use of these commercial instruments will surely continue to promote the combination of CDMS with ESI and MS methods commonly employed for smaller biomolecules to obtain more information about high molecular weight species relevant to human health and disease.

1.6.3 CDMS for Investigating Protein Aggregates

CDMS has been applied to the investigation of heterogeneous protein complexes,[180,213,215,227] replication and folding machinery,[108,228,229] intact viruses,[116,230–235] virus-like particles,[14,217,236] and vaccine formulations,[236] as well as synthetic polymers,[199,201] large salt clusters,[237] aqueous nanodroplets,[216,238] and synthetic nanoparticles with masses extending into the GDa mass range.[217,239,240] Modern CDMS instruments have a demonstrated ability to simultaneously measure across a wide range of mass and charge. Historically, the high charge uncertainty and charge threshold of CDMS instruments have enabled only the average mass of large protein aggregates to be obtained. Chapters 10, 11, and 12 of this work describe the application of a high resolution homemade CDMS instrument for quantifying the size and conformation of individual protein and antibody oligomers formed in response to purification, freeze-thaw cycles, and thermal stress, building upon a recent body of CDMS literature where

protein and antibody assemblies are well-resolved. CDMS appears to be well-suited for characterizing protein aggregation products with high resolution for both size and shape that could prove beneficial at different stages of drug development, for quality control, for optimizing formulation buffers for biopharmaceutical stability and for the discovery of novel compounds for inhibiting the aggregation of disease-causing amyloid-forming proteins.

1.7 References

(1) Glish, G. L.; Vachet, R. W. The Basics of Mass Spectrometry in the Twenty-First Century. *Nat. Rev. Drug. Discov.* **2003**, *2* (2), 140–150.

(2) Peters-Clarke, T. M.; Coon, J. J.; Riley, N. M. Instrumentation at the Leading Edge of Proteomics. *Anal. Chem.* **2024**, *96* (20), 7976–8010.

(3) Barber, M.; Bordoli, R. S.; Sedgwick, R. D.; Tyler, A. N. Fast Atom Bombardment of Solids (F.A.B.): A New Ion Source for Mass Spectrometry. *J. Chem. Soc. Chem. Commun.* **1981**, No. 7, 325.

(4) Benninghoven, Alfred.; Sichtermann, W. K. Detection, Identification, and Structural Investigation of Biologically Important Compounds by Secondary Ion Mass Spectrometry. *Anal. Chem.* **1978**, *50* (8), 1180–1184.

(5) Sundqvist, B.; Kamensky, I.; Håkansson, P.; Kjellberg, J.; Salehpour, M.; Widdiyasekera, S.; Fohlman, J.; Peterson, P. A.; Roepstorff, P. Californium-252 Plasma Desorption Time of Flight Mass Spectroscopy of Proteins. *Biol. Mass Spectrom.* **1984**, *11* (5), 242–257.

(6) Torgerson, D. F.; Skowronski, R. P.; Macfarlane, R. D. New Approach to the Mass Spectroscopy of Non-Volatile Compounds. *Biochem. Biophys. Res. Commun.* **1974**, *60* (2), 616–621.

(7) Fenn, J. B.; Mann, M.; Meng, C. K.; Wong, S. F.; Whitehouse, C. M. Electrospray Ionization for Mass Spectrometry of Large Biomolecules. *Science* **1989**, *246* (4926), 64–71.

(8) Tanaka, K.; Waki, H.; Ido, Y.; Akita, S.; Yoshida, Y.; Yoshida, T.; Matsuo, T. Protein and Polymer Analyses up to *m/z* 100 000 by Laser Ionization Time-of-flight Mass Spectrometry. *Rapid Commun. Mass Spectrom.* **1988**, *2* (8), 151–153.

(9) Leney, A. C.; Heck, A. J. R. Native Mass Spectrometry: What Is in the Name? *J. Am. Soc. Mass Spectrom.* **2017**, *28* (1), 5–13.

(10) Lebedev, A. T. Environmental Mass Spectrometry. *Ann. Rev. Anal. Chem.* **2013**, *6* (1), 163–189.

(11) Alberts, B.; Johnson, A.; Lewis, J.; Morgan, D.; Raff, M.; Roberts, K.; Walter, P. *Molecular Biology of the Cell*; Wilson, J., Hunt, T., Eds.; W.W. Norton & Company, 2017.

(12) Fort, K. L.; Silveira, J. A.; Pierson, N. A.; Servage, K. A.; Clemmer, D. E.; Russell, D. H. From Solution to the Gas Phase: Factors That Influence Kinetic Trapping of Substance P in the Gas Phase. *J. Phys. Chem. B* **2014**, *118* (49), 14336–14344.

(13) Breuker, K.; Mclafferty, F. W. Electrospray Into the Gas Phase, 10^{-12} To 10^{2} s. *Proc. Nat. Acad. Sci.* **2008**, *105* (47), 18145–18152.

(14) Tamara, S.; den Boer, M. A.; Heck, A. J. R. High-Resolution Native Mass Spectrometry. *Chem. Rev.* **2022**, *122* (8), 7269–7326.

(15) Schachner, L. F.; Ives, A. N.; McGee, J. P.; Melani, R. D.; Kafader, J. O.; Compton, P. D.; Patrie, S. M.; Kelleher, N. L. Standard Proteoforms and Their Complexes for Native Mass Spectrometry. *J. Am. Soc. Mass Spectrom.* **2019**, *30* (7), 1190–1198.
(16) Susa, A. C.; Xia, Z.; Williams, E. R. Native Mass Spectrometry from Common Buffers with Salts That Mimic the Extracellular Environment. *Angew. Chem., Int. Ed.* **2017**, *56* (27), 7912–7915.
(17) Wyttenbach, T.; Pierson, N. A.; Clemmer, D. E.; Bowers, M. T. Ion Mobility Analysis of Molecular Dynamics. *Annu. Rev. Phys. Chem.* **2014**, *65* (1), 175–196.
(18) Bohrer, B. C.; Merenbloom, S. I.; Koeniger, S. L.; Hilderbrand, A. E.; Clemmer, D. E. Biomolecule Analysis by Ion Mobility Spectrometry. *Ann. Rev. Anal. Chem.* **2008**, *1* (1), 293–327.
(19) Stiving, A. Q.; VanAernum, Z. L.; Busch, F.; Harvey, S. R.; Sarni, S. H.; Wysocki, V. H. Surface-Induced Dissociation: An Effective Method for Characterization of Protein Quaternary Structure. *Anal. Chem.* **2019**, *91* (1), 190–209.
(20) Benesch, J. L. P.; Aquilina, J. A.; Ruotolo, B. T.; Sobott, F.; Robinson, C. V. Tandem Mass Spectrometry Reveals the Quaternary Organization of Macromolecular Assemblies. *Chem. Biol.* **2006**, *13* (6), 597–605.
(21) Laganowsky, A.; Clemmer, D. E.; Russell, D. H. Variable-Temperature Native Mass Spectrometry for Studies of Protein Folding, Stabilities, Assembly, and Molecular Interactions. *Annu. Rev. Biophys.* **2022**, *51* (1), 63–77.
(22) Muneeruddin, K.; Thomas, J. J.; Salinas, P. A.; Kaltashov, I. A. Characterization of Small Protein Aggregates and Oligomers Using Size Exclusion Chromatography with Online Detection by Native Electrospray Ionization Mass Spectrometry. *Anal. Chem.* **2014**, *86* (21), 10692–10699.
(23) Wang, G.; Johnson, A. J.; Kaltashov, I. A. Evaluation of Electrospray Ionization Mass Spectrometry as a Tool for Characterization of Small Soluble Protein Aggregates. *Anal. Chem.* **2012**, *84* (3), 1718–1724.
(24) Bernstein, S. L.; Dupuis, N. F.; Lazo, N. D.; Wyttenbach, T.; Condron, M. M.; Bitan, G.; Teplow, D. B.; Shea, J.-E.; Ruotolo, B. T.; Robinson, C. V.; Bowers, M. T. Amyloid-β Protein Oligomerization and the Importance of Tetramers and Dodecamers in the Aetiology of Alzheimer's Disease. *Nat. Chem.* **2009**, *1* (4), 326–331.
(25) Jordan, J. S.; Harper, C. C.; Zhang, F.; Kofman, E.; Li, M.; Sathiyamoorthy, K.; Zaragoza, J. P.; Fayadat-Dilman, L.; Williams, E. R. Charge Detection Mass Spectrometry Reveals Conformational Heterogeneity in Megadalton-Sized Monoclonal Antibody Aggregates. *J. Am. Chem. Soc.* **2024**, *146* (33), 23297–23305.
(26) Wilm, M. Principles of Electrospray Ionization. *Mol. Cell Proteomics* **2011**, *10* (7), M111.009407.
(27) Wilm, M. S.; Mann, M. Electrospray and Taylor-Cone Theory, Dole's Beam of Macromolecules at Last? *Int. J. Mass Spectrom. Ion Processes* **1994**, *136* (2–3), 167–180.
(28) Taylor, G. Disintegration of Water Drops in an Electric Field. *Proc. R. Soc. Lond. A Math Phys. Sci.* **1964**, *280* (1382), 383–397.
(29) Olumee, Z.; Callahan, J. H.; Vertes, A. Droplet Dynamics Changes in Electrostatic Sprays of Methanol−Water Mixtures. *J. Phys. Chem. A* **1998**, *102* (46), 9154–9160.
(30) Smith, J. N.; Flagan, R. C.; Beauchamp, J. L. Droplet Evaporation and Discharge Dynamics in Electrospray Ionization. *J. Phys. Chem. A* **2002**, *106* (42), 9957–9967.
(31) Gañán-Calvo, A. M.; Dávila, J.; Barrero, A. Current and Droplet Size in the Electrospraying of Liquids. Scaling Laws. *J. Aerosol Sci.* **1997**, *28* (2), 249–275.

(32) Gomez, A.; Tang, K. Charge and Fission of Droplets in Electrostatic Sprays. *Phys. Fluids* **1994**, *6* (1), 404–414.
(33) Tang, K.; Gomez, A. Generation of Monodisperse Water Droplets from Electrosprays in a Corona-Assisted Cone-Jet Mode. *J. Colloid Interface Sci.* **1995**, *175* (2), 326–332.
(34) Tang, K.; Gomez, A. On the Structure of an Electrostatic Spray of Monodisperse Droplets. *Phys. Fluids* **1994**, *6* (7), 2317–2332.
(35) Winger, B. E.; Light-Wahl, K. J.; Ogorzalek Loo, R. R.; Udseth, H. R.; Smith, R. D. Observation and Implications of High Mass-to-Charge Ratio Ions from Electrospray Ionization Mass Spectrometry. *J. Am. Soc. Mass Spectrom.* **1993**, *4* (7), 536–545.
(36) Mack, L. L.; Kralik, P.; Rheude, A.; Dole, M. Molecular Beams of Macroions. *J. Chem. Phys.* **1970**, *52* (10), 4977–4986.
(37) Fernandez de la Mora, J. Electrospray Ionization of Large Multiply Charged Species Proceeds via Dole's Charged Residue Mechanism. *Anal. Chim. Acta* **2000**, *406* (1), 93–104.
(38) Susa, A. C.; Xia, Z.; Tang, H. Y. H.; Tainer, J. A.; Williams, E. R. Charging of Proteins in Native Mass Spectrometry. *J. Am. Soc. Mass Spectrom.* **2017**, *28* (2), 332–340.
(39) Iribarne, J. V.; Thomson, B. A. On the Evaporation of Small Ions from Charged Droplets. *J. Chem. Phys.* **1976**, *64* (6), 2287.
(40) Thomson, B. A.; Iribarne, J. V. Field Induced Ion Evaporation from Liquid Surfaces at Atmospheric Pressure. *J. Chem. Phys.* **1979**, *71* (11), 4451–4463.
(41) Gamero-Castaño, M.; Fernández De La Mora, J. Mechanisms of Electrospray Ionization of Singly and Multiply Charged Salt Clusters. *Anal. Chim. Acta* **2000**, *406* (1), 67–91.
(42) Hogan, C. J.; Biswas, P.; Chen, D. R. Charged Droplet Dynamics in the Submicrometer Size Range. *J. Phys. Chem. B* **2009**, *113* (4), 970–976.
(43) Hogan, C. J.; Carroll, J. A.; Rohrs, H. W.; Biswas, P.; Gross, M. L. Combined Charged Residue-Field Emission Model of Macromolecular Electrospray Ionization. *Anal. Chem.* **2009**, *81* (1), 369–377.
(44) Aliyari, E.; Konermann, L. Formation of Gaseous Proteins via the Ion Evaporation Model (IEM) in Electrospray Mass Spectrometry. *Anal. Chem.* **2020**, *92* (15), 10807–10814.
(45) Konermann, L.; Metwally, H.; Duez, Q.; Peters, I. Charging and Supercharging of Proteins for Mass Spectrometry: Recent Insights into the Mechanisms of Electrospray Ionization. *Analyst* **2019**, *144* (21), 6157–6171.
(46) Metwally, H.; Duez, Q.; Konermann, L. Chain Ejection Model for Electrospray Ionization of Unfolded Proteins: Evidence from Atomistic Simulations and Ion Mobility Spectrometry. *Anal. Chem.* **2018**, *90* (16), 10069–10077.
(47) Whitehouse, C. M.; Dreyer, R. N.; Yamashita, M.; Fenn, J. B. Electrospray Interface for Liquid Chromatographs and Mass Spectrometers. *Anal. Chem.* **1985**, *57* (3), 675–679.
(48) Markert, C.; Thinius, M.; Lehmann, L.; Heintz, C.; Stappert, F.; Wissdorf, W.; Kersten, H.; Benter, T.; Schneider, B. B.; Covey, T. R. Observation of Charged Droplets from Electrospray Ionization (ESI) Plumes in API Mass Spectrometers. *Anal. Bioanal. Chem.* **2021**, *413* (22), 5587–5600.
(49) Wilm, M.; Mann, M. Analytical Properties of the Nanoelectrospray Ion Source. *Anal. Chem.* **1996**, *68* (1), 1–8.
(50) Shen, Y.; Zhao, R.; Berger, S. J.; Anderson, G. A.; Rodriguez, N.; Smith, R. D. High-Efficiency Nanoscale Liquid Chromatography Coupled On-Line with Mass Spectrometry Using Nanoelectrospray Ionization for Proteomics. *Anal. Chem.* **2002**, *74* (16), 4235–4249.

(51) Gibson, G. T. T.; Mugo, S. M.; Oleschuk, R. D. Nanoelectrospray Emitters: Trends and Perspective. *Mass Spectrom. Rev.* **2009**, *28* (6), 918–936.
(52) Jordan, J. S.; Xia, Z.; Williams, E. R. Tips on Making Tiny Tips: Secrets to Submicron Nanoelectrospray Emitters. *J. Am. Soc. Mass Spectrom.* **2022**, *33* (3), 607–611.
(53) Davidson, K. L.; Oberreit, D. R.; Hogan, C. J.; Bush, M. F. Nonspecific Aggregation in Native Electrokinetic Nanoelectrospray Ionization. *Int. J. Mass Spectrom.* **2017**, *420*, 35–42.
(54) Hollerbach, A.; Logsdon, D.; Iyer, K.; Li, A.; Schaber, J. A.; Graham Cooks, R. Sizing Sub-Diffraction Limit Electrosprayed Droplets by Structured Illumination Microscopy. *Analyst* **2018**, *143* (1), 232–240.
(55) Susa, A. C.; Xia, Z.; Williams, E. R. Small Emitter Tips for Native Mass Spectrometry of Proteins and Protein Complexes from Nonvolatile Buffers That Mimic the Intracellular Environment. *Anal. Chem.* **2017**, *89* (5), 3116–3122.
(56) Juraschek, R.; Dülcks, T.; Karas, M. Nanoelectrospray—More than Just a Minimized-Flow Electrospray Ionization Source. *J. Am. Soc. Mass Spectrom.* **1999**, *10* (4), 300–308.
(57) El-Faramawy, A.; Siu, K. W. M.; Thomson, B. A. Efficiency of Nano-Electrospray Ionization. *J. Am. Soc. Mass Spectrom.* **2005**, *16* (10), 1702–1707.
(58) Li, H.; Allen, N.; Li, M.; Li, A. Conducting and Characterizing Femto Flow Electrospray Ionization. *Analyst* **2022**, *147* (6), 1071–1075.
(59) Allen, N.; Li, H.; Wang, T.; Li, A. Gigaohm and Teraohm Resistors in Femtoamp and Picoamp Electrospray Ionization. *J. Am. Soc. Mass Spectrom.* **2022**, *34* (5), 913-921.
(60) Allen, N. R.; Li, H.; Cheung, A.; Xu, G.; Zi, Y.; Li, A. Femtoamp and Picoamp Modes of Electrospray and Paper Spray Ionization. *Int. J. Mass Spectrom.* **2021**, *469*, 116696.
(61) Xiang, P.; Zhu, Y.; Yang, Y.; Zhao, Z.; Williams, S. M.; Moore, R. J.; Kelly, R. T.; Smith, R. D.; Liu, S. Picoflow Liquid Chromatography–Mass Spectrometry for Ultrasensitive Bottom-Up Proteomics Using 2-μm-i.d. Open Tubular Columns. *Anal. Chem.* **2020**, *92* (7), 4711–4715.
(62) Marginean, I.; Tang, K.; Smith, R. D.; Kelly, R. T. Picoelectrospray Ionization Mass Spectrometry Using Narrow-Bore Chemically Etched Emitters. *J. Am. Soc. Mass Spectrom.* **2014**, *25* (1), 30–36.
(63) Jordan, J. S.; Williams, E. R. Effects of Electrospray Droplet Size on Analyte Aggregation: Evidence for Serine Octamer in Solution. *Anal. Chem.* **2021**, *93* (3), 1725–1731.
(64) Susa, A. C.; Lippens, J. L.; Xia, Z.; Loo, J. A.; Campuzano, I. D. G.; Williams, E. R. Submicrometer Emitter ESI Tips for Native Mass Spectrometry of Membrane Proteins in Ionic and Nonionic Detergents. *J. Am. Soc. Mass Spectrom.* **2018**, *29* (1), 203–206.
(65) Xia, Z.; DeGrandchamp, J. B.; Williams, E. R. Native Mass Spectrometry beyond Ammonium Acetate: Effects of Nonvolatile Salts on Protein Stability and Structure. *Analyst* **2019**, *144* (8), 2565–2573.
(66) Xia, Z.; Williams, E. R. Protein-Glass Surface Interactions and Ion Desalting in Electrospray Ionization with Submicron Emitters. *J. Am. Soc. Mass Spectrom.* **2018**, *29* (1), 194–202.
(67) Chen, Y.; Yuan, S.; Liu, Y.; Huang, G. Rapid Desalting during Electrospray Ionization Mass Spectrometry for Investigating Protein-Ligand Interactions in the Presence of Concentrated Salts. *Anal. Chim. Acta* **2021**, *1141*, 120–126.
(68) Agasid, M. T.; Sørensen, L.; Urner, L. H.; Yan, J.; Robinson, C. V. The Effects of Sodium Ions on Ligand Binding and Conformational States of G Protein-Coupled Receptors-Insights from Mass Spectrometry. *J. Am. Chem. Soc.* **2021**, *143* (11), 4085–4089.

(69) Hu, J.; Guan, Q. Y.; Wang, J.; Jiang, X. X.; Wu, Z. Q.; Xia, X. H.; Xu, J. J.; Chen, H. Y. Effect of Nanoemitters on Suppressing the Formation of Metal Adduct Ions in Electrospray Ionization Mass Spectrometry. *Anal. Chem.* **2017**, *89* (3), 1838–1845.
(70) Huang, G.; Li, G.; Cooks, R. G. Induced Nanoelectrospray Ionization for Matrix-Tolerant and High-Throughput Mass Spectrometry. *Angew. Chem., Int. Ed.* **2011**, *50* (42), 9907–9910.
(71) Yuill, E. M.; Sa, N.; Ray, S. J.; Hieftje, G. M.; Baker, L. A. Electrospray Ionization from Nanopipette Emitters with Tip Diameters of Less than 100 nm. *Anal. Chem.* **2013**, *85* (18), 8498–8502.
(72) Kenderdine, T.; Xia, Z.; Williams, E. R.; Fabris, D. Submicrometer Nanospray Emitters Provide New Insights into the Mechanism of Cation Adduction to Anionic Oligonucleotides. *Anal. Chem.* **2018**, *90* (22), 13541–13548.
(73) Hofmeister, F. Zur Lehre von Der Wirkung Der Salze - Dritte Mittheilung. *Arch. Exp. Path. Pharm.* **1888**, *25* (1), 1–30.
(74) Xia, Z.; Williams, E. R. Effect of Droplet Lifetime on Where Ions Are Formed in Electrospray Ionization. *Analyst* **2019**, *144* (1), 237–248.
(75) Bui, D. T.; Li, Z.; Kitov, P. I.; Han, L.; Kitova, E. N.; Fortier, M.; Fuselier, C.; Granger Joly de Boissel, P.; Chatenet, D.; Doucet, N.; Tompkins, S. M.; St-Pierre, Y.; Mahal, L. K.; Klassen, J. S. Quantifying Biomolecular Interactions Using Slow Mixing Mode (SLOMO) Nanoflow ESI-MS. *ACS Cent. Sci.* **2022**, *8* (7), 963–974.
(76) Nguyen, G. T. H.; Bennett, J. L.; Liu, S.; Hancock, S. E.; Winter, D. L.; Glover, D. J.; Donald, W. A. Multiplexed Screening of Thousands of Natural Products for Protein–Ligand Binding in Native Mass Spectrometry. *J. Am. Chem. Soc.* **2021**, *143* (50), 21379–21387.
(77) Nguyen, G. T. H.; Tran, T. N.; Podgorski, M. N.; Bell, S. G.; Supuran, C. T.; Donald, W. A. Nanoscale Ion Emitters in Native Mass Spectrometry for Measuring Ligand–Protein Binding Affinities. *ACS Cent. Sci.* **2019**, *5* (2), 308–318.
(78) Nguyen, G. T. H.; Leung, W. Y.; Tran, T. N.; Wang, H.; Murray, V.; Donald, W. A. Mechanism for the Binding of Netropsin to Hairpin DNA Revealed Using Nanoscale Ion Emitters in Native Mass Spectrometry. *Anal. Chem.* **2020**, *92* (1), 1130–1137.
(79) Báez Bolivar, E. G.; Bui, D. T.; Kitova, E. N.; Han, L.; Zheng, R. B.; Luber, E. J.; Sayed, S. Y.; Mahal, L. K.; Klassen, J. S. Submicron Emitters Enable Reliable Quantification of Weak Protein-Glycan Interactions by ESI-MS. *Anal. Chem.* **2021**, *93* (9), 4231–4239.
(80) Nguyen, G. T. H.; Nocentini, A.; Angeli, A.; Gratteri, P.; Supuran, C. T.; Donald, W. A. Perfluoroalkyl Substances of Significant Environmental Concern Can Strongly Inhibit Human Carbonic Anhydrase Isozymes. *Anal. Chem.* **2020**, *92* (6), 4614–4622.
(81) Bennett, J. L.; Nguyen, G. T. H.; Donald, W. A. Protein–Small Molecule Interactions in Native Mass Spectrometry. *Chem. Rev.* **2022**, *122* (8), 7327–7385.
(82) Panczyk, E. M.; Gilbert, J. D.; Jagdale, G. S.; Stiving, A. Q.; Baker, L. A.; Wysocki, V. H. Ion Mobility and Surface Collisions: Submicrometer Capillaries Can Produce Native-like Protein Complexes. *Anal. Chem.* **2020**, *92* (3), 2460–2467.
(83) Saikusa, K.; Kato, D.; Nagadoi, A.; Kurumizaka, H.; Akashi, S. Native Mass Spectrometry of Protein and DNA Complexes Prepared in Nonvolatile Buffers. *J. Am. Soc. Mass Spectrom.* **2020**, *31* (3), 711–718.
(84) Panczyk, E. M. Tip Pulling - Nanoelectrospray Capillary Preparation for Native MS. **2019**. https://nativems.osu.edu/sites/nativems.osu.edu/files/TipPulling3-19.pdf.
(85) Behrens, S. H.; Grier, D. G. The Charge of Glass and Silica Surfaces. *J. Chem. Phys.* **2001**, *115* (14), 6716–6721.

(86) Brinker, C. J. Hydrolysis and Condensation of Silicates: Effects on Structure. *J. Non-Cryst. Solids* **1988**, *100* (1–3), 31–50.
(87) Mortensen, D. N.; Williams, E. R. Surface-Induced Protein Unfolding in Submicron Electrospray Emitters. *Anal. Chem.* **2016**, *88* (19), 9662–9668.
(88) Kostelic, M. M.; Hsieh, C.; Sanders, H. M.; Zak, C. K.; Ryan, J. P.; Baker, E. S.; Aspinwall, C. A.; Marty, M. T. Surface Modified Nano-Electrospray Needles Improve Sensitivity for Native Mass Spectrometry. *J. Am. Soc. Mass Spectrom.* **2022**, *33* (6), 1031–1037.
(89) Yong, S. C.; Wood, T. D. Silanization of Inner Surfaces of Nanoelectrospray Ionization Emitters for Reduced Analyte Adsorption. *Rapid Commun. Mass Spectrom.* **2008**, *22* (8), 1265–1274.
(90) Chowdhury, S. K.; Katta, V.; Chait, B. T. Probing Conformational Changes in Proteins by Mass Spectrometry. *J. Am. Chem. Soc.* **1990**, *112* (24), 9012–9013.
(91) Loo, J. A.; Loo, R. R. O.; Udseth, H. R.; Edmonds, C. G.; Smith, R. D. Solvent-induced Conformational Changes of Polypeptides Probed by Electrospray-ionization Mass Spectrometry. *Rapid Commun. Mass Spectrom.* **1991**, *5* (3), 101–105.
(92) Dobo, A.; Kaltashov, I. A. Detection of Multiple Protein Conformational Ensembles in Solution via Deconvolution of Charge-State Distributions in ESI MS. *Anal. Chem.* **2001**, *73* (20), 4763–4773.
(93) Frimpong, A. K.; Abzalimov, R. R.; Uversky, V. N.; Kaltashov, I. A. Characterization of Intrinsically Disordered Proteins with Electrospray Ionization Mass Spectrometry: Conformational Heterogeneity of α-synuclein. *Proteins* **2010**, *78* (3), 714–722.
(94) Dodds, J. N.; Baker, E. S. Ion Mobility Spectrometry: Fundamental Concepts, Instrumentation, Applications, and the Road Ahead. *J. Am. Soc. Mass Spectrom.* **2019**, *30* (11), 2185–2195.
(95) Bush, M. F.; Hall, Z.; Giles, K.; Hoyes, J.; Robinson, C. V.; Ruotolo, B. T. Collision Cross Sections of Proteins and Their Complexes: A Calibration Framework and Database for Gas-Phase Structural Biology. *Anal. Chem.* **2010**, *82* (22), 9557–9565.
(96) Ruotolo, B. T.; Benesch, J. L. P.; Sandercock, A. M.; Hyung, S. J.; Robinson, C. V. Ion Mobility–Mass Spectrometry Analysis of Large Protein Complexes. *Nat. Protoc.* **2008**, *3* (7), 1139–1152.
(97) El-Baba, T. J.; Clemmer, D. E. Solution Thermochemistry of Concanavalin A Tetramer Conformers Measured by Variable-Temperature ESI-IMS-MS. *Int. J. Mass Spectrom.* **2019**, *443*, 93–100.
(98) Sharon, E. M.; Henderson, L. W.; Clemmer, D. E. Resolving Hidden Solution Conformations of Hemoglobin Using IMS-IMS on a Cyclic Instrument. *J. Am. Soc. Mass Spectrom.* **2023**, *34* (8), 1559–1568.
(99) Koeniger, S. L.; Merenbloom, S. I.; Clemmer, D. E. Evidence for Many Resolvable Structures within Conformation Types of Electrosprayed Ubiquitin Ions. *J. Phys. Chem. B* **2006**, *110* (13), 7017–7021.
(100) Li, J.; Taraszka, J. A.; Counterman, A. E.; Clemmer, D. E. Influence of Solvent Composition and Capillary Temperature on the Conformations of Electrosprayed Ions: Unfolding of Compact Ubiquitin Conformers from Pseudonative and Denatured Solutions. *Int. J. Mass Spectrom.* **1999**, *185*, 37–47.
(101) Woodall, D. W.; Henderson, L. W.; Raab, S. A.; Honma, K.; Clemmer, D. E. Understanding the Thermal Denaturation of Myoglobin with IMS-MS: Evidence for Multiple Stable Structures and Trapped Pre-Equilibrium States. *J. Am. Soc. Mass Spectrom.* **2021**, *32* (1), 64–72.

(102) Pan, H.; Raab, S. A.; El-Baba, T. J.; Schrecke, S. R.; Laganowsky, A.; Russell, D. H.; Clemmer, D. E. Variation of CI-2 Conformers upon Addition of Methanol to Water: An IMS-MS-Based Thermodynamic Analysis. *J. Phys. Chem. A* **2023**, *127* (45), 9399–9408.
(103) Raab, S. A.; El-Baba, T. J.; Woodall, D. W.; Liu, W.; Liu, Y.; Baird, Z.; Hales, D. A.; Laganowsky, A.; Russell, D. H.; Clemmer, D. E. Evidence for Many Unique Solution Structures for Chymotrypsin Inhibitor 2: A Thermodynamic Perspective Derived from vT-ESI-IMS-MS Measurements. *J. Am. Chem. Soc.* **2020**, *142* (41), 17372–17383.
(104) Woodall, D. W.; El-Baba, T. J.; Fuller, D. R.; Liu, W.; Brown, C. J.; Laganowsky, A.; Russell, D. H.; Clemmer, D. E. Variable-Temperature ESI-IMS-MS Analysis of Myohemerythrin Reveals Ligand Losses, Unfolding, and a Non-Native Disulfide Bond. *Anal. Chem.* **2019**, *91* (10), 6808–6814.
(105) Shi, H.; Pierson, N. A.; Valentine, S. J.; Clemmer, D. E. Conformation Types of Ubiquitin $[M+8H]^{8+}$ Ions from Water:Methanol Solutions: Evidence for the N and A States in Aqueous Solution. *J. Phys. Chem. B* **2012**, *116* (10), 3344–3352.
(106) Harrison, J. A.; Pruška, A.; Oganesyan, I.; Bittner, P.; Zenobi, R. Temperature-Controlled Electrospray Ionization: Recent Progress and Applications. *Chem. Eur. J.* **2021**, *27* (72), 18015–18028.
(107) Wang, G.; Bondarenko, P. V.; Kaltashov, I. A. Multi-Step Conformational Transitions in Heat-Treated Protein Therapeutics Can Be Monitored in Real Time with Temperature-Controlled Electrospray Ionization Mass Spectrometry. *Analyst* **2018**, *143* (3), 670–677.
(108) El-Baba, T. J.; Raab, S. A.; Buckley, R. P.; Brown, C. J.; Lutomski, C. A.; Henderson, L. W.; Woodall, D. W.; Shen, J.; Trinidad, J. C.; Niu, H.; Jarrold, M. F.; Russell, D. H.; Laganowsky, A.; Clemmer, D. E. Thermal Analysis of a Mixture of Ribosomal Proteins by VT-ESI-MS: Toward a Parallel Approach for Characterizing the Stabilitome. *Anal. Chem.* **2021**, *93* (24), 8484–8492.
(109) El-Baba, T. J.; Woodall, D. W.; Raab, S. A.; Fuller, D. R.; Laganowsky, A.; Russell, D. H.; Clemmer, D. E. Melting Proteins: Evidence for Multiple Stable Structures upon Thermal Denaturation of Native Ubiquitin from Ion Mobility Spectrometry-Mass Spectrometry Measurements. *J. Am. Chem. Soc.* **2017**, *139* (18), 6306–6309.
(110) Benesch, J. L. P.; Sobott, F.; Robinson, C. V. Thermal Dissociation of Multimeric Protein Complexes by Using Nanoelectrospray Mass Spectrometry. *Anal. Chem.* **2003**, *75* (10), 2208–2214.
(111) Wang, G.; Abzalimov, R. R.; Kaltashov, I. A. Direct Monitoring of Heat-Stressed Biopolymers with Temperature-Controlled Electrospray Ionization Mass Spectrometry. *Anal. Chem.* **2011**, *83* (8), 2870–2876.
(112) Shirzadeh, M.; Poltash, M. L.; Laganowsky, A.; Russell, D. H. Structural Analysis of the Effect of a Dual-FLAG Tag on Transthyretin. *Biochemistry* **2020**, *59* (9), 1013–1022.
(113) Jeanne Dit Fouque, K.; Fernandez-Lima, F. Following Structural Changes by Thermal Denaturation Using Trapped Ion Mobility Spectrometry–Mass Spectrometry. *J. Phys. Chem. B* **2020**, *124* (29), 6257–6265.
(114) Geels, R. B. J.; Calmat, S.; Heck, A. J. R.; van der Vies, S. M.; Heeren, R. M. A. Thermal Activation of the Co-Chaperonins GroES and Gp31 Probed by Mass Spectrometry. *Rapid Commun. Mass Spectrom.* **2008**, *22* (22), 3633–3641.
(115) Harrison, J. A.; Pruška, A.; Bittner, P.; Muck, A.; Cooper-Shepherd, D. A.; Zenobi, R. Advancing Cyclic Ion Mobility Mass Spectrometry Methods for Studying Biomolecules: Toward the Conformational Dynamics of Mega Dalton Protein Aggregates. *Anal. Chem.* **2022**, *94* (36), 12435–12443.

(116) Kostelic, M. M.; Ryan, J. P.; Brown, L. S.; Jackson, T. W.; Hsieh, C.; Zak, C. K.; Sanders, H. M.; Liu, Y.; Chen, V. S.; Byrne, M.; Aspinwall, C. A.; Baker, E. S.; Marty, M. T. Stability and Dissociation of Adeno-Associated Viral Capsids by Variable Temperature-Charge Detection-Mass Spectrometry. *Anal. Chem.* **2022**, *94* (34), 11723–11727.
(117) Pruška, A.; Marchand, A.; Zenobi, R. Novel Insight into Proximal DNA Domain Interactions from Temperature-Controlled Electrospray Ionization Mass Spectrometry. *Angew. Chem., Int. Ed.* **2021**, *60* (28), 15390–15398.
(118) Pruška, A.; Harrison, J. A.; Granzhan, A.; Marchand, A.; Zenobi, R. Solution and Gas-Phase Stability of DNA Junctions from Temperature-Controlled Electrospray Ionization and Surface-Induced Dissociation. *Anal. Chem.* **2023**, *95* (38), 14384–14391.
(119) Marchand, A.; Czar, M. F.; Eggel, E. N.; Kaeslin, J.; Zenobi, R. Studying Biomolecular Folding and Binding Using Temperature-Jump Mass Spectrometry. *Nat. Commun.* **2020**, *11* (1), 566.
(120) Jordan, J. S.; Lee, K. J.; Williams, E. R. Overcoming Aggregation with Laser Heated Nanoelectrospray Mass Spectrometry: Thermal Stability and Pathways for Loss of Bicarbonate from Carbonic Anhydrase II. *Analyst* **2024**, *149* (8), 2281–2290.
(121) Jordan, J. S.; Williams, E. R. Laser Heating Nanoelectrospray Emitters for Fast Protein Melting Measurements with Mass Spectrometry. *Anal. Chem.* **2022**, *94* (48), 16894–16900.
(122) Brown, C. J.; Woodall, D. W.; El-Baba, T. J.; Clemmer, D. E. Characterizing Thermal Transitions of IgG with Mass Spectrometry. *J. Am. Soc. Mass Spectrom.* **2019**, *30* (11), 2438–2445.
(123) Cong, X.; Liu, Y.; Liu, W.; Liang, X.; Russell, D. H.; Laganowsky, A. Determining Membrane Protein–Lipid Binding Thermodynamics Using Native Mass Spectrometry. *J. Am. Chem. Soc.* **2016**, *138* (13), 4346–4349.
(124) Qiao, P.; Schrecke, S.; Walker, T.; McCabe, J. W.; Lyu, J.; Zhu, Y.; Zhang, T.; Kumar, S.; Clemmer, D.; Russell, D. H.; Laganowsky, A. Entropy in the Molecular Recognition of Membrane Protein–Lipid Interactions. *J. Phys. Chem. Lett.* **2021**, *12* (51), 12218–12224.
(125) McCabe, J. W.; Shirzadeh, M.; Walker, T. E.; Lin, C.-W.; Jones, B. J.; Wysocki, V. H.; Barondeau, D. P.; Clemmer, D. E.; Laganowsky, A.; Russell, D. H. Variable-Temperature Electrospray Ionization for Temperature-Dependent Folding/Refolding Reactions of Proteins and Ligand Binding. *Anal. Chem.* **2021**, *93* (18), 6924–6931.
(126) Walker, T. E.; Shirzadeh, M.; Sun, H. M.; McCabe, J. W.; Roth, A.; Moghadamchargari, Z.; Clemmer, D. E.; Laganowsky, A.; Rye, H.; Russell, D. H. Temperature Regulates Stability, Ligand Binding (Mg^{2+} and ATP), and Stoichiometry of GroEL–GroES Complexes. *J. Am. Chem. Soc.* **2022**, *144* (6), 2667–2678.
(127) Liu, J.; Wang, Y.; Wang, X.; Qin, W.; Li, G. Measuring Protein Unfolding Thermodynamic Stability in One Minute with Digital Temperature Control-Equipped NanoESI-Mass Spectrometry. *Int. J. Mass Spectrom.* **2023**, *494*, 117151.
(128) Shi, X.; Nishimura, Y.; Akashi, S.; Takamizawa, A.; Hiraoka, K. Evaluation of Binding Affinity of Protein-Mutant DNA Complexes in Solution by Laser Spray Mass Spectrometry. *J. Am. Soc. Mass Spectrom.* **2006**, *17* (4), 611–620.
(129) Kudaka, I.; Kojima, T.; Saito, S.; Hiraoka, K. A Comparative Study of Laser Spray and Electrospray. *Rapid Commun. Mass Spectrom.* **2000**, *14* (16), 1558–1562.
(130) Shi, X.; Takamizawa, A.; Nishimura, Y.; Hiraoka, K.; Akashi, S. Thermal Unfolding of Proteins Probed by Laser Spray Mass Spectrometry. *Rapid Commun. Mass Spectrom.* **2008**, *22* (9), 1430–1436.

(131) Nakamura, M.; Takamizawa, A.; Yamada, H.; Hiraoka, K.; Akashi, S. Denaturation Ofα-Lactalbumin and Ubiquitin Studied by Electrospray and Laser Spray. *Rapid Commun. Mass Spectrom.* **2007**, *21* (10), 1635–1643.
(132) Shi, X.; Takamizawa, A.; Nishimura, Y.; Hiraoka, K.; Akashi, S. Stability Analysis for Double-Stranded DNA Oligomers and Their Noncovalent Complexes with Drugs by Laser Spray. *J. Mass Spectrom.* **2006**, *41* (8), 1086–1095.
(133) Hiraoka, K.; Saito, S.; Katsuragawa, J.; Kudaka, I. A New Liquid Chromatography/Mass Spectrometry Interface: Laser Spray. *Rapid Commun. Mass Spectrom.* **1998**, *12* (17), 1170–1174.
(134) Takamizawa, A.; Itoh, Y.; Osawa, R.; Iwasaki, N.; Nishimura, Y.; Akashi, S.; Hiraoka, K. Selective Dissociation of Non-Covalent Bonds in Biological Molecules by Laser Spray. *J. Mass Spectrom.* **2004**, *39* (9), 1053–1058.
(135) Hiraoka, K.; Asakawa, Y.; Ueda, K.; Hori, A.; Sakai, T.; Okazaki, S.; Nakamura, M. Does Thermal Degradation Occur in Laser Spray Ionization? *Rapid Commun. Mass Spectrom.* **2002**, *16* (11), 1100–1105.
(136) Hiraoka, K.; Matsushita, F.; Hukasawa, H. Enhancement of Ion Evaporation by the CO_2 Laser Irradiation on the Electrospray and Ion Spray. *Int. J. Mass Spectrom. Ion Processes* **1997**, *162* (1–3), 35–44.
(137) El-Baba, T. J.; Fuller, D. R.; Woodall, D. W.; Raab, S. A.; Conant, C. R.; Dilger, J. M.; Toker, Y.; Williams, E. R.; Russell, D. H.; Clemmer, D. E. Melting Proteins Confined in Nanodroplets with 10.6 μm Light Provides Clues about Early Steps of Denaturation. *Chem. Commun.* **2018**, *54* (26), 3270–3273.
(138) Mortensen, D. N.; Williams, E. R. Ultrafast (1 μs) Mixing and Fast Protein Folding in Nanodrops Monitored by Mass Spectrometry. *J. Am. Chem. Soc.* **2016**, *138* (10), 3453–3460.
(139) Mortensen, D. N.; Williams, E. R. Theta-Glass Capillaries in Electrospray Ionization: Rapid Mixing and Short Droplet Lifetimes. *Anal. Chem.* **2014**, *86* (18), 9315–9321.
(140) Ross, C. A.; Poirier, M. A. Protein Aggregation and Neurodegenerative Disease. *Nat. Med.* **2004**, *10* (S7), S10–S17.
(141) Stefani, M.; Dobson, C. M. Protein Aggregation and Aggregate Toxicity: New Insights into Protein Folding, Misfolding Diseases and Biological Evolution. *J. Mol. Med.* **2003**, *81* (11), 678–699.
(142) Ratanji, K. D.; Derrick, J. P.; Dearman, R. J.; Kimber, I. Immunogenicity of Therapeutic Proteins: Influence of Aggregation. *J. Immunotoxicol.* **2014**, *11* (2), 99–109.
(143) Swanson, M. D.; Rios, S.; Mittal, S.; Soder, G.; Jawa, V. Immunogenicity Risk Assessment of Spontaneously Occurring Therapeutic Monoclonal Antibody Aggregates. *Front. Immunol.* **2022**, *13* (July), 1–11.
(144) Wang, W.; Singh, S. K.; Li, N.; Toler, M. R.; King, K. R.; Nema, S. Immunogenicity of Protein Aggregates—Concerns and Realities. *Int. J. Pharm.* **2012**, *431* (1–2), 1–11.
(145) Mahler, H. C.; Friess, W.; Grauschopf, U.; Kiese, S. Protein Aggregation: Pathways, Induction Factors and Analysis. *J. Pharm. Sci.* **2009**, *98* (9), 2909–2934.
(146) Pedersen, J. T.; Heegaard, N. H. H. Analysis of Protein Aggregation in Neurodegenerative Disease. *Anal. Chem.* **2013**, *85* (9), 4215–4227.
(147) Ye, H. Simultaneous Determination of Protein Aggregation, Degradation, and Absolute Molecular Weight by Size Exclusion Chromatography–Multiangle Laser Light Scattering. *Anal. Biochem.* **2006**, *356* (1), 76–85.

(148) Kükrer, B.; Filipe, V.; van Duijn, E.; Kasper, P. T.; Vreeken, R. J.; Heck, A. J. R.; Jiskoot, W. Mass Spectrometric Analysis of Intact Human Monoclonal Antibody Aggregates Fractionated by Size-Exclusion Chromatography. *Pharm. Res.* **2010**, *27* (10), 2197–2204.
(149) Hong, P.; Koza, S.; Bouvier, E. S. P. Size-Exclusion Chromatography for the Analysis of Protein Biotherapeutics and their Aggregates. *J. Liq. Chromatogr. Relat. Technol.* **2012**, *35* (20), 2923–2950.
(150) Fekete, S.; Beck, A.; Veuthey, J. L.; Guillarme, D. Theory and Practice of Size Exclusion Chromatography for the Analysis of Protein Aggregates. *J. Pharm. Biomed. Anal.* **2014**, *101*, 161–173.
(151) Knowles, P. Biophysical Chemistry: Part II 'Techniques for the Study of Biological Structure and Function.' *Biochem. Educ.* **1981**, *9* (4), 157.
(152) Brown, P. H.; Balbo, A.; Schuck, P. Characterizing Protein-Protein Interactions by Sedimentation Velocity Analytical Ultracentrifugation. *Curr. Protoc. Immunol.* **2008**, *81* (1), 1–39.
(153) Arthur, K. K.; Gabrielson, J. P.; Kendrick, B. S.; Stoner, M. R. Detection of Protein Aggregates by Sedimentation Velocity Analytical Ultracentrifugation (SV-AUC): Sources of Variability and Their Relative Importance. *J. Pharm. Sci.* **2009**, *98* (10), 3522–3539.
(154) Bartels, T.; Choi, J. G.; Selkoe, D. J. α-Synuclein Occurs Physiologically as a Helically Folded Tetramer That Resists Aggregation. *Nature* **2011**, *477* (7362), 107–110.
(155) Xue, C.; Lin, T. Y.; Chang, D.; Guo, Z. Thioflavin T as an Amyloid Dye: Fibril Quantification, Optimal Concentration and Effect on Aggregation. *R. Soc. Open Sci.* **2017**, *4* (1), 160696.
(156) Lee, S.; Choi, M. C.; Al Adem, K.; Lukman, S.; Kim, T. Y. Aggregation and Cellular Toxicity of Pathogenic or Non-Pathogenic Proteins. *Sci. Rep.* **2020**, *10* (1), 5120.
(157) D'Amico, M.; Di Carlo, M. G.; Groenning, M.; Militello, V.; Vetri, V.; Leone, M. Thioflavin T Promotes Aβ(1–40) Amyloid Fibrils Formation. *J. Phys. Chem. Lett.* **2012**, *3* (12), 1596–1601.
(158) Rovnyagina, N. R.; Sluchanko, N. N.; Tikhonova, T. N.; Fadeev, V. V.; Litskevich, A. Y.; Maskevich, A. A.; Shirshin, E. A. Binding of Thioflavin T by Albumins: An Underestimated Role of Protein Oligomeric Heterogeneity. *Int. J. Biol. Macromol.* **2018**, *108*, 284–290.
(159) Khurana, R.; Coleman, C.; Ionescu-Zanetti, C.; Carter, S. A.; Krishna, V.; Grover, R. K.; Roy, R.; Singh, S. Mechanism of Thioflavin T Binding to Amyloid Fibrils. *J. Struct. Biol.* **2005**, *151* (3), 229–238.
(160) Jachimska, B.; Wasilewska, M.; Adamczyk, Z. Characterization of Globular Protein Solutions by Dynamic Light Scattering, Electrophoretic Mobility, and Viscosity Measurements. *Langmuir* **2008**, *24* (13), 6866–6872.
(161) Mehalebi, S.; Nicolai, T.; Durand, D. Light Scattering Study of Heat-Denatured Globular Protein Aggregates. *Int. J. Biol. Macromol.* **2008**, *43* (2), 129–135.
(162) Lorber, B.; Fischer, F.; Bailly, M.; Roy, H.; Kern, D. Protein Analysis by Dynamic Light Scattering: Methods and Techniques for Students. *Biochem. Mol. Biol. Ed.* **2012**, *40* (6), 372–382.
(163) Li, H.; Rahimi, F.; Sinha, S.; Maiti, P.; Bitan, G.; Murakami, K. Amyloids and Protein Aggregation—Analytical Methods. In *Encyclopedia of Analytical Chemistry*; Wiley, 2009.
(164) Hoyer, W.; Antony, T.; Cherny, D.; Heim, G.; Jovin, T. M.; Subramaniam, V. Dependence of α-Synuclein Aggregate Morphology on Solution Conditions. *J. Mol. Biol.* **2002**, *322* (2), 383–393.
(165) Flyvbjerg, H.; Jobs, E.; Leibler, S. Kinetics of Self-Assembling Microtubules: An "Inverse Problem" in Biochemistry. *Proc. Nat. Acad. Sci.* **1996**, *93* (12), 5975–5979.

(166) Young, G.; Hundt, N.; Cole, D.; Fineberg, A.; Andrecka, J.; Tyler, A.; Olerinyova, A.; Ansari, A.; Marklund, E. G.; Collier, M. P.; Chandler, S. A.; Tkachenko, O.; Allen, J.; Crispin, M.; Billington, N.; Takagi, Y.; Sellers, J. R.; Eichmann, C.; Selenko, P.; Frey, L.; Riek, R.; Galpin, M. R.; Struwe, W. B.; Benesch, J. L. P.; Kukura, P. Quantitative Mass Imaging of Single Biological Macromolecules. *Science* **2018**, *360* (6387), 423–427.
(167) Paul, S. S.; Lyons, A.; Kirchner, R.; Woodside, M. T. Quantifying Oligomer Populations in Real Time during Protein Aggregation Using Single-Molecule Mass Photometry. *ACS Nano* **2022**, *16* (10), 16462–16470.
(168) Liebthal, M.; Kushwah, M. S.; Kukura, P.; Dietz, K. J. Single Molecule Mass Photometry Reveals the Dynamic Oligomerization of Human and Plant Peroxiredoxins. *iScience* **2021**, *24* (11), 103258.
(169) Wu, D.; Piszczek, G. Measuring the Affinity of Protein-Protein Interactions on a Single-Molecule Level by Mass Photometry. *Anal. Biochem.* **2020**, *592*, 113575.
(170) den Boer, M. A.; Lai, S.-H.; Xue, X.; van Kampen, M. D.; Bleijlevens, B.; Heck, A. J. R. Comparative Analysis of Antibodies and Heavily Glycosylated Macromolecular Immune Complexes by Size-Exclusion Chromatography Multi-Angle Light Scattering, Native Charge Detection Mass Spectrometry, and Mass Photometry. *Anal. Chem.* **2022**, *94* (2), 892–900.
(171) Hundt, N.; Cole, D.; Hantke, M. F.; Miller, J. J.; Struwe, W. B.; Kukura, P. Direct Observation of the Molecular Mechanism Underlying Protein Polymerization. *Sci. Adv.* **2022**, *8* (35), eabm7935.
(172) Ray, S.; Mason, T. O.; Boyens-Thiele, L.; Farzadfard, A.; Larsen, J. A.; Norrild, R. K.; Jahnke, N.; Buell, A. K. Mass Photometric Detection and Quantification of Nanoscale α-Synuclein Phase Separation. *Nat. Chem.* **2023**, *15* (9), 1306–1316.
(173) Bernstein, S. L.; Wyttenbach, T.; Baumketner, A.; Shea, J. E.; Bitan, G.; Teplow, D. B.; Bowers, M. T. Amyloid β-Protein: Monomer Structure and Early Aggregation States of Aβ42 and Its Pro^{19} Alloform. *J. Am. Chem. Soc.* **2005**, *127* (7), 2075–2084.
(174) Bleiholder, C.; Dupuis, N. F.; Wyttenbach, T.; Bowers, M. T. Ion Mobility–Mass Spectrometry Reveals a Conformational Conversion from Random Assembly to β-Sheet in Amyloid Fibril Formation. *Nat. Chem.* **2011**, *3* (2), 172–177.
(175) Österlund, N.; Moons, R.; Ilag, L. L.; Sobott, F.; Graslund, A. Native Ion Mobility-Mass Spectrometry Reveals the Formation of β-barrel Shaped Amyloid-β Hexamers in a Membrane-Mimicking Environment. *J. Am. Chem. Soc.* **2019**, *141* (26), 10440–10450.
(176) Shahpasand-Kroner, H.; Portillo, J.; Lantz, C.; Seidler, P. M.; Sarafian, N.; Loo, J. A.; Bitan, G. Three-repeat and Four-repeat Tau Isoforms Form Different Oligomers. *Prot. Sci.* **2022**, *31* (3), 613–627.
(177) Stroganova, I.; Willenberg, H.; Tente, T.; Depraz Depland, A.; Bakels, S.; Rijs, A. M. Exploring the Aggregation Propensity of PHF6 Peptide Segments of the Tau Protein Using Ion Mobility Mass Spectrometry Techniques. *Anal. Chem.* **2024**, *96* (13), 5115–5124.
(178) Stroganova, I.; Toprakcioglu, Z.; Willenberg, H.; Knowles, T. P. J.; Rijs, A. M. Unraveling the Structure and Dynamics of Ac-PHF6-NH_2 Tau Segment Oligomers. *ACS Chem. Neurosci.* **2024**, *15* (18), 3391–3400.
(179) Depraz Depland, A.; Stroganova, I.; Wootton, C. A.; Rijs, A. M. Developments in Trapped Ion Mobility Mass Spectrometry to Probe the Early Stages of Peptide Aggregation. *J. Am. Soc. Mass Spectrom.* **2023**, *34* (2), 193–204.

(180) McGee, J. P.; Melani, R. D.; Yip, P. F.; Senko, M. W.; Compton, P. D.; Kafader, J. O.; Kelleher, N. L. Isotopic Resolution of Protein Complexes up to 466 kDa Using Individual Ion Mass Spectrometry. *Anal. Chem.* **2021**, *93* (5), 2723–2727.
(181) Moons, R.; Konijnenberg, A.; Mensch, C.; Van Elzen, R.; Johannessen, C.; Maudsley, S.; Lambeir, A. M.; Sobott, F. Metal Ions Shape α-Synuclein. *Sci. Rep.* **2020**, *10* (1), 16293.
(182) Phillips, A. S.; Gomes, A. F.; Kalapothakis, J. M. D.; Gillam, J. E.; Gasparavicius, J.; Gozzo, F. C.; Kunath, T.; MacPhee, C.; Barran, P. E. Conformational Dynamics of α-Synuclein: Insights from Mass Spectrometry. *Analyst* **2015**, *140* (9), 3070–3081.
(183) Zhao, B.; Zhuang, X.; Pi, Z.; Liu, S.; Liu, Z.; Song, F. Determining the Effect of Catechins on SOD1 Conformation and Aggregation by Ion Mobility Mass Spectrometry Combined with Optical Spectroscopy. *J. Am. Soc. Mass Spectrom.* **2018**, *29* (4), 734–741.
(184) Hilton, G. R.; Thalassinos, K.; Grabenauer, M.; Sanghera, N.; Slade, S. E.; Wyttenbach, T.; Robinson, P. J.; Pinheiro, T. J. T.; Bowers, M. T.; Scrivens, J. H. Structural Analysis of Prion Proteins by Means of Drift Cell and Traveling Wave Ion Mobility Mass Spectrometry. *J. Am. Soc. Mass Spectrom.* **2010**, *21* (5), 845–854.
(185) Van der Rest, G.; Rezaei, H.; Halgand, F. Monitoring Conformational Landscape of Ovine Prion Protein Monomer Using Ion Mobility Coupled to Mass Spectrometry. *J. Am. Soc. Mass Spectrom.* **2017**, *28* (2), 303–314.
(186) Landreh, M.; Alvelius, G.; Johansson, J.; Jörnvall, H. Insulin, Islet Amyloid Polypeptide and C-Peptide Interactions Evaluated by Mass Spectrometric Analysis. *Rapid Commun. Mass Spectrom.* **2014**, *28* (2), 178–184.
(187) Nettleton, E. J.; Tito, P.; Sunde, M.; Bouchard, M.; Dobson, C. M.; Robinson, C. V. Characterization of the Oligomeric States of Insulin in Self-Assembly and Amyloid Fibril Formation by Mass Spectrometry. *Biophys. J.* **2000**, *79* (2), 1053–1065.
(188) Cole, H.; Porrini, M.; Morris, R.; Smith, T.; Kalapothakis, J.; Weidt, S.; Mackay, C. L.; MacPhee, C. E.; Barran, P. E. Early Stages of Insulin Fibrillogenesis Examined with Ion Mobility Mass Spectrometry and Molecular Modelling. *Analyst* **2015**, *140* (20), 7000–7011.
(189) Fabris, D.; Fenselau, C. Characterization of Allosteric Insulin Hexamers by Electrospray Ionization Mass Spectrometry. *Anal. Chem.* **1999**, *71* (2), 384–387.
(190) Hoffmann, W.; Folmert, K.; Moschner, J.; Huang, X.; von Berlepsch, H.; Koksch, B.; Bowers, M. T.; von Helden, G.; Pagel, K. NFGAIL Amyloid Oligomers: The Onset of Beta-Sheet Formation and the Mechanism for Fibril Formation. *J. Am. Chem. Soc.* **2018**, *140* (1), 244–249.
(191) Seo, J.; Hoffmann, W.; Warnke, S.; Huang, X.; Gewinner, S.; Schöllkopf, W.; Bowers, M. T.; von Helden, G.; Pagel, K. An Infrared Spectroscopy Approach to Follow β-Sheet Formation in Peptide Amyloid Assemblies. *Nat. Chem.* **2017**, *9* (1), 39–44.
(192) Bakels, S.; Daly, S.; Doğan, B.; Baerenfaenger, M.; Commandeur, J.; Rijs, A. M. Probing High-Order Transient Oligomers Using Ion Mobility Mass Spectrometry Coupled with Infrared Action Spectroscopy. *Anal. Chem.* **2024**, *96* (34), 13962-13970.
(193) Wörner, T. P.; Thurman, H. A.; Makarov, A. A.; Shvartsburg, A. A. Expanding Differential Ion Mobility Separations into the MegaDalton Range. *Anal. Chem.* **2024**, *96* (14), 5392-5398.
(194) Shelton, H.; Hendricks, C. D.; Wuerker, R. F. Electrostatic Acceleration of Microparticles to Hypervelocities. *J. Appl. Phys.* **1960**, *31* (7), 1243–1246.
(195) Schultz, J. C.; Hack, C. A.; Benner, W. H. Mass Determination of Megadalton-DNA Electrospray Ions Using Charge Detection Mass Spectrometry. *J. Am. Soc. Mass Spectrom.* **1998**, *9* (4), 305–313.

(196) Fuerstenau, S. D.; Benner, W. H.; Thomas, J. J.; Brugidou, C.; Bothner, B.; Siuzdak, G. Mass Spectrometry of an Intact Virus. *Angew. Chem., Int. Ed.* **2001**, *40* (3), 541–544.
(197) Fuerstenau, S. D.; Benner, W. H. Molecular Weight Determination of Megadalton DNA Electrospray Ions Using Charge Detection Time-of-flight Mass Spectrometry. *Rapid Commun. Mass Spectrom.* **1995**, *9* (15), 1528–1538.
(198) Maze, J. T.; Jones, T. C.; Jarrold, M. F. Negative Droplets from Positive Electrospray. *J. Phys. Chem. A* **2006**, *110* (46), 12607–12612.
(199) Doussineau, T.; Désert, A.; Lambert, O.; Taveau, J. C.; Lansalot, M.; Dugourd, P.; Bourgeat-Lami, E.; Ravaine, S.; Duguet, E.; Antoine, R. Charge Detection Mass Spectrometry for the Characterization of Mass and Surface Area of Composite Nanoparticles. *J. Phys. Chem. C* **2015**, *119* (20), 10844–10849.
(200) Doussineau, T.; Kerleroux, M.; Dagany, X.; Clavier, C.; Barbaire, M.; Maurelli, J.; Antoine, R.; Dugourd, P. Charging Megadalton Poly(Ethylene Oxide)s by Electrospray Ionization. A Charge Detection Mass Spectrometry Study. *Rapid Commun. Mass Spectrom.* **2011**, *25* (5), 617–623.
(201) Doussineau, T.; Bao, C. Y.; Antoine, R.; Dugourd, P.; Zhang, W.; D'Agosto, F.; Charleux, B. Direct Molar Mass Determination of Self-Assembled Amphiphilic Block Copolymer Nanoobjects Using Electrospray-Charge Detection Mass Spectrometry. *ACS Macro Lett.* **2012**, *1* (3), 414–417.
(202) Pansieri, J.; Halim, M. A.; Vendrely, C.; Dumoulin, M.; Legrand, F.; Sallanon, M. M.; Chierici, S.; Denti, S.; Dagany, X.; Dugourd, P.; Marquette, C.; Antoine, R.; Forge, V. Mass and Charge Distributions of Amyloid Fibers Involved in Neurodegenerative Diseases: Mapping Heterogeneity and Polymorphism. *Chem. Sci.* **2018**, *9* (10), 2791–2796.
(203) Doussineau, T.; Mathevon, C.; Altamura, L.; Vendrely, C.; Dugourd, P.; Forge, V.; Antoine, R. Mass Determination of Entire Amyloid Fibrils by Using Mass Spectrometry. *Angew. Chem., Int. Ed.* **2016**, *55* (7), 2340–2344.
(204) Gamero-Castaño, M. Induction Charge Detector with Multiple Sensing Stages. *Rev. Sci. Instrum.* **2007**, *78* (4), 043301.
(205) Smith, J. W.; Siegel, E. E.; Maze, J. T.; Jarrold, M. F. Image Charge Detection Mass Spectrometry: Pushing the Envelope with Sensitivity and Accuracy. *Anal. Chem.* **2011**, *83* (3), 950–956.
(206) Benner, W. H. A Gated Electrostatic Ion Trap To Repetitiously Measure the Charge and *m/z* of Large Electrospray Ions. *Anal. Chem.* **1997**, *69* (20), 4162–4168.
(207) Contino, N. C.; Jarrold, M. F. Charge Detection Mass Spectrometry for Single Ions with a Limit of Detection of 30 Charges. *Int. J. Mass Spectrom.* **2013**, *345–347*, 153–159.
(208) Todd, A. R.; Alexander, A. W.; Jarrold, M. F. Implementation of a Charge-Sensitive Amplifier without a Feedback Resistor for Charge Detection Mass Spectrometry Reduces Noise and Enables Detection of Individual Ions Carrying a Single Charge. *J. Am. Soc. Mass Spectrom.* **2020**, *31* (1), 146–154.
(209) Pierson, E. E.; Contino, N. C.; Keifer, D. Z.; Jarrold, M. F. Charge Detection Mass Spectrometry for Single Ions with an Uncertainty in the Charge Measurement of 0.65 *e*. *J. Am. Soc. Mass Spectrom.* **2015**, *26* (7), 1213–1220.
(210) Contino, N. C.; Pierson, E. E.; Keifer, D. Z.; Jarrold, M. F. Charge Detection Mass Spectrometry with Resolved Charge States. *J. Am. Soc. Mass Spectrom.* **2013**, *24* (1), 101–108.
(211) Keifer, D. Z.; Shinholt, D. L.; Jarrold, M. F. Charge Detection Mass Spectrometry with Almost Perfect Charge Accuracy. *Anal. Chem.* **2015**, *87* (20), 10330–10337.

(212) Harper, C. C.; Miller, Z. M.; Williams, E. R. Combined Multiharmonic Frequency Analysis for Improved Dynamic Energy Measurements and Accuracy in Charge Detection Mass Spectrometry. *Anal. Chem.* **2023**, *95* (45), 16659–16667.
(213) Harper, C. C.; Williams, E. R. Enhanced Multiplexing in Fourier Transform Charge Detection Mass Spectrometry by Decoupling Ion Frequency from Mass to Charge Ratio. *J. Am. Soc. Mass Spectrom.* **2019**, *30* (12), 2637–2645.
(214) Elliott, A. G.; Harper, C. C.; Lin, H.-W.; Williams, E. R. Effects of Individual Ion Energies on Charge Measurements in Fourier Transform Charge Detection Mass Spectrometry (FT-CDMS). *J. Am. Soc. Mass Spectrom.* **2019**, *30* (6), 946–955.
(215) Harper, C. C.; Elliott, A. G.; Oltrogge, L. M.; Savage, D. F.; Williams, E. R. Multiplexed Charge Detection Mass Spectrometry for High-Throughput Single Ion Analysis of Large Molecules. *Anal. Chem.* **2019**, *91* (11), 7458–7465.
(216) Hanozin, E.; Harper, C. C.; McPartlan, M. S.; Williams, E. R. Dynamics of Rayleigh Fission Processes in ∼100 nm Charged Aqueous Nanodrops. *ACS Cent. Sci.* **2023**, *9* (8), 1611–1622.
(217) Harper, C. C.; Avadhani, V. S.; Hanozin, E.; Miller, Z. M.; Williams, E. R. Dynamic Energy Measurements in Charge Detection Mass Spectrometry Eliminate Adverse Effects of Ion–Ion Interactions. *Anal. Chem.* **2023**, *95* (26), 10077–10086.
(218) Kafader, J. O.; Durbin, K. R.; Melani, R. D.; Des Soye, B. J.; Schachner, L. F.; Senko, M. W.; Compton, P. D.; Kelleher, N. L. Individual Ion Mass Spectrometry Enhances the Sensitivity and Sequence Coverage of Top-Down Mass Spectrometry. *J. Proteome Res.* **2020**, *19* (3), 1346–1350.
(219) Deslignière, E.; Yin, V. C.; Ebberink, E. H. T. M.; Rolland, A. D.; Barendregt, A.; Wörner, T. P.; Nagornov, K. O.; Kozhinov, A. N.; Fort, K. L.; Tsybin, Y. O.; Makarov, A. A.; Heck, A. J. R. Ultralong Transients Enhance Sensitivity and Resolution in Orbitrap-Based Single-Ion Mass Spectrometry. *Nat. Methods* **2024**, *21* (4), 619–622.
(220) Deslignière, E.; Rolland, A.; Ebberink, E. H. T. M.; Yin, V.; Heck, A. J. R. Orbitrap-Based Mass and Charge Analysis of Single Molecules. *Acc. Chem. Res.* **2023**, *56* (12), 1458–1468.
(221) Wörner, T. P.; Aizikov, K.; Snijder, J.; Fort, K. L.; Makarov, A. A.; Heck, A. J. R. Frequency Chasing of Individual Megadalton Ions in an Orbitrap Analyser Improves Precision of Analysis in Single-Molecule Mass Spectrometry. *Nat. Chem.* **2022**, *14* (5), 515–522.
(222) Rosati, S.; Yang, Y.; Barendregt, A.; Heck, A. J. R. Detailed Mass Analysis of Structural Heterogeneity in Monoclonal Antibodies Using Native Mass Spectrometry. *Nat. Protoc.* **2014**, *9* (4), 967–976.
(223) Yin, V.; Deslignière, E.; Mokiem, N.; Gazi, I.; Lood, R.; de Haas, C. J. C.; Rooijakkers, S. H. M.; Heck, A. J. R. Not All Arms of IgM Are Equal: Following Hinge-Directed Cleavage by Online Native SEC-Orbitrap-Based CDMS. *J. Am. Soc. Mass Spectrom.* **2024**, *35* (6), 1320–1329.
(224) Wörner, T. P.; Bennett, A.; Habka, S.; Snijder, J.; Friese, O.; Powers, T.; Agbandje-McKenna, M.; Heck, A. J. R. Adeno-Associated Virus Capsid Assembly Is Divergent and Stochastic. *Nat. Commun.* **2021**, *12* (1), 1642.
(225) Uetrecht, C.; Versluis, C.; Watts, N. R.; Roos, W. H.; Wuite, G. J. L.; Wingfield, P. T.; Steven, A. C.; Heck, A. J. R. High-Resolution Mass Spectrometry of Viral Assemblies: Molecular Composition and Stability of Dimorphic Hepatitis B Virus Capsids. *Proc. Nat. Acad. Sci.* **2008**, *105* (27), 9216–9220.
(226) Kafader, J. O.; Melani, R. D.; Durbin, K. R.; Ikwuagwu, B.; Early, B. P.; Fellers, R. T.; Beu, S. C.; Zabrouskov, V.; Makarov, A. A.; Maze, J. T.; Shinholt, D. L.; Yip, P. F.; Tullman-Ercek,

D.; Senko, M. W.; Compton, P. D.; Kelleher, N. L. Multiplexed Mass Spectrometry of Individual Ions Improves Measurement of Proteoforms and Their Complexes. *Nat. Methods* **2020**, *17* (4), 391–394.
(227) Du, C.; Cleary, S. P.; Kostelic, M. M.; Jones, B. J.; Kafader, J. O.; Wysocki, V. H. Combining Surface-Induced Dissociation and Charge Detection Mass Spectrometry to Reveal the Native Topology of Heterogeneous Protein Complexes. *Anal. Chem.* **2023**, *95* (37), 13889–13896.
(228) Anthony, A. J.; Gautam, A. K. S.; Miller, L. M.; Ma, Y.; Hardwick, A. G.; Sharma, A.; Ghatak, S.; Matouschek, A.; Jarrold, M. F.; Clemmer, D. E. CDMS Analysis of Intact 19S, 20S, 26S, and 30S Proteasomes: Evidence for Higher-Order 20S Assemblies at a Low pH. *Anal. Chem.* **2023**, *95* (33), 12209–12215.
(229) Lai, S. H.; Tamara, S.; Heck, A. J. R. Single-Particle Mass Analysis of Intact Ribosomes by Mass Photometry and Orbitrap-Based Charge Detection Mass Spectrometry. *iScience* **2021**, *24* (11), 103211.
(230) Harper, C. C.; Miller, Z. M.; Lee, H.; Bischoff, A. J.; Francis, M. B.; Schaffer, D. V.; Williams, E. R. Effects of Molecular Size on Resolution in Charge Detection Mass Spectrometry. *Anal. Chem.* **2022**, *94* (33), 11703–11712.
(231) Grande, A. E.; Li, X.; Miller, L. M.; Zhang, J.; Draper, B. E.; Herzog, R. W.; Xiao, W.; Jarrold, M. F. Antibody Binding to Recombinant Adeno Associated Virus Monitored by Charge Detection Mass Spectrometry. *Anal. Chem.* **2023**, *95* (29), 10864–10868.
(232) Barnes, L. F.; Draper, B. E.; Jarrold, M. F. Analysis of Recombinant Adenovirus Vectors by Ion Trap Charge Detection Mass Spectrometry: Accurate Molecular Weight Measurements beyond 150 MDa. *Anal. Chem.* **2022**, *94* (3), 1543–1551.
(233) Barnes, L. F.; Draper, B. E.; Kurian, J.; Chen, Y.-T.; Shapkina, T.; Powers, T. W.; Jarrold, M. F. Analysis of AAV-Extracted DNA by Charge Detection Mass Spectrometry Reveals Genome Truncations. *Anal. Chem.* **2023**, *95* (9), 4310–4316.
(234) Miller, Z. M.; Harper, C. C.; Lee, H.; Bischoff, A. J.; Francis, M. B.; Schaffer, D. V.; Williams, E. R. Apodization Specific Fitting for Improved Resolution, Charge Measurement, and Data Analysis Speed in Charge Detection Mass Spectrometry. *J. Am. Soc. Mass Spectrom.* **2022**, *33* (11), 2129–2137.
(235) Pierson, E. E.; Keifer, D. Z.; Selzer, L.; Lee, L. S.; Contino, N. C.; Wang, J. C. Y.; Zlotnick, A.; Jarrold, M. F. Detection of Late Intermediates in Virus Capsid Assembly by Charge Detection Mass Spectrometry. *J. Am. Chem. Soc.* **2014**, *136* (9), 3536–3541.
(236) Miller, L. M.; Bond, K. M.; Draper, B. E.; Jarrold, M. F. Characterization of Classical Vaccines by Charge Detection Mass Spectrometry. *Anal. Chem.* **2021**, *93* (35), 11965–11972.
(237) McPartlan, M. S.; Harper, C. C.; Hanozin, E.; Williams, E. R. Ion Emission from 1–10 MDa Salt Clusters: Individual Charge State Resolution with Charge Detection Mass Spectrometry. *Analyst* **2024**, *149* (3), 735–744.
(238) Harper, C. C.; Brauer, D. D.; Francis, M. B.; Williams, E. R. Direct Observation of Ion Emission from Charged Aqueous Nanodrops: Effects on Gaseous Macromolecular Charging. *Chem. Sci.* **2021**, *12* (14), 5185–5195.
(239) Harper, C. C.; Miller, Z. M.; McPartlan, M. S.; Jordan, J. S.; Pedder, R. E.; Williams, E. R. Accurate Sizing of Nanoparticles Using a High-Throughput Charge Detection Mass Spectrometer without Energy Selection. *ACS Nano* **2023**, *17* (8), 7765–7774.
(240) Harper, C. C.; Jordan, J. S.; Papanu, S.; Williams, E. R. Characterization of Mass, Diameter, Density, and Surface Properties of Colloidal Nanoparticles Enabled by Charge Detection Mass Spectrometry. *ACS Nano* **2024**, *18* (27), 17806–17814.

Chapter 2

Effects of Electrospray Droplet Size on Analyte Aggregation: Evidence for Serine Octamer in Solution

This chapter is reproduced with permission from:

Jacob S. Jordan, Evan R. Williams

"Effects of Electrospray Droplet Size on Analyte Aggregation: Evidence for Serine Octamer in Solution"

Analytical Chemistry, **2021**, *93*(3):1725-1731

2.1 Abstract

Spraying solutions of serine under a wide variety of conditions results in unusually abundant gaseous octamer clusters that exhibit significant homochiral specificity, but the extent to which these clusters exist in solution or are formed by clustering during droplet evaporation has been debated. Electrospray ionization emitters with tip sizes between 210 nm and 9.2 μm were used to constrain the number of serine molecules that droplets initially contain. Protonated octamer was observed for all tip sizes with 10 mM serine solution, but the abundance decreases from 10% of the serine population at the largest tip size to ~5.6% for the two smallest tip sizes. At 100 μM, the population abundance of the protonated serine octamer decreases from 1% to 0.6% from the largest to the smallest tip size, respectively. At 100 μM, fewer than 10% of the initial droplets should contain even a single analyte molecule with 210 nm emitter tips. These results indicate that the majority of protonated octamer observed in mass spectra under previous conditions is formed by clustering inside the electrospray droplet, but ≤5.6% and ~0.6% of serine exists as an octamer complex in 10 mM and 100 μM solutions, respectively. These results show that aggregation occurs in large droplets, but this aggregation can be eliminated using emitters with sufficiently small tips. Use of these emitters with small tips is advantageous for clearly distinguishing between species that exist in solution and species formed by clustering inside droplets as solvent evaporation occurs.

2.2 Introduction

Since the initial report by Cooks and coworkers in 2000[1] that protonated serine octamer is unusually abundant in electrospray ionization (ESI) mass spectra of serine solutions under a wide

range of conditions, many groups have investigated both the origin and potential structures of this unusual species.[1-25] Protonated octamer can be even more abundant with sonic spray ionization (SSI), indicating that the formation of this cluster does not depend on direct electrostatic charging of droplets.[2-5,25] Two distinct forms of the octamer have been identified. The most abundant "A" form exhibits extraordinary preference for forming a homochiral structure, and this preference has led to the proposal that this species may have played an important role in the origin of homochirality in living organisms.[3-14] The relative abundances of the two forms of the octamer depend on desolvation conditions,[5,15,16] and the A isomer is exclusively formed with soft source conditions.[5] The structures of various forms of ionic serine octamer have been investigated using a variety of techniques.[1-25] Recently, Scutelnic et al. reported that the A form of the protonated octamer is composed entirely of zwitterionic serine molecules held together by hydrogen-bond interactions in a spherical, asymmetric geometry.[17] The homochirality of the structure was found to be a result of hydrogen-bonding interactions of six serine molecules.[17] Two of the serine molecules have a free hydroxyl group that enables exchange of these residues, consistent with earlier reports that the protonated octamer could exchange up to two of the component serine molecules.[4,5,7,13,14,18-20] A collision cross-section (CCS) value of 191 ± 2 $Å^2$ for the octamer from ion mobility measurements[17] matches well with the predicted CCS for the proposed structure (189 ± 1 $Å^2$) and with previously reported CCS values.[7,11,21] Although the gaseous structure of the protonated serine octamer is now well characterized, there is ambiguity about the extent to which this cluster exists in solution or is formed by aggregation in evaporating droplets.[2-9,14,15,21-24]

Julian and co-workers reported that protonated serine octamer was the predominant species in ESI mass spectra at both high and low ion transfer capillary temperatures, but abundant high mass clusters, corresponding to sixty serine molecules or more, were also observed under the former condition.[15] This led to the conclusion that the protonated octamer was formed by ion evaporation and that it either exists in solution or is formed at the surface in the charged droplets.[15] Cooks and co-workers reported evidence for a neutral form of the serine octamer in experiments where droplets were nebulized, heated, and ions deflected before remaining neutral molecules/clusters were subsequently ionized by solvent droplets formed by electrospray ionization or by atmospheric pressure chemical ionization where analyte enrichment in droplets should not occur.[9] Protonated serine octamer was the predominant ion in the resulting mass spectra and tandem MS data were consistent with these ions having the same structure as those ions formed directly by ESI. Based on these results, the authors concluded that the neutral octamer is formed during solution nebulization and that the octamer is the only neutral cluster species in the droplet.[9] Remarkably, neutral serine octamer can also be formed by sublimation, indicating that octamers are preferred structures even without solution droplets.[3,8]

Results from NMR and IR spectroscopy of serine solutions by Vandenbussche et al. do not show evidence for serine clusters in solution at the concentrations used in most MS studies.[22] The diffusion coefficients of serine in solution were measured using diffusion ordered spectroscopy NMR at 25 °C and a diffusion coefficient corresponding to that of the serine monomer was reported. Based on these results, the authors reported an upper limit to the existence of clusters in solution of less than 4%. Results from IR spectroscopy of L-serine in D_2O revealed symmetrical C=O stretching, a bond that is expected to be sensitive to clustering, suggesting the presence of only the serine monomer in solution. This conclusion is consistent with earlier work characterizing serine in D_2O in which all IR bands could be assigned solely to the serine monomer.[26] Additional mass spectrometry studies performed by Vandenbussche et al. on serine solutions in solvent mixtures of different polarities displayed the same clustering pattern, indicating that cluster

formation does not depend on solvent conditions.[22] The authors concluded from these combined experiments that serine octamers do not exist in solution and that they are likely formed during the droplet evaporation process.

The number of analyte molecules in an initial droplet depends on the droplet size and the solution concentration. The size of electrospray droplets depends on a number of factors, but droplet size can be controlled by varying the emitter tip diameter or by changing the backing pressure on a nanospray emitter of a given size to control solution flow rates.[27-34] Droplets formed either at small tip sizes or with low or no backing pressure have lifetimes as short as 1 μs.[29] ESI emitters with small tip diameters have been used to reduce adduction of non-volatile salts to biomolecules, such as sodium or potassium chloride, even when the concentration of these salts is ≥150 mM.[35-37] This occurs under conditions where there is on average fewer than one analyte molecule per initial electrospray droplet. The desalting effect improves with decreasing tip size so that most droplets contain salt but no analyte molecule. Thus, the analyte molecule is separated from the majority of the salt ions during droplet formation. Under these conditions, non-specific aggregation of analyte molecules that can occur inside of electrospray droplets is also reduced or prevented. For example, both dimers and monomers of β-lactoglobulin are produced by ESI from a 10 μM solution in aqueous 100 mM ammonium acetate.[34] The dimer signal is 35% of the overall protein signal with 4.4 μm emitters, but it is less than 9% with 317 nm tips.[34] These results indicate that the dimers produced with the larger tips are predominantly formed by non-specific protein aggregation during solvent evaporation inside the droplet and that they do not exist in significant abundance in solution at this concentration. This result is consistent with the known dimerization characteristics of this protein wherein the dimer is the predominant species at concentrations >50 μM in physiological conditions.[38] Droplets formed with the smallest nanoelectrospray emitters are sufficiently short lived that they do not enter the mass spectrometer.[34] Under these conditions, the droplet temperature is unaffected by heated interface capillaries that can increase the temperature of larger droplets, so that solution-phase equilibria of non-covalent complexes should not be adversely affected with the smallest tips.[34,39,40]

Here, the average number of serine molecules inside of the initial electrospray droplet is varied by changing the diameter of nanoscale ESI emitters and by changing the concentration of serine in solution. By constraining the number of serine molecules inside of the initial droplets to on average, fewer than one, information about the extent to which the serine octamer exists in solution is deduced.

2.3 Experimental Methods

Borosilicate capillaries (1.0 mm outer diameter, 0.78 mm inner diameter, Sutter Instruments, Novato, CA) were pulled using a Flaming/Brown P-87 micropipette puller (Sutter Instruments) to produce nanoelectrospray emitters with five different tip sizes with inner diameters between 210 nm and 9.2 μm. Tip diameters were measured using a Hitachi TM-1000 scanning electron microscope (Schaumburg, IL) in the Electron Microscope Laboratory at the University of California at Berkeley for each set of puller parameters. Four tips were pulled for each set of pulling parameters to measure the standard deviation of the resulting diameters. The five tip sizes used in this experiment had inner diameters of 210 ± 11 nm, 377 ± 17 nm, 1.2 μm ± 0.1 μm, 3.6 μm ± 0.1 μm, and 9.2 μm ± 0.3 μm.

Solutions of 10 mM or 100 μM L-serine (Sigma-Aldrich, St. Louis, MI) in 49.95:49.95:0.1 methanol:water:acetic acid (Sigma-Aldrich, St. Louis, MI) were electrosprayed and signal was monitored between *m*/*z* 50 – 1500 using a Finnigan LTQ mass spectrometer (Thermo Fisher Scientific, San Jose, CA). Data was acquired in the linear ion trap. Instrument parameters were optimized for the protonated octamer signal using the automated tuning feature of the control software while spraying a 10 mM solution from a 1.2 μm diameter emitter tip. The same instrument parameters were then used for all subsequent experiments. The transfer capillary voltage, tube lens voltage, and transfer capillary temperature were set to 23 V, 135 V, and 100 °C respectively. Automatic gain control was turned off on the instrument and the injection time was maintained at a constant value of 2.5 ms that was optimized to prevent space-charge distortion of the mass spectra.

Nanoelectrospray was initiated by applying a voltage of approximately 0.4 – 1.4 kV to a 0.127 mm diameter platinum wire that is inserted inside of the capillary and that is in contact with the solution. The electrospray voltage was increased until the spray was stable and then allowed to equilibrate for one minute before data acquisition. Stable sprays are obtained at lower voltage for emitters with smaller tips. Five replicate measurements using different emitters for each tip diameter were acquired by averaging for one minute at a scan rate of 8.33 Hz.

The abundance of each ion that is >0.1% of the protonated monomer is reported relative to the abundance of the protonated monomer, which is the most abundant ion in each spectrum. Variance from the mean is reported as the standard error of five replicates for each tip size at each concentration. Overlapping clusters with different charge states were identified using high-resolution data obtained with an FT-ICR mass spectrometer (Thermo Fisher Scientific, San Jose, CA) for each tip size. Automatic gain control was used to obtain sufficient signal to isotopically resolve any overlapping contributions at each cluster *m*/*z*. Some replicate data were acquired on a Velos Pro mass spectrometer (Thermo Fisher Scientific, San Jose, CA) and a Q-TOF Premier quadrupole time-of-flight mass spectrometer (Waters Corporation, Milford, MA) using conditions reported in Supporting Information.

2.4 Results and Discussion

2.4.1 Effects of Emitter Tip Size at 10 mM

Mass spectra were obtained by electrospray ionization of a 10 mM solution of L-serine using emitters with tips sizes of 9.2 μm, 3.6 μm, 1.2 μm, 0.38 μm and 0.21 μm. A 10 mM concentration was chosen because it has been commonly used in prior studies.[1-3,5-10,15,17,21-25] The relative abundances of the most abundant cluster ions formed by ESI as a function of tip size is shown in Figure 1a. The identity of the peak at *m*/*z* = 841 was confirmed by high-resolution measurements with an FT-ICR instrument to be predominantly protonated serine octamer (>95%) at all tip sizes. The abundances of doubly protonated 16-mer and triply protonated 24-mer metaclusters were an average of 2.5 ± 0.4% and 0.6 ± 0.1%, respectively. The abundance of protonated octamer obtained from the lower resolution data was corrected for the presence of these metaclusters.

The protonated octamer is the most abundant cluster at all tip sizes, consistent with results from previous ESI studies of serine solutions at this concentration. At larger tip sizes, the relative abundances of the protonated octamer and other clusters are significantly higher than at smaller tip sizes. The relative abundance of the protonated octamer decreases from an average of 23.6 ± 1.7% for the two largest emitter tips to 9.1 ± 1.6% for the two smallest tip sizes (Figure 2, top). These data indicate that the majority (≥61%) of the protonated octamer that is observed at the larger tip sizes is formed by aggregation of serine molecules inside of the electrospray droplet as a result of solvent evaporation. To the extent that no aggregation inside of the droplet occurs in the two smallest tip sizes, these results suggest that ≤5.6% of the serine population exists in the octameric form in 10 mM solution.

A similar decrease in abundance with decreasing emitter tip size occurs for the larger clusters. For example, the abundance of the 26^{3+} cluster decreases from an average of 3.4 ± 0.1% at the largest two tip sizes to 1.6 ± 0.2% at the smallest two tip sizes (Figure 1b). The two-fold lower abundance at small tip size indicates that a substantial population of the larger clusters are also formed by aggregation within the bigger droplets formed by emitters with larger tips.

2.4.2 Droplet Size and Initial Number of Serine Molecules

The initial size of droplets produced from nano-ESI emitters depends on the diameter of the emitter tip.[27-34] The number of analyte molecules that are contained in each of the initially formed droplets also depends on droplet size and concentration. Davidson et al. reported that the initial droplets produced with 1 – 3 μm emitter tips were, on average, 60 nm in diameter or ~1/17th the emitter tip diameter.[27] They also showed that the percentage of droplets that contain a single analyte molecule increases from 24% to 98% when the solution concentration is reduced from 40 μM to 0.4 μM at this same tip size.[27] A similar estimate of initial droplet diameters produced by micron size and smaller emitters was inferred from the effectiveness of desalting protein ions to be between 1/14th and 1/20th the size of the emitter tip diameter.[35]

A rough estimate of the number of analyte molecules that are contained in the initial droplets produced by electrospray ionization at each tip size was obtained using an average droplet size of 1/17th the tip diameter.[27,35] This estimated average number of analyte molecules per droplet is determined using equation 1:

$$\#\ of\ molecules = \left(\frac{D_E \times \left(\frac{1}{17}\right)}{2}\right)^3 \times \frac{4}{3}\pi \times 10^{-24} \times M \times N_A \qquad (1)$$

where D_E is the emitter tip diameter in nm, 10^{-24} is a unit conversion from nm^3 to L, M is the concentration of the solution in M, and N_A is Avogadro's number. The average number of molecules in droplets produced from various tip sizes at a solution concentration of 10 mM and at 100 μM are given in Table 1. At 10 mM, even an emitter tip size of 210 nm will produce droplets that contain an average of approximately six analyte molecules. Because of the variability of droplet sizes that are formed, it is not possible to rule out aggregation inside these droplets as a potential source of protonated octamer in ESI mass spectra. For this reason, these experiments were repeated with a 100-fold less concentrated serine solution. At this same 210 nm tip size, only one in about 17 droplets should contain an analyte species from solution. Even with a wide

distribution of droplet sizes, these conditions should significantly reduce any potential for aggregation inside an electrospray droplet. Any clusters observed under these conditions would provide strong evidence that the cluster exists in solution prior to droplet formation.

2.4.3 Effects of Emitter Tip Size at 100 μM

In order to ensure conditions where there are substantially fewer than one analyte molecule per initial droplet at the smallest tip size, electrospray mass spectra were acquired from 100 μM solutions at each emitter tip size. Under these conditions, clusters up to a triply protonated 26-mer were observed at >0.1% relative abundance with the largest tip size (Figure 3). Protonated dimer is the most abundant cluster and the abundance decreased from 6.1 ± 0.9% to 2.7 ± 0.6% at the largest and smallest tip sizes, respectively.

The relative abundance of the protonated octamer decreases with decreasing tip size from 1.2 ± 0.1% to 0.7 ± 0.1% (Figure 2, bottom). As was the case at 10 mM, the peak at m/z = 841 consists of >95% protonated octamer with 16-mer and 24-mer at an average of 4.4 ± 1.4 % and 0.5 ± 0.1%, respectively. There is no significant difference in protonated octamer abundance at the smallest two tip sizes for which each droplet should contain either one or zero analyte molecules on average. These results indicate that the protonated octamer is only 0.6 ± 0.1% of the total serine population in 100 μM solution. This value is much lower than the upper limit of 5.6 ± 1% determined for a 10 mM solution. At 10 mM, there are on average six serine molecules per droplet at the smallest tip size, so aggregation inside the evaporating droplets may contribute to the protonated octamer signal. Thus, the 5.6% value derived from the 10 mM data is an upper limit to the true solution abundance of the octamer. The significantly lower value of solution-phase octamer obtained for the 100 μM experiments, however, can also be explained by a shift in equilibrium towards the monomer at the significantly lower concentration.

The abundances of clusters larger than the octamer are all less than half that of the octamer. The abundance of these clusters is lowest for the smallest two tip sizes (377 nm and 210 nm) which produce clusters with similar abundances. These tip sizes correspond to conditions where each droplet is expected to contain one or zero analyte molecules on average. The similar abundance of clusters at these two tip sizes indicates that these molecular assemblies entered the droplet from solution, indicating that a number of these oligomers exist in solution at low abundance. Assuming that the abundances of the clusters obtained from the 210 nm emitter tips reflect their corresponding abundances in solution, then clusters larger than the dimer, excluding the octamer, each compose <0.35% of the total serine population and, combined, represent only 2.2% of the population.

To determine the extent to which these results are instrument dependent, additional data were acquired using a Thermo Fisher Velos Pro mass spectrometer and a Waters Q-TOF Premier quadrupole time-of-flight mass spectrometer. The population abundances of the protonated octamer determined with the Q-TOF instrument at the smallest tip size are 5.8 ± 0.2% and 2.8 ± 0.3% at 10 mM and 100 μM, respectively. In these experiments, clusters as large as 57^{4+} were observed. Values of 5.6 ± 0.1% and 0.8 ± 0.2% were obtained using a Velos Pro mass spectrometer. The similar results with three different instruments indicate that, although there is some instrument dependent variability, serine octamer exists in solution at low abundance.

Protonated octamer can also be formed by gas-phase dissociation of larger clusters[15] and interface conditions can affect the distributions of a variety of different clusters.[41-43] In order to determine the extent to which source conditions affect the population abundance of the protonated octamer in these experiments, the transfer capillary temperature, transfer capillary voltage and the tube lens voltage were varied and ions were formed from a 100 μM serine solution with a 210 nm emitter. The transfer capillary temperature was varied between 60 °C and 220 °C. There were no significant trends in the abundances of the protonated octamer or higher order clusters over this temperature range (Figure S1, supporting information). The transfer capillary temperature used in these experiments (100 °C) is at the lower end of this temperature range indicating that gas-phase dissociation of higher order clusters that may be induced by higher transfer capillary temperatures does not contribute substantially to the protonated octamer abundance under these conditions.

The extent to which the potential applied to the transfer capillary induces dissociation was investigated over a range between 5 V and 120 V. The population abundance of the protonated octamer at 5 V and 23 V (the potential used in these experiments) is similar, but decreases substantially at the higher voltages, consistent with collisional dissociation of this and other higher order clusters (Figure S2a, supporting information). The population abundance of the protonated octamer varies with tube lens voltage with a minimum value of 0.4% around 90 V (Figure S2b, supporting information). The origin of the higher abundance at higher and lower tube lens voltages is unclear, but may be related to relative ion transmission efficiencies of clusters at different *m/z,* which would affect the calculated ion population abundances. In sum, these data indicate that the protonated octamer observed with the 210 nm tip size under the operating conditions of these experiments, is not a result of in-source activation and dissociation of larger clusters, consistent with these ions originating from solution.

2.4.4 Serine Octamer in Solution

The observation of protonated octamer at the 100 μM concentration with the smallest tip size, where only one in roughly 17 droplets initially formed by electrospray ionization contain a single analyte molecule, provides compelling evidence for the existence of the octamer in solution at ~0.6% of the serine population. Even at this low concentration, the octamer is a magic number cluster, which is indicative of its special stability *in solution*. It is interesting to speculate about differences in results and conclusions from prior experiments. There was no signal detected for any clusters in the NMR study by Vandenbussche et al., but the authors report a detection limit of 4% relative abundance if the octamer is the only cluster present in solution.[22] The value of ≤5.6 ± 1% serine octamer abundance in a 10 mM solution is consistent with the NMR results. We cannot rule out that some aggregation occurs inside the droplets at this concentration even with the smallest tip size. There are also effects of ion transmission and detection efficiency that are not taken into account in our study.

Data from many previous mass spectrometry studies show the protonated octamer is the most abundant form of serine in the spectra, yet our results show an upper limit of ~5.6% of serine octamer in solution at similar concentrations. Previous studies have typically been done using much larger emitters compared to those used here. These include the commercial Thermo Finnigan/Thermo Fisher electrospray source (76 or 102 μm in diameter depending on needle gauge)[6,7,15,44], homebuilt SSI sources (100 μm in diameter)[2-4,14,25] and homebuilt nebulization

sources (200 μm in diameter)[9]. A notable exception to extensive formation of protonated octamer are results from Myung et al., which showed that clusters containing over 600 serine molecules can be generated using sonic spray with large diameter capillaries, high flow rates, and soft source conditions.[25] Under these conditions, protonated octamer comprises only ~0.3% of the total ion distribution. Based on our results where aggregation is observed to form the octamer with our largest tip, which is less than 10 μm, it is expected that the even larger emitters used in many prior studies will produce much larger droplets with a corresponding significantly larger number of serine molecules in each droplet. Formation of even larger clusters and subsequent dissociation of these larger clusters may also contribute to the abundant protonated octamer signal observed in prior studies.[15]

2.5 Conclusions

Under readily achievable conditions, the number of analyte molecules that are inside of an initially produced electrospray droplet can be reduced below an average of a single molecule per droplet. This can be achieved by lowering analyte concentration or by decreasing the size of the electrospray emitter tip diameter. With a 210 nm emitter tip diameter and 100 μM serine solution, on average, only one droplet in 17 contains an analyte molecule from solution. Under these conditions, protonated octamer is a magic number cluster and is about 0.6% of the serine population. Although the abundance is low, these results provide compelling evidence that the serine octamer is a special cluster that exists in solution even at this low concentration. The upper limit of 5.6% protonated serine octamer population obtained from a 10 mM solution is consistent with results from a prior NMR solution study that reported a population that must be below the detection limit of ~4%. These results indicate that aggregation of analyte molecules inside of evaporating electrospray droplets can lead to a significant abundance of clusters in electrospray mass spectra that are not indicative of the concentrations of these species in the original solution. By reducing the emitter tip size, aggregation can be significantly reduced and even eliminated, making it possible to establish the concentration of noncovalent complexes that exist in solution and that are not formed as an artifact of the electrospray ionization process. These results should be equally applicable to studies of protein-substrate and higher order macromolecular interactions where careful control studies of different analytes are typically required to provide evidence for the extent of specificity that may exist between binding partners in solution.

2.6 Acknowledgments

This material is based upon work supported by the National Science Foundation Division of Chemistry under grant number CHE-1609866 as well as a Graduate Research Fellowship (DGE-1752814). The authors are also grateful for financial support from CALSOLV and thank Dr. Anthony T. Iavarone for assistance with instrumentation during the course of this work.

2.7 References

(1) Zhang, D.; Koch, K. J.; Tao, W. A.; Cooks, R. G. Clustering of Amino Acids in the Gas Phase by Electrospray Ionization Mass Spectrometry. *Proceedings of the 48th ASMS Conference on Mass Spectrometry and Allied Topics.* **2000**, 1361-1362, Abstract ID: 274850.
(2) Takats, Z.; Nanita, S. C.; Cooks, R. G.; Schlosser, G.; Vekey, K. Amino Acid Clusters Formed by Sonic Spray Ionization. *Anal. Chem.* **2003**, *75*, 1514-1523.
(3) Yang, P.; Xu. R.; Nanita, S. C.; Cooks, R. G. Thermal Formation of Homochiral Serine Clusters and Implications for the Origin of Homochirality. *J. Am. Chem. Soc.* **2006**, *128*, 17074-17086.
(4) Takats, Z.; Nanita, S. C.; Cooks, R. G. Serine Octamer Reactions: Indicators of Prebiotic Relevance. *Angew. Chem. Int. Ed.* **2003**, *42*, 3521-3523.
(5) Takats, Z.; Nanita, S. C.; Schlosser, G.; Vekey, K.; Cooks, R. G. Atmospheric Pressure Gas-Phase H/D Exchange of Serine Octamers. *Anal. Chem.* **2003**, *75*, 6147-6154.
(6) Cooks, R. G.; Zhang, D.; Koch, K. J.; Gozzo, F. C.; Eberlin, M. N. Chiroselective Self-Directed Octamerization of Serine: Implications for Homochirogenesis. *Anal. Chem.* **2001**, *73*, 3646-3655.
(7) Julian, R. R.; Hodyss, R.; Kinnear, B.; Jarrold, M. F.; Beauchamp, J. L. Nanocrystalline Aggregation of Serine Detected by Electrospray Ionization Mass Spectrometry: Origin of the Stable Homochiral Gas-Phase Serine Octamer. *J. Phys. Chem. B* **2002**, *106*, 1219-1228.
(8) Takats, Z.; Cooks, R. G. Thermal Formation of Serine Octamer Ions. *Chem. Commun.* **2004**, 444-445.
(9) Zhang, H.; Wei, Z.; Jiang, J.; Cooks, R. G. Nebulization Prior to Isolation, Ionization, and Dissociation of the Neutral Serine Octamer Allows Its Characterization. *Angew. Chem. Int. Ed.* **2018**, *57*, 17141-17145.
(10) Koch, K. J.; Gozzo, F. C.; Zhang, D.; Eberlin, M. N.; Cooks, R. G. Serine Octamer Metaclusters: Formation, Structure Elucidation and Implications for Homochiral Polymerization. *Chem. Commun.* **2001**, 1854-1855.
(11) Schalley, C. A.; Weis, P. Unusually Stable Magic Number Clusters of Serine with a Surprising Preference for Homochirality. *Int. J. Mass Spectrom.* **2002**, *221*, 9-19.
(12) Sunahori, F. X.; Yang, G.; Kitova, E. N.; Klassen, J. S.; Xu, Y. Chirality Recognition of the Protonated Serine Dimer and Octamer by Infrared Multiphoton Dissociation Spectroscopy. *Phys. Chem. Chem. Phys.* **2013**, *15*, 1873-1886.
(13) Koch, K. J.; Gozzo, F. C.; Nanita, S. C.; Takats, Z.; Eberlin, M. N.; Cooks, R. G. Chiral Transmission between Amino Acids: Chirally Selective Amino Acid Substitution in the Serine Octamer as a Possible Step in Homochirogenesis. *Angew. Chem. Int. Ed.* **2002**, *41*, 1721-1724.
(14) Nanita, S. C.; Cooks, R. G. Serine Octamers: Cluster Formation, Reactions, and Implications for Biomolecule Homochirality. *Angew. Chem. Int. Ed.* **2006**, *45*, 554-569.
(15) Spencer, E. A. C.; Ly, T.; Julian, R. R. Formation of the Serine Octamer: Ion Evaporation or Charge Residue? *Int. J. Mass Spectrom.* **2008**, *270*, 166-172.
(16) Mazurek, U.; Geller, O.; Lifshitz, C.; McFarland, M. A.; Marshall, A. G.; Reuben, B. G. Protonated Serine Octamer Cluster: Structure Elucidation by Gas-Phase H/D Exchange Reactions. *J. Phys. Chem. A* **2005**, *109*, 2107-2112.
(17) Scutelnic, V.; Perez, M. A. S.; Marianski, M.; Warnke, S.; Gregor, A.; Rothlisberger, U.; Bowers, M. T.; Baldauf, C.; von Helden, G.; Rizzo, T. R.; Seo, J. The Structure of the Protonated Serine Octamer. *J. Am. Chem. Soc.* **2018**, *140*, 7554-7560.

(18) Gronert, S.; O'Hair, R. A. J.; Fagin, A. E. Ion/Molecule Reactions of the Protonated Serine Octamer. *Chem. Commun.* **2004**, 1944-1945.
(19) Ren, J.; Wang, Y.; Feng, R.; Kong, X. Investigation of L/D-Threonine Substituted L-Serine Octamer Ions by Mass Spectrometry and Infrared Photodissocation Spectroscopy. *Chin. Chem. Lett.* **2017**, *28*, 537-540.
(20) Liao, G.; Yang, Y.; Kong, X. Chirality Effects on Proline-Substituted Serine Octamers Revealed by Infrared Photodissociation Spectroscopy. *Phys. Chem. Chem. Phys.* **2014**, *16*, 1554-1558.
(21) Counterman, A. E.; Clemmer, D. E. Magic Number Clusters of Serine in the Gas Phase. *J. Phys. Chem. B* **2001**, *105*, 8092-8096.
(22) Vandenbussche, S.; Vandenbussche, G.; Reisse, J.; Bartik, K. Do Serine Octamers Exist in Solution? Relevance to this Question in the Context of the Origin of Homochirality on Earth. *Eur. J. Org. Chem.* **2006**, 3069-3073.
(23) Seo, J.; Warnke, S.; Pagel, K.; Bowers, M. T.; von Helden, G. Infrared Spectrum and Structure of the Homochiral Serine Octamer-Dichloride Complex. *Nat. Chem.* **2017**, *9*, 1263-1268.
(24) Nemes, P.; Schlosser, G.; Vekey, K. Amino Acid Cluster Formation Studied by Electrospray Ionization Mass Spectrometry. *J. Mass Spectrom.* **2005**, *40*, 43-49.
(25) Myung, S.; Julian, R. R.; Nanita, S. C.; Cooks, R. G.; Clemmer, D. E. Formation of Nanometer-Scale Serine Clusters by Sonic Spray. *J. Phys. Chem. B* **2004**, *108*, 6105-6111.
(26) Ramirez, F. J.; Tunon, I.; Silla, E. Amino Acid Chemistry in Solution: Structural Properties and Vibrational Dynamics of Serine using Density Functional Theory and a Continuum Solvent Model. *Chem. Phys.* **2004**, *303*, 85-96.
(27) Davidson, K. L.; Oberreit, D. R.; Hogan Jr., C. J.; Bush, M. F. Nonspecific Aggregation in Native Electrokinetic Nanoelectrospray Ionization. *Int. J. Mass Spectrom.* **2017**, *420*, 35-42.
(28) Mortensen, D. N.; Williams, E. R. Theta-Glass Capillaries in Electrospray Ionization: Rapid Mixing and Short Droplet Lifetimes. *Anal. Chem.* **2014**, *86*, 9315-9321.
(29) Mortensen, D. N.; Williams, E. R. Ultrafast (1 μs) Mixing and Fast Protein Folding in Nanodrops Monitored by Mass Spectrometry. *J. Am. Chem. Soc.* **2016**, *138*, 3453-3460.
(30) Mortensen, D. N.; Williams, E. R. Investigating Protein Folding and Unfolding in Electrospray Nanodrops Upon Rapid Mixing Using Theta-Glass Emitters. *Anal. Chem.* **2015**, *87*, 1281-1287.
(31) Pfeifer, R. J.; Hendricks Jr., C. D. Parametric Studies of Electrohydrodynamic Spraying. *AIAA J.* **1968**, *6*, 496-502.
(32) Olumee, Z.; Callahan, J. H.; Vertes, A. Droplet Dynamics Changes in Electrostatic Sprays of Methanol-Water Mixtures. *J. Phys. Chem. A* **1998**, *102*, 9154-9160.
(33) Tang, K.; Gomez, A. Monodisperse Electrosprays of Low Electric Conductivity Liquids in the Cone-Jet Mode. *J. Colloid Interface Sci.* **1996**, *184*, 500-511.
(34) Xia, Z.; Williams, E. R. Effect of Droplet Lifetime on Where Ions are Formed in Electrospray Ionization. *Analyst* **2019**, *144*, 237-248.
(35) Susa, A. C.; Xia, Z.; Williams, E. R. Small Emitter Tips for Native Mass Spectrometry of Proteins and Protein Complexes from Nonvolatile Buffers that Mimic the Intracellular Environment. *Anal. Chem.* **2017**, *89*, 3116-3122.
(36) Susa, A. C.; Xia, Z.; Williams, E. R. Native Mass Spectrometry from Common Buffers with Salts That Mimic the Extracellular Environment. *Angew. Chem. Int. Ed.* **2017**, *56*, 7912-7915.

(37) Susa, A. C.; Lippens, J. L.; Xia, Z.; Loo, J. A.; Campuzano, I. D. G.; Williams, E. R. Submicrometer Emitter ESI Tips for Native Mass Spectrometry of Membrane Proteins in Ionic and Nonionic Detergents. *J. Am. Soc. Mass Spectrom.* **2018**, *29*, 203-206.
(38) Gottschalk, M.; Nilsson, H.; Roos, H.; Halle, B. Protein Self-Association in Solution: The Bovine β-lactoglobulin Dimer and Octamer. *Protein Sci.* **2003**, *12*, 2404-2411.
(39) Xia, Z.; Williams, E. R. Protein-Glass Surface Interactions and Ion Desalting in Electrospray Ionization. *J. Am. Soc. Mass Spectrom.* **2017**, *29*, 194-202.
(40) Nguyen, G. T. H.; Tran, T. N.; Podgorski, M. N.; Bell, S. G.; Supuran, C. T.; Donald, W. A. Nanoscale Ion Emitters in Native Mass Spectrometry for Measuring Ligand-Protein Binding Affinities. *ACS Cent. Sci.* **2019**, *5*, 308-318.
(41) Counterman, A. E.; Valentine, S. J.; Srebalus, C. A.; Henderson, S. C.; Hoaglund, C. S.; Clemmer, D. A. High-Order Structure and Dissociation of Gaseous Peptide Aggregates that are Hidden in Mass Spectra. *J. Am. Soc. Mass Spectrom.* **1998**, *9*, 743-759.
(42) Hogan, C. J.; de la Mora, J. F. Ion-Pair Evaporation from Ionic Liquid Clusters. *J. Am. Soc. Mass Spectrom.* **2010**, *21*, 1382-1386.
(43) Rodriguez-Cruz, S. E.; Klassen, J. S.; Williams, E. R. Hydration of Gas-Phase Ions Formed by Electrospray Ionization. *J. Am. Soc. Mass Spectrom.* **1999**, *10*, 958-968.
(44) Thermo Fisher Scientific. *HESI-II Probe User Guide,* Revision C.; Thermo Fisher Scientific Inc.: Waltham, MA, 2009.

2.8 Figures

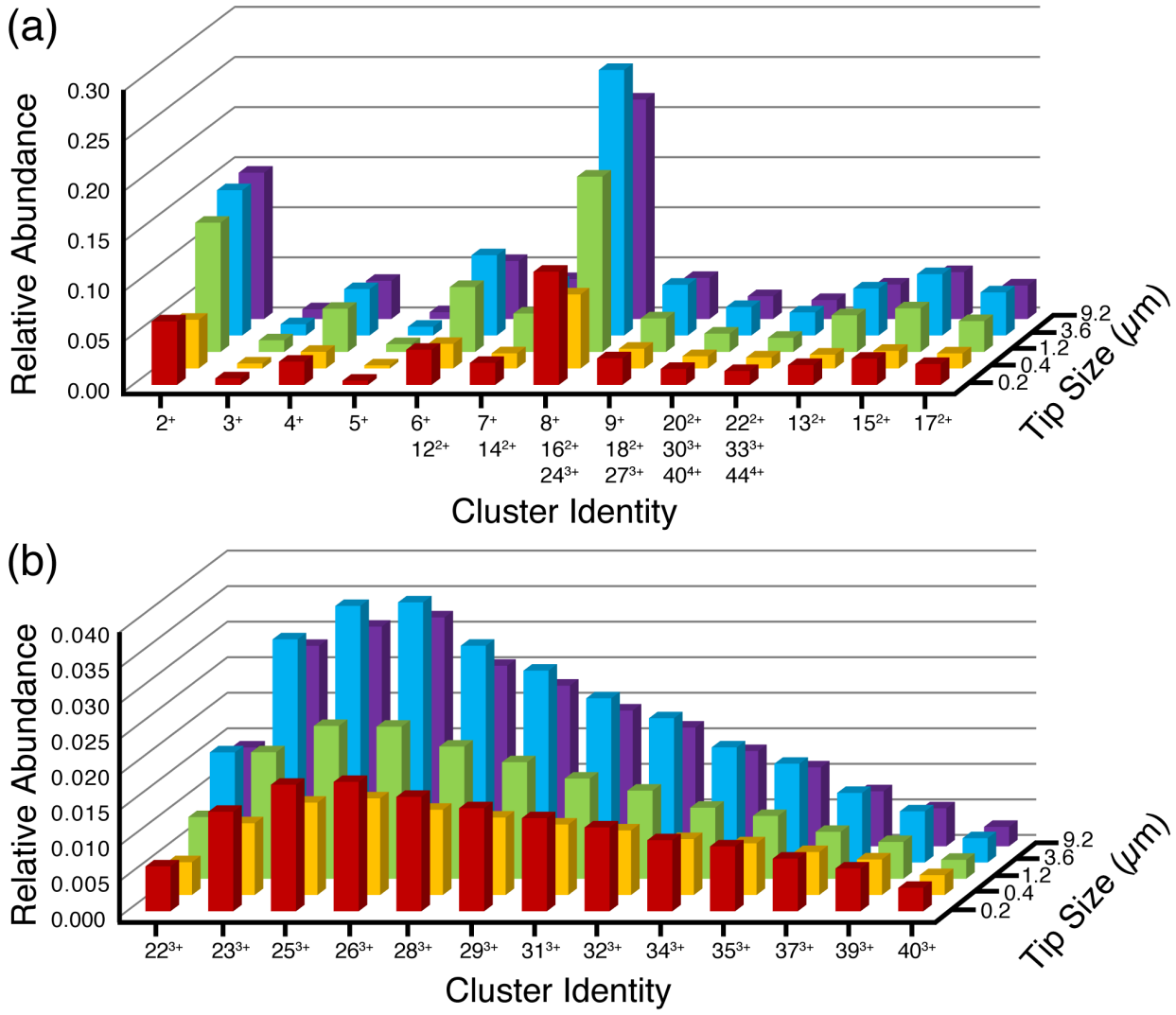

Figure 2.1. Relative abundances of protonated serine clusters formed by electrospray ionization of a 10 mM L-serine solution as a function of electrospray emitter tip diameter. Clusters shown are (a) the most abundant singly and doubly charged clusters or (b) the most abundant unambiguously identifiable triply charged clusters. A comprehensive list of the cluster assignments is given in Table S1.

Table 2.1. Approximate Average Number of Molecules in Each Initial Droplet Produced by NanoESI

Tip Size	**10 mM**	**100 µM**
210 nm	6	0.06
377 nm	34	0.34
1.2 µm	1,109	11
3.6 µm	29,943	299
9.2 µm	499,754	4,998

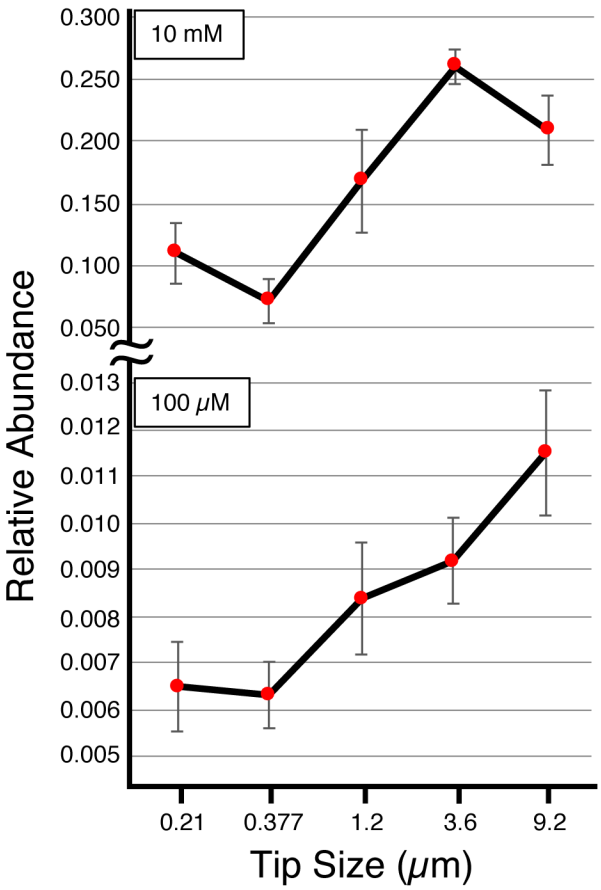

Figure 2.2. Relative abundance of protonated octamer formed by electrospray ionization of a L-serine solution at 10 mM (top) and at 100 µM (bottom) concentration as a function of electrospray emitter tip diameter.

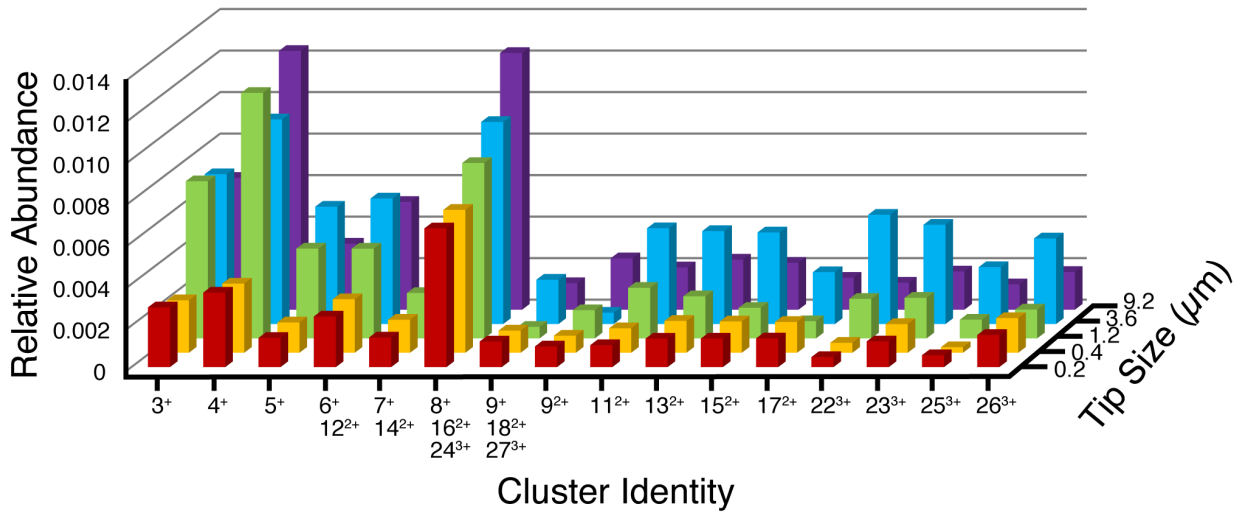

Figure 2.3. Relative abundances of protonated serine clusters larger than the dimer formed by electrospray ionization of a 100 μM L-serine solution as a function of electrospray emitter tip diameter.

2.9 Supplemental Information

2.9.1 Derivation of Equation One

Equation one is based on several approximations: the initial ESI droplet is a sphere with a diameter that is 1/17th the diameter of the ESI emitter tip, the distribution of analyte molecules within the initial droplet and the solution prior to droplet formation is homogeneous, fusion of the highly charged droplets after their initial formation does not occur, and that all droplets produced by ESI are the same diameter. The volume of a droplet is modeled as the volume of a sphere from the approximations listed above. To convert the value from nm^3 to L when the ESI emitter diameter is expressed in units of nm, a unit conversion of 10^{-24} is applied. Multiplying the volume by the molarity of the solution and then Avogadro's number gives the estimated number of molecules in each droplet produced under the stated approximations.

$$m = \left(\frac{4}{3}\right)\pi\left(\frac{D_E\left(\frac{1}{17}\right)}{2}\right)^3 * 10^{-24} * M * N_A$$

2.9.2 Ion Transfer Capillary Temperature

The ion transfer capillary temperature was optimized by tuning the instrument ion optics for protonated octamer signal using the automated tuning feature of the instrument control software, then changing the transfer capillary temperature to the following values: 60 °C, 100 °C, 140 °C, 180 °C and 220 °C. A 100 μM serine solution was sprayed using 210 nm emitter tips in order to determine the effect of transfer capillary temperature on cluster abundances. There were no significant trends in the abundances of clusters over this temperature range (Figure S1). The large variability in the abundance of the octamer is likely due to these experiments being performed over several hours in order to allow the ion transfer capillary to equilibrate at each temperature. The average for the octamer abundance across all temperatures was calculated to be 0.56 ± 0.1%, closely matching the value found in the initial experiments at 100 °C. Similarly, the average population abundances of the 15^{2+} and 23^{3+} clusters across the temperature range are 0.11 ± 0.02% and 0.13 ± 0.03% respectively, which agree with the reported value at 100 °C in the tip size experiment, 0.11 ± 0.02% and 0.12 ± 0.02%, respectively. These results indicate that gas-phase dissociation of higher order clusters that may be induced by higher transfer capillary temperatures is not a significant contribution to the protonated octamer abundance observed under these conditions.

2.9.3 In-Source Activation of Larger Clusters at Various Electrospray Source Conditions

In order to examine the effect of voltage on the transfer capillary and tube lens on gas-phase dissociation of large clusters, a 100 μM solution of L-serine was electrosprayed using 210 nm emitters and the transfer capillary voltage and the tube lens voltage were varied. The transfer capillary voltage was varied between 5 V and 120 V. The abundance of the protonated octamer was similar at 5 V and 23 V, but decreased significantly at larger voltages, consistent with collisional dissociation of both the octamer and higher order clusters (Figure S2a).

The tube lens voltage was varied between 50 V and 250 V to determine the effect on the protonated octamer population abundance. The octamer abundance varies with tube lens voltage, from a minimum value of 0.4% at 91 V to a maximum of 1.2% at 250 V (Figure S2b). The reason for the variation in abundance with increasing tube lens voltage is unclear, but may be related to relative ion transmission efficiencies of clusters at different *m/z,* which would affect the calculated population abundances of clusters. This data indicates that the tube lens voltage used in the tip size experiments does not result in breakdown of larger clusters into the protonated octamer in the gas phase.

In sum, these data indicate that the protonated octamer observed with the 210 nm tip size under the conditions of these experiments is not a result of gas-phase dissociation of larger clusters, consistent with these ions originating from solution.

2.9.4 Waters Q-TOF Premier Mass Spectrometer Instrument Parameters and Protonated Octamer Data

A Q-TOF Premier quadrupole time-of-flight mass spectrometer (Waters Corporation, Milford, MA) was also used in these experiments in order to investigate the extent to which source design and ion transmission in different instruments affect our reported results. Instrument parameters were manually tuned to maximize the protonated octamer abundance with ions formed from a 10 mM L-serine solution using an ESI emitter with a 1.2 μm tip. Experiments were then performed using ESI emitters with 210 nm tips to measure the population abundances of the protonated octamer at both 10 mM and 100 μM. The source temperature was 80 °C, the sampling cone and extraction cone voltages were 20 V and 2.0 V respectively. The ion guide voltage was 2.0 V. The collision cell parameters were optimized to a cell entrance potential of 0 V and a cell exit potential of -10 V with a collision gas flow rate of 0.35 mL/min, resulting in a pressure of ~4.4 x 10^{-3} mbar in the collision cell. Stable ion formation was typically obtained at a spray voltage of 0.6 – 0.7 kV.

The population abundance of the protonated octamer was 5.8 ± 0.2% and 2.8 ± 0.3% at 10 mM and 100 μM, respectively. Abundant high mass clusters up to 57^{4+} were observed with a 10 mM solution. The largest clusters were not observed with the LTQ instrument. In contrast, the same distribution of clusters were observed with the LTQ instrument and the Q-TOF instrument at 100 μM albeit at higher abundance with the Q-TOF instrument. These data indicate that the observed abundance of the protonated octamer does have some instrument dependent variability.

2.9.5 Thermo Fisher Velos Pro Mass Spectrometer Instrument Parameters and Protonated Octamer Data

The L-serine solutions were also analyzed using a Thermo Fisher Velos Pro mass spectrometer. Instrument parameters were optimized using the automated tuning feature of the control software while spraying a 10 mM L-serine solution using a 1.2 μm emitter tip. The ion transfer capillary temperature was set to 100 °C to mimic conditions in the LTQ instrument and the S-lens RF percentage was optimized to 67.5% by the automatic tuning process. The data was recorded using the same protocol described in the methods section. Using 210 nm emitter tips, the population abundance of the octamer was found to be 5.6 ± 0.1% and 0.8 ± 0.2% for the 10 mM and 100 μM concentrations respectively.

Supplementary Table 2.1. Cluster Assignments for Each Peak in ESI Mass Spectra of 10 mM L-Serine

m/z	**Cluster Number**	**Charge**
106	1 + H	1
128	1 + Na	1
211	2 + H	1
233	2 + Na	1
316	3 + H	1
421	4 + H, 8 + 2H	1, 2
474	9 + 2H	2
526	5 + H	1
579	11 + 2H	2
631	6 + H, 12 + 2H	1, 2
684	13 + 2H	2
736	7 + H, 14 + 2H	1, 2
772	22 + 3H	3
789	15 + 2H	2
807	23 + 3H	3
841	8 + H, 16 + 2H, 24 + 3H	1, 2, 3
877	25 + 3H	3
894	17 + 2H	2

912	26 + 3H	3
946	9 + H, 18 + 2H, 27 + 3H	1, 2, 3
982	28 + 3H	3
999	19 + 2H	2
1016	29 + 3H	3
1051	20 + 2H, 30 + 3H, 40 + 4H	2, 3, 4
1077	41 + 4H	4
1086	31 + 3H	3
1104	21 + 2H, 42 + 4H	2, 4
1121	32 + 3H	3
1130	43 + 4H	4
1156	22 + 2H, 33 + 3H, 44 + 4H	2, 3, 4
1182	45 + 4H	4
1191	34 + 3H	3
1209	23 + 2H, 46 + 4H	2, 4
1226	35 + 3H	3
1235	47 + 4H	4
1261	24 + 2H, 36 + 3H, 48 + 4H	2, 3, 4
1287	49 + 4H	4
1296	37 + 3H	3
1314	25 + 2H, 50 + 4H	2, 4
1331	38 + 3H	3
1340	51 + 4H	4

1366	26 + 2H, 39 + 3H, 52 + 4H	2, 3, 4
1392	53 + 4H	4
1401	40 + 3H	3
1419	27 + 2H, 54 + 4H	2, 4
1436	41 + 3H	3
1445	55 + 4H	4
1471	28 + 2H, 42 + 3H, 56 + 4H	2, 3, 4
1497	57 + 4H	4

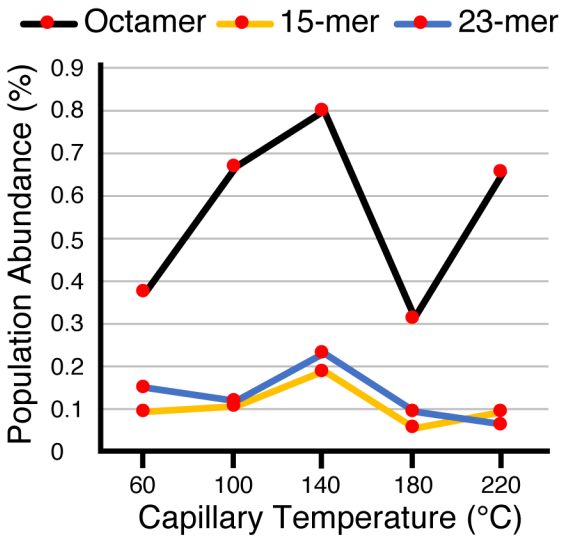

Supplementary Figure 2.1. This figure shows the population abundance of the protonated octamer, 15^{2+}, and 23^{3+} clusters with increasing transfer capillary temperature. There is no significant trend in any of the cluster abundances within this temperature range, indicating that the capillary temperature does not lead to significant dissociation of gas-phase serine clusters under these conditions.

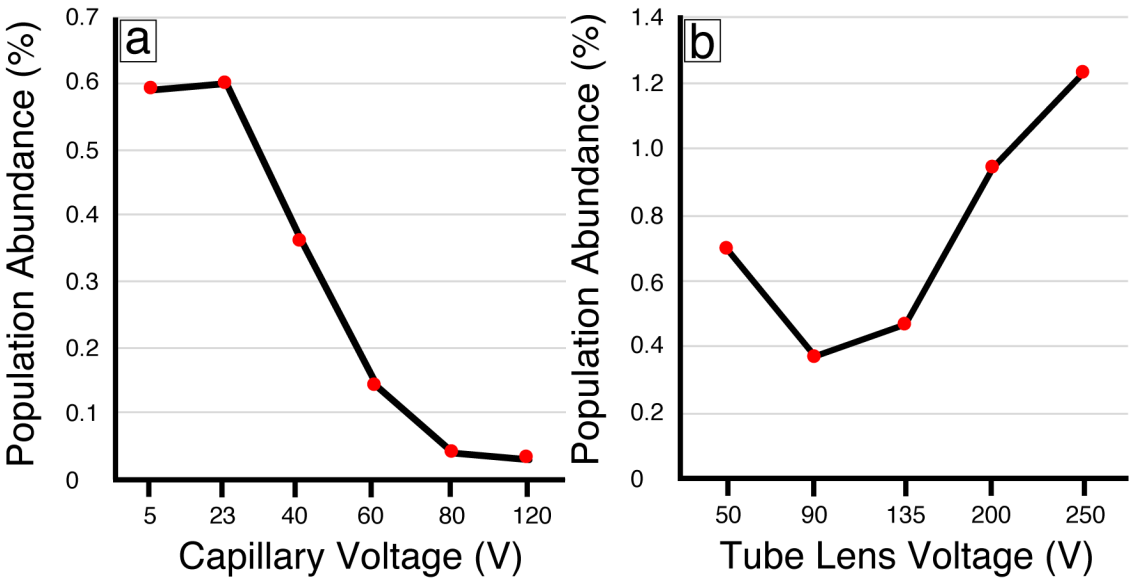

Supplementary Figure 2.2. The effect of the MS operating conditions on the population abundance of the octamer is shown as a function of (a) transfer capillary voltage and (b) tube lens voltage. The abundance of the octamer is similar at 5 V and 23 V (used in the tip size experiments) but decreases at higher voltages. Results from varying the tube lens show a minimum value in the population abundance of protonated octamer at ~90 V, possibly due to differences in ion transmission at different *m*/*z*.

Chapter 3

Dissociation of large gaseous serine clusters produces abundant protonated serine octamer

This chapter is reproduced with permission from:

Jacob S. Jordan, Evan R. Williams

"Dissociation of large gaseous serine clusters produces abundant protonated serine octamer"

Analyst, **2021**, *146*:2617-2625

3.1 Abstract

Protonated serine octamer is especially abundant in spray ionization mass spectra of serine solutions under a wide range of conditions. Although serine octamer exists in low abundance in solution, abundant clusters, including octamer, can be formed by aggregation inside evaporating electrospray droplets. A minimum cluster size of 8 and 21 serine molecules was observed for doubly protonated and triply protonated clusters, respectively, formed by electrospray ionization of a 10 mM serine solution. Dissociation of these clusters results in charge separation to produce predominantly protonated serine dimer and some trimer and the complimentary charged ion. Dissociation of clusters significantly larger than the minimum cluster size occurs by sequential loss of serine molecules. Dissociation of all large clusters investigated leads to protonated octamer as the second most abundant cluster (protonated dimer is most abundant) at optimized collision energies. All larger clusters dissociate through a combination of charge separation and neutral serine loss to form small doubly protonated clusters, and the vast majority of protonated octamer is produced by dissociation of the doubly protonated decamer by charge separation. Protonated octamer abundance is optimized at a uniform energy per degrees of freedom for all clusters indicating that simultaneous dissociation of all large clusters will lead to abundant protonated octamer at an optimum ion temperature. These results provide evidence for another route to formation of abundant protonated octamer in spray ionization or other methods that promote formation and subsequent dissociation of large clusters.

3.2 Introduction

Protonated serine octamer has generated significant interest since the discovery of its unusually large abundance in electrospray ionization (ESI) mass spectra.[1–3] It has an unusually

high homochiral preference when produced from solution using spray ionization methods[1–7] and even when the cluster is sublimed directly from heated solid serine.[8,9] The high homochiral preference has led to the suggestion that this complex may have played a role in homochirogenesis.[1,3,5,8–15] The octamer is also formed as a neutral structure from spraying solutions and it can also be assembled by condensation of serine molecules in the gas phase.[5,16] The structure of this and related structures have been extensively investigated.[1–3,7,12–15,17–28]

Protonated octamer is almost always a significant cluster in the mass spectrum under a wide variety of conditions leading to debates about the extent to which serine octamer exists in solution.[1–6,8–11,14,17,26,29,30] Serine octamer may be formed in evaporating droplets, possibly enhanced at the liquid-gas interface.[26] Results from both NMR and IR studies indicate that the octamer does not exist in solution,[29] but more recent experiments show that serine octamer does exist in solution, albeit at relative low concentrations.[30] Nanoelectrospray emitters with small tips can be used to form sufficiently small droplets that only one or zero analyte molecules are likely to be present at a given solution concentration. Under these conditions, protonated octamer as well as larger clusters are observed indicating that these species exist in solution.[30] The use of larger tips leads to increased protonated octamer and other large clusters indicating that the additional ion signal is a result of aggregation inside the larger evaporating droplets that contain multiple analyte species.

Formation of clusters with up to 600 serine molecules have been reported, and under these conditions, protonated octamer is a minor species.[7] Dissociation of large serine clusters in the gas phase has also been reported to produce protonated octamer.[25,26] Spencer et al. suggested that the octamer produced by dissociation of larger clusters by collision induced dissociation (CID) does not have homochiral specificity, but the precursor ions were not identified.[26] Dissociation of $(Ser_{15} + H + Na)^{2+}$ at 50 kV collision energies results in the formation of smaller doubly and singly charged clusters formed by a combination of neutral serine loss and charge separation pathways.[25] The octamer formed in these experiments was exclusively sodiated. The dissociation of the octameric serine cluster occurs by neutral serine loss.

Dissociation of a variety of different multiply charged clusters has been investigated and can occur by neutral loss and/or charge separation pathways.[31–36] The extent to which clusters dissociate by these pathways depends on cluster size, charge state and subunit identity. For example, dissociation of $La^{3+}(H_2O)_{18}$ occurs by loss of a neutral water molecule and by charge separation to produce protonated water clusters and the corresponding doubly charged hydrated metal hydroxide.[31] Water loss occurs exclusively at larger cluster size whereas charge separation occurs for smaller clusters. The competition between charge separation and neutral molecule loss has been investigated for a wide variety of clusters.[31–36] For doubly charged metal ion clusters, the transition between charge separation reactions and neutral metal atom loss occurs at critical ratios of z^2/n, where z is the charge of the cluster and n the number of subunits in the cluster, that depends on the metal ion identity.[32] Values of 0.39 to 0.97 were reported for a variety of different metal ions, and values for other multiply charged clusters of inorganic[33,37–39] and multiply protonated peptide clusters[35] fall within this range.

Here, dissociation of multiply protonated serine clusters is investigated with the aim of understanding the dissociation pathways as a function of cluster size and charge state. An important finding is that protonated octamer can be formed from all of the doubly and triply protonated clusters investigated and is the second most abundant cluster ion at an optimized collision energy. The dissociation pathways for these clusters are determined and the primary precursor for formation of protonated octamer from larger multiply charged clusters is identified.

3.3 Experimental Methods

Borosilicate capillaries (1.0 mm outer diameter, 0.78 mm inner diameter, Sutter Instruments, Novato, CA) were pulled using a Flaming/Brown P-87 micropipette puller (Sutter Instruments, Novato, CA) to produce nanoelectrospray ionization (nESI) emitter tips that have an inner diameter of 1.2 ± 0.1 μm. The inner diameter of the emitters was measured using a Hitachi TM-1000 scanning electron microscope (Schaumberg, IL) in the Electron Microscopy Laboratory at the University of California, Berkeley. Four replicate tips were pulled in order to measure the standard deviation of the tip diameters.

Ions were formed by nESI using 10 mM L-serine solutions (Sigma Aldrich, St. Louis, MI) in 49.95:49.95:0.1 water:methanol:acetic acid (Sigma Aldrich) and mass spectral data were acquired using a Waters Q-TOF Premier quadrupole time-of-flight mass spectrometer (Waters Corporation, Milford, MA). Ion formation is initiated by applying a voltage of 0.9 – 1.0 kV to a 0.127 mm diameter platinum wire that is inserted into the capillary and in contact with the solution. The voltage was increased until ion signal was stable and the spray was allowed to equilibrate for 1 min. before data acquisition. Instrument conditions were optimized to produce abundant protonated octamer. The source temperature was 80 °C and the extraction cone, sampling cone, and ion guide voltages were 2.0 V, 20 V, and 2.0 V respectively. The entrance and exit potentials of the collision cell were 0 V and -10 V, respectively with a collision gas (Argon) flow rate of 0.35 mL/min, resulting in a pressure of ~4.4 x 10^{-3} mbar in the collision cell. Mass selection for collision induced dissociation experiments were done with a m/z = 4 isolation window. The collision voltage was varied from 0 V to 60 V. Spectra were averaged for 30 s. The abundance of protonated serine octamer produced by CID was measured as a function of collision voltage in 1.0 V increments to determine the value at which maximum octamer is produced. The charge and composition of peaks consisting of overlapping clusters with different charge states was determined from the isotopic distributions. Protonated serine is the most abundant ion that is formed, but sodium and potassium adducted serine is also produced at ~14% and 2% relative abundance, respectively. Much larger clusters with one or more sodium or potassium ions attached are also formed in low abundance. In some cases, these ions overlap in m/z with purely protonated clusters but can be distinguished based on their isotopic spacing owing to their non-overlapping charge states.

3.4 Results and Discussion

3.4.1 Fragmentation Pathways of Protonated Octamer and Octameric Metaclusters

Electrospray ionization of a 10 mM serine solution results in abundant ions at m/z = 841 consisting of mostly protonated serine octamer (93%) and minor overlapping contributions from octameric metaclusters corresponding to doubly protonated 16-mer (4%) and triply protonated 24-mer (3%) (Figure 1). The abundances of the octameric metaclusters are sensitive to instrument parameters and gaseous collisions.[1,10,15,24] The slightly higher abundance of the 24-mer compared

to that reported previously may be due to the relatively soft ion introduction conditions used here.[1,15,30] With zero volts collision energy, there is sufficient ion energy to induce all three precursor ions at m/z = 841 to dissociate as a result of the relatively high Ar collision gas pressure that was used throughout all experiments, including those with additional collision energy. The triply protonated 24-mer (24^{3+}) dissociates by loss of neutral serine molecules to form smaller triply charged clusters. Dissociation of this ion also results in doubly charged ions at higher m/z that are formed through a charge separation process to produce two complimentary charged fragment ions. Both monomer loss and charge separation reactions have been reported for several multiply charged serine cluster ions.[25,26] Doubly charged ions at lower m/z are formed by dissociation of the 16^{2+} by neutral serine loss. The singly charged ions are formed primarily by dissociation of the protonated octamer as well as possible minor contributions from charge separation of the smaller doubly charged ions. The low abundance of the protonated heptamer compared to that of the protonated hexamer is indicative of the relative stabilities of these ions.[1,3,14–16,19]

3.4.2 Minimum Cluster Size and Charge Separation

The smallest doubly and triply protonated cluster ions that are formed directly by electrospray ionization are 8^{2+} and 21^{3+}, respectively. These minimum cluster sizes are similar to the values of 9^{2+} and 22^{3+} reported by Concina et al.[25] Charge separation and neutral loss pathways typically have different entropies so that the minimum observed cluster size can depend on ion energies.[33,35,39] The transition between charge separation and monomer loss depends on both cluster size and charge state. The approximate cluster sizes where this transition occurs for serine correspond to z^2/n values of 0.44 and 0.39 for the doubly and triply protonated clusters, respectively. These values are similar to those reported for many multiply charged clusters and for doubly protonated peptide clusters that undergo a similar charge separation pathway.[35]

Dissociation of the doubly protonated octamer results in formation of a series of singly protonated ions up to the hexamer (Figure 2a). These ions must be formed by charge separation in which both fragment ions from a dissociation pathway are charged. The charge separation pathways are more readily identified for larger clusters. This is illustrated for dissociation of 23^{3+} where neutral serine loss results in formation of triply protonated clusters as small as 21^{3+} (Figure 2b). Abundant singly protonated dimer as well as monomer and trimer are also formed. These results indicate that protonated dimer and to a much lesser extent protonated trimer are the main charge separation pathways. Charge separation by protonated monomer formation may also occur but this ion can also be formed by neutral serine loss from the protonated dimer. The absence of protonated heptamer in the dissociation spectrum of the doubly protonated octamer may indicate that the loss of protonated monomer is not a significant pathway. However, subsequent dissociation of the unstable protonated heptamer may obscure direct observation of this complimentary fragmentation product ion. Dissociation of 9^{2+} results in some protonated heptamer but no protonated octamer, again indicating that charge separation by formation of protonated monomer is not favored.

Charge separation upon dissociation of small doubly charged serine clusters has been reported previously.[25] Dissociation of 15^{2+} charged with one proton and one sodium ion with 50 kV collisions resulted in formation of octamer that was exclusively sodiated. Protonated serine

clusters as large as the tetramer were observed. This suggests that protonated tetramer may also be a charge separation pathway at these high collision energies, but this ion may be formed from larger protonated clusters that subsequently undergo neutral loss. Charge separation has also been observed for two multiply protonated groups of metaclusters dissociated at low energy, but the charge separation pathways were not identified.[3,25] The observation of protonated serine dimer as the main charge separation pathway is consistent with results from dissociation of multiply protonated peptide clusters in which formation of protonated peptide dimers was the main charge separation pathway observed.[35]

3.4.3 Charge Separation versus Neutral Monomer Loss Pathways

For doubly and triply protonated clusters that are substantially above the minimum cluster size, loss of neutral serine molecules is favored. For example, dissociation of 29^{3+} at a collision voltage of 0 V results in predominantly the loss of neutral serine molecules to produce triply protonated ions as small as 21^{3+} (Figure 3a). Charge separation to produce singly protonated monomer and dimer is a minor dissociation pathway. Doubly charged ions as large as 25^{2+} are formed by charge separation at 5 V collisions (Figure 3b). Because formation of protonated dimer is the dominant charge separation pathway, this result indicates that the onset of charge separation as a minor reaction pathway starts at 27^{3+} and is the only process for 21^{3+}. At 28 V, doubly protonated ions as small as 8^{2+} and singly protonated ions up to the octamer are formed through a combination of both dissociation processes (Figure 3c). At this collision voltage, protonated octamer is the second most abundant cluster ion in the dissociation spectrum, as it is when these clusters ions are formed directly from solution. Protonated octamer was reported to be formed by CID of larger clusters but the minimum cluster sizes and dissociation pathways were not identified.[26] These results suggest an alternative pathway to formation of protonated octamer that is widely observed to be a highly abundant "magic number" cluster when solutions of serine are ionized using various spray ionization methods.

3.4.4 Formation of Protonated Octamer from Large Multiply Charged Clusters

Abundant protonated octamer can be produced by dissociation of each of the large multiply charged clusters investigated. For example, dissociation of 37^{3+} at 0 V results in exclusively neutral serine loss (Figure 4a). The appearance of protonated monomer and dimer in this spectrum originates from dissociation of 41^{4+} that is triply protonated with a potassium adduct at overlapping m/z. This ion undergoes neutral charge loss and charge separation, which produces singly protonated serine monomer, dimer, trimer and the corresponding 3+ ions that retain the potassium adduct. With 15 V collisions, smaller triply protonated clusters formed by loss of neutral serine molecules are observed, and singly protonated and corresponding doubly protonated ions are also formed by charge separation (Figure 4b). With 30 V collisions, only doubly and small singly charged ions are observed (Figure 4c). Doubly charged ions as small as 11^{2+} are formed, but no protonated octamer is observed. With 47 V collisions, the protonated octamer is the second most abundant cluster, and doubly protonated ions as small as the octamer are formed (Figure 4d). The

protonated octamer abundance is maximized at this collision voltage. This voltage is higher than that required to produce an optimum abundance of protonated octamer from 29^{3+} (Figure 3c). The sequential dissociation pathways for dissociation of 37^{3+} are summarized in Scheme 1.

The optimum collision voltage for production of abundant protonated octamer from both doubly and triply protonated clusters was identified by varying the collision voltage in 1 V increments, and these data are shown in Figure 5a. Abundant protonated octamer is produced over a relatively broad range of collision voltages (Figure 5a, inset). The optimum voltage increases linearly with cluster size for both the +2 and +3 clusters but these two ion series show different trend lines. Converting the collision voltages into center-of-mass collision energies for each cluster results in a linear relationship with cluster size independent of the precursor ion charge state (Figure 5b). The 11^{2+} is entirely dissociated into smaller clusters at 0 V collision energy, so these data are not included in Figure 5. It is important to note that the center-of-mass collision energies correspond to single collisions at the initial energy induced by the applied collision voltage and do not account for multiple collisions that occur in these experiments. Thus, these values are more an indicator of relative energies transferred into the different clusters. These results indicate that formation of the octamer from gas-phase dissociation of larger clusters depends on the number of degrees of freedom in the cluster. The linearity of these data show that the protonated octamer abundance is optimized when the energy deposited per degree of freedom is the same for all the clusters. This result indicates that there is an optimum cluster temperature for producing protonated octamer by dissociation of larger clusters.

It is interesting to note that protonated octamer is not formed directly as a dissociation product from the much larger triply protonated clusters under the conditions investigated. Loss of neutral serine molecules occurs at large cluster size but charge separation to produce complimentary doubly charged clusters and corresponding singly protonated serine dimer, trimer and possibly monomer occurs at smaller cluster size. Thus, protonated octamer is only produced from doubly charged precursors. With 0 V collisions, charge separation and production of protonated octamer was observed for all of the doubly protonated clusters (11^{2+}, 13^{2+}, 15^{2+}, 17^{2+}). The observation of 11^{2+} with 30 V collisions of the 37^{3+} indicates that 12^{2+} undergoes neutral loss and not charge separation; charge separation from this ion would produce primarily singly protonated decamer, which is not observed (Figure 4c). Thus, the majority of protonated octamer must be formed directly by dissociation of doubly protonated serine clusters with 10 or 11 serine molecules, with the major contribution coming from 10^{2+} by charge separation and formation of protonated dimer.

Even dissociation of octameric metaclusters does not lead to direct formation of protonated octamer. The main dissociation pathway for these clusters is loss of neutral serine molecules, not ejection of protonated octamer. The more abundant 15^{2+} than 14^{2+} from dissociation of 16^{2+} (Figure 1) suggests that this ion does not likely consist of two minimally interacting protonated octamers with the same structures as those formed either directly from solution or by dissociation of larger clusters. Loss of a serine molecule from one of the octamers would lead to an unstable heptamer, which would quickly dissociate to favor production of 14^{2+} over 15^{2+}. These results indicate that, unlike the neutral serine octamer that has been reported to be introduced directly into the gas phase by sublimation of crystalline serine,[8,9] the protonated serine octamer is not "sublimed" directly from large gaseous cluster ions but rather formed through sequential charge separation and neutral serine loss pathways to ultimately form doubly protonated decamers that are responsible for direct formation of protonated octamer through charge separation and formation of the complimentary protonated serine dimer.

3.5 Conclusions

The dissociation of large multiply protonated serine clusters occurs by two pathways that depend on cluster size. Clusters substantially larger than the minimum cluster size dissociate by sequential loss of neutral serine molecules whereas charge separation to produce primarily protonated serine dimer and the complimentary ion occurs for clusters close to the minimum cluster size. Protonated octamer is formed by charge separation primarily from doubly protonated decamer to form the complimentary protonated serine dimer. This dissociation pathway can be accessed for any of the large doubly and triply charged clusters investigated. At an optimized collision energy, the singly protonated octamer can be the second most abundant cluster ion (with the protonated dimer the most abundant cluster) in the dissociation mass spectra of all of the clusters investigated. A significant finding is that optimum production of protonated octamer that is formed by dissociation of larger clusters occurs at a uniform energy per degrees of freedom for the large clusters. This result indicates that the protonated octamer should be the second most abundant cluster ion formed by dissociation of higher order clusters at an optimized *temperature*. Thus, these results indicate another mechanism for formation of highly abundant protonated serine octamer for ions produced from serine solutions by various spray ionization methods.

Recent results indicate that serine octamer exists in solution albeit at low abundance and that significant protonated octamer can be formed by aggregation inside droplets as solvent evaporation occurs and the concentration of serine increases prior to gaseous ion formation.[30] Aggregation inside droplets can be minimized or even eliminated by using ESI emitters with tiny tips (100's of nm in diameter) or by reducing analyte concentration with the goal of producing initial droplets that contain either one or no analyte molecule per droplet. Under conditions commonly employed in many previous studies of serine octamer, aggregation inside the electrospray droplet likely contributes substantially to formation of abundant protonated octamer.

Much larger clusters can also be formed by aggregation. Sonic spray using large diameter emitters and soft source conditions can result in the formation of clusters consisting of over 600 serine molecules.[7] Under these conditions, the protonated octamer comprises only ~0.3% of the total ion population. Our results indicate that with an optimized source temperature, these large clusters would all dissociate to form protonated serine octamer as the second most abundant cluster ion. Such a temperature could be achieved in a heated metal capillary ion introduction system, and this may explain results from other spray experiments where the protonated octamer is the most abundant ion in the mass spectra.[1–4,6,14,23,25,26] Variability in the magic number character of the protonated octamer observed in previous studies[1,4–14,16,17,23,27–29] may also be explained by different effective temperatures of the ion populations as a result of different source conditions or ionization processes.

3.6 Acknowledgements

This material is based upon work supported by the National Science Foundation Division of Chemistry under grant number CHE-1609866 as well as a Graduate Research Fellowship (DGE-1752814). The authors are also grateful for financial support from CALSOLV.

3.7 References

(1) R. G. Cooks, D. Zhang, K. J. Koch, F. C. Gozzo and M. N. Eberlin, *Anal. Chem.*, 2001, **73**, 3646–3655.
(2) A. E. Counterman and D. E. Clemmer, *J. Phys. Chem. B*, 2001, **105**, 8092–8096.
(3) R. R. Julian, R. Hodyss, B. Kinnear, M. F. Jarrold and J. L. Beauchamp, *J. Phys. Chem. B*, 2002, **106**, 1219–1228.
(4) P. Nemes, G. Schlosser and K. Vékey, *J. Mass Spectrom.*, 2005, **40**, 43–49.
(5) H. Zhang, Z. Wei, J. Jiang and R. G. Cooks, *Angew. Chemie - Int. Ed.*, 2018, **57**, 17141–17145.
(6) Z. Takats, S. C. Nanita, R. G. Cooks, G. Schlosser and K. Vekey, *Anal. Chem.*, 2003, **75**, 1514–1523.
(7) S. Myung, R. R. Julian, S. C. Nanita, R. G. Cooks and D. E. Clemmer, *J. Phys. Chem. B*, 2004, **108**, 6105–6111.
(8) Z. Takáts and R. G. Cooks, *Chem. Commun.*, 2004, 444–445.
(9) P. Yang, R. Xu, S. C. Nanita and R. G. Cooks, *J. Am. Chem. Soc.*, 2006, **128**, 17074–17086.
(10) S. C. Nanita and R. G. Cooks, *Angew. Chemie - Int. Ed.*, 2006, **45**, 554–569.
(11) Z. Takats, S. C. Nanita and R. G. Cooks, *Angew. Chemie - Int. Ed.*, 2003, **42**, 3521–3523.
(12) C. A. Schalley and P. Weis, *Int. J. Mass Spectrom.*, 2002, **221**, 9–19.
(13) F. X. Sunahori, G. Yang, E. N. Kitova, J. S. Klassen and Y. Xu, *Phys. Chem. Chem. Phys.*, 2013, **15**, 1873–1886.
(14) Z. Takats, S. C. Nanita, G. Schlosser, K. Vekey and R. G. Cooks, *Anal. Chem.*, 2003, **75**, 6147–6154.
(15) K. J. Koch, F. C. Gozzo, D. Zhang, M. N. Eberlin and R. G. Cooks, *Chem. Commun.*, 2001, **1**, 1854–1855.
(16) R. Chen, Z. Wei and R. G. Cooks, *Anal. Chem.*, 2021, **93**, 1092–1099.
(17) J. Seo, S. Warnke, K. Pagel, M. T. Bowers and G. Von Helden, *Nat. Chem.*, 2017, **9**, 1263–1268.
(18) S. Gronert, R. A. J. O'Hair and A. E. Fagin, *Chem. Commun.*, 2004, 1944–1945.
(19) U. Mazurek, O. Geller, C. Lifshitz, M. A. McFarland, A. G. Marshall and B. G. Reuben, *J. Phys. Chem. A*, 2005, **109**, 2107–2112.
(20) J. Ren, Y. Y. Wang, R. X. Feng and X. L. Kong, *Chinese Chem. Lett.*, 2017, **28**, 537–540.
(21) G. Liao, Y. Yang and X. Kong, *Phys. Chem. Chem. Phys.*, 2014, **16**, 1554–1558.
(22) A. B. Costa and R. G. Cooks, *Phys. Chem. Chem. Phys.*, 2011, **13**, 877–885.
(23) S. C. Nanita, E. Sokol and R. G. Cooks, *J. Am. Soc. Mass Spectrom.*, 2007, **18**, 856–868.
(24) U. Mazurek, *Eur. J. Mass Spectrom.*, 2006, **12**, 63–69.
(25) B. Concina, P. Hvelplund, A. B. Nielsen, S. B. Nielsen, J. Rangama, B. Liu and S. Tomita, *J. Am. Soc. Mass Spectrom.*, 2006, **17**, 275–279.
(26) E. A. C. Spencer, T. Ly and R. R. Julian, *Int. J. Mass Spectrom.*, 2008, **270**, 166–172.

(27) K. J. Koch, F. C. Gozzo, S. C. Nanita, Z. Takats, M. N. Eberlin and R. Graham Cooks, *Angew. Chemie - Int. Ed.*, 2002, **41**, 1721–1724.
(28) V. Scutelnic, M. A. S. Perez, M. Marianski, S. Warnke, A. Gregor, U. Rothlisberger, M. T. Bowers, C. Baldauf, G. Von Helden, T. R. Rizzo and J. Seo, *J. Am. Chem. Soc.*, 2018, **140**, 7554–7560.
(29) S. Vandenbussche, G. Vandenbussche, J. Reisse and K. Bartik, *European J. Org. Chem.*, 2006, 3069–3073.
(30) J. S. Jordan and E. R. Williams, *Anal. Chem.*, 2021, **93**, 1725–1731.
(31) M. F. Bush, R. J. Saykally and E. R. Williams, *J. Am. Chem. Soc.*, 2008, **130**, 9122–9128.
(32) W. A. Saunders, *Phys. Rev. A*, 1992, **46**, 7028–7041.
(33) R. L. Wong and E. R. Williams, *J. Phys. Chem. A*, 2003, **107**, 10976–10983.
(34) K. Sattler, J. Mühlbach, O. Echt, P. Pfau and E. Recknagel, *Phys. Rev. Lett.*, 1981, **47**, 160–163.
(35) J. C. Jurchen, D. E. Garcia and E. R. Williams, *J. Am. Soc. Mass Spectrom.*, 2003, **14**, 1373–1386.
(36) T. E. Cooper and P. B. Armentrout, *J. Phys. Chem. A*, 2009, **113**, 13742–13751.
(37) X. Yang, X. Bin Wang and L. S. Wang, *J. Phys. Chem. A*, 2002, **106**, 7607–7616.
(38) X. B. Wang, X. Yang, J. B. Nicholas and L. S. Wang, *Science*, 2001, **294**, 1322–1325.
(39) M. J. DiTucci and E. R. Williams, *Chem. Sci.*, 2017, **8**, 1391–1399.

3.8 Figures

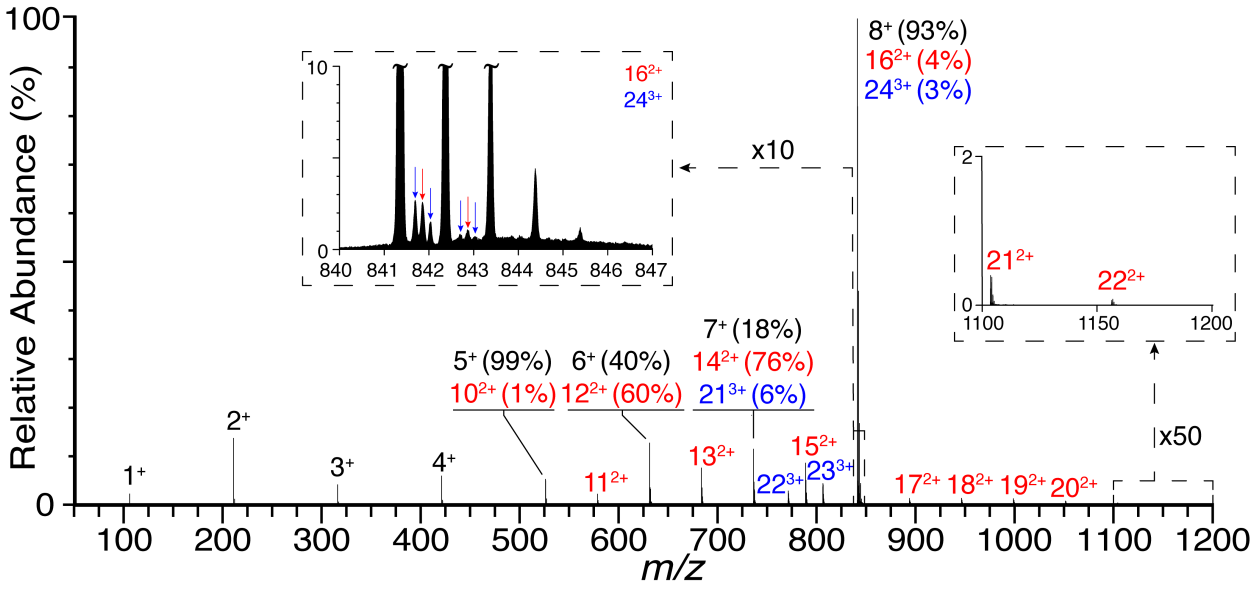

Figure 3.1. Collision induced dissociation mass spectrum of protonated serine cluster ions at *m/z* = 841 corresponding to protonated octamer and multiply protonated metaclusters measured with Ar collision gas in the cell but with 0 V additional collision energy. The percentage at each cluster indicates the abundance of each ion at overlapping *m/z* values.

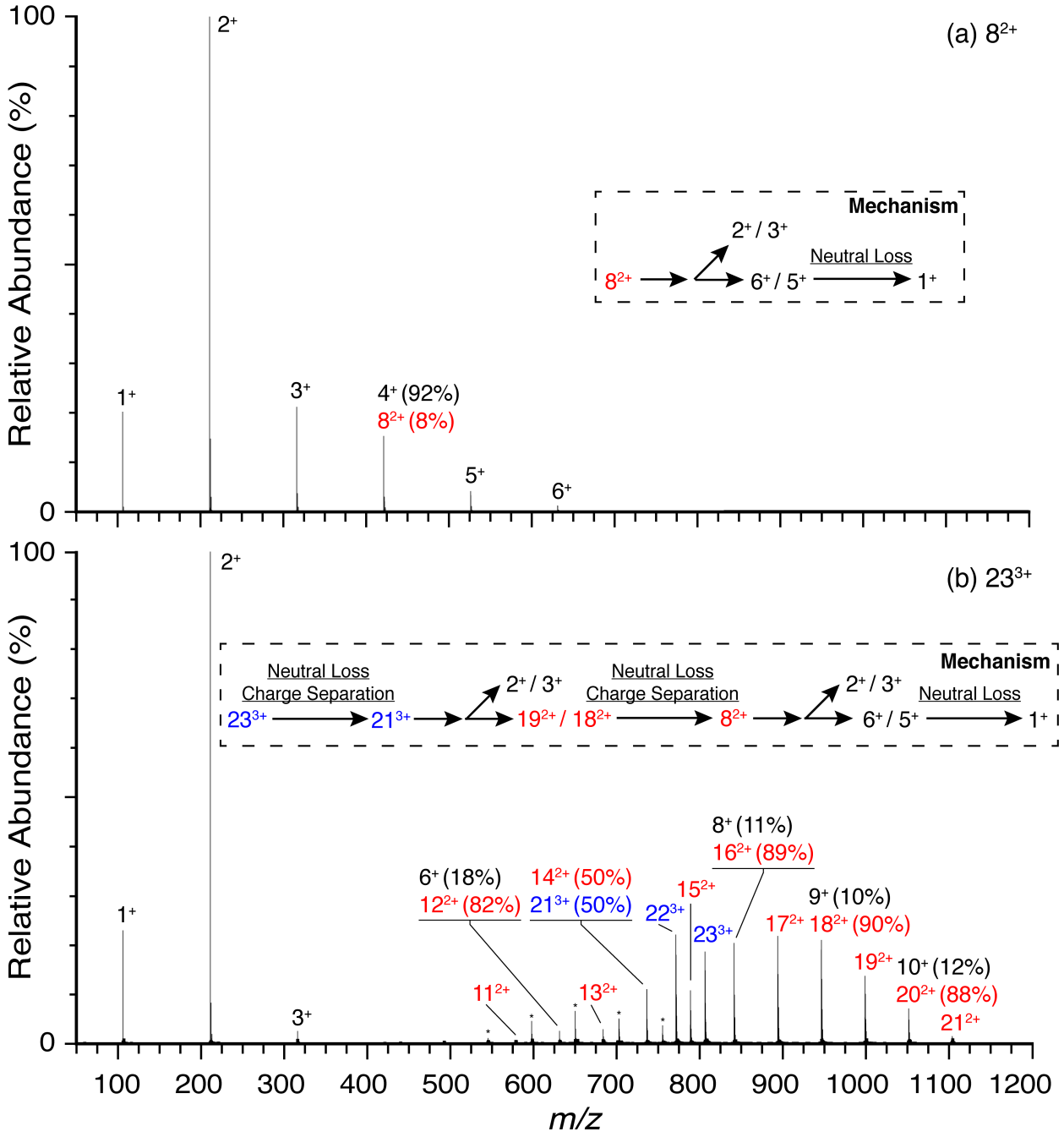

Figure 3.2. Collision induced dissociation mass spectra of (a) doubly protonated serine octamer (8^{2+}) and (b) triply protonated cluster with 23 serine molecules (23^{3+}) with Ar collision gas in the cell and 0 V additional collision energy. Peaks denoted with an asterisk are potassium adducted fragment ions produced from $(Ser_{15} + H + K)^{2+}$ that overlaps in *m/z* with the 23^{3+}. These low abundance ions are formed as a result of low levels of potassium present in solution.

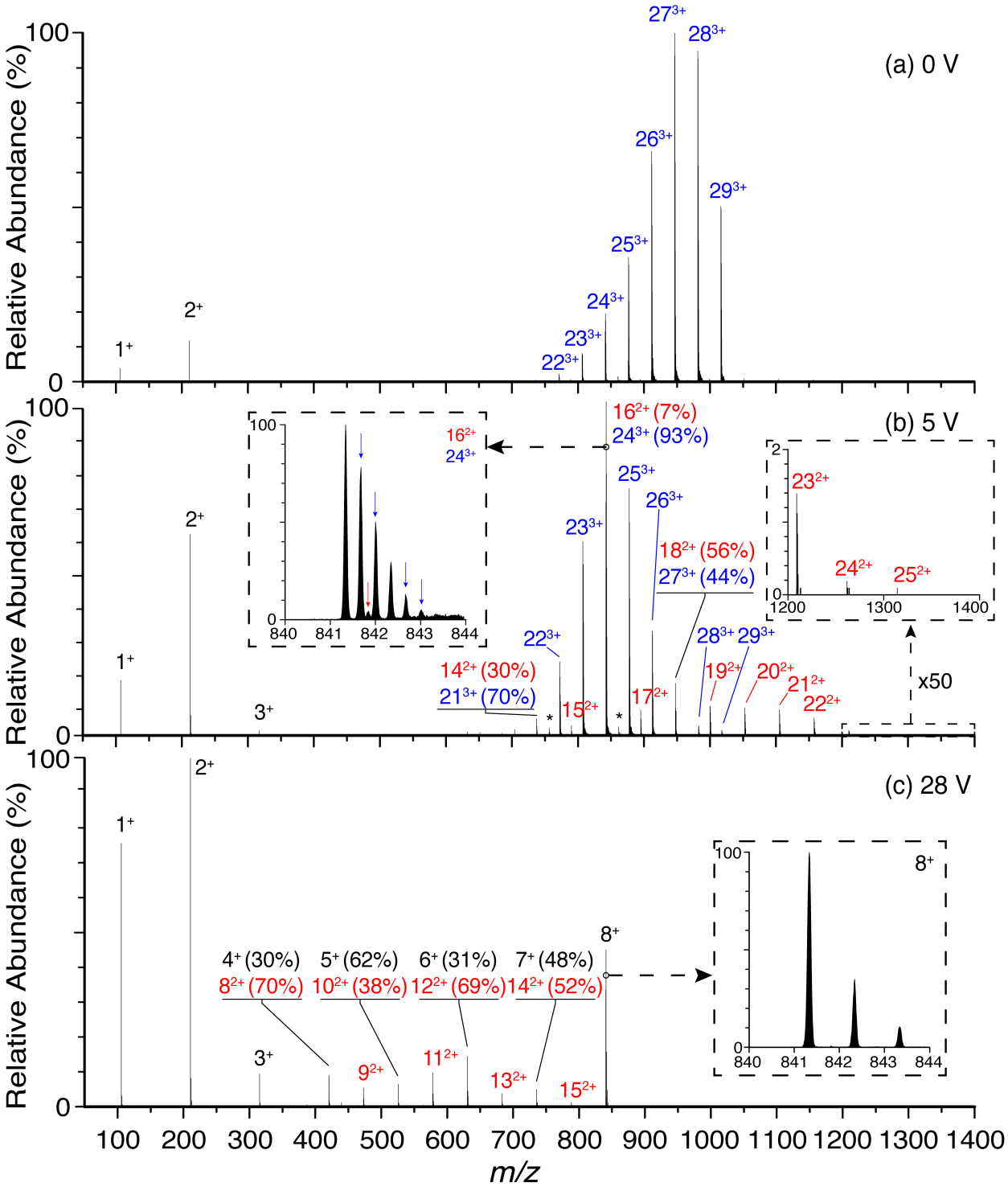

Figure 3.3. Collision induced dissociation spectra of 29^{3+} at collision voltages of (a) 0 V, (b) 5 V and (c) 28 V. Protonated octamer abundance is a maximum at 28 V collision voltage. Peaks marked with an asterisk are potassium adducted fragment ions formed by $(Ser_{19} + H + K)^{2+}$ that overlaps in *m/z* with the 29^{3+}.

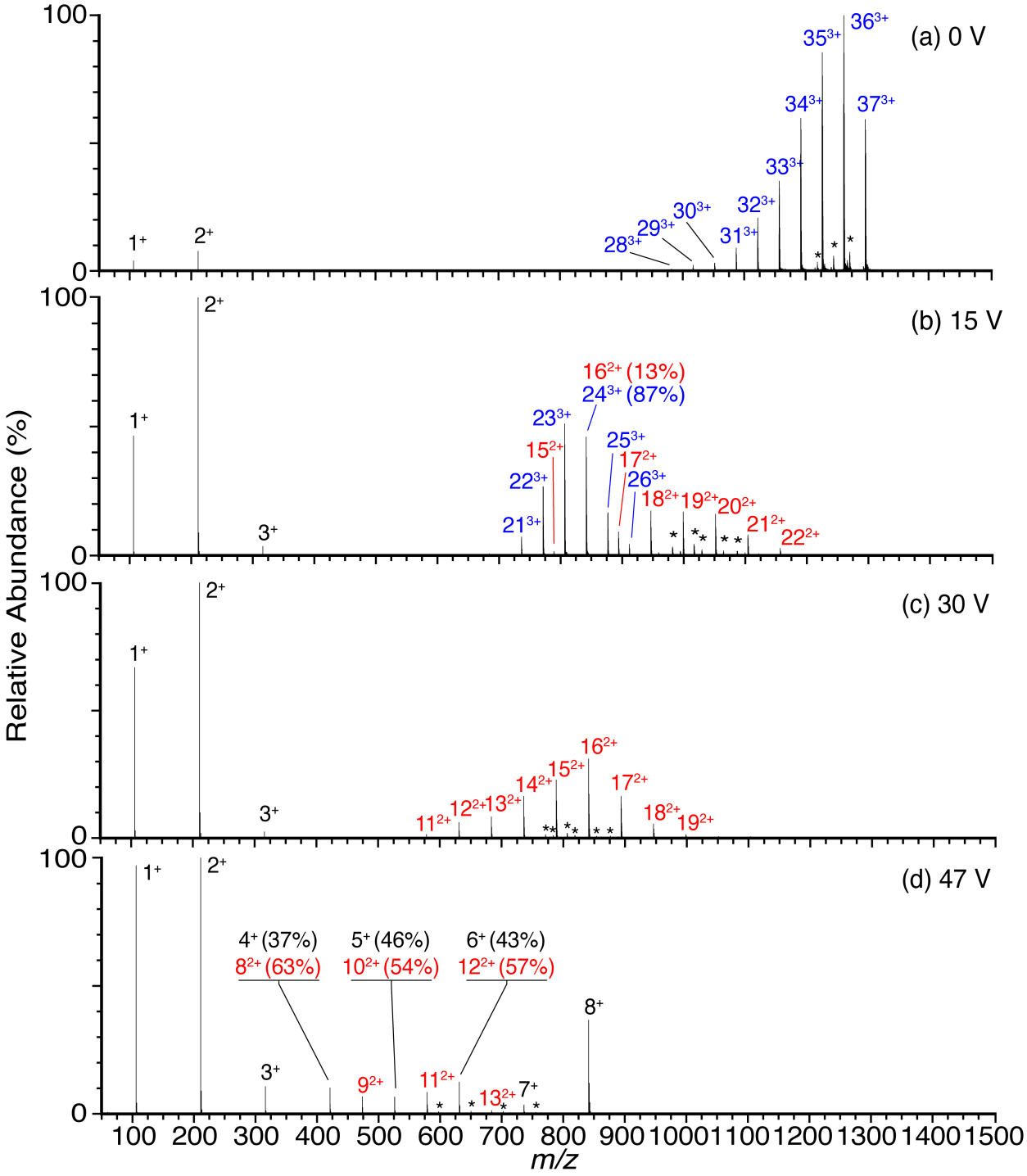

Figure 3.4. Collision induced dissociation of serine 37^{3+} at (a) 0 V, (b) 15 V, (c) 30 V and (d) 47 V collisional voltage. Dissociation by loss of neutral serine molecules occurs when the cluster sizes are significantly above the minimum cluster size whereas charge separation occurs when the clusters approach this size. The protonated octamer abundance is a maximum at 47 V. Peaks marked with an asterisk are potassium adducted fragments produced from $(Ser_{49} + 3H + K)^{4+}$ that overlaps in *m/z* with the 37^{3+} cluster.

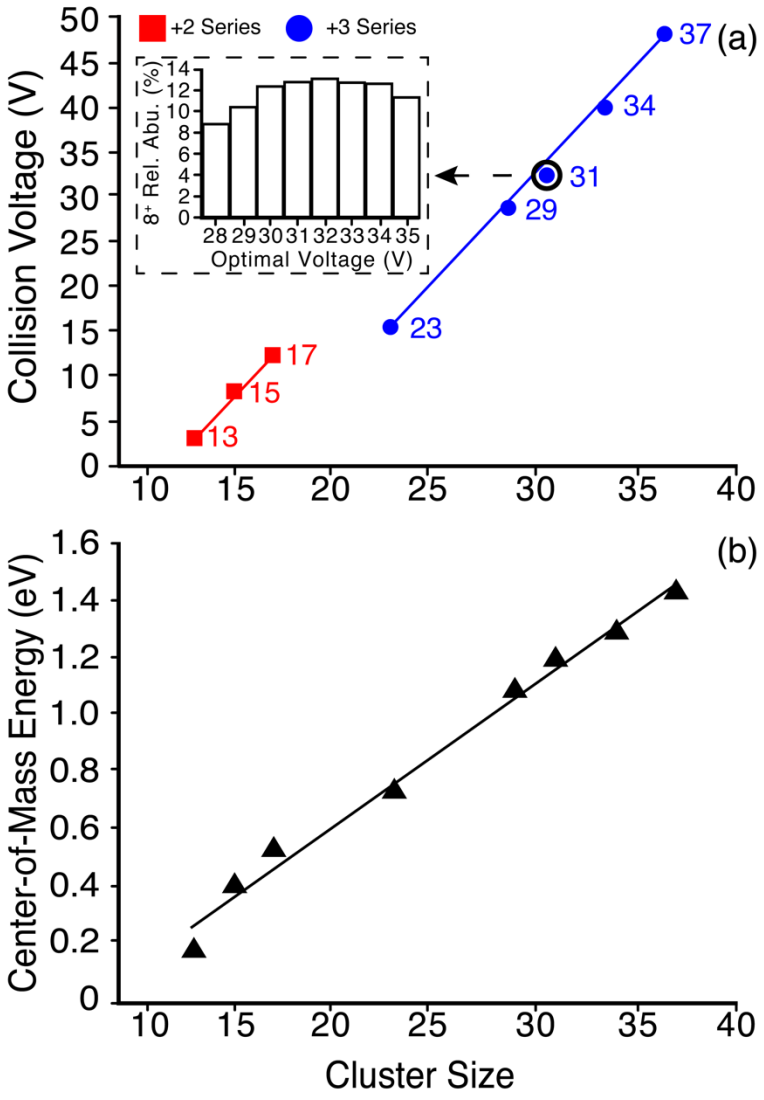

Figure 3.5. Optimum (a) collision voltage and (b) center-of-mass collision energy as a function of cluster size and charge state for maximum abundance of protonated octamer (relative to total ion abundance), which is the second most abundant cluster ion (the protonated dimer is most abundant) produced by CID of each cluster.

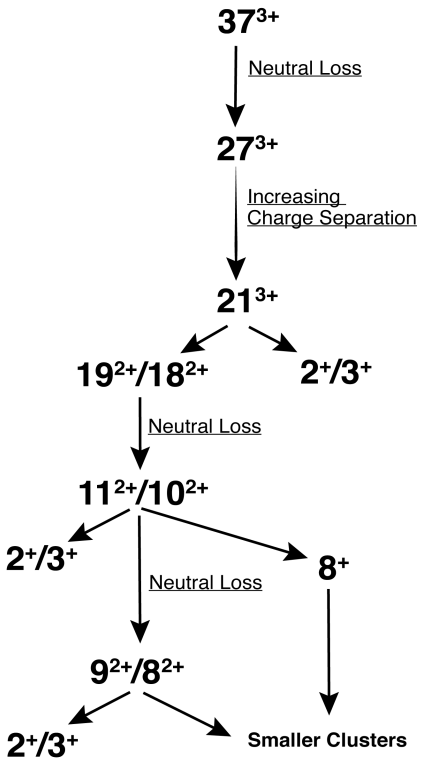

Scheme 3.1. Fragmentation pathways for serine 37^{3+}.

Chapter 4

Homochiral preference of serine octamer in solution and formed by dissociation of large gaseous clusters

This chapter is reproduced with permission from:

Jacob S. Jordan, Evan R. Williams

"Homochiral preference of serine octamer in solution and formed by dissociation of large gaseous clusters"

Analyst, **2021**, *146*:6822-6830

4.1 Abstract

The ability of electrospray emitters with submicron tip diameters to significantly reduce and even eliminate aggregation of analyte molecules that can occur inside evaporating droplets was recently demonstrated to show that serine octamer exists in bulk solution, albeit in low abundance. Results using 222 nm emitter tips for D-serine and deuterium labeled L-serine show that the serine octamer that exists in 100 μM solution has a strong homochiral preference. Dissociation of large multiply protonated clusters results in formation of protonated octamer through a doubly protonated decamer intermediate. Remarkably, dissociation of the doubly protonated decamer from solution, which has a *heterochiral* preference, results in protonated octamer with strong *homochiral* preference. This homochiral preference is higher when protonated octamer is formed from larger clusters and approaches the chiral preference of the octamer in solution. These results show that the doubly protonated decamer has a different structure when formed from solution than when formed by dissociation of larger clusters. These results indicate that the unusually high abundance of protonated homochiral octamer that has been reported previously can be largely attributed to aggregation of serine that occurs in rapidly evaporating electrospray droplets and from dissociation of large clusters that form abundant protonated octamer at an optimized effective temperature.

4.2 Introduction

Protonated serine octamer has been widely studied since the initial discoveries of its strong homochiral preference and unusually high abundance in electrospray ionization (ESI) mass spectra.[1–5] These remarkable characteristics have been observed from a variety of different spray

ionization methods,[6–10] from vaporization of serine during rapid solvent evaporation[11] and by pyrolysis,[12] leading to the suggestion that this complex may have played a role in homochirogenesis.[1,3,4,7,11–16] The structures of the protonated octamer and of related complexes have been extensively investigated.[1–4,7,9,10,15–27] The homochiral preference was reported to be the result of 3-point hydrogen bonding interactions between six of the constituent serine molecules.[26] The side-chain hydroxyl groups of the remaining two molecules are not involved in hydrogen bonding within the octamer, making them exchangeable with serine molecules of different chirality.[26] Neutral serine octamer is also formed by spray ionization[28] and by condensation of sublimated serine in the gas phase.[29] Both the protonated and neutral forms of the octamer have similar homochiral preferences, suggesting that their structures may be related.[28,29]

The homochiral preference of protonated serine octamer formed from racemic solutions has been investigated using deuterium labeled L-serine in order to distinguish the two enantiomeric forms of the amino acid by mass.[3–5,8–10,13–15,21,22,27–31] Homochiral 8D:0L and 0D:8L cluster compositions are much more abundant than expected from a binomial distribution whereas the more heterochiral 5D:3L, 4D:4L, and 3D:5L compositions are significantly lower in abundance.[1,3,5,9,11,29–31] This indicates that these clusters are not formed by statistical aggregation of serine molecules. The chiral preference of other serine clusters has also been investigated.[9,29,31] Protonated trimer (3^+), 6^+, and doubly protonated 8^{2+} - 11^{2+} serine clusters have a heterochiral preference, where mixed compositions, such as 3D:3L for the hexamer, are more abundant than expected from a binomial distribution.[29,31]

Beauchamp and coworkers characterized the homochiral preference of serine clusters using the ratio of the ion abundance to the abundance expected from a binomial distribution.[3] These data indicate that the pure homochiral forms of the protonated octamer were 15x more abundant than expected. Similarly, Nanita *et al.* introduced the "magnitude of chiral preference" (M_{cp}) as a measure of the chiral preference of a cluster.[8,29] The M_{cp} is defined as the observed probability of a cluster composition divided by the theoretical probability of a cluster composition predicted by a binomial distribution and normalized to one. Thus, the M_{cp} is similar to the ratio used by Beauchamp and coworkers but normalized such that all compositions sum to one. A plot of the M_{cp} or the ratio of the observed to statistical intensities versus the cluster composition results in a "V"-shaped curve for protonated octamer, characteristic of a homochiral preference.[3,29,31] In contrast, heterochiral species result in an inverted "V"-shaped plot and clusters with no chiral preference are characterized by a flat plot.[31]

Whether serine octamer exists *in solution* has been extensively debated. Results from NMR and IR spectroscopy experiments showed no evidence for any serine clusters in solution indicating that its high abundance in spray ionization mass spectra is likely a result of aggregation inside evaporating electrospray droplets.[32] However, recent data using small emitter tips indicate that protonated octamer does exist in solution, albeit in low abundance.[33] In these experiments, small emitter tips and low serine concentrations were used such that there is, on average, one or zero analyte molecules present in electrospray droplets that are initially formed. Under these conditions, aggregation inside an electrospray droplet should not occur to a significant extent, yet a variety of serine clusters were observed, indicating that the octamer and other clusters exist in solution. These data also indicate that the unusually high abundance of protonated octamer observed in many prior studies, in which significantly larger emitters were used, results from aggregation within ESI droplets. Solvent evaporation leads to smaller droplets and more concentrated serine in the remaining solution, enhancing aggregation during the ESI process. However, the chiral preference of the octamer that exists in solution prior to electrospray ionization has not been reported.

Protonated octamer can also be formed by dissociation of larger serine clusters in the gas phase.[23,24,34] Dissociation of multiply protonated serine clusters with between 10 and 37 serine molecules produces protonated octamer as the most abundant cluster consisting of three or more serine molecules at an optimum dissociation energy through charge loss and neutral evaporation processes.[34] Thus, protonated octamer can also be a significant magic number cluster in mass spectra where larger clusters are dissociated in the gas phase. Doubly protonated decamer was found to be the critical precursor to formation of protonated octamer in the gas phase through charge separation to form the corresponding protonated dimer. Formation of clusters containing up to 600 serine molecules was reported with sonic spray ionization[9] and these clusters are expected to dissociate under source conditions optimized to produce abundant protonated octamer.[34] Spencer *et al*. reported that the protonated octamer formed by dissociation of large clusters from racemic solutions does not display a homochiral preference, but the precursor identities and collision energies were not reported.[24] The dimer to octamer abundance ratio was used to deduce the extent of homochiral preference in these experiments instead of isotopically labeled enantiomers.

The heterochiral preference of the doubly protonated decamer, the critical intermediate for formation of protonated octamer by gaseous dissociation of larger clusters, seems to be consistent with the conclusion that protonated octamer formed by gaseous dissociation of larger clusters does not have a significant homochiral preference. Yet the dominant abundance and homochiral preference of protonated octamer in many previous experiments where large clusters are likely formed due to aggregation and dissociated warrants further investigation into the chiral preference of protonated octamer formed both in solution prior to droplet formation and by dissociation of large clusters.

4.3 Experimental Methods

Nanoelectrospray ionization (nESI) emitters with diameters of 222 ± 8 nm and 2.4 ± 0.04 μm were pulled from borosilicate capillaries (1.0 mm outer diameter, 0.78 mm inner diameter, Sutter Instruments, Novato, CA) using a Flaming/Brown P-87 micropipette puller (Sutter Instruments). The tip puller parameters used to produce these emitters are given in Table S1. The inner diameters of the emitters were measured using a Hitachi TM-1000 scanning electron microscope (Schaumberg, IL) in the Electron Microscopy Lab at the University of California, Berkeley. Four replicate tips were pulled in order to measure the standard deviation of the tip diameters.

Serine cluster ions were formed from a 50% D-serine (Sigma Aldrich, St. Louis, MI, 98% purity) and 50% 2,3,3-d_3-L-serine (Cambridge Isotopes Labs, Andover, MA, 98% purity) solution at a total serine concentration of 10 mM or 100 μM in 49.95:49.95:0.1 water:methanol:acetic acid (Sigma Aldrich). Mass spectra were acquired between 50 – 2000 *m*/*z* using a Waters Q-TOF Premier quadrupole time-of-flight mass spectrometer (Waters Corporation, Milford, MA). Electrospray was initiated by applying a voltage of 0.4 – 1.0 kV to a 0.127 mm platinum wire inserted into the capillary and in contact with the solution. The spray voltage was increased until stable spray was achieved and the spray was allowed to reach a steady state for one minute prior to data acquisition. Instrument conditions were optimized to produce abundant protonated serine octamer. The sampling cone, extraction cone, and ion guide voltages were 20 V, 2.0 V, and 2.0 V, respectively. Unless otherwise noted, the collision cell entrance and exit potentials were 0 V and -

10 V, respectively, with an argon gas flow rate of 0.35 mL/min, resulting in a pressure of ~4.2 x 10^{-3} mbar in the collision cell. Data were analyzed using MassLynx V4.1.

Mass selection for collision induced dissociation experiments was done with a ~30 *m/z* window tuned to include all constituents of a given cluster size while preventing transmission of neighboring cluster ions. The collision voltage was varied between 0 and 60 V and spectra were averaged for 1 min. The charges and abundances of clusters were determined from the isotopic distributions.

Mass isolation of the individual isotopically labeled forms of the protonated decamer was performed under conditions that minimized ion activation with a *m/z* = 3 isolation window. The gas flow rate was 0.01 mL/min, resulting in a pressure of 5.4 x 10^{-5} mbar in the collision cell region. Data was averaged for 15 min for each cluster composition. To measure the change in the chiral preference of clusters with increasing collision voltage, the collision voltage was increased until the precursor abundance was reduced by over 70%. The gas flow rate was tuned between 0.01 mL/min and 0.1 mL/min to produce minimal activation at 0 V collision potential while still being able to acquire sufficient signal for the dissociation products at higher collision energies.

4.4 Results and Discussion

4.4.1 Chiral Preference of Protonated Serine Clusters in Solution

A nanoESI mass spectrum of a solution containing D-serine and 2,3,3-d_3-L-serine at 50 μM each in 49.95:49.95:0.1 water:methanol:acetic acid is shown in Figure 1a. Numerous protonated clusters, including an octamer, are observed. The highest mass cluster with an abundance >0.01% relative to the protonated monomer is 30^{3+}. An electrospray emitter with a 222 nm diameter tip was used in order to minimize any cluster formation due to aggregation inside a rapidly evaporating electrospray droplet. The initial droplet size produced from these emitters is estimated to be roughly 1/17 of the emitter tip diameter[35,36] corresponding to droplet diameters of ~13 nm. At a 100 μM total analyte concentration, only one out of every 14 initially formed ESI droplets is expected to contain an analyte molecule. When the average number of analyte molecules per droplet is significantly less than one, clusters observed in a mass spectrum should reflect their existence in the bulk solution.[33,37] Thus, these results indicate that clusters with up to ~30 serine molecules exist *in solution* and are not produced by aggregation within the droplet.

At 10 mM, where on average there are more than one analyte molecules per droplet, the largest clusters observed at >0.01% relative abundance from 222 nm and 2.4 μm diameter emitters were 75^{5+} and 85^{5+}, respectively. The larger clusters formed with larger emitter diameters is consistent with some aggregation occurring within the ESI droplets. The large clusters formed with the smaller emitters at this higher concentration could be due to a shift in the solution-phase equilibrium that favors formation of higher order clusters at higher serine concentrations, although aggregation inside the droplets may also occur.[33] The similar maximum cluster size using the 222 nm and 2.4 μm emitter tips, where droplets are expected to contain approximately 7 and ~9200 analyte molecules on average, indicates that most of these larger clusters are likely present in solution because of a shift in equilibrium owing to higher serine concentration.

The minimum cluster sizes for the doubly and triply protonated clusters are 8 and 21, respectively, the same as those from enantiopure solutions, suggesting that the presence of an enantiomer and mixed clusters does not significantly affect cluster charging.[33] The abundances of clusters formed from 100 μM solutions are significantly lower than those formed from 10 mM, similar to trends from enantiopure solutions.[33] This result is consistent with a shift in the equilibrium that makes clusters less favorable at lower serine concentrations. The protonated octamer is a magic number cluster, but the relative abundance of any single form of the octamer is significantly lower in spectra acquired from racemic solutions compared to enantiopure solutions consistent with previous reports.[1,22,23] This is primarily due to splitting of the octamer signal into nine different compositions. The population abundance of the protonated octamer from enantiopure solutions is ~1.2 ± 0.6 % compared to ~0.8 ± 0.2 % (all protonated octameric forms) from racemic solutions. These numbers are approximate because effects of *m*/*z* dependent ion transmission and detection efficiency are not taken into account. The similar population abundances indicate that the presence of another enantiomer in solution does not significantly affect the formation of the protonated octamer. The population abundance of all other clusters is higher from racemic solutions than from enantiopure solutions, similar to results reported by Julian *et al*.[30]

The extent of chiral preference of a cluster is determined by modeling the cluster composition as a binomial distribution and comparing the simulated and experimental data.[3,8,29] The ratio of the observed abundance to that expected from a statistical distribution, or enhancement factor (EF), and the magnitude of chiral preference (M_{cp}) can be used to measure the degree of chiral preference. An EF of greater than one indicates that a particular cluster composition is preferred, a value of less than one indicates a disfavored composition, and a value of one indicates no preference, i.e., a statistical distribution of constituents.[3] Chiral preferences are reported in both EF and M_{cp} in order to compare results to prior literature. The protonated octamer is the only cluster with resolvable isotope peaks that has a homochiral preference. The 3^+, 6^+ and 8^{2+} - 11^{2+} clusters have resolvable isotope peaks and these clusters have heterochiral preference. All other clusters, including the 2^+, 4^+, 5^+, and 7^+ have no chiral preference. These results are in excellent agreement with those reported previously.[3,29,31]

There is a strong preference for homochirality of the octamer in solution. The EF value for the 8D form of the octamer is ~16.7 ± 0.9 (M_{cp} = 0.37 ± 0.03; Figure 1b). This is slightly higher than the value of ~15 (calculated M_{cp} = 0.39) reported by Beauchamp and co-workers. Cooks and co-workers have reported M_{cp} values between 0.33 and ~0.4 from which we compute an average value of 0.36 ± 0.03 from these prior reports.[8,10,28,29] This value does not take into account any differences in measurement uncertainty in the individual studies. Thus, the value of the homochiral preference of serine octamer in solution is among the highest values previously reported in mass spectral data. In contrast, the doubly protonated decamer has EF values slightly greater than one for 4D:6L, 5D:5L and 6D:4L forms and values as low as 0.3 for more homochiral forms (Figure 1c). This pattern indicates a structure or structures where heterochirality is significantly preferred. The heterochiral preference of 8^{2+} could indicate a different form of protonated octamer in solution, or it could be formed by loss of serine molecules from higher order doubly protonated clusters, such as the 10^{2+} that have a heterochiral preference.

Different extents of sodium adduction to clusters formed with small and large emitters provide support for our conclusion that aggregation does not occur to a significant extent with the smaller emitters at 100 μM concentration. With 2.4 μm emitters and 10 mM solution, ~12% of the dimer population is sodiated (Figure S1a). A similar result is obtained with 222 nm emitters, where initial

droplets contain multiple analyte molecules (Figure S1b). However, less than ~0.9% of the dimer population that is formed from 100 μM serine solution is sodiated with 222 nm emitters (Figure S1c). These data are consistent with a reduction in aggregation within electrospray droplets with smaller tip sizes and concentrations and provide further evidence that the clusters observed in mass spectra under these conditions are not formed during the electrospray process.

4.4.2 Homochirality Emerges from Dissociation of Heterochiral Precursors

Racemic serine clusters consisting of between 8 and 37 serine molecules with between one and three protons were collisionally activated to investigate the dissociation products, pathways, and minimum cluster sizes for each charge state as a function of precursor cluster size. Loss of neutral serine molecules and/or charge separation to produce predominantly protonated dimer and the corresponding fragment ion occurs to various extents depending on cluster size and charge. Charge separation is increasingly favored as the cluster size approaches the minimum cluster size for each charge series. The minimum cluster size observed for the doubly and triply charged series was 8^{2+} and 21^{3+} respectively. The dissociation pathways for clusters produced from a racemic solution are the same as those for clusters from enantiopure solutions and are described as a function of cluster size in detail elsewhere.[34]

The protonated octamer is produced by CID of serine clusters consisting of 10 – 37 serine molecules at sufficient collision energies. Activation of 8^{2+} and 9^{2+} results in no protonated octamer. There are no singly protonated ions larger than the octamer. This indicates that the doubly protonated decamer is the smallest precursor to form protonated octamer by charge separation of a protonated dimer, in agreement with results from enantiopure cluster dissociation.[34] Results for protonated octamer formed by CID of 10^{2+} are shown in Figure 2a,b. The EF/M_{cp} values do not depend on collision voltage within a range of 0 – 10 V. As can be inferred from the "V" shape of the EF/M_{cp} plot, the protonated octamer has a significant *homochiral* preference (Figure 2b) despite being formed from a precursor with a *heterochiral* preference (Figure 1c). The magnitude of homochiral preference of the protonated octamer formed by dissociation is lower than that of the protonated octamer formed from solution (Figures 1b and 2b for protonated octamer formed in solution and by CID of 10^{2+}, respectively). The maximum EF value (3.94, M_{cp} value = 0.25) occurs for the 7D:1L composition of the protonated octamer formed by CID of 10^{2+} compared to the stronger preference for a purely homochiral 8D octamer in solution (EF = 16.7, M_{cp} = 0.37).

4.4.3 Homochiral Enrichment of Protonated Octamer from Dissociation of 10^{2+}

To gain insight into how dissociation of a *heterochiral* precursor leads to protonated octamer with a strong *homochiral* preference, constituents of the doubly protonated decamer were isolated and dissociated individually. Dissociation of the 5D:5L form of 10^{2+} produces protonated octamer that is composed of 3D:5L (19%), 4D:4L (32%), and 5D:3L (20%) and protonated dimers in roughly corresponding abundances (Figure 3a). These data are consistent with statistical formation of protonated dimer and protonated octamer that does not show a significant homochiral preference. The presence of 6D:2L and 2D:6L in the protonated octamer distribution reflects the

low resolution used for precursor selection in order to acquire adequate signal under very gentle dissociation conditions and the high abundances of adjacent 6D:4L and 4D:6L forms of 10^{2+}.

Dissociation of 4D:6L results in preferential loss of protonated 2D:0L to form a protonated 2D:6L octamer with an EF of 3.3 (Figure 3b). The corresponding 2D:0L dimer has an EF of ~2. These results indicate that there is a strong homochiral enrichment when a slightly homochiral form of the doubly protonated decamer complex dissociates.

Dissociation of 2D:8L results in the formation of 0D:8L (5%), 1D:7L (52%) and 2D:6L (43%). Both 1D:7L and 2D:6L have an EF of ~1.5 but 0D:8L has an EF ~0.3 indicating that loss of a protonated D homodimer is unfavored. The protonated heterodimer is significantly more abundant than expected. This is likely due to interference as a result of sequential serine loss from protonated pentamer, which overlaps in *m*/*z* with the precursor. Differences in binding energies for the different enantiomeric forms of the protonated dimer that can dissociate to protonated monomer could contribute to this as well. The abundances of the protonated dimer are roughly consistent with the trends in the corresponding protonated octamer. These data indicate that the strong homochiral preference of the protonated octamer formed from dissociation of 10^{2+} from racemic solutions is primarily due to dissociation of clusters with a disproportionate number of D and L forms of serine. Even though 10^{2+} has a heterochiral preference when formed from solution, the majority of this cluster composition has differing numbers of D and L serine. It is these clusters that have an intrinsic bias that results in the homochiral enhancement of the protonated octamer upon dissociation. For larger clusters, the proportion of clusters that have the same number of the two forms of serine decreases relative to the cluster population, suggesting that protonated octamers formed by dissociation of even larger clusters may lead to greater homochiral enhancement.

4.4.4 Homochiral Enrichment of Protonated Octamer Formed by CID of Large Clusters

Dissociation of large serine clusters to produce protonated octamer occurs primarily through a 10^{2+} intermediate. In order to investigate the extent to which dissociation of larger clusters leads to a chiral preference of product ions, clusters up to 37^{3+} were dissociated at sufficient collision energies to produce protonated octamer. A wide *m*/*z* window was used for precursor isolation to ensure that the majority of cluster compositions for a given cluster size were activated. Precursor ions were chosen to avoid interferences from other ions. Dissociation of 17^{2+}, 19^{2+}, 23^{3+}, 29^{3+}, and 37^{3+} all lead to protonated octamer with significant homochirality despite the fact that these initial precursor clusters do not have a homochiral preference (Figure S2). For example, protonated octamer produced by dissociation of 37^{3+} (Figure 2c,d) has a strong homochiral preference with an EF value of ~10.1 (M_{cp} = 0.30) for the pure enantiomeric 8D form. This extent of homochiral preference is significantly closer to that of the protonated octamer formed directly from solution (Figure 1b) than when protonated octamer is formed by dissociation of 10^{2+} formed directly from solution (Figure 2b). The chiral preference of the 10^{2+} that is formed from solution and that formed by dissociation of larger clusters is remarkably similar (Figures 1c and S3). Because the octamer formed by dissociation passes through a decamer intermediate, this suggests that 10^{2+} formed from solution has a different structure than this same ion formed by dissociation of larger clusters.

Because larger clusters require higher collision energies to produce the octamer, the effect of collision energy on the chiral selectivity of the protonated octamer was investigated. To investigate

effects of collision energy, dissociation spectra for all of the larger clusters were measured as a function of increasing collision voltage until no protonated octamer remained. There was no significant change in the chiral preference of the protonated octamer with collision voltage. The absence of a significant change in the chiral preference of the octamer formed by dissociation of the doubly protonated decamer at different collision energies indicates that the chiral enhancement of the protonated octamer is not due to differences in stabilities of the different forms of the doubly protonated decamer.

The chiral preference of the doubly protonated decamer from dissociation of larger clusters does not change significantly with cluster size (Figure S3) and is similar to that from solution. For example, dissociation of 37^{3+} shows that the 5D:5L decamer formed in the gas phase has nearly the same magnitude of heterochiral preference as the 5D:5L decamer from solution (EF = 1.07; M_{cp} = 0.16 and EF = 1.07; M_{cp} = 0.15, respectively) (Figures 1c and S3). Similarly, a comparison of the protonated octamer chiral preference with increasing precursor cluster size reveals no obvious trend for clusters larger than 10^{2+} (Figure S2). Interestingly, the EF of the homochiral octamers produced by dissociation of the 37^{3+} (10.1, M_{cp} = 0.30) is ~60% of the magnitude of the homochiral octamers produced directly from solution (16.7, M_{cp} = 0.37). Although the homochiral preference of protonated octamer formed in solution and by dissociation of 10^{2+} is significantly different, this difference is much smaller for protonated octamer produced by dissociation of larger multiply protonated serine clusters. Larger clusters of serine dissociate into the octamer under a wide range of experimental conditions often used in studies of amino acid clustering and our results indicate that both clusters formed by aggregation in droplets and by gas-phase dissociation of larger clusters likely contribute to the large abundance of homochiral protonated octamer observed in prior reports.

Our findings that dissociation of larger serine clusters produces protonated octamer that has a strong homochiral preference is in striking contrast to a prior report by Spencer *et al.* who concluded that the octamer generated by successive dissociation of serine clusters in the gas-phase has no preference for homochirality.[24] In this study, homochiral preference was inferred from the relative abundances of the protonated octamer and the protonated dimer formed from enantiopure and racemic mixtures without a deuterium label. No change was observed in the octamer/dimer ratio when the octamer was produced by gas-phase dissociation from solutions of enantiopure and racemic mixtures. This is likely a result of similar dissociation energies for the enantiomeric forms of the clusters, consistent with our findings that there is no significant energy dependence to the enantiomeric preference of the protonated octamer formed by dissociation of larger multiply protonated clusters.

4.5 Conclusions

Prior results using electrospray emitters that have submicron diameter tips showed that protonated octamer exists in solution, albeit in low abundance.[33] Extending these measurements here, we show that the octamer that exists *in solution has a strong homochiral preference*. Thus, the strong homochiral preference of the octamer is an intrinsic property of serine in solution and is not solely the result of rapid aggregation in droplets or a reflection of differences in gas-phase stabilities. Protonated octamer can also be formed by aggregation that occurs inside an electrospray droplet and by gaseous dissociation of larger serine clusters.[33,34] Dissociation of larger

clusters consisting of mixed L and D forms of serine to form protonated octamer follows the same mechanisms observed for enantiopure clusters and results in abundant protonated octamer that has a strong homochiral preference.

A surprising result of this study is that the doubly protonated decamer formed from solution has a heterochiral preference, yet dissociation of this cluster results in a protonated octamer with a homochiral preference. This homochiral selectivity upon dissociation is a result of the decamer population that has a greater abundance of one chiral form of serine. Dissociation of larger clusters leads to an even higher chiral selectivity in the protonated octamer that is formed. The homochiral preference of the protonated octamer formed by larger clusters is close to that of serine octamer that exists in solution.

These results support the hypothesis that the high abundance of protonated octamer observed in many prior experiments using spray ionization methods with large emitter tips is due to aggregation that occurs inside the electrospray droplets. The presence of protonated octamer as a magic number cluster is further enhanced by gas-phase dissociation of large clusters, which produce protonated octamer as the most abundant cluster (except protonated dimer) at a normalized collision energy, i.e., temperature.[34]

The chiral preference of protonated octamer is different in solution than it is when the protonated octamer is formed by dissociation of the doubly protonated decamer that is also formed from solution. Dissociation of larger multiply protonated clusters leads to a protonated octamer with a homochiral preference that is only slightly less than that of the octamer in solution. These results indicate that the decamer in solution and that formed by dissociation have different structures, providing further evidence for the existence of clusters larger than the octamer in solution. Structural differences in these ions may be identified using ion mobility or ion spectroscopy, which may provide insights into how homochiral enhancement of the protonated octamer formed by dissociation occurs. These results also indicate that the magnitude of chiral preference of the protonated octamer may be used to distinguish octamer that exists or is formed in solution from that formed in the gas-phase by dissociation of larger clusters.

4.6 Acknowledgements

This material is based upon work supported by the National Science Foundation Division of Chemistry under grant number CHE-1609866 as well as a Graduate Research Fellowship (DGE-1752814). The authors are also grateful for financial support from CALSOLV and thank the staff at the University of California, Berkeley Electron Microscope Laboratory for advice and assistance with electrospray emitter imaging.

4.7 References

(1) R. G. Cooks, D. Zhang, K. J. Koch, F. C. Gozzo and M. N. Eberlin, *Anal. Chem.*, 2001, **73**, 3646–3655.

(2) A. E. Counterman and D. E. Clemmer, *J. Phys. Chem. B*, 2001, **105**, 8092–8096.

(3) R. R. Julian, R. Hodyss, B. Kinnear, M. F. Jarrold and J. L. Beauchamp, *J. Phys. Chem. B*, 2002, **106**, 1219–1228.
(4) C. A. Schalley and P. Weis, *Int. J. Mass Spectrom.*, 2002, **221**, 9–19.
(5) R. Hodyss, R. R. Julian and J. L. Beauchamp, *Chirality*, 2001, **13**, 703–706.
(6) P. Nemes, G. Schlosser and K. Vékey, *J. Mass Spectrom.*, 2005, **40**, 43–49.
(7) Z. Takats, S. C. Nanita, R. G. Cooks, G. Schlosser and K. Vekey, *Anal. Chem.*, 2003, **75**, 1514–1523.
(8) S. C. Nanita, Z. Takats, R. G. Cooks, S. Myung and D. E. Clemmer, *J. Am. Soc. Mass Spectrom.*, 2004, **15**, 1360–1365.
(9) S. Myung, R. R. Julian, S. C. Nanita, R. G. Cooks and D. E. Clemmer, *J. Phys. Chem. B*, 2004, **108**, 6105–6111.
(10) S. C. Nanita, E. Sokol and R. G. Cooks, *J. Am. Soc. Mass Spectrom.*, 2007, **18**, 856–868.
(11) P. Yang, R. Xu, S. C. Nanita and R. G. Cooks, *J. Am. Chem. Soc.*, 2006, **128**, 17074–17086.
(12) Z. Takáts and R. G. Cooks, *Chem. Commun.*, 2004, 444–445.
(13) S. C. Nanita and R. G. Cooks, *Angew. Chem. Int. Ed.*, 2006, **45**, 554–569.
(14) Z. Takats, S. C. Nanita and R. G. Cooks, *Angew. Chem. Int. Ed.*, 2003, **42**, 3521–3523.
(15) F. X. Sunahori, G. Yang, E. N. Kitova, J. S. Klassen and Y. Xu, *Phys. Chem. Chem. Phys.*, 2013, **15**, 1873–1886.
(16) K. J. Koch, D. Zhang, R. G. Cooks, F. C. Gozzo and M. N. Eberlin, *Chem. Commun.*, 2001, **1**, 1854–1855.
(17) S. Gronert, R. A. J. O'Hair and A. E. Fagin, *Chem. Commun.*, 2004, 1944–1945.
(18) U. Mazurek, O. Geller, C. Lifshitz, M. A. McFarland, A. G. Marshall and B. G. Reuben, *J. Phys. Chem. A*, 2005, **109**, 2107–2112.
(19) J. Ren, Y. Y. Wang, R. X. Feng and X. L. Kong, *Chinese Chem. Lett.*, 2017, **28**, 537–540.
(20) G. Liao, Y. Yang and X. L. Kong, *Phys. Chem. Chem. Phys.*, 2014, **16**, 1554–1558.
(21) A. B. Costa and R. G. Cooks, *Phys. Chem. Chem. Phys.*, 2011, **13**, 877–885.
(22) U. Mazurek, *Eur. J. Mass Spectrom.*, 2006, **12**, 63–69.
(23) B. Concina, P. Hvelplund, A. B. Nielsen, S. B. Nielsen, J. Rangama, B. Liu and S. Tomita, *J. Am. Soc. Mass Spectrom.*, 2006, **17**, 275–279.
(24) E. A. C. Spencer, T. Ly and R. R. Julian, *Int. J. Mass Spectrom.*, 2008, **270**, 166–172.
(25) K. J. Koch, F. C. Gozzo, S. C. Nanita, Z. Takats, M. N. Eberlin and R. G. Cooks, *Angew. Chem. Int. Ed.*, 2002, 41, 1721–1724.
(26) V. Scutelnic, M. A. S. Perez, M. Marianski, S. Warnke, A. Gregor, U. Rothlisberger, M. T. Bowers, C. Baldauf, G. von Helden, T. R. Rizzo and J. Seo, *J. Am. Chem. Soc.*, 2018, **140**, 7554–7560.
(27) J. Seo, S. Warnke, K. Pagel, M. T. Bowers and G. von Helden, *Nat. Chem.*, 2017, **9**, 1263–1268.
(28) H. Zhang, Z. Wei, J. Jiang and R. G. Cooks, *Angew. Chem. Int. Ed.*, 2018, **130**, 17387–17391.
(29) R. Chen, Z. Wei and R. G. Cooks, *Anal. Chem.*, 2021, **93**, 1092–1099.
(30) R. R. Julian, S. Myung and D. E. Clemmer, *J. Phys. Chem. B*, 2005, **109**, 440–444.
(31) R. R. Julian, S. Myung and D. E. Clemmer, *J. Am. Chem. Soc.*, 2004, **126**, 4110–4111.
(32) S. Vandenbussche, G. Vandenbussche, J. Reisse and K. Bartik, *Eur. J. Org. Chem.*, 2006, **2006**, 3069–3073.
(33) J. S. Jordan and E. R. Williams, *Anal. Chem.*, 2021, **93**, 1725–1731.
(34) J. S. Jordan and E. R. Williams, *Analyst*, 2021, **146**, 2617–2625.

(35) K. L. Davidson, D. R. Oberreit, C. J. B. Hogan and M. F. Bush, *Int. J. Mass Spectrom.*, 2017, **420**, 35–42.
(36) A. C. Susa, Z. Xia and E. R. Williams, *Anal. Chem.*, 2017, **89**, 3116–3122.
(37) Z. Xia and E. R. Williams, *Analyst*, 2019, **144**, 237–248.

4.8 Figures

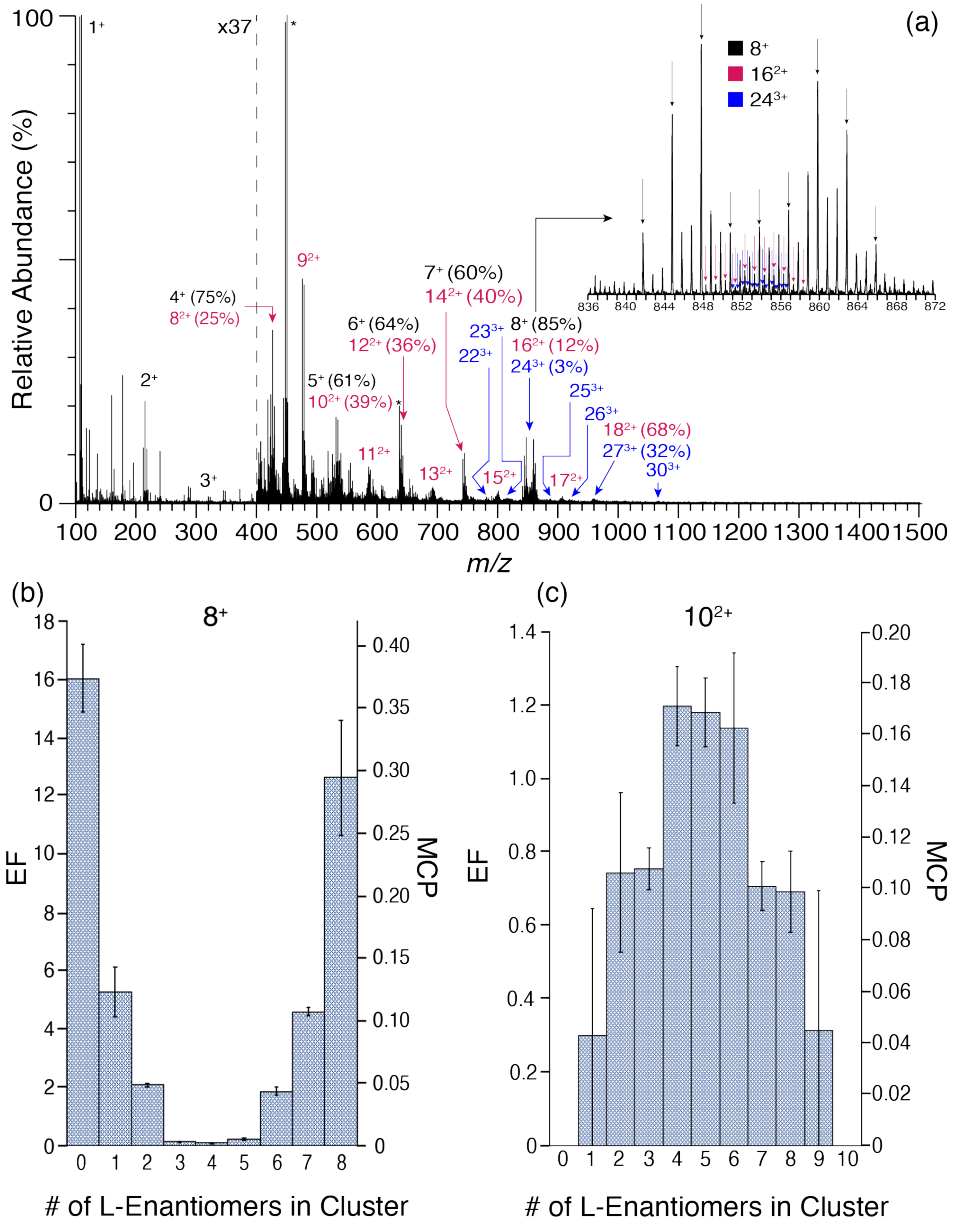

Figure 4.1. Electrospray mass spectrum of a solution consisting of a) an equimolar concentration of D-serine and 2,3,3-d_3-L-serine at 50 µM each in 49.95:49.95:0.1 water:methanol:acetic acid with an expansion of the various forms of protonated octamer inset, and chiral enhancement factors and magnitude of chiral preference for b) protonated octamer showing strong homochiral preference and c) doubly protonated decamer showing heterochiral preference. Signal for 16^{2+} and 24^{3+} overlaps that of the protonated octamer but can be deconvolved based on their isotopic signatures. The 30^{3+} ion is the largest cluster observed (S/N ~5) that has both a resolved isotope distribution and an abundance greater than 0.01% of the monomer abundance. Asterisks denote PDMS contamination peaks.

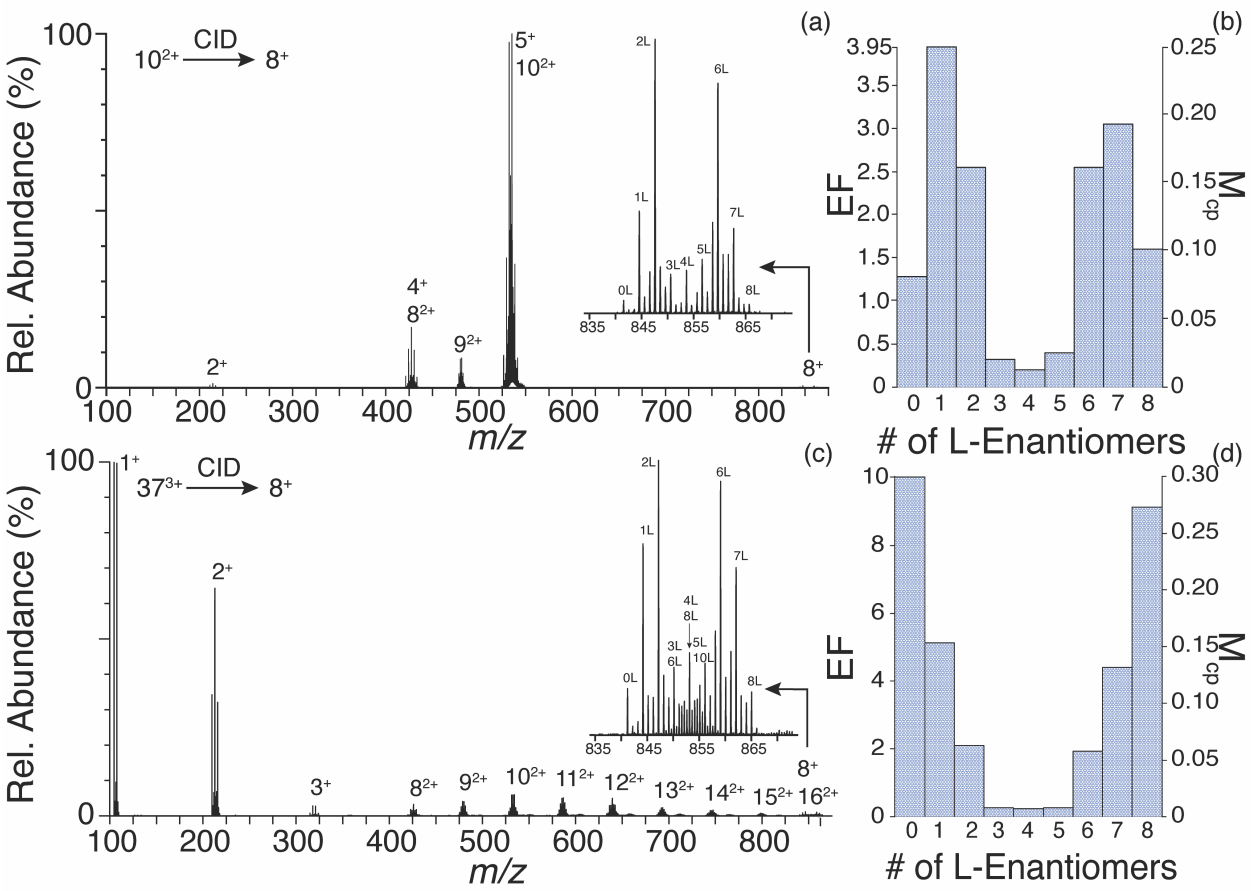

Figure 4.2. Dissociation of a) serine 10^{2+} and c) serine 37^{3+} produces protonated octamer with distinct homochiral chiral preferences (b and d, respectively), with that formed by dissociation of the heterochiral 10^{2+} (b) having lower homochiral preference than that formed from the 37^{3+} (d).

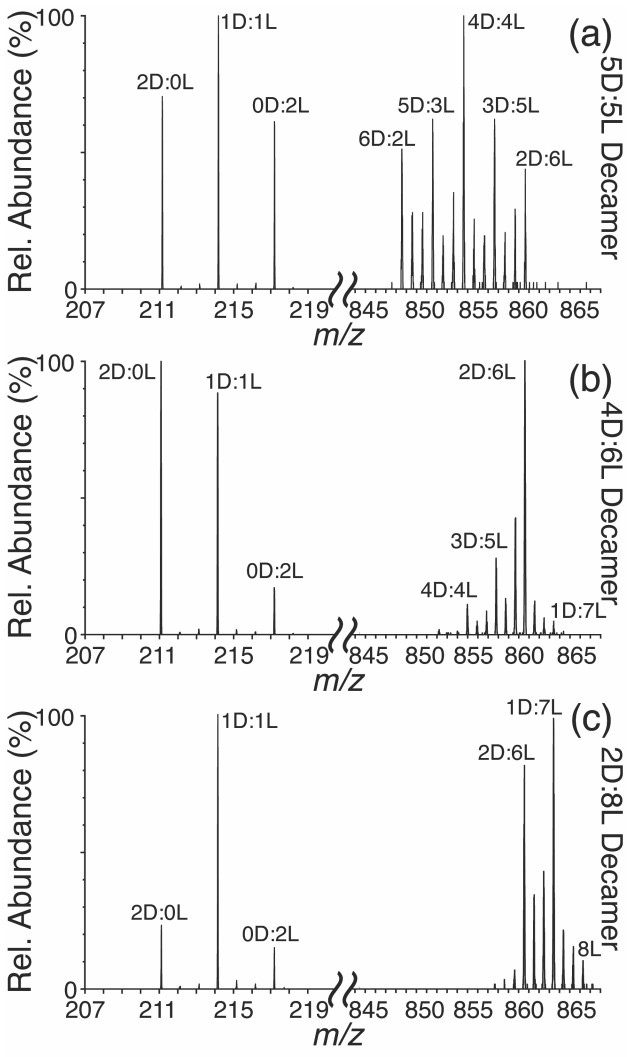

Figure 4.3. Dissociation of different chiral forms of doubly protonated decamer consisting of a) 5D:5L, b) 4D:6L, and c) 2D:8L; regions around the protonated dimer and protonated octamer are shown.

4.9 Supplementary Information

Supplementary Table 4.1. Tip Puller Parameters for P-87 Tip Puller

Heat	Pull	Velocity	Time	Tip Diameter
555	0	70	235	2.4 ± 0.04 μm
580	250	230	235	222 ± 8 nm

Additional factors also affect the diameters of emitter tips that are independent of these parameters used for pulling the capillaries. The orientation of the filament, the age of the filament, the outer and inner diameters of the capillary, and even the humidity in the laboratory can change the tip diameters that are produced, making it important to frequently image the tips to determine tip diameters.

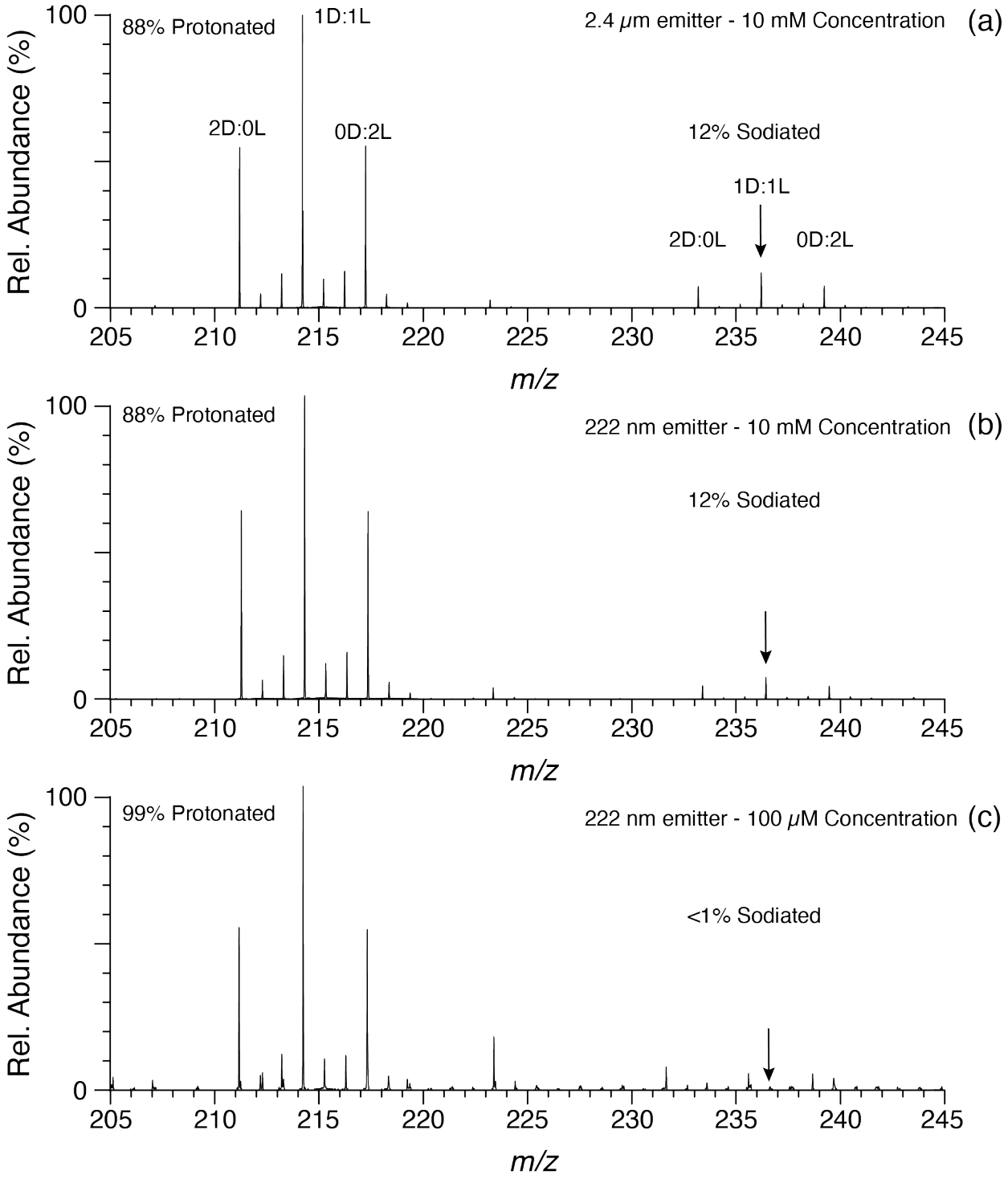

Supplementary Figure 4.1. Electrospray ionization mass spectra of an equimolar concentration of D-serine and 2,3,3-d_3-L-serine at in 49.95:49.95:0.1 water:methanol:acetic acid at 10 mM total concentration with a) a 2.4 μm emitter, b) a 222 nm emitter and c) a 100 μM total concentration with a 222 nm emitter.

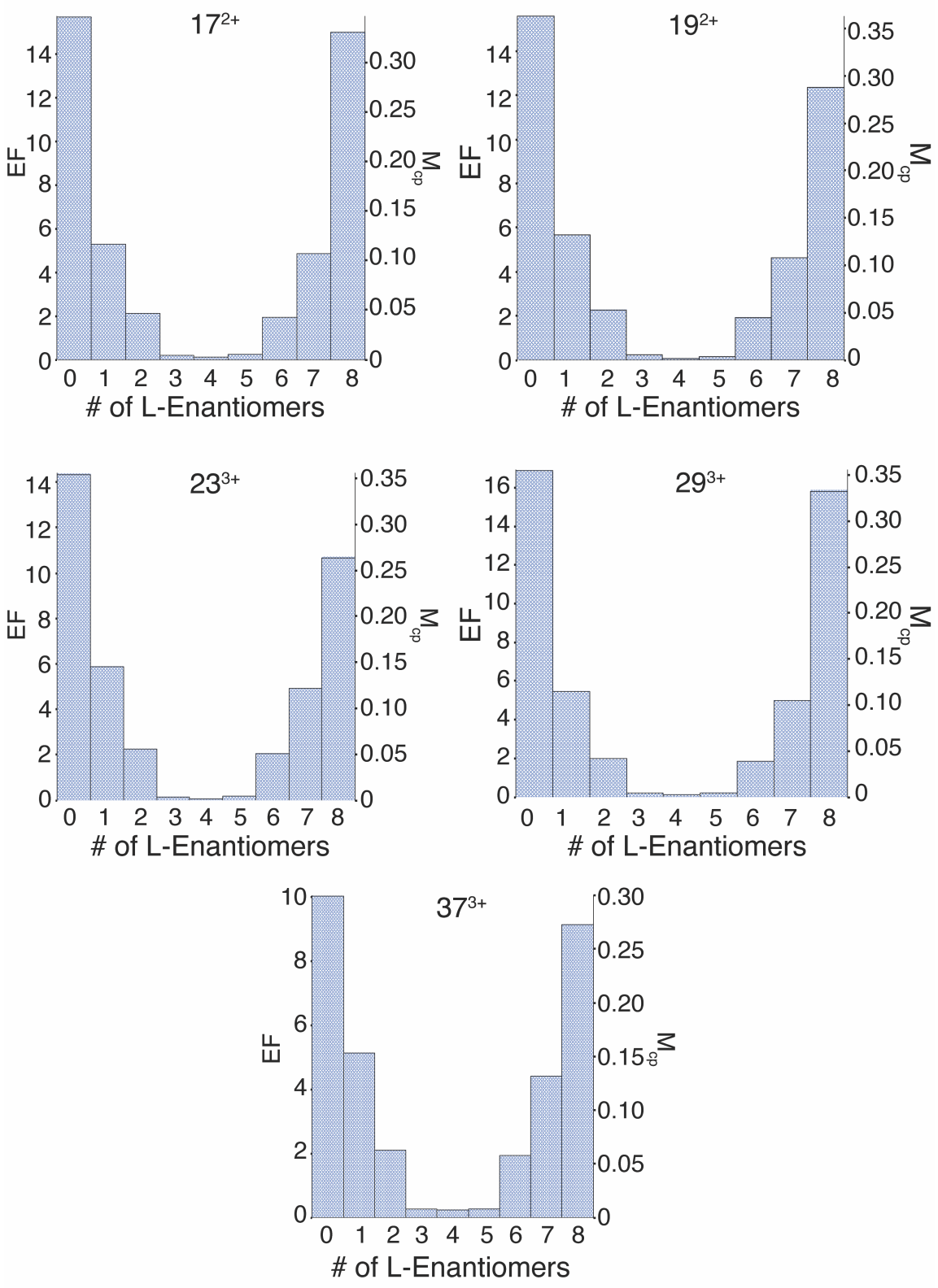

Supplementary Figure 4.2. Extent of homochiral preference of protonated octamer formed by dissociation of the 17^{2+}, 19^{2+}, 23^{3+}, 29^{3+}, and 37^{3+}.

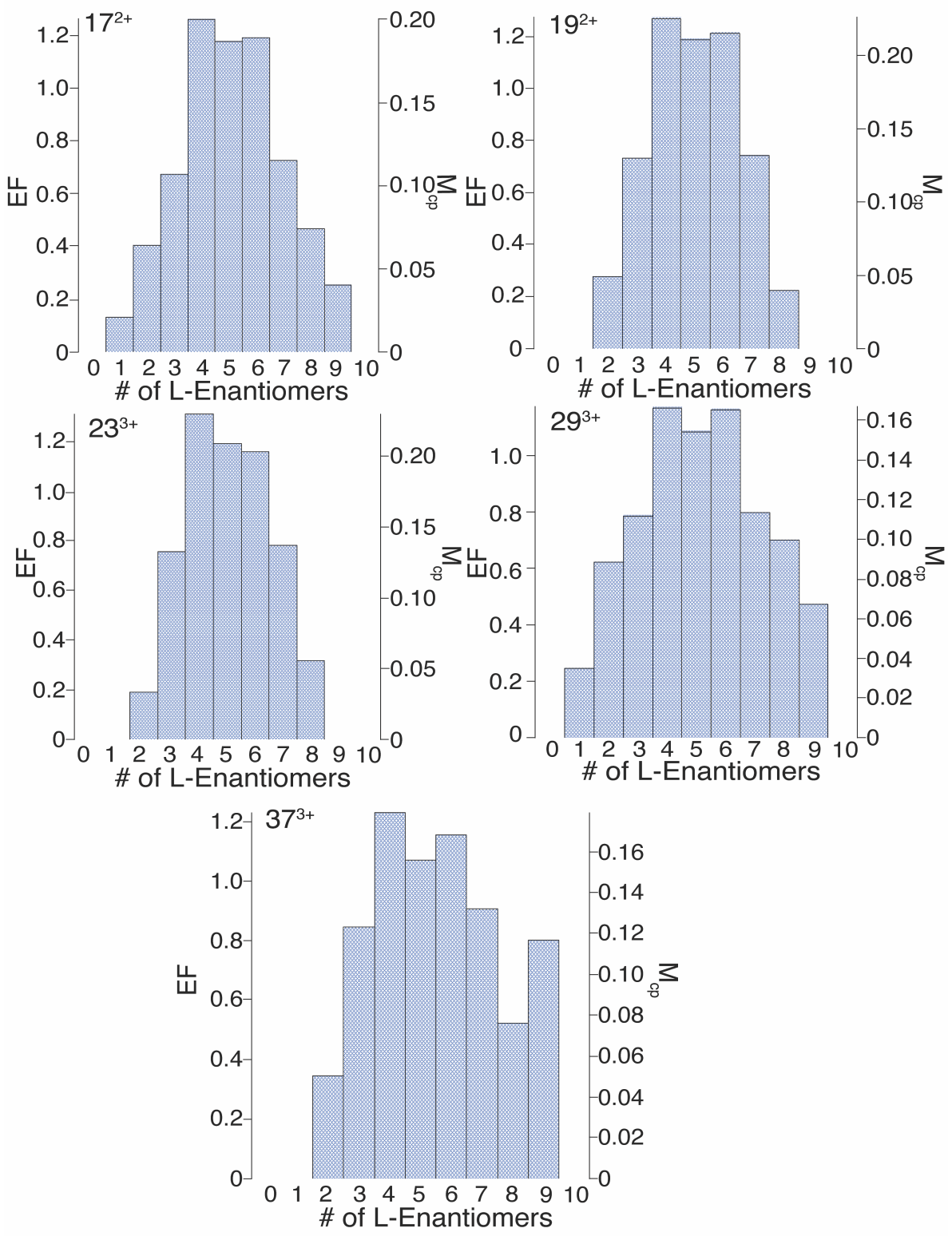

Supplementary Figure 4.3. Extent of homochiral preference of protonated decamer formed by dissociation of the 17^{2+}, 19^{2+}, 23^{3+}, 29^{3+}, and 37^{3+}. There is no significant change in chiral preference of the decamer produced by dissociation with increasing precursor cluster size

Chapter 5

Tips on Making Tiny Tips: Secrets to Submicron Nanoelectrospray Emitters

This chapter is reproduced with permission from:

Jacob S. Jordan, Zijie Xia, Evan R. Williams

"Tips on Making Tiny Tips: Secrets to Submicron Nanoelectrospray Emitters"

Journal of the American Society for Mass Spectrometry, **2022**, *33*(3):607-611

5.1 Abstract

Nanoelectrospray ionization emitters with submicron tip diameters have significant advantages for use in native mass spectrometry, including the ability to produce resolved charge-state distributions for proteins and macromolecular complexes from standard biochemical buffers that contain high concentrations of nonvolatile salts and to prevent non-specific aggregation that can occur during droplet evaporation. We report on various factors affecting the tip morphology and provide tips to producing and using emitters with submicron tips. Effects of pulling parameters for a Sutter Instrument P-87 tip puller on the resulting tip diameter and morphology are shown. The "Pull" parameter has the largest effect on tip diameter, followed by "Velocity", "Pressure", and "Heat", whereas the "Time" parameter has minimal effect beyond a lower threshold. High "Pull" values generate emitters with multiple tapers, whereas high "Velocity" values generate a tip with only a single tapered region. A protocol for producing reproducible emitters in the submicron size range, as well as guidelines and tips for using these emitters with standard biochemical buffers that contain high concentrations of non-volatile salts is presented with the aim of expanding their use within the native MS community.

5.2 Introduction

Nanoelectrospray ionization (nESI) is widely used in native mass spectrometry to produce gaseous ions of biomolecules and intact macromolecular complexes from aqueous solutions. The majority of nESI emitters that are currently used have tip diameters substantially larger than a micron. Electrospray emitters with submicron tip diameters have several demonstrated advantages, including the ability to desalt macromolecular ions from biochemical buffers consisting of high concentrations of nonvolatile salts,[1–6] prevent aggregation inside electrospray

droplets to identify complexes that exist in solution,[7–9] and improve measurements of dissociation constants of metal ions or ligands bound to biopolymers.[6,10–14] Narrow bore emitters have been used to sample nanoliters of solution and to rapidly mix two solutions to investigate fast processes on the 1 to 100 μs timescale.[15,16]

Despite these advantages, emitters with submicron tips are not widely used, in part due to reported issues with clogging and complications with obtaining reproducible tip diameters and ion currents. Differences in performance between labs may in part be related to the lack of a standard protocol for tip pulling and effects of ambient conditions, which may lead to different emitter morphologies. Detailed here is a guide to producing nESI emitters with tips that have submicron diameters as well as recommendations on using these emitters for native MS. This guide is in response to questions from many in the native MS community and incorporates notes from the Sutter Instrument manual,[17] published tip puller parameters,[13,18] and a helpful guide on tip pulling by Erin M. Panczyk.[19]

5.3 Experimental Methods

Thin-walled, filamented borosilicate capillaries (1.0 mm outer diameter, 0.78 mm inner diameter, Sutter Instrument, Novato, CA, BF100-78-10) were pulled using a Flaming/Brown P-87 micropipette puller (Sutter Instrument) equipped with a box-filament (FB255B). Tip pulling parameters were systematically varied to determine the effects of each parameter on tip size with the goal of producing a range of small tip sizes. The cooling gas (dry air) pressure was varied between 100 and 350. For each set of parameters, four tips were imaged using a Hitachi TM-1000 scanning electron microscope (Schaumberg, IL) in the Electron Microscopy Lab at University of California, Berkeley. The resulting images were analyzed in ImageJ (v. 1.53k) using the "Find Edges" function to enhance the contrast between the inner and outer diameters of the tip.

5.4 Results and Discussion

5.4.1 Effects of Tip Puller Parameters

In the following discussion, the words capillary, emitter, and tip are used to refer to the borosilicate tube prior to pulling, the pulled electrospray emitter, and the pulled end of the emitter, respectively. Five pulling parameters were varied independently to determine their effects on the final tip diameter. The starting parameters (Heat = 545, Pull = 0, Vel = 70, Time = 235, Pressure = 300) were chosen because they produce highly reproducible tips with an inner diameter of 2.33 ± 0.02 μm. Readers may find Figure 10 in the P-87 user manual (Rev. 0299c (20081016)) helpful for understanding each of the following parameters,[17] which are briefly described here. The "Pull" parameter controls the force applied to the pulley arms and has the largest effect on tip diameter. An increase from 0 to 150 results in a reduction in the tip diameter from 2.33 ± 0.02 μm to 350 ± 50 nm, respectively. Both low and high values produce a similar initial taper (Figure 1a inset, blue box), but higher values produce a distinctly different, narrower taper closer to the end of the tip

(Figure 1a inset, orange box). The "Velocity" parameter controls when the filament is turned off during the initial capillary deformation and initiates the flow of the cooling gas 40 ms prior to the start of the "Pull" event. This parameter has the second largest effect. An increase from 56 to 230 reduced the diameter from 2.5 ± 0.1 μm to 760 ± 60 nm, respectively (Figure 1b). Increasing "Velocity" increases the length of the taper but does not produce a second tapered region. In general, emitters with shorter tapers are easier to load with sample although some difficulties have been reported for emitters with very short tapers.[11] Increasing the "Heat" parameter, which controls the current supplied to the heating filament, from 535 to 575 resulted in a small decrease in the diameter from 2.3 ± 0.2 μm to 1.9 ± 0.1 μm with no significant change in the taper (Figure 1c). However, the reproducibility improved significantly at intermediate "Heat" values to a minimum of 2.33 μm ± 20 nm at a value of 545. Adjusting the cooling gas pressure from 350 to 100 results in a longer taper and a reduction in the tip diameter from 2.4 ± 0.5 μm to 660 ± 30 nm (Figure 1d). The tip diameters are less reproducible at a pressure setting higher than 300. This may be due to over-cooling during the heating step, resulting in the capillary snapping instead of separating into a fine point. The "Time" parameter controls the length of time that cooling gas is on (in units of ½ ms) during the pulling process. Above a lower threshold value, the "Time" parameter has very little effect on the resulting tip diameter. Changing "Time" from 235 to 125 resulted in no significant difference in tip diameter. Below a value of ~100, the tip is inadequately cooled during pulling and is drawn into a thin glass fiber with no discernable tip opening. Values above this minimum result in similar tip sizes. Overall, higher "Velocity", "Heat" and "Pull" settings, and lower cooling gas pressures, will result in smaller tip diameters (Table 1).

It is important to note that if the "Heat" or "Velocity" parameters are near a threshold value, then changes in ambient laboratory conditions may cause the instrument to cycle through multiple program loops, which will change the final tip diameter.[17] The ambient temperature, humidity, and temperature of the filament mounting block can all influence the number of loops, so it is recommended to optimize parameters to be distant from the looping threshold.

The reproducibility in tip sizes that are produced can be high. The average standard deviation (s.d.) in the diameter of the 21 emitters used to obtain the above data was ~6.8%. After characterizing the trends for each of the pulling parameters, emitters with tips as small as 220 ± 8 nm (s.d. = 3.6%) were made (Table 1). A reliable spray was maintained for ~30 min in variable-temperature ESI measurements of cytochrome *c* in 20 mM 7:3 sodium chloride:Tris buffer with these emitters.

5.4.2 Tips for Making Submicron Diameter Emitters

The parameters required to make reproducible emitters with submicron tips will differ for each capillary pulling instrument depending on the heating mechanism (filament or laser), orientation of the heating element with respect to the capillary, composition of the capillary, and a myriad of other factors.[17] Thus, the optimal parameters must be determined for each puller. Emitter composition (borosilicate vs. quartz) has minimal effect on the performance of emitters with submicron tips.[20] However, Na^+ may leach into solution with borosilicate emitters, and lead to some salt adduction and reduced signals.[20] This does not occur with quartz due to lower sodium content (~0.2 ppm).[20] Emitter openings should be broken by the tip puller because diameters can

be irreproducible when the tips are clipped manually.[20] The following protocol may assist users in finding parameters that reproducibly generate emitters with submicron tip diameters:

1. Run a ramp test using the capillary of choice; thin-walled, filamented borosilicate capillaries were used here. Sutter Instrument recommends filamented glass for emitters pulled below 3 µm in diameter.[21] Subtract 20 units from the ramp test value and use this as the starting "Heat" parameter.[17] To start, set the "Pull" parameter to 0 and set the "Velocity" parameter to a value between 80 – 120 that results in the capillaries being pulled in <8 s.[17]
2. Identify the lowest "Time" parameter that generates usable tips. On our device, this value is ~125. Set Time value to be ~100 units higher than this to ensure reproducible tips. For ultra-fine tips (below 200 nm), Sutter Instrument recommends setting the "Time" parameter to only 5 units higher than the lowest value that generates a usable tip.[17]
3. Vary the "Heat" parameter to determine the optimum value that results in the most reproducible emitter diameters. The "Heat" parameter should not be more than ~100 units lower than "Ramp" to avoid uneven snapping of the tips.
4. Vary the "Velocity", "Pull", and "Pressure" parameters systematically until tip diameters of the desired size are obtained. Typically, large "Pull" or "Velocity" values (>150) are necessary to reach tip diameters smaller than 400 nm. Large "Pull" and "Velocity" values are necessary to achieve similar size tips with theta glass capillaries. Lower "Pressure" values may be used to obtain smaller diameters as well, but result in a longer taper.
5. Run the ramp test every six months and check a minimum of three emitter tip diameters on both sides of the pulled capillary once every three months to ensure even pulling. The condition of the cooling gas desiccant is also important for tip reproducibility. Frequent checking of the emitter tip diameters is recommended to ensure precise values.

This protocol should also be applicable to other filament-based capillary pulling instruments, such as the Sutter Instrument P-97 or P-1000. For laser-heated capillary pullers, such as the P-2000 from Sutter Instrument, the "Pull", "Velocity", and "Heat" parameters should follow similar trends to those shown here, albeit with different absolute values. However, the P-2000 also has two additional parameters: the "Filament" parameter, which adjusts the scanning pattern of the laser, and the "Delay" parameter, which adjusts the time between the laser turning off and the hard pull. Users of laser-heated capillary pulling instruments must also optimize these additional parameters.

5.4.3 Tips for Using Submicron Emitters for Native Protein MS

Care must be taken when loading the emitters and during electrospray in order to obtain native protein charge-state distributions. The following advice may help users maintain stable ion signal and achieve effective protein desalting.

1. Sample can be loaded into an emitter using a 10 µL syringe to deposit the sample near the beginning of the taper and avoid bubbles entering the tapered portion of the tip. Then, the emitter can be shaken or a centrifuge can be used to move the sample down to the tip and remove bubbles. Small bubbles can be visualized by holding the emitter up to a light. To avoid clogs from solution contaminants, we recommend filtering all buffers through a 0.22 µm filter

prior to use.[20] Centrifuging the sample and pipetting from the bulk of the solution (rather than near the surface or bottom of a sample container) may also reduce clogging of the emitters.

2. High spray voltages and short distances between the emitter and MS inlet can result in discharge due to the large electric field at the tip, breaking the emitter and interrupting spray. Spray may still occur but will typically be unstable and result in larger droplets, as evidenced by increased aggregation of analyte molecules resulting in higher abundance clusters in mass spectra.[8] We recommend positioning emitters ~3 – 5 mm from the instrument inlet and slowly increasing the spray voltage until there is stable ion current, typically at values of ~0.4 – 0.6 kV for emitters <500 nm in diameter (voltage difference referenced to instrument inlet). For emitters smaller than 1 μm, spray voltages in excess of 1.4 kV within 5 mm of the instrument inlet have a high risk of discharge between the emitter and instrument. A slight reduction in voltage (100 – 200 V) a few seconds after the spray stabilizes can improve the stability of the total ion signal.
3. In our experiments, spray voltage is provided via a platinum wire inserted into the back of the capillary that is in contact with the solution (Figure 2). This avoids the need to coat the emitter tips with an electrically conductive material to establish electrical contact. Metal-coated emitters with submicron diameter tips can also desalt ions effectively. They have the potential advantage of eliminating cross-contamination between samples,[14] although we have never observed contamination as a result of re-using the platinum wire. However, the metal coating can make visualizing bubbles in the tapered region more difficult.
4. Surface effects have been observed when using emitters with submicron tips as a result of protein-glass interactions. This can lead to time-dependent protein signals due to differences in absorption and higher protein charging due to surface-induced unfolding.[22,23] It is important to keep these effects in mind when analyzing samples using these emitters.
5. When solutions containing high concentrations of nonvolatile salts are used with emitters that have small tips diameters, protein ion desalting should occur spontaneously within the distances and voltages given above. The desalting phenomenon is characterized by a large drop in the total ion signal (primarily salt clusters), significant reduction in salt clusters in the mass spectrum, and resolved protein charge-state distributions. The onset of desalting occurs more readily with decreasing tip diameter and smaller emitter tip diameters leads to less salt adduction.[1] The effect of desalting and tip size is illustrated in Figure 3, which shows a spectrum of 10 μM yeast alcohol dehydrogenase obtained from a 150 mM NaCl/25 mM Tris solution using emitters with either a 9.2 μm (top) or 220 nm (bottom) tip. For the emitter with the larger tip diameter, the ion count is high (8.8×10^5) but any protein signal that may be present is obscured by abundant signal from large, unresolved salt clusters. In contrast, the ion count obtained with the emitter with the smaller tip diameter is significantly lower (1.8×10^4). Signal from salt clusters at higher m/z is dramatically reduced and charge-state distributions for the monomer, dimer and tetramer of the protein, from which their respective masses can be determined, are obtained.

This document encompasses advice gained over years of experience pulling and using submicron diameter emitters. We hope that this aids in fostering discussion about the issues encountered when using submicron emitters and encourages their more widespread use in the analysis of proteins and protein complexes by native MS.

5.5 Acknowledgements

This material is based upon work supported by the National Science Foundation Division of Chemistry under grant number CHE-1609866 as well as a Graduate Research Fellowship (DGE-2146752). The authors are grateful for financial support from CALSOLV, and thank the staff at the University of California, Berkeley Electron Microscope Laboratory for advice on electrospray emitter imaging. The authors also thank the anonymous reviewers for their helpful suggestions.

5.6 References

(1) Susa, A. C.; Xia, Z.; Williams, E. R. Small Emitter Tips for Native Mass Spectrometry of Proteins and Protein Complexes from Nonvolatile Buffers That Mimic the Intracellular Environment. *Anal. Chem.* 2017, 89 (5), 3116–3122.
(2) Susa, A. C.; Xia, Z.; Williams, E. R. Native Mass Spectrometry from Common Buffers with Salts That Mimic the Extracellular Environment. *Angew. Chem., Int. Ed.* 2017, 56 (27), 7912–7915.
(3) Xia, Z.; Degrandchamp, J. B.; Williams, E. R. Native Mass Spectrometry beyond Ammonium Acetate: Effects of Nonvolatile Salts on Protein Stability and Structure. *Analyst* 2019, 144 (8), 2565–2573.
(4) Hu, J.; Guan, Q. Y.; Wang, J.; Jiang, X. X.; Wu, Z. Q.; Xia, X. H.; Xu, J. J.; Chen, H. Y. Effect of Nanoemitters on Suppressing the Formation of Metal Adduct Ions in Electrospray Ionization Mass Spectrometry. *Anal. Chem.* 2017, 89 (3), 1838–1845.
(5) Yuill, E. M.; Sa, N.; Ray, S. J.; Hieftje, G. M.; Baker, L. A. Electrospray Ionization from Nanopipette Emitters with Tip Diameters of Less than 100 nm. *Anal. Chem.* 2013, 85 (18), 8498–8502.
(6) Agasid, M. T.; Sørensen, L.; Urner, L. H.; Yan, J.; Robinson, C. V. The Effects of Sodium Ions on Ligand Binding and Conformational States of G Protein-Coupled Receptors-Insights from Mass Spectrometry. *J. Am. Chem. Soc.* 2021, 143 (11), 4085–4089.
(7) Xia, Z.; Williams, E. R. Effect of Droplet Lifetime on Where Ions Are Formed in Electrospray Ionization. *Analyst* 2019, 144 (1), 237–248.
(8) Jordan, J. S.; Williams, E. R. Effects of Electrospray Droplet Size on Analyte Aggregation: Evidence for Serine Octamer in Solution. *Anal. Chem.* 2021, 93 (3), 1725–1731.
(9) Jordan, J. S.; Williams, E. R. Homochiral Preference of Serine Octamer in Solution and Formed by Dissociation of Large Gaseous Clusters. *Analyst* 2021, 146 (22), 6822–6830.
(10) Chen, Y.; Yuan, S.; Liu, Y.; Huang, G. Rapid Desalting during Electrospray Ionization Mass Spectrometry for Investigating Protein-Ligand Interactions in the Presence of Concentrated Salts. *Anal. Chim. Acta* 2021, 1141, 120–126.
(11) Nguyen, G. T. H.; Bennett, J. L.; Liu, S.; Hancock, S. E.; Winter, D. L.; Glover, D. J.; Donald, W. A. Multiplexed Screening of Thousands of Natural Products for Protein–Ligand Binding in Native Mass Spectrometry. *J. Am. Chem. Soc.* 2021, 143 (50), 21379–21387.
(12) Báez Bolivar, E. G.; Bui, D. T.; Kitova, E. N.; Han, L.; Zheng, R. B.; Luber, E. J.; Sayed, S. Y.; Mahal, L. K.; Klassen, J. S. Submicron Emitters Enable Reliable Quantification of Weak Protein–Glycan Interactions by ESI-MS. *Anal. Chem.* 2021, 93 (9), 4231–4239.

(13) Nguyen, G. T. H.; Tran, T. N.; Podgorski, M. N.; Bell, S. G.; Supuran, C. T.; Donald, W. A. Nanoscale Ion Emitters in Native Mass Spectrometry for Measuring Ligand–Protein Binding Affinities. *ACS Cent. Sci.* 2019, 5 (2), 308–318.
(14) Nguyen, G. T. H.; Nocentini, A.; Angeli, A.; Gratteri, P.; Supuran, C. T.; Donald, W. A. Perfluoroalkyl Substances of Significant Environmental Concern Can Strongly Inhibit Human Carbonic Anhydrase Isozymes. *Anal. Chem.* 2020, 92 (6), 4614–4622.
(15) Saha-Shah, A.; Weber, A. E.; Karty, J. A.; Ray, S. J.; Hieftje, G. M.; Baker, L. A. Nanopipettes: Probes for Local Sample Analysis. *Chem. Sci.* 2015, 6 (6), 3334–3341.
(16) Mortensen, D. N.; Williams, E. R. Ultrafast (1 μs) Mixing and Fast Protein Folding in Nanodrops Monitored by Mass Spectrometry. *J. Am. Chem. Soc.* 2016, 138 (10), 3453–3460.
(17) Sutter Instrument Company. P-87 Flaming/Brown Micropipette Puller Operation Manual, Rev. 0299c. 2008.
(18) Nguyen, G. T. H.; Leung, W. Y.; Tran, T. N.; Wang, H.; Murray, V.; Donald, W. A. Mechanism for the Binding of Netropsin to Hairpin DNA Revealed Using Nanoscale Ion Emitters in Native Mass Spectrometry. *Anal. Chem.* 2020, 92 (1), 1130–1137.
(19) Panczyk, E. M. Tip Pulling - Nanoelectrospray Capillary Preparation for Native MS. 2019.
(20) Kenderdine, T.; Xia, Z.; Williams, E. R.; Fabris, D. Submicrometer Nanospray Emitters Provide New Insights into the Mechanism of Cation Adduction to Anionic Oligonucleotides. *Anal. Chem.* 2018, 90 (22), 13541–13548.
(21) Oesterle, A. TECHNOTES: What is “Filamented” Glass & Who Needs It? https://www.sutter.com/PDFs/technote_FilamentGlass.pdf (accessed 2021 -11 -23).
(22) Mortensen, D. N.; Williams, E. R. Surface-Induced Protein Unfolding in Submicron Electrospray Emitters. *Anal. Chem.* 2016, 88 (19), 9662–9668.
(23) Xia, Z.; Williams, E. R. Protein-Glass Surface Interactions and Ion Desalting in Electrospray Ionization with Submicron Emitters. *J. Am. Soc. Mass Spectrom.* 2018, 29 (1), 194–202.

5.7 Figures

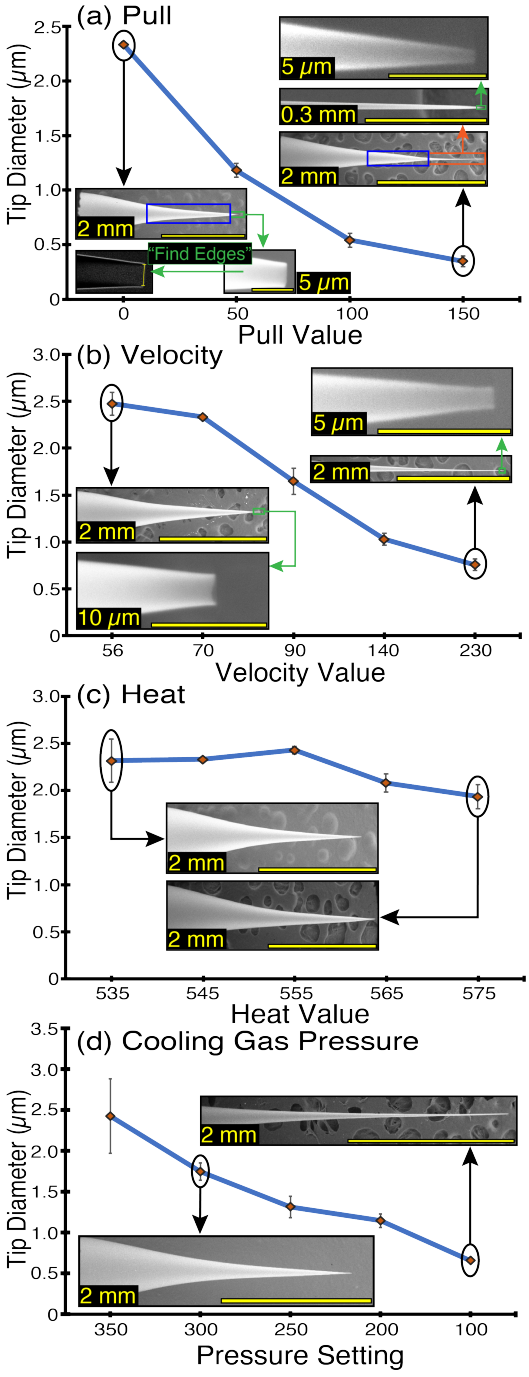

Figure 5.1. The effect of tip puller parameters on the resulting inner diameter of the nESI tip: (a) Pull, (b) Velocity, (c) Heat, (d) Cooling Gas Pressure. Insets show the emitter morphology and close-up views of the tips. Numbers in yellow denote the size of the scale bars.

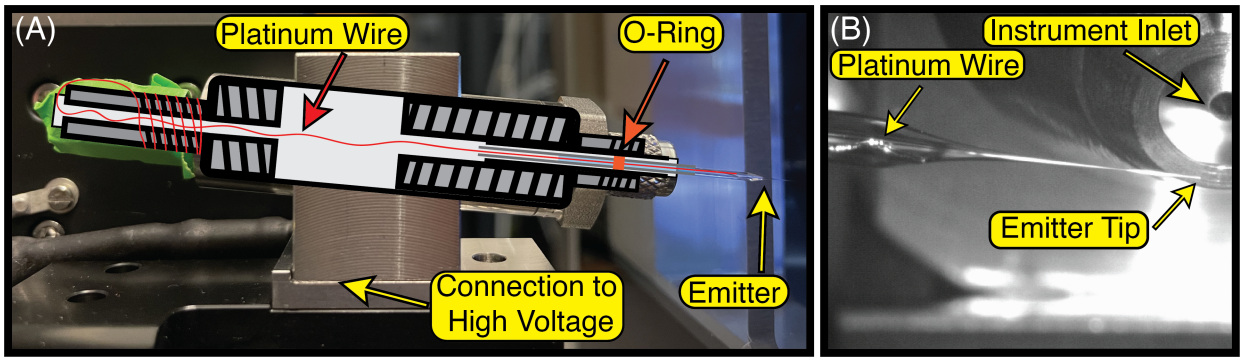

Figure 5.2. Photographs of (a) a Waters source block with a graphic cutaway illustrating the connection of the high voltage from the power supply to the solution by means of a platinum wire that is inserted into the solution and (b) a close-up view of an electrospray emitter with a 220 nm diameter tip and with a platinum wire inserted that is aligned to the inlet of a Waters Q-TOF Premier mass spectrometer used to obtain the data shown in Figure 3.

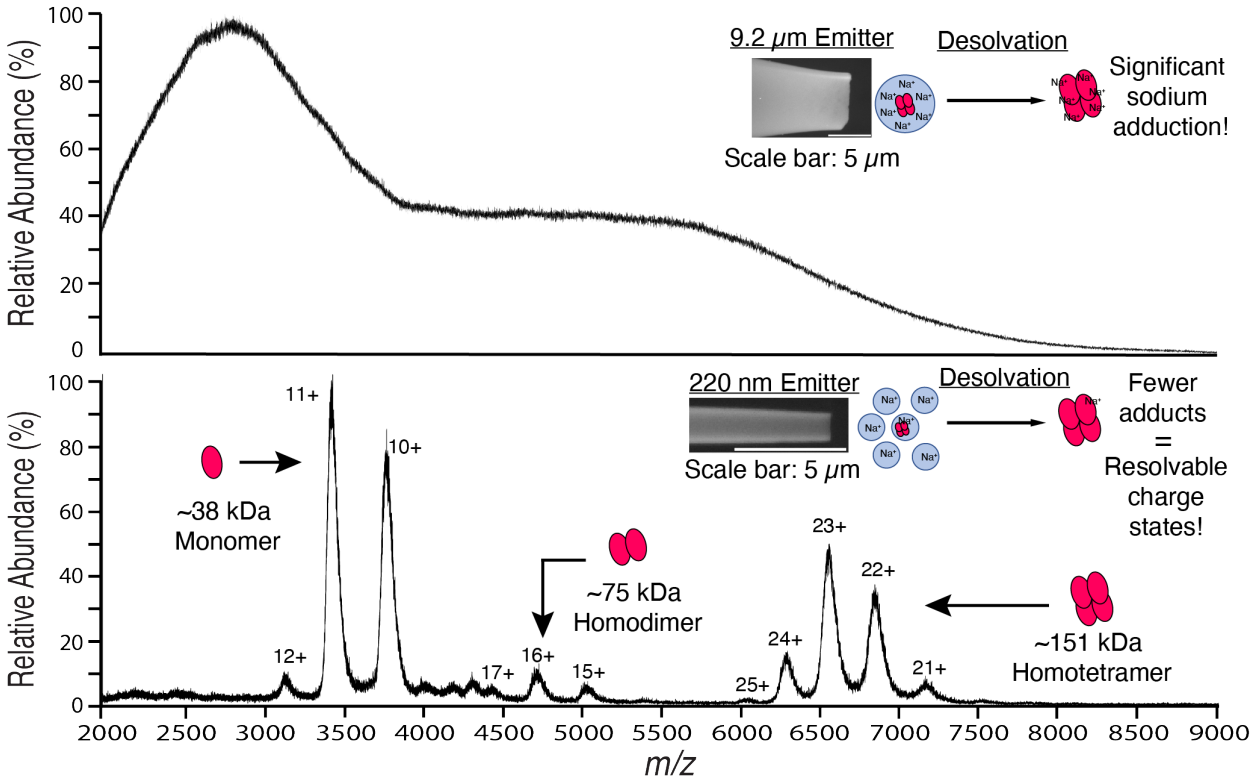

Figure 5.3. Electrospray mass spectra of 10 μM yeast alcohol dehydrogenase in 150 mM NaCl/25 mM Tris buffer solution (titrated to pH = 6.8) obtained using an emitter with a 9.2 μm (top) or 220 nm (bottom) diameter tip obtained with electrospray voltages of 1.1 kV and 0.5 kV, respectively. In both cases, spectra were acquired at the lowest voltage where consistent signal was obtained.

Table 5.1. Average Diameters and Standard Deviations (S.D.) of Electrospray Emitters Prepared Using Various Parameters in Order of Descending Emitter Diameter

Heat	Pull	Velocity	Time	Pressure	Average Diameter (µm)	S.D. (µm)
545	0	56	235	300	2.48	0.12
555	0	70	235	300	2.43	0.040
545	0	70	235	350	2.43*	0.46
545	0	70	235	300	2.33	0.021
535	0	70	235	300	2.32	0.23
565	0	70	235	300	2.08	0.097
575	0	70	235	300	1.94	0.13
545	0	70	235	300	1.75*	0.10
545	0	90	235	300	1.65	0.14
545	0	70	235	250	1.31*	0.13
545	50	70	235	300	1.18	0.064
545	0	70	235	200	1.15*	0.083
580	0	230	235	300	1.06	0.037
545	0	140	235	300	1.03	0.064
545	0	230	235	300	0.756	0.059
545	0	70	235	100	0.655*	0.029
580	175	230	235	300	0.550	0.022
545	100	70	235	300	0.542	0.062
545	150	70	235	300	0.350	0.049
580	200	230	235	300	0.250	0.010
580	250	230	235	300	0.223	0.008

* Diameters marked with asterisk were measured approximately 6 months after other sizes.

Chapter 6

Lighting Up at High Potential: Effects of Voltage and Emitter Size in Nanoelectrospray Ionization

This chapter is reproduced with permission from:

Jacob S. Jordan, Zachary M. Miller, Conner C. Harper, Emeline Hanozin, Evan R. Williams

"Lighting Up at High Potential: Effects of Voltage and Emitter Size in Nanoelectrospray Ionization"

Journal of the American Society for Mass Spectrometry, **2023**, *34*(6):1186-1195

6.1 Abstract

Effects of electrospray emitter voltage on cluster size and abundance formed from aqueous CsI were investigated with emitter tip diameters between 260 ± 7 nm and 2.45 ± 0.30 μm. Cluster size increases with increasing voltage, increasing solution concentration and increasing emitter diameter consistent with formation of larger initial droplet sizes. For emitters with tip diameters above ~1 μm, varying the voltage either up or down leads to reproducible extents of cluster formation. In contrast, higher voltages with submicron diameter emitters can lead to only Cs^+ and $Cs(H_2O)^+$ and no clusters. This change in ion formation reproducibly occurs at spray potentials >1.3 kV for 260 nm emitters and appears to be induced by a corona discharge and material build-up at the emitter tip. Under conditions where abundant Cs^+ is observed and no clusters are formed, ions such as K^+ and Cu^{1+} are also observed but ions with more negative solvation energies, such as Ba^{2+}, are not. Similarly, ions from bradykinin and ubiquitin are observed pre-discharge but not post discharge. Ions with more positive solvation energies can desorb directly from the air-water interface that is created at the tip of these emitters whereas ions with more negative solvation energies as well as peptide and protein ions do not. These results indicate that ion desorption directly from solution can occur and similar experiments with even smaller emitters may lead to new insights into ion formation in electrospray ionization.

6.2 Introduction

The nanoflow regime of electrospray ionization (<1 μL min^{-1} flow rates) can lead to higher ionization efficiency and lower sample consumption than conventional electrospray ionization that

uses large bore capillaries.[1,2] Nanospray also enables more reproducible ion formation from solvents that have high surface tension, most notably aqueous solutions that contain volatile buffers.[1,2] These advantages make nanospray an indispensable technique in native mass spectrometry. Nanospray emitters that have tips with inner diameters <1 μm have some additional advantages, including the ability to obtain charge-state resolved spectra of proteins and other molecules in standard biochemical buffers, such as Tris or 1x phosphate buffered saline solutions, that contain high concentrations of nonvolatile salts (e.g., ≥150 mM NaCl).[3–6] The initial droplet size formed by submicron emitters is less than 100 nm.[4,7–9] At an initial droplet diameter of 100 nm, there will be, on average, only one analyte molecule per droplet at concentrations below 3 μM.[10] At even lower concentrations or droplet diameters, the majority of nanodrops will not contain an analyte molecule. Under these conditions, nonvolatile salts are separated from analytes because most of the salts partition into nanodrops that do not contain an analyte ion. Nonspecific aggregation of analytes within the ESI droplet can also be reduced or prevented using sufficiently small diameter emitters. Narrow bore emitters have been used to investigate small molecule clusters,[10,11] as well as ligand-protein,[12–18] ligand-DNA,[19,20] and protein-protein[21] complexes without interference from nonspecific aggregation during the ESI process.

The diameters and size distribution of droplets that are initially formed in electrospray depends on many factors, including solution composition and surface tension,[22,23] viscosity,[24,25] conductivity,[23,26,27] sheath gas flow,[28,29] electrospray voltage,[22,23,26,30,31] capillary diameter,[23] distance from the capillary to the instrument inlet,[23] spray mode,[23,32] and solution flow rate.[22] Droplets produced during ESI from larger diameter capillaries (>20 μm) can be characterized using optical methods, including phase doppler anemometry/interferometry, flash shadowgraphy, or microscope imaging and are typically on the 1 – 100 μm size scale across a range of solution and electrospray conditions.[23] Lower solution flow rates[22,33–36] and lower electrospray voltages[26,30,37] have been correlated with the production of smaller initial droplet sizes, although some deviations from this trend have been noted due to changes in the spray mode at different spray potentials.[37]

The initial nanodrops that are produced by nanoelectrospray ionization (nESI) emitters with tip diameters of a few microns or less are too small to size using standard optical methods, but some information about size and size distributions has been obtained from more indirect methods. Davidson *et al.* combined charge reduction with differential mobility analysis to determine the size of sucrose clusters formed from an aqueous sucrose solution with emitters that had 1 – 3 μm diameter tips.[7] From these results, they concluded that the initial droplet size was ~60 nm, or ~1/17th the emitter tip diameter. The average droplet diameter increased to ~500 nm with an increase in spray voltage from 0.8 kV to 1.5 kV. The initial size of droplets from nanospray emitters with small diameter tips was also estimated based on trends in sodium adduction to a protein as a function of emitter tip size. Sodium adduction to protein ions significantly decreases when there is less than one protein molecule per droplet, from which an estimate of the initial ESI droplet diameters of ~1/14th – 1/20th the emitter tip diameter was reported.[4] Calculations from Li *et al.* based on the measured flow rate and ionization current from submicron tips also resulted in droplet diameters that were 1/6th – 1/32nd the emitter diameter.[9] This relationship between tip diameter and droplet diameter also appears to be true for solvents other than water. Cooks and coworkers formed droplets containing rhodamine B onto a glass coverslip and used fluorescence microscopy to investigate the droplet sizes produced from a solution of 9:1 methanol:glycerol with ~5 μm, ~10 μm, and ~20 μm diameter emitters.[8] The droplet size distribution from ~5 μm emitters at 1.5 kV spray voltage was broad with a center at 335 nm, or ~1/15th the emitter diameter, and the droplet diameter increased with increasing spray voltage to 463 nm at 2.5 kV. Droplets produced from ~10

μm and ~20 μm diameter emitters were larger than those produced from ~5 μm emitters.[8] These and other results indicate that there is a clear trend toward smaller initial droplet sizes with decreasing emitter tip sizes and larger initial droplet sizes with increasing spray voltage.

Here, effects of both voltage and emitter tip diameter are investigated for emitters with inner diameters between 260 ± 7 nm and 2.45 ± 0.30 μm. Emitters with diameters above ~1 μm show expected trends in ion formation as a function of emitter tip size and voltage whereas emitters with tip diameters below ~1 μm show unusual behavior when the electrospray voltage exceeds a threshold value that is commonly used with the larger emitters. Corona discharge and a change in ion formation mechanism after discharge provides insights into different ways that ions can be formed with electrostatic potentials.

6.3 Experimental Methods

Borosilicate nanoelectrospray emitters (1.0 mm outer diameter, 0.78 mm inner diameter, with filament, Part #BF100-78-10, Sutter Instrument, Novato, CA) were pulled to final inner diameters of 260 ± 7 nm, 608 ± 17 nm, 1.75 ± 0.11 μm, and 2.45 ± 0.30 μm using a Sutter Instrument Flaming/Brown P-87 pipette puller.[38] Emitters were imaged without sputter coating using a Hitachi TM-1000 scanning electron microscope (Tokyo, Japan) at the Electron Microscopy Laboratory at the University of California, Berkeley.

All mass spectral data were acquired using a Waters Q-TOF Premier mass spectrometer (Milford, MA). The pressure of argon in the collision cell was ~4 mbar and the sample cone, extraction cone, and ion guide voltages were 20.0 V, 2.0 V, and 2.0 V, respectively. A microscope consisting of a Dino-Lite digital camera and an objective lens (Olympus CK20, Tokyo, Japan) was mounted to the source region of the mass spectrometer to monitor emitter tips during electrospray. Emitters were positioned ~3 mm from the instrument inlet and a voltage between 0.4 kV and 1.5 kV was applied to a platinum wire that was in contact with an aqueous solution of 10 mM or 100 μM CsI (Sigma-Aldrich, St. Louis, MO). The voltage was increased or decreased in increments of 100 V every 15 s and the cluster distribution was measured as a function of spray voltage. All data were analyzed using MassLynx v. 4.1.

The emitter flow rate was determined by measuring the mass of the emitter loaded with ~10 μL of solution using an Ohaus Analytical Plus balance (Parsippany, NJ) before and after electrospray at a voltage of 1.0 kV for 5 minutes.[39] To measure the solution flow rate after corona discharge, the spray voltage was increased to ~1.5 kV until corona discharge was observed and then reduced back to 1.0 kV for 5 minutes followed by a mass measurement. To measure mass loss due to evaporation, the mass of the emitter and solution was measured before and after 5 minutes in the source with no spray voltage applied. The same emitter was used for measuring the mass loss due to evaporation, during electrospray, and after corona discharge to reduce variability caused by tip-to-tip differences in size and shape. Reported flow rates are the average of three replicate experiments.

Solutions of 10 mM tetraethylammonium chloride (TEACl), RbCl, KCl, NaCl, LiCl, CuCl (saturated solution), and $BaCl_2$ were mixed 1:1 with 10 mM CsCl (final concentration of 5 mM each) in MilliQ water. Bradykinin and ubiquitin solutions were prepared in 1:1 $BaCl_2$:CsCl (5 mM each) to a final peptide or protein concentration of 10 μM. All reagents were obtained from Sigma-Aldrich and were used without further purification.

6.4 Results and Discussion

6.4.1 Effects of Emitter Tip Size and Voltage on CsI Cluster Distributions

The effects of nanoelectrospray emitter tip size and electrospray voltage on the formation of CsI clusters formed from either 100 μM or 10 mM aqueous solutions was investigated with emitters that have tip diameters between 260 ± 7 nm and 2.45 ± 0.30 μm and with electrospray voltages between 0.4 kV and 1.5 kV. At a given emitter tip diameter and solution concentration, higher spray voltage results in greater abundances of $[Cs_nI_{n-x}]^{x+}$ (x = 1, 2, 3). This effect is illustrated for singly charged clusters formed from a 10 mM aqueous CsI solution using an emitter with a 2.45 μm diameter tip (Figure 1a). Cs^+ and cluster ion abundances were normalized to the total mass of Cs by weighting each cluster abundance by the number of Cs atoms in the cluster (e.g., Cs_2Cl abundance multiplied by two, Cs_3Cl_2 abundance multiplied by three). The abundance of the Cs^+ ion decreases from 8.4 ± 2.3% of the Cs mass at 0.7 kV to 3.4 ± 0.4% at 1.5 kV. The fraction of singly charged clusters relative to multiply charged clusters decreases from 74.0 ± 2.0% to 59.1 ± 1.7% of the total Cs mass at these respective spray voltages reflecting the shift in the population to larger clusters (Figure 1a) that are more highly charged. The cluster abundances shift to smaller size as voltage is reduced from the maximum of 1.5 kV (Figure 1a) and the results at each voltage are highly reproducible. The difference between the abundance of Cs^+ at 1.0 kV on the increasing and decreasing voltage ramp is only ~0.1%. A similar trend occurs for emitters with diameters of 1.75 μm, 608 nm, and 260 nm (Figure 1b, 1c, 1d, respectively) when the initially low voltage is increased. For 260 nm emitters, Cs^+ is 47.6 ± 3.7% and 15.3 ± 6.0% of the total Cs mass at 0.4 kV and 1.1 kV, respectively. The fractional mass of singly charged clusters increases from 52.0 ± 1.4% to 64.4 ± 3.2%, and the fraction of multiply (+2, +3) charged clusters increases from 0.4 ± 0.5% to 21.1 ± 15.2% across the same range of spray voltages. The higher uncertainty in the fraction of multiply charged clusters produced from 260 nm tips may be related to changes in the electrospray mode that occur when spraying from submicron emitters (Figure 1c,d).

CsI is highly soluble in water (848 g/L or ~3.3 M at 25 °C)[40] so extensive clustering or ion pairing in solution at the original solution concentrations is not expected. Both emitter tip size and voltage can affect the initial droplet size that is formed by electrospray with larger emitters and higher voltages leading to higher solution flow rates and larger initial droplet sizes.[7,8] Solvent evaporation can lead to nonspecific aggregation and cluster formation in the ESI droplet prior to gaseous ion formation resulting in formation of salt clusters.[7,10,41] The abundances and maximum size of these clusters can indicate the original size of an ESI droplet.[7] The population and size of clusters decreases with emitter tip size at 1.0 kV, consistent with smaller emitters producing smaller

initial droplet sizes and hence less clustering (Figure 1a, 1b, 1c, 1d). At the lowest spray voltage for each emitter size and 100 μM concentrations, Cs^+ is >90% of the total Cs mass across all tip sizes compared to values of 8.4 ± 2.3%, 7.7 ± 5.1 %, 54.4 ± 5.2% and 47.6 ± 3.7% from 2.45 μm, 1.75 μm, 608 nm, and 260 nm at 10 mM concentrations, respectively (Figure S1). These data are consistent with fewer CsI ions within each initially formed electrospray droplet at lower solution concentrations, smaller emitter tip diameters, and at lower electrospray voltages. All of these factors reduce non-specific cluster formation or aggregation during ESI owing to the formation of smaller initial droplets.

For emitters with tips larger than 1 μm, the change in cluster distributions with increasing voltage were the same as those observed when the voltage was decreased (Figures 1a, 1b). However, for emitters with diameters smaller than 1 μm, decreasing the voltage after reaching 1.5 kV results in the disappearance of CsI clusters from the mass spectra (Figures 1c, 1d). With the 608 nm emitters, increasing the spray voltage from 0.8 kV to 1.5 kV can lead to a large drop (typically ~50-80%) in the total ion signal (Figure 2a, between points labeled B and C). The time at which this drop in current occurs upon reaching voltages >0.8 kV is highly variable between emitters, with the fastest occurring immediately upon reaching 0.8 kV (~1.1 min from the start of spray) and the latest occurring upon a second ramp in voltage at 0.9 kV (~7 min from start of spray). This reduction in current occurred upon the first voltage ramp in 12 out of 15 replicates with different 608 nm emitters, typically at voltages of ~1.0 – 1.5 kV. In contrast, this drop in current occurred for every 260 nm emitter upon the first voltage ramp. Across all experiments using submicron diameter tips, the onset voltage for ion formation (0.4 kV) is not significantly different before and after this transition (Figure S2). The change in ion current between ~1.3 – 2.2 min (Figure 2a) is likely a result of a change in the spraying mode. Abundant CsI clusters are observed during this time period. When spraying 10 mM CsI from 608 nm diameter emitters at 1.2 kV, abundant CsI clusters were observed prior to this drop in current (Figure 2b). After this transition, there is abundant Cs^+ and some $Cs(H_2O)^+$ but no clusters of CsI (Figure 2c). Experiments were performed under gentle conditions to minimize gas-phase dissociation, as demonstrated by the abundant water adduct to Cs^+ at *m/z* ~151 (Figure 2b and 2c). Dissociation of this ion results in formation of Cs^+ confirming the identity of this ion.

In order to determine if the large drop in ion current initiated by higher voltages in the emitters with the small tips is accompanied by a change in the solution flow rate, the flow rate of a 608 nm emitter was determined by measuring the change in the mass of the emitter over 5 min while spraying at 1.0 kV.[42–44] Solvent loss also occurs due to evaporation, the rate of which can be determined from changes in mass without an applied voltage. Solvent evaporation occurs at a rate of 2.0 ± 0.2 nL min^{-1}. The flow rates before and after the significant drop in total ion current with voltage applied after subtracting the water lost to evaporation were 5.0 ± 3.6 nL min^{-1} and 0.1 ± 0.3 nL min^{-1}, respectively. The higher uncertainty during standard spray is due to variations in flow from the different emitters and could be due to small differences in emitter position or morphology, which are not factors in evaporative loss. After the transition, the mass loss due to solution flow is indistinguishable from the evaporation rate, yet the abundance of the Cs^+ ion indicates that ion formation from the emitter still occurs.

6.4.2 Imaging submicron diameter emitters during electrospray

Emitter tips were visually monitored during electrospray using a Dino-Lite digital microscope camera (50x maximum magnification) and a 20x objective lens mounted to the mass spectrometer source housing. Ions were formed from a 10 mM aqueous CsI solution and emitters with a tip diameter of 608 nm at voltages between 0.8 and 1.5 kV. Below 1.0 kV, the emitter tips are clear (Figure 3a). The large drop in the total ion current corresponds to what appears to be the onset of corona discharge at the end of the emitter (Figure 3b, supporting video 1). Light emission is commonly observed at the onset of corona discharge initiated at high voltages.[45–47] Material is observed at the end of the emitter after discharge occurs (Figure 3c, supporting video 1). Scanning electron microscopy images of these emitters after drying overnight indicate that there is no observable change to the inner diameter of the emitters (Figure 3d). The resolution of the SEM at 10000x magnification is ~16.3 nm/pixel, indicating that any changes to the tip size and shape that may have occurred are less than ~16 nm. The image shows material at the end of the capillary, consistent with what was observed optically after discharge. However, crystallized CsI after water evaporation may also contribute significantly to the deposited material in this image.

The SEM data indicate that the corona discharge process does not irreversibly damage the emitters, but that material build-up at the end of the emitter disrupts the spray process. This material appears after corona discharge even when a blank containing just pure milliQ water was used. Passing the milliQ water through a 0.22 μm filter did not affect the appearance of this material indicating that if any microorganisms or particles larger than this are present in the water, they do not contribute to this material buildup. Increasing the spray voltage by ~500 V can dislodge the material, restoring spray along with formation of clusters.

The abundant signal for Cs^+ post-discharge shows that ions are still generated from the ESI emitter despite a flow rate too low to measure. The disappearance of CsI clusters indicates that larger droplets capable of containing multiple Cs^+ and I^- are not being formed consistent with the unmeasureable flow rate. The discharge may partially block the aperture of the emitter with debris, resulting in the production of small droplets such that each droplet contains few ions preventing the formation of CsI clusters. Ions can also be produced by desorption from crystals. In field desorption mass spectrometry (FD-MS), ions are produced by applying a high voltage (8 – 20 kV) and heat (>100 °C) to crystalline samples deposited onto a filament. For inorganic salts, the most abundant ions tend to be the bare cation and clusters of the form $[C + (CA)_n]^+$, where C and A are the cation and anion, respectively.[48,49] Schulten and Rollgen observed clusters with up to six sodium acetate molecules are formed from sodium acetate crystals and Rollgen *et al.* reported $Ca_2Cl_2^{2+}$ in FD mass spectra of $CaCl_2$ crystals.[48,50] The absence of cluster ions after corona discharge from submicron emitters suggests that the ions are not desorbed from a solid crystal.

A change to the emitter opening may also affect the electric field at the air-water interface, potentially resulting in the desorption of ions directly from the tip of the emitter. In this case, the abundance of ions after discharge are expected to follow trends in the solvation energy of the cations. To investigate this apparent desorption process after corona discharge, solutions containing Cs^+ and other cations of varying solvation energies were formed by electrospray and the abundance of these cations before and after discharge were compared.

6.4.3 Effects of Ion Solvation

nESI mass spectra of an aqueous solution containing $BaCl_2$ and CsCl from an emitter with a 608 nm tip show abundant $Ba(H_2O)_{0\text{-}4}^{2+}$ in addition to clusters of the form $Cs_nCl_{n-1}^+$, $Ba_nCl_{2n-1}^+$, $Ba_nCl_{2n-2}^{2+}$ and mixed clusters containing both Ba^{2+} and Cs^+ (Figure 4a). After discharge is induced at a voltage of 1.5 kV, Cs^+ and $Cs(H_2O)^+$ are over 97% of the ion signal and no Ba^{2+} or Ba-containing cluster ions are detected (Figure 4b). Some minor peaks (<2.5% of the total ion abundance) are attributed to Cs-adducted background organic contaminants also present in the solvent blank, which may contribute to material build up at the end of the emitter. The abundances of Ba^{2+} and $Ba(H_2O)_{1\text{-}4}^{2+}$ relative to the abundances of Cs^+ and $Cs(H_2O)^+$ before and after discharge were determined. This value prior to discharge was 2.66 and after discharge was less than 1.46 x 10^{-4}. The value after discharge is an upper limit determined from the noise level in these spectra. The ratio of these values before and after discharge, abbreviated as the ratio of relative abundances (RRA), is <0.00035. The absence of detectable Ba^{2+} and $Ba(H_2O)_{1\text{-}4}^{2+}$ after discharge indicates that droplets are not formed, yet abundant Cs^+ signal shows that selective ion formation still occurs. The Gibbs solvation free energy (GSFE) of Cs^+ is 800 kJ mol^{-1} compared to -200 kJ mol^{-1} for Ba^{2+} (all values are referenced to H^+),[51] indicating that the energetic cost to remove Ba^{2+} from water is substantially larger than for Cs^+. These data are consistent with desorption of Cs^+ directly from solution at the tip of the emitter whereas Ba^{2+} is retained in water due to its more negative GSFE value.

Tetraethylammonium, TEA^+, has a higher Gibbs solvation free energy (GSFE = 1050 kJ mol^{-1})[51] than Cs^+. A nESI spectrum of an equimolar aqueous solution of TEACl and CsCl obtained using emitters with 608 nm tip diameters results in TEA^+, Cs^+ and $Cs(H_2O)^+$ in nearly equal abundances (Figure S3a). Singly charged clusters with CsCl and TEACl are also observed. After discharge, TEA^+, Cs^+ and $Cs(H_2O)^+$ are the dominant ion signal (Figure S3b) and no clusters are observed. The RRA_{TEA} value of 0.77 indicates that TEA^+ relative to Cs^+ does not change significantly after discharge. There are many differences in the physical properties of Ba^{2+} compared to TEA^+, but the striking difference in RRA values for Ba^{2+} (<0.00035) compared to TEA^+ (0.77) suggests that this may be due to a large difference in GSFE values (~1250 kJ mol^{-1}).

The effects of Gibbs solvation free energy on RRA values for cations with intermediate GSFE values were investigated. Results for Rb^+, K^+, Na^+, Li^+, and Cu^{1+}, along with Cs^+, Ba^{2+}, and TEA^+ are shown in Figure 5. Results for ions with low *m*/*z* are more challenging to detect in the Q-TOF instrument due to poor transmission efficiency. To account for this, the instrument settings were tuned to favor lower *m*/*z* ions and favor the transmission of hydrated clusters that have higher *m*/*z* by increasing the sample cone voltage. The GSFE value for Rb^+ (GSFE = 775 kJ mol^{-1})[51] is similar to Cs^+ and Rb^+ has a RRA of ~1 (Figure 5, Figure S4). RRA values for K^+ (GSFE = 755 kJ mol^{-1}), Na^+ (GSFE = 685 kJ mol^{-1}) and Li^+ (GSFE = 575 kJ mol^{-1}) determined from the abundances of $X(H_2O)_{0\text{-}4}^+$ (X = K, Na, Li) are 0.97, 1.03, and 1.00 respectively (Figures S5, S6, and S7, respectively).[51] The RRA for Cu^{1+} (GSFE = 521 kJ mol^{-1})[51] determined from the abundances of $Cu(H_2O)_{0\text{-}3}^{1+}$ is 0.28, suggesting that this ion is near the energetic threshold for desorption (Figure S8). A corona discharge reproducibly occurred at ~0.7 kV with the CuCl:CsCl solution. This may be related to the saturated concentration of CuCl that was used in these samples. The presence of undissolved solids or crystallization near the tip of the emitter could create an irregular surface more prone to corona discharge at lower voltages. Further increasing the spray voltage from 0.7 kV to 1.5 kV resulted in no significant change in the RRA. Ions corresponding to $Cu(H_2O)_{0\text{-}2}(OH)^+$ were also observed before and after discharge with an RRA of 0.21. No doubly charged copper or copper clusters (GSFE = -960 kJ mol^{-1})[51] were observed, consistent with results from Ba^{2+} that indicate doubly charged ions do not desorb from the emitter due to more negative solvation

energies. These data suggest that $Cu(II)(OH)^+$ desorbs from the emitter as a singly charged ion and likely has a similar GSFE to Cu^+. Ions with GSFE values higher than ~540 kJ mol^{-1} (where the RRA = 0.5 between Cu^{1+} and Li^+) are formed both before and after discharge occurs whereas below this value, ions are significantly suppressed or eliminated after discharge occurs.

After discharge, the absence of cluster ions and ions that have GSFE values below ~540 kJ mol^{-1} indicates that droplets are no longer being formed. If droplet formation still occurred after discharge, then ions with low GSFE values should still incorporate into the droplets and result in ion formation. The absence of these ions and cluster ions indicates that ions with GSFE values above ~540 kJ mol^{-1} are formed by desorption directly from the emitter after discharge. To desorb, ions must overcome an energy barrier due to the GSFE. Energy related to any surface deformation that may be necessary to emit ions also contributes to this energetic barrier. High electric fields at the air-water interface, which depend on interface size and applied voltage, may drive this process. After corona discharge, the appearance of material at the end of the emitter could reduce the effective diameter of the emitter or may lead to uneven surface morphology that may promote distortion of water at the interface. In both cases, the result is a much larger effective electric field at the air-water interface, which may drive desorption directly from the solution contained within the emitter without the formation of nanodroplets. Thomson and Iribarne[52] noted that multiply charged cations showed no evidence of evaporation, consistent with the more negative solvation energies of these analytes.[51]

Cooks and coworkers have suggested that the strong electric fields and irregular morphology at the tip of paper emitters could cause ions to desorb from solution during paper spray ionization.[53,54] It is possible that a similar mechanism occurs for submicron emitters due to material build-up at the emitter tip after corona discharge, which may form an irregular surface with strong electric fields at the tip that allows ions to desorb directly from solution.

6.4.4 Desorption of peptides and proteins from a charged air-liquid interface

In order to investigate whether desorption of peptides and proteins can also occur directly from charged air-water interfaces, mass spectra of aqueous solutions of 5 mM $BaCl_2$, 5 mM CsCl and 10 μM bradykinin or ubiquitin were acquired using emitters with 608 nm diameter tips both pre- and post-corona discharge. The presence or absence of Ba^{2+} in the mass spectra along with the presence or absence of $Cs(CsCl)_n^+$ was used to indicate whether droplets were formed after discharge. For solutions with bradykinin, both Ba^{2+} and $Cs(CsCl)_n^+$ are observed at voltages below 1 kV indicating that ion formation from droplets occurs. Protonated, Cs-adducted, and Ba-adducted bradykinin ions with charge states between +1 and +3 are also observed (Figure 6a). Cs- and Ba-adduction to bradykinin only occurs for the +2 and +3 charge states. Increasing the spray voltage to ~1.3 kV induced corona-discharge. After discharge, there are no bradykinin ions of any form, nor are Ba^{2+} or $Cs(CsCl)_n^+$ formed. However, abundant Cs^+ and $Cs(H_2O)_1^+$ are observed indicating selective ion formation continues after the discharge (Figure 6b). After discharge, several ions corresponding to Cs-adducted organic contaminant ions are also observed at low abundance (<10% relative to Cs^+) as confirmed by MS/MS experiments. These results indicate that under conditions where Cs^+ appears to readily desorb from the emitter tip after discharge, bradykinin ions do not. Prior measurements during sustained corona discharge for large metal

electrospray emitters indicate that there can be more consistent peptide signal during the discharge, but the spectra are otherwise unaffected.[45]

Similar results were obtained from these same experiments where ubiquitin was added in place of bradykinin. Prior to discharge, ubiquitin ions with charge states between +5 and +8 and extensive Cs-adduction are observed (Figure 6c). After discharge, there are no ubiquitin ions, Ba^{2+} or $Cs(CsCl)_n^+$ but abundant Cs^+ and $Cs(H_2O)_{1,2}^+$ remain (Figure 6d). The absence of protein ion signal after discharge indicates that ubiquitin does not desorb from solution at the tip of the emitter under the voltages and tip diameters employed here (Figure 6c,d). It has been speculated that proteins can desorb directly from the air-water interface from much larger emitters at higher spray voltages.[55] Li *et al.* reported the disappearance of cytochrome *c* signal during femtoelectrospray of a mixture of cytochrome *c* and the peptide MRFA from 30 – 160 nm emitters at spray voltages between 0.4 – 2.0 kV.[9] Interestingly, solvent evaporation was not blocked and MRFA signal was still observed after the loss of protein signal. This effect was attributed to size-selective partial clogging of the emitter that preferentially filtered out larger protein molecules. The ionic diameters of Cu^{1+}, Ba^{2+}, Cs^+, TEA^+, bradykinin, and ubiquitin are ~0.09 nm (coordination II),[56] ~0.27 nm (coordination VI),[56] ~0.33 nm (coordination VI),[56] ~0.77 nm,[57] ~1.14 nm (approximated from calculated topological surface area and assuming a sphere), and ~2.64 nm (native form, calculated from radius of gyration),[58] respectively. Ba^{2+} and Cu^{1+} are among the smallest ions, yet they have the lowest RRA values. The hydrated diameter of ions can be significantly larger than the ionic diameter. The hydrated diameter of Ba^{2+} (0.81 nm)[59], is nearly the same as that of TEA^+ (0.80 nm),[59] yet these two ions have significantly different RRA values of ~0 and ~0.77, respectively. These data indicate that size-selective partial clogging of the emitters is not the cause for the absence of Ba^{2+} or peptide and protein signal in our experiments. The high solubility limit of ubiquitin and bradykinin (>1 mM) suggests that these molecules have significant negative solvation energies, consistent with desorption being an unfavorable process for their transfer into the gas-phase.

6.5 Conclusions

The electrospray voltage and emitter tip diameter have a significant effect on the size distribution of CsI clusters indicating a significant effect on the size of the initial droplets that are formed. The least clustering occurs at the lowest voltage where stable spray is obtained at any tip size and clustering increases with larger diameter tips and higher solution concentrations. Changing the voltage on emitters with tip diameters greater than ~1 μm leads to a reproducible change in cluster size independent of raising or lowering the voltage between 0.4 kV and 1.5 kV. In contrast, corona discharge reproducibly occurred for emitters with 260 nm diameter tips at voltages >1.2 kV. Material deposition at the emitter tip occurs and leads to a flow rate that is too low to measure despite continued formation of Cs^+ but no CsI clusters. Under these conditions, ions such as Ba^{2+} are not observed nor are ions of bradykinin or ubiquitin which are readily ionized pre-discharge. These results indicate that ions with more positive solvation energies can be desorbed directly from the solution-air interface whereas those with negative and less positive (<540 kJ mol^{-1}) solvation energies are not.

Results from some molecular dynamics simulations indicate that peptides and proteins can be desorbed from charged droplets either as an extended chain or as intact, folded complexes.[60–62]

Our results indicate that under conditions where ion desorption from the liquid-air interface occurs for Cs^+, Rb^+, K^+, Na^+, Li^+ and Cu^+, desorption of peptides and proteins does not occur consistent with a large negative solvation energy for these ions. Future work with emitters with even smaller tip diameters may shed additional light into ion formation mechanisms in electrospray ionization.

6.6 Acknowledgments

The authors thank Dr. Anthony T. Iavarone for help with instrumentation and insightful discussions, as well as the staff at the University of California, Berkeley Electron Microscopy Laboratory for advice on electrospray emitter imaging. This material is based on work supported by the National Science Foundation Division of Chemistry under grant number CHE-2203907, a NSF Graduate Research Fellowship for JSJ (DGE-2146752), and the Merck DBL SEEDS program.

6.7 References

(1) Marginean, I.; Kelly, R. T.; Prior, D. C.; LaMarche, B. L.; Tang, K.; Smith, R. D. Analytical Characterization of the Electrospray Ion Source in the Nanoflow Regime. *Anal. Chem.* **2008**, *80*, 6573–6579.

(2) Wilm, M.; Mann, M. Analytical Properties of the Nanoelectrospray Ion Source. *Anal. Chem.* **1996**, *68*, 1–8.

(3) Susa, A. C.; Xia, Z.; Williams, E. R. Native Mass Spectrometry from Common Buffers with Salts That Mimic the Extracellular Environment. *Angew. Chem. Int. Ed.* **2017**, *56*, 7912–7915.

(4) Susa, A. C.; Xia, Z.; Williams, E. R. Small Emitter Tips for Native Mass Spectrometry of Proteins and Protein Complexes from Nonvolatile Buffers That Mimic the Intracellular Environment. *Anal. Chem.* **2017**, *89*, 3116–3122.

(5) Susa, A. C.; Lippens, J. L.; Xia, Z.; Loo, J. A.; Campuzano, I. D. G.; Williams, E. R. Submicrometer Emitter ESI Tips for Native Mass Spectrometry of Membrane Proteins in Ionic and Nonionic Detergents. *J. Am. Soc. Mass Spectrom.* **2018**, *29*, 203–206.

(6) Yuill, E. M.; Sa, N.; Ray, S. J.; Hieftje, G. M.; Baker, L. A. Electrospray Ionization from Nanopipette Emitters with Tip Diameters of Less than 100 nm. *Anal. Chem.* **2013**, *85*, 8498–8502.

(7) Davidson, K. L.; Oberreit, D. R.; Hogan, C. J.; Bush, M. F. Nonspecific Aggregation in Native Electrokinetic Nanoelectrospray Ionization. *Int. J. Mass Spectrom.* **2017**, *420*, 35–42.

(8) Hollerbach, A.; Logsdon, D.; Iyer, K.; Li, A.; Schaber, J. A.; Graham Cooks, R. Sizing Sub-Diffraction Limit Electrosprayed Droplets by Structured Illumination Microscopy. *Analyst* **2018**, *143*, 232–240.

(9) Li, H.; Allen, N.; Li, M.; Li, A. Conducting and Characterizing Femto Flow Electrospray Ionization. *Analyst* **2022**, *147*, 1071–1075.
(10) Jordan, J. S.; Williams, E. R. Effects of Electrospray Droplet Size on Analyte Aggregation: Evidence for Serine Octamer in Solution. *Anal. Chem.* **2021**, *93*, 1725–1731.
(11) Jordan, J. S.; Williams, E. R. Homochiral Preference of Serine Octamer in Solution and Formed by Dissociation of Large Gaseous Clusters. *Analyst* **2021**, *146*, 6822–6830.
(12) Nguyen, G. T. H.; Nocentini, A.; Angeli, A.; Gratteri, P.; Supuran, C. T.; Donald, W. A. Perfluoroalkyl Substances of Significant Environmental Concern Can Strongly Inhibit Human Carbonic Anhydrase Isozymes. *Anal. Chem.* **2020**, *92*, 4614–4622.
(13) Nguyen, G. T. H.; Tran, T. N.; Podgorski, M. N.; Bell, S. G.; Supuran, C. T.; Donald, W. A. Nanoscale Ion Emitters in Native Mass Spectrometry for Measuring Ligand–Protein Binding Affinities. *ACS Cent. Sci.* **2019**, *5*, 308–318.
(14) Nguyen, G. T. H.; Bennett, J. L.; Liu, S.; Hancock, S. E.; Winter, D. L.; Glover, D. J.; Donald, W. A. Multiplexed Screening of Thousands of Natural Products for Protein–Ligand Binding in Native Mass Spectrometry. *J. Am. Chem. Soc.* **2021**, *143*, 21379–21387.
(15) Báez Bolivar, E. G.; Bui, D. T.; Kitova, E. N.; Han, L.; Zheng, R. B.; Luber, E. J.; Sayed, S. Y.; Mahal, L. K.; Klassen, J. S. Submicron Emitters Enable Reliable Quantification of Weak Protein-Glycan Interactions by ESI-MS. *Anal. Chem.* **2021**, *93*, 4231–4239.
(16) Agasid, M. T.; Sørensen, L.; Urner, L. H.; Yan, J.; Robinson, C. V. The Effects of Sodium Ions on Ligand Binding and Conformational States of G Protein-Coupled Receptors-Insights from Mass Spectrometry. *J. Am. Chem. Soc.* **2021**, *143*, 4085–4089.
(17) Bui, D. T.; Li, Z.; Kitov, P. I.; Han, L.; Kitova, E. N.; Fortier, M.; Fuselier, C.; Granger Joly de Boissel, P.; Chatenet, D.; Doucet, N.; Tompkins, S. M.; St-Pierre, Y.; Mahal, L. K.; Klassen, J. S. Quantifying Biomolecular Interactions Using Slow Mixing Mode (SLOMO) Nanoflow ESI-MS. *ACS Cent. Sci.* **2022**, *8*, 963–974.
(18) Bennett, J. L.; Nguyen, G. T. H.; Donald, W. A. Protein–Small Molecule Interactions in Native Mass Spectrometry. *Chem. Rev.* **2022**, *122*, 7327–7385.
(19) Nguyen, G. T. H.; Leung, W. Y.; Tran, T. N.; Wang, H.; Murray, V.; Donald, W. A. Mechanism for the Binding of Netropsin to Hairpin DNA Revealed Using Nanoscale Ion Emitters in Native Mass Spectrometry. *Anal. Chem.* **2020**, *92*, 1130–1137.
(20) Lei, W.; Hu, J.; Chen, H.-Y.; Xu, J.-J. Combined Strategies for Suppressing Nonspecific Cationic Adduction to G-Quadruplexes in Electrospray Ionization Mass Spectrometry. *Anal. Chim. Acta.* **2022**, *1220*, 340146.
(21) Xia, Z.; Williams, E. R. Effect of Droplet Lifetime on Where Ions Are Formed in Electrospray Ionization. *Analyst* **2019**, *144*, 237–248.
(22) Smith, J. N.; Flagan, R. C.; Beauchamp, J. L. Droplet Evaporation and Discharge Dynamics in Electrospray Ionization. *J. Phys. Chem. A* **2002**, *106*, 9957–9967.
(23) Olumee, Z.; Callahan, J. H.; Vertes, A. Droplet Dynamics Changes in Electrostatic Sprays of Methanol−Water Mixtures. *J. Phys. Chem. A* **1998**, *102*, 9154–9160.

(24) Kim, J. Y.; Lee, S. J.; Baik, G. Y.; Hong, J. G. Viscosity Effect on the Electrospray Characteristics of Droplet Size and Distribution. *ACS Omega* **2021**, *6*, 29724–29734.
(25) Ku, B. K.; Kim, S. S. Electrospray Characteristics of Highly Viscous Liquids. *J. Aerosol Sci.* **2002**, *33*, 1361–1378.
(26) Gañán-Calvo, A. M.; Dávila, J.; Barrero, A. Current and Droplet Size in the Electrospraying of Liquids. Scaling Laws. *J. Aerosol Sci.* **1997**, *28*, 249–275.
(27) Tang, K.; Gomez, A. Monodisperse Electrosprays of Low Electric Conductivity Liquids in the Cone-Jet Mode. *J. Colloid Interface Sci.* **1996**, *184*, 500–511.
(28) Banerjee, S.; Mazumdar, S. Electrospray Ionization Mass Spectrometry: A Technique to Access the Information beyond the Molecular Weight of the Analyte. *Int. J. Anal. Chem.* **2012**, *2012*, 282574.
(29) Liyanage, O. T.; Brantley, M. R.; Calixte, E. I.; Solouki, T.; Shuford, K. L.; Gallagher, E. S. Characterization of Electrospray Ionization (ESI) Parameters on In-ESI Hydrogen/Deuterium Exchange of Carbohydrate-Metal Ion Adducts. *J. Am. Soc. Mass Spectrom.* **2019**, *30*, 235–247.
(30) Gomez, A.; Tang, K. Charge and Fission of Droplets in Electrostatic Sprays. *Phys. Fluids* **1994**, *6*, 404–414.
(31) Tang, K.; Gomez, A. Generation of Monodisperse Water Droplets from Electrosprays in a Corona-Assisted Cone-Jet Mode. *J. Colloid Interface Sci.* **1995**, *175*, 326–332.
(32) Juraschek, R.; Röllgen, F. W. Pulsation Phenomena during Electrospray Ionization. *Int. J. Mass Spectrom.* **1998**, *177*, 1–15.
(33) De La Mora, J. F.; Loscertales, I. G. The Current Emitted by Highly Conducting Taylor Cones. *J. Fluid Mech.* **1994**, *260*, 155–184.
(34) Pfeifer, R. J.; Hendricks, C. D. Parametric Studies of Electrohydrodynamic Spraying. *AIAA J.* **1968**, *6*, 496–502.
(35) Wilm, M. S.; Mann, M. Electrospray and Taylor-Cone Theory, Dole's Beam of Macromolecules at Last? *Int. J. Mass Spectrom. Ion Process* **1994**, *136*, 167–180.
(36) Schmidt, A.; Karas, M.; Dülcks, T. Effect of Different Solution Flow Rates on Analyte Ion Signals in Nano-ESI MS, or: When Does ESI Turn into Nano-ESI? *J. Am. Soc. Mass Spectrom.* **2003**, *14*, 492–500.
(37) Alexander, M. S.; Paine, M. D.; Stark, J. P. W. Pulsation Modes and the Effect of Applied Voltage on Current and Flow Rate in Nanoelectrospray. *Anal. Chem.* **2006**, *78*, 2658–2664.
(38) Jordan, J. S.; Xia, Z.; Williams, E. R. Tips on Making Tiny Tips: Secrets to Submicron Nanoelectrospray Emitters. *J. Am. Soc. Mass Spectrom.* **2022**, *33*, 607–611.
(39) Mortensen, D. N.; Williams, E. R. Theta-Glass Capillaries in Electrospray Ionization: Rapid Mixing and Short Droplet Lifetimes. *Anal. Chem.* **2014**, *86*, 9315–9321.
(40) Haynes, W. M. *CRC Handbook of Chemistry and Physics*; CRC Press, 2014.
(41) Gamero-Castaño, M.; Fernández De La Mora, J. Mechanisms of Electrospray Ionization of Singly and Multiply Charged Salt Clusters. *Anal. Chim. Acta* **2000**, *406*, 67–91.
(42) Mortensen, D. N.; Williams, E. R. Ultrafast (1 μs) Mixing and Fast Protein Folding in Nanodrops Monitored by Mass Spectrometry. *J. Am. Chem. Soc.* **2016**, *138*, 3453–3460.

(43) Mortensen, D. N.; Williams, E. R. Investigating Protein Folding and Unfolding in Electrospray Nanodrops Upon Rapid Mixing Using Theta-Glass Emitters. *Anal. Chem.* **2015**, *87*, 1281–1287.
(44) Mortensen, D. N.; Williams, E. R. Microsecond and Nanosecond Polyproline II Helix Formation in Aqueous Nanodrops Measured by Mass Spectrometry. *Chem. Commun.* **2016**, *52*, 12218–12221.
(45) Davis, E. J.; Walker, D.; Gibney, M.; Clowers, B. H. Optical and Mass Spectral Characterization of the Electrospray Ionization/Corona Discharge Ionization Interface. *Talanta* **2021**, *224*, 121870.
(46) Li, C.; Attanayake, K.; Valentine, S. J.; Li, P. Facile Improvement of Negative Ion Mode Electrospray Ionization Using Capillary Vibrating Sharp-Edge Spray Ionization. *Anal. Chem.* **2020**, *92*, 2492–2502.
(47) McClory, P. J.; Håkansson, K. Corona Discharge Suppression in Negative Ion Mode Nanoelectrospray Ionization via Trifluoroethanol Addition. *Anal. Chem.* **2017**, *89*, 10188–10193.
(48) Schulten, H. R.; Röllgen, F. W. On Field Desorption Mass Spectrometry of Salts. *Organic Mass Spectrometry* **1975**, *10*, 649–659.
(49) Lehmann, W. D.; Schulten, H. R. Determination of Alkali Elements by Field Desorption Mass Spectrometry. *Anal. Chem.* **1977**, *49*, 1744–1746.
(50) Röllgen, F. W.; Ott, K. H. On the Formation of Cluster Ions and Molecular Ions in Field Desorption of Salts. *Int. J. Mass Spectrom. Ion Physics* **1980**, *32*, 363–367.
(51) Marcus, Y. Thermodynamics of Solvation of Ions. Part 5.—Gibbs Free Energy of Hydration at 298.15 K. *J. Chem. Soc. Faraday Trans.* **1991**, *87*, 2995–2999.
(52) Thomson, B. A.; Iribarne, J. V. Field Induced Ion Evaporation from Liquid Surfaces at Atmospheric Pressure. *J. Chem. Phys.* **1979**, *71*, 4451–4463.
(53) Espy, R. D.; Muliadi, A. R.; Ouyang, Z.; Cooks, R. G. Spray Mechanism in Paper Spray Ionization. *Int. J. Mass Spectrom.* **2012**, *325–327*, 167–171.
(54) Li, A.; Wang, H.; Ouyang, Z.; Cooks, R. G. Paper Spray Ionization of Polar Analytes Using Non-Polar Solvents. *Chem. Commun.* **2011**, *47*, 2811.
(55) Siu, K. W. M.; Guevremont, R.; Le Blanc, J. C. Y.; O'Brien, R. T.; Berman, S. S. Is Droplet Evaporation Crucial in the Mechanism of Electrospray Mass Spectrometry? *Organic Mass Spectrometry* **1993**, *28*, 579–584.
(56) Shannon, R. D. Revised Effective Ionic Radii and Systematic Studies of Interatomic Distances in Halides and Chalcogenides. *Acta Crystallogr.* **1976**, *A32*, 751–767.
(57) Aue, D. H.; Webb, H. M.; Bowers, M. T. A Thermodynamic Analysis of Solvation Effects on the Basicities of Alkylamines. An Electrostatic Analysis of Substituent Effects. *J. Am. Chem. Soc.* **1976**, *98*, 318–329.
(58) Kamatari, Y. O.; Ohji, S.; Konno, T.; Seki, Y.; Soda, K.; Kataoka, M.; Akasaka, K. The Compact and Expanded Denatured Conformations of Apomyoglobin in the Methanol-Water Solvent. *Protein Sci.* **1999**, *8*, 873–882.

(59) Nightingale, E. R. Phenomenological Theory of Ion Solvation. Effective Radii of Hydrated Ions. *J. Phys. Chem.* **1959**, *63*, 1381–1387.
(60) Aliyari, E.; Konermann, L. Atomistic Insights into the Formation of Nonspecific Protein Complexes during Electrospray Ionization. *Anal. Chem.* **2021**, *93*, 12748–12757.
(61) Aliyari, E.; Konermann, L. Formation of Gaseous Proteins via the Ion Evaporation Model (IEM) in Electrospray Mass Spectrometry. *Anal. Chem.* **2020**, *92*, 10807–10814.
(62) Aliyari, E.; Konermann, L. Formation of Gaseous Peptide Ions from Electrospray Droplets: Competition between the Ion Evaporation Mechanism and Charged Residue Mechanism. *Anal. Chem.* **2022**, *94*, 7713–7721.

6.8 Figures

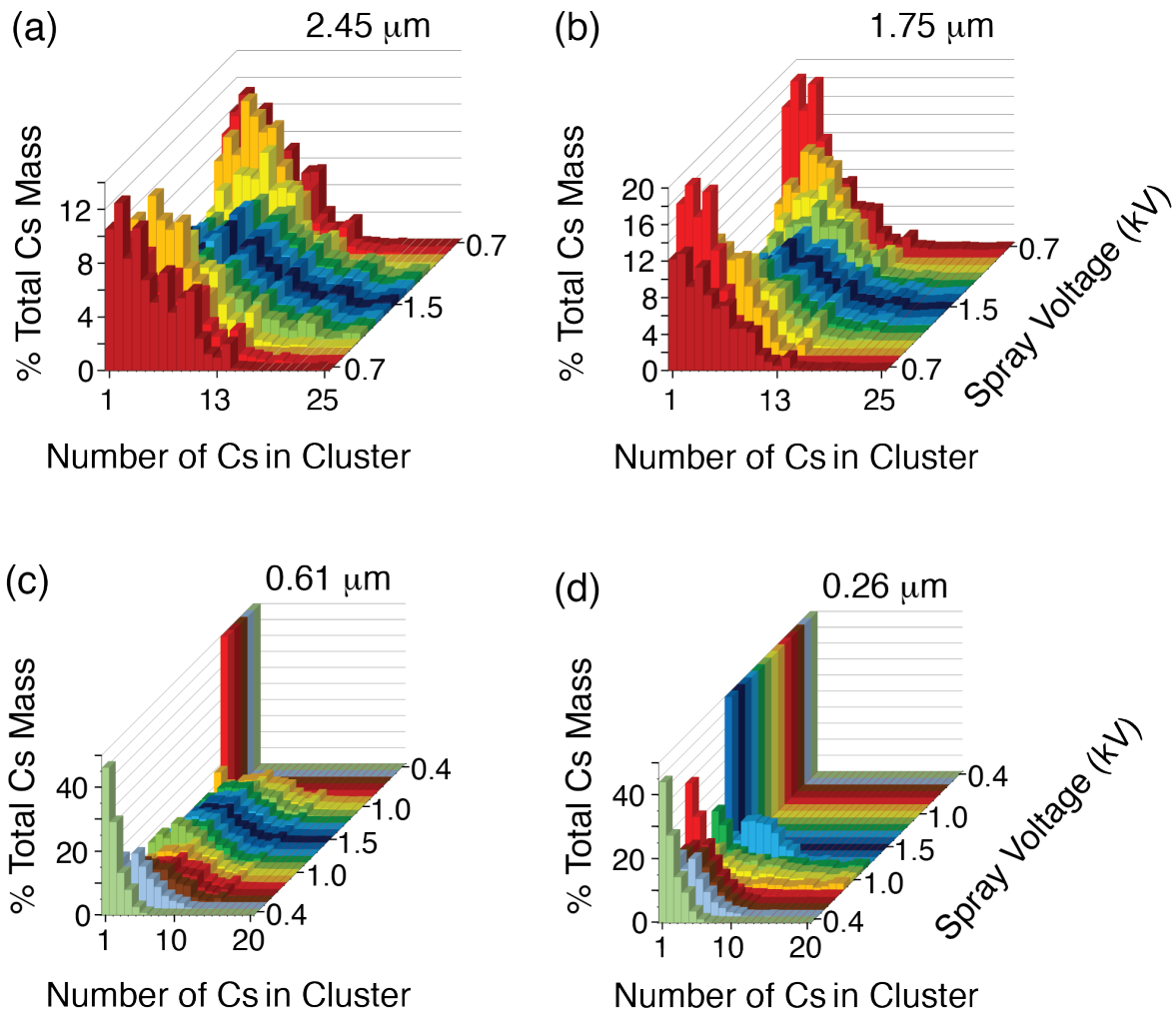

Figure 6.1. Representative cluster distributions obtained from 10 mM CsI as a function of electrospray voltage and emitter tip size of (a) ~2.45 μm, (b) ~1.75 μm, (c) 0.61 μm, and (d) 0.26 μm. Larger tips show cluster size distributions that change reproducibly with spray voltage, but the smallest tips in (c) and (d), undergo a transition that results in only formation of Cs^+ and $Cs(H_2O)^+$. The cluster distributions from submicron emitters have greater variability with increasing spray voltage that may be related to changes in the electrospray mode.

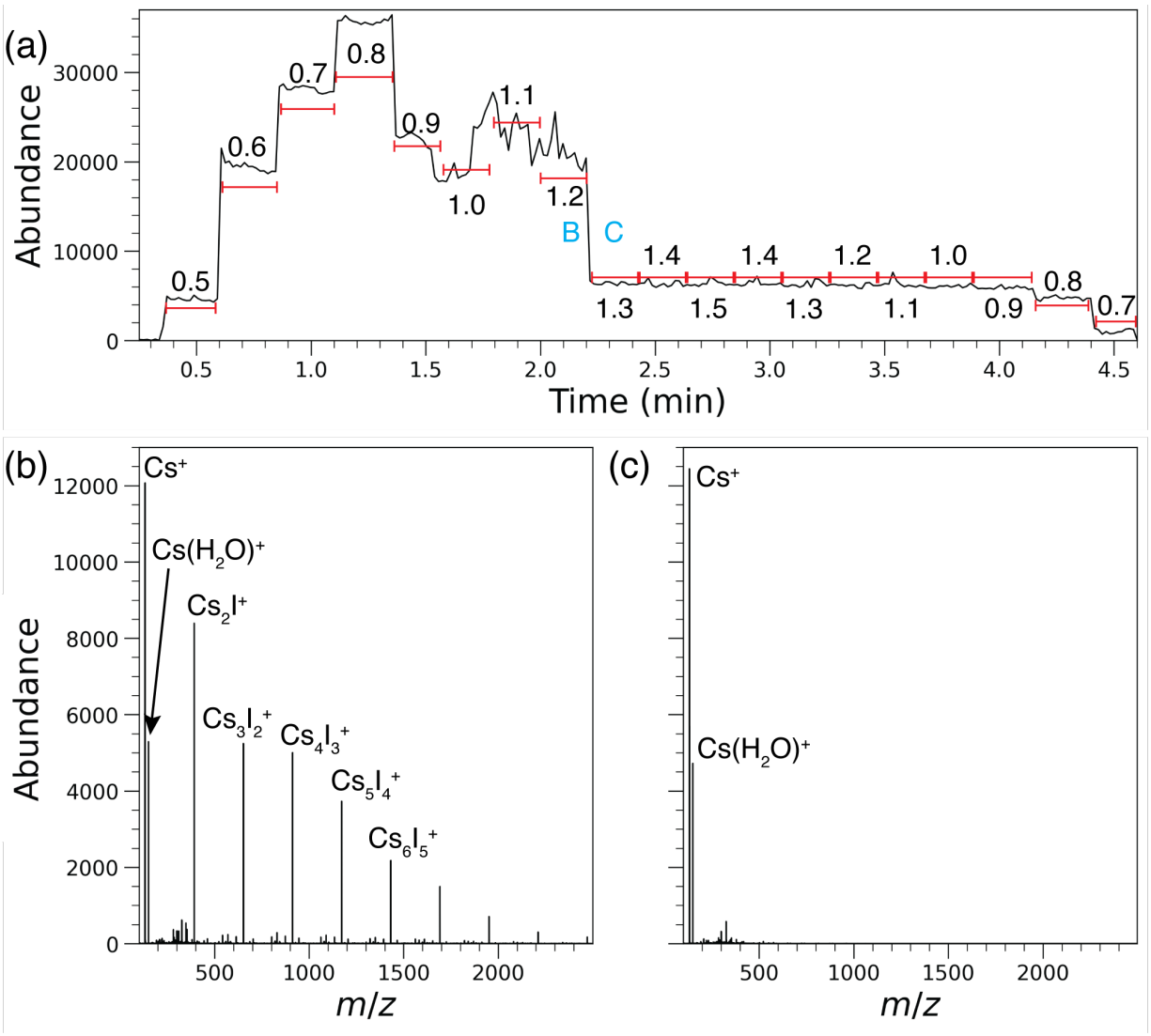

Figure 6.2. (a) Representative total ion current resulting from electrospray of a 10 mM CsI solution as a function of time from an emitter with ~608 nm diameter tip showing a significant reduction in total ion current that occurs upon corona discharge. The numbers above each time increment indicate the spray voltage in kV. Representative mass spectra from time periods labeled B and C are shown in (b) and (c), respectively. The abundance values on the *y*-axis are the same in (b) and (c), indicating that the abundance of Cs^+ is similar before and after corona discharge.

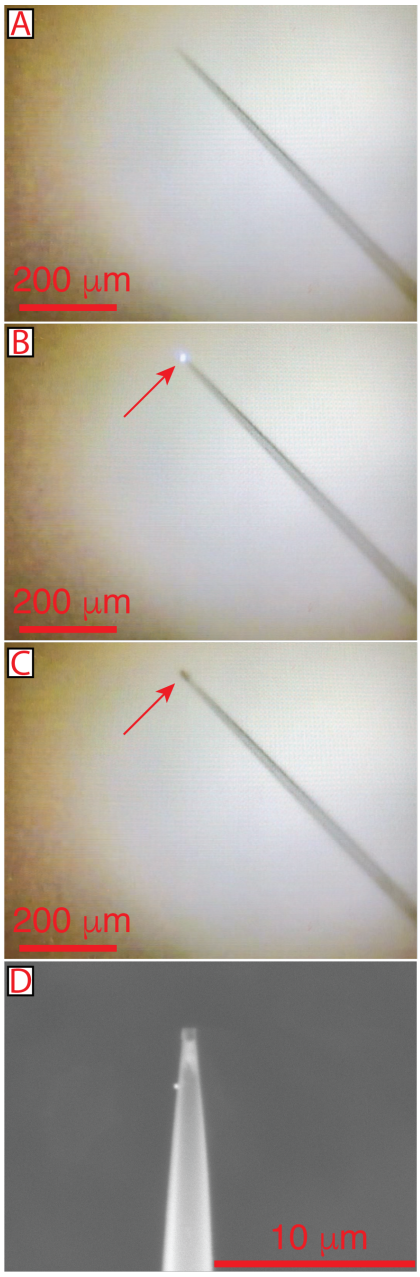

Figure 6.3. Optical and scanning electron microscope images of a single emitter with a 608 nm diameter tip used to spray a 10 mM CsI aqueous solution: (a) at low spray voltages (<1 kV), emitters appear to have transparent tips and mass spectra show a distribution of Cs_nI_{n-1} clusters (Figure 2b). At voltages between 1 and 1.5 kV, (b) corona discharge may occur, resulting in mass spectra where Cs^+ is the most abundant ion (Figure 2c). After corona discharge, (c) visible material is present at the tip of the emitter. (d) scanning electron microscopy image obtained from an emitter that was dried overnight reveals no change to the inner diameter or to the rest of the tip, indicating that corona discharge does not damage the borosilicate glass. Material can often be dislodged at higher voltages and a return to normal electrospray occurs further indicating that the emitters are not damaged by the discharge.

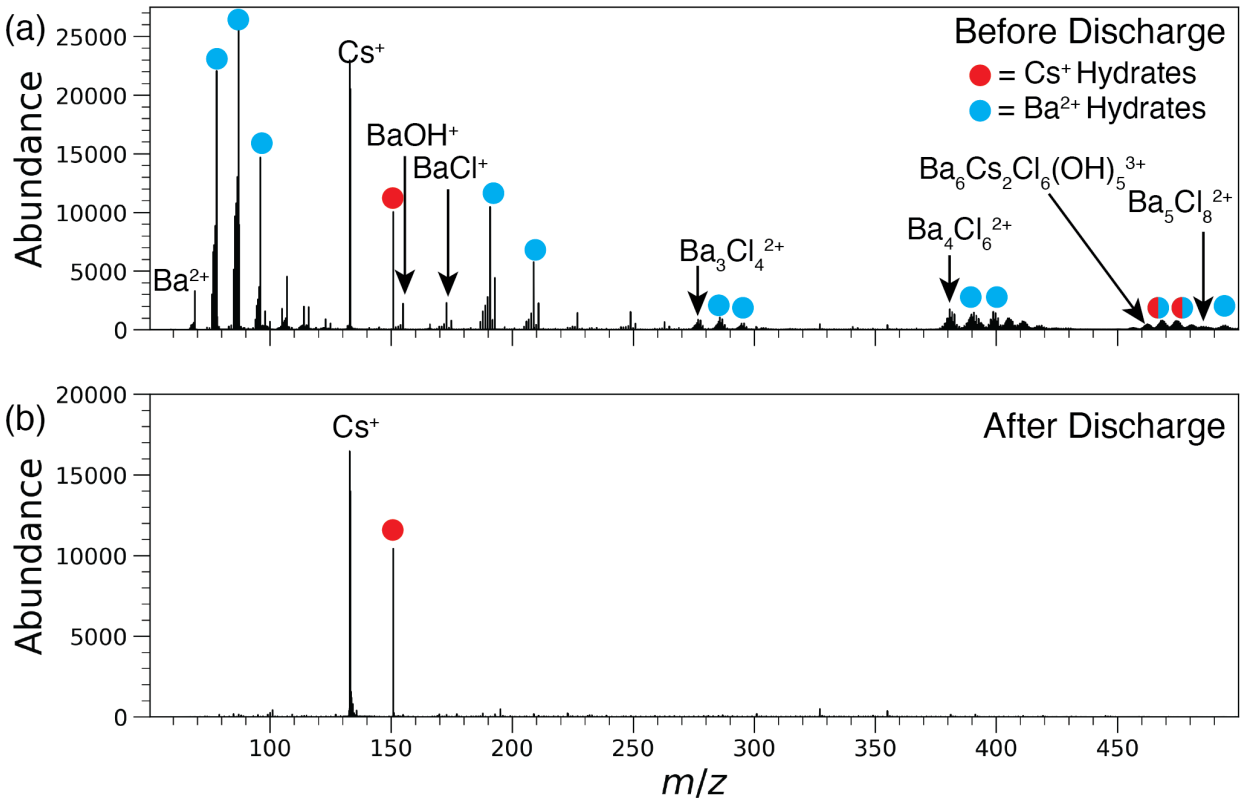

Figure 6.4. nESI mass spectra of an aqueous solution of 5 mM $BaCl_2$ and 5 mM CsCl obtained with an emitter with a 608 nm diameter tip (a) before and (b) after corona discharge.

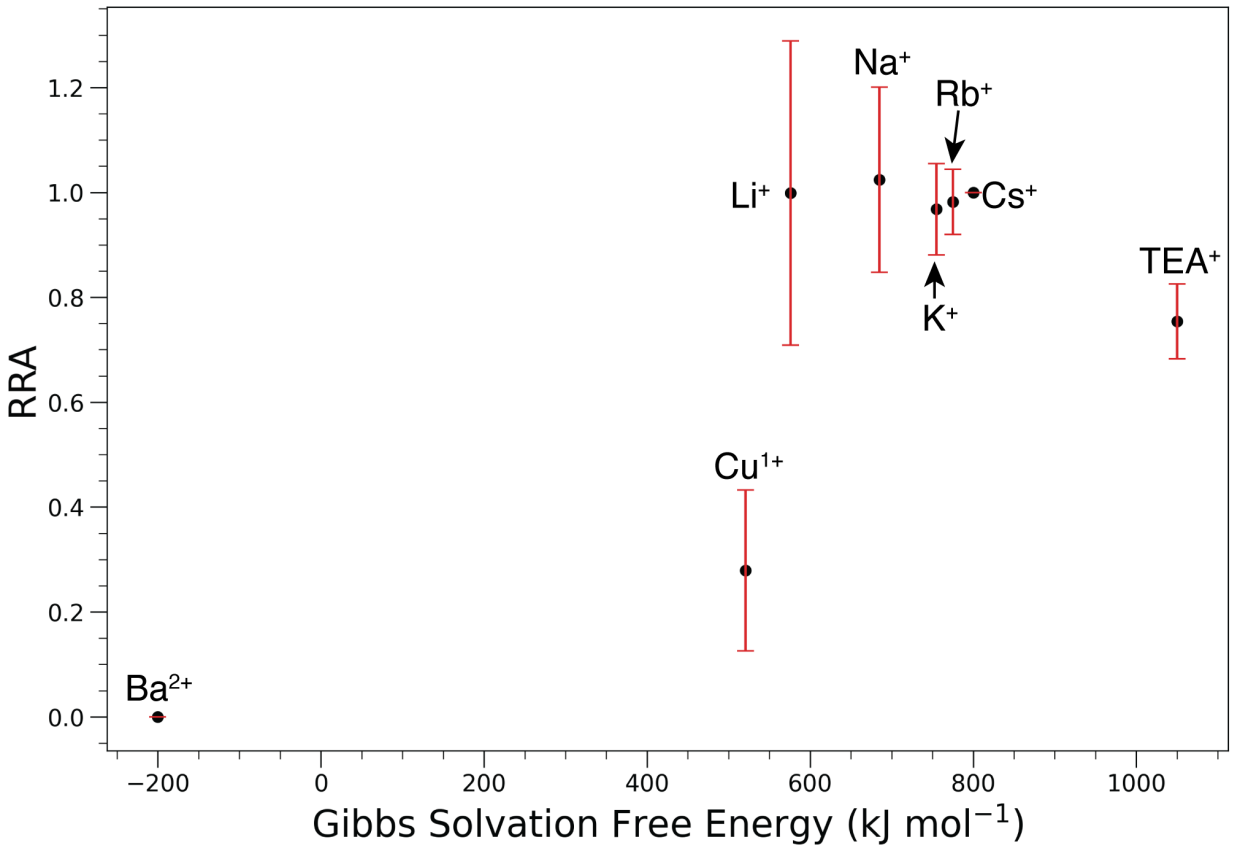

Figure 6.5. The ratio of relative abundances of cations to Cs^+ before and after the discharge event (RRA) as a function of Gibbs solvation free energy (GSFE). Error bars represent the standard deviation of the RRA value measured with three different emitters. Ions with GSFE values lower than ~540 kJ mol^{-1} are significantly suppressed or not observed after discharge.

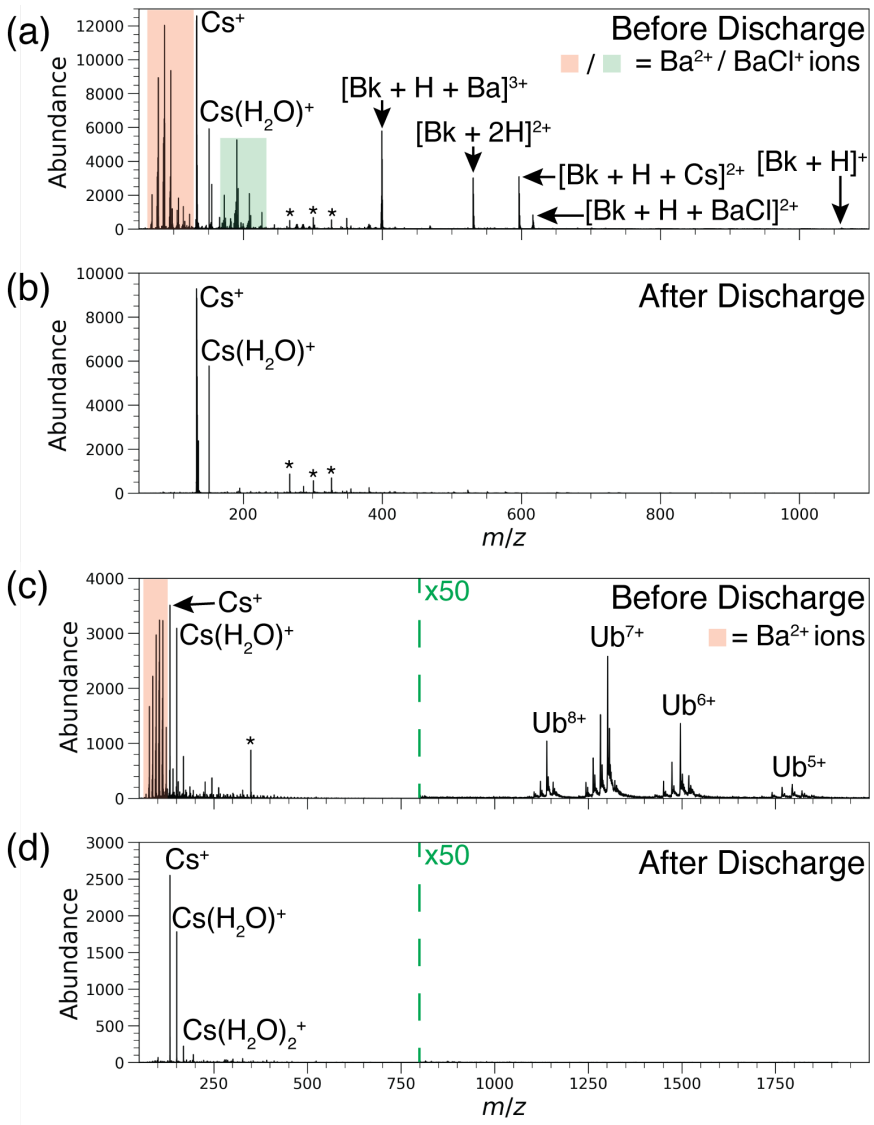

Figure 6.6. nESI mass spectra of a 10 µm solution of bradykinin (a,b) or ubiquitin (c,d) in 1:1 CsCl:$BaCl_2$ obtained from an emitter with a 608 nm diameter tip before and after corona discharge. Light red and green regions indicate Ba^{2+} and $BaCl^+$ ions, respectively, and associated hydrates. Prior to discharge, bradykinin and ubiquitin ions are observed with cesium and barium adduction, consistent with formation of these ions from nanodrops. After discharge, abundant Cs^+ is observed, but bradykinin, ubiquitin or barium ions are not, consistent with desorption of Cs^+, but not Ba^{2+}, bradykinin, or ubiquitin. Asterisk indicates Cs-adducted organic contaminants that were confirmed by MS/MS. Regions from 800 – 2000 *m*/*z* are expanded by 50x in (c) and (d).

6.9 Supplemental Information

6.9.1 Description of Supplemental Video 1

Supporting video 1 can be accessed from the publishers website at the following link: https://pubs.acs.org/doi/10.1021/jasms.3c00121. Supporting video 1 shows the corona discharge process occurring while spraying a solution of 10 mM CsI from a ~608 nm emitter. The corona discharge is evident from the purple light emanating from the tip upon increasing the voltage from 1.2 kV to 1.3 kV, followed by the formation of visible debris. The video is played at 2x speed. Prior to corona discharge and debris formation, mass spectra acquired from this emitter appear similar to that in figure 2b. After discharge, mass spectra acquired during this experiment resemble figure 2c.

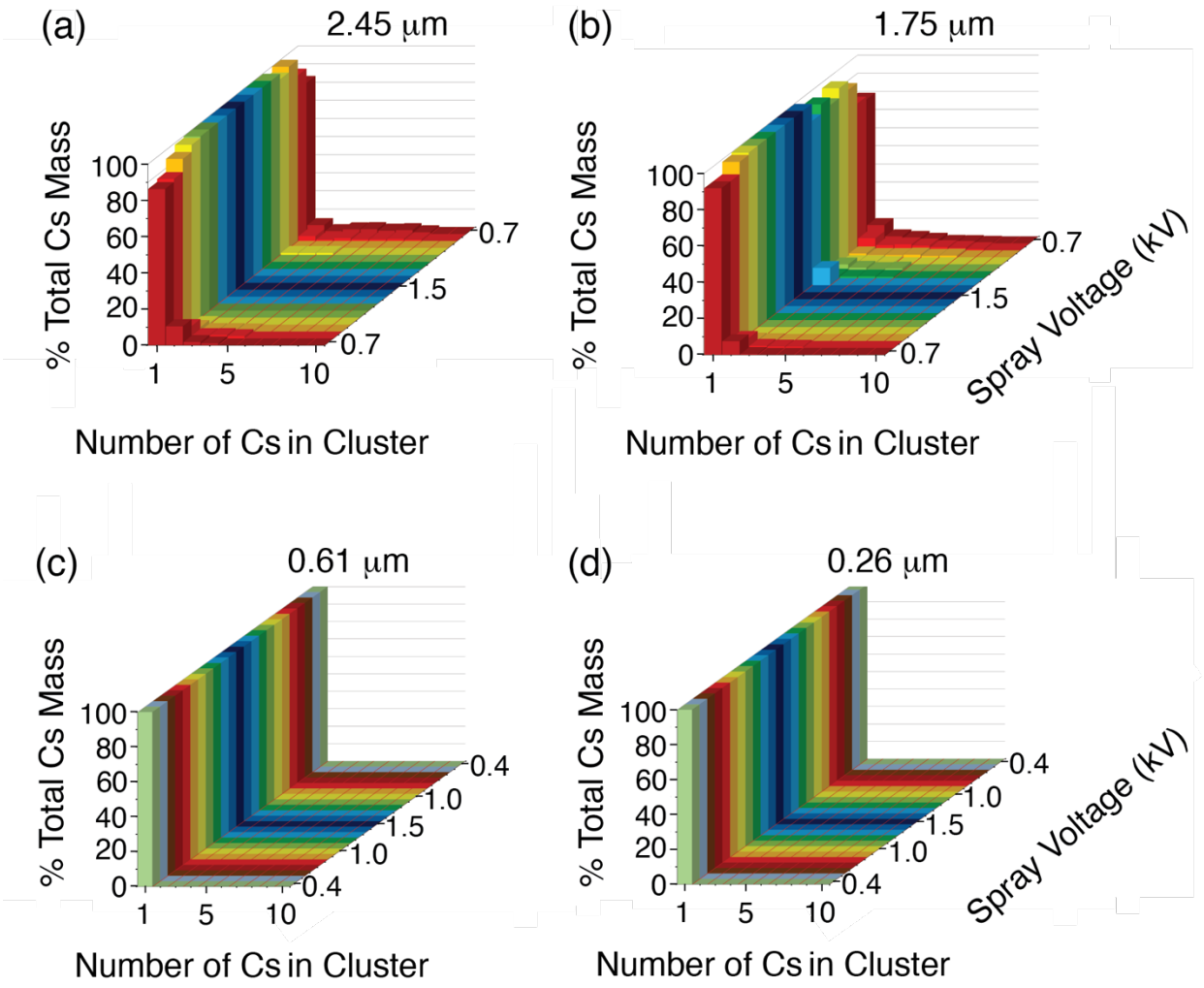

Supplemental Figure 6.1. Representative cluster distributions obtained from 100 μM CsI as a function of electrospray voltage and emitter tip size of (a) ~2.45 μm, (b) ~1.75 μm, (c) 0.61 μm, and (d) 0.26 μm.

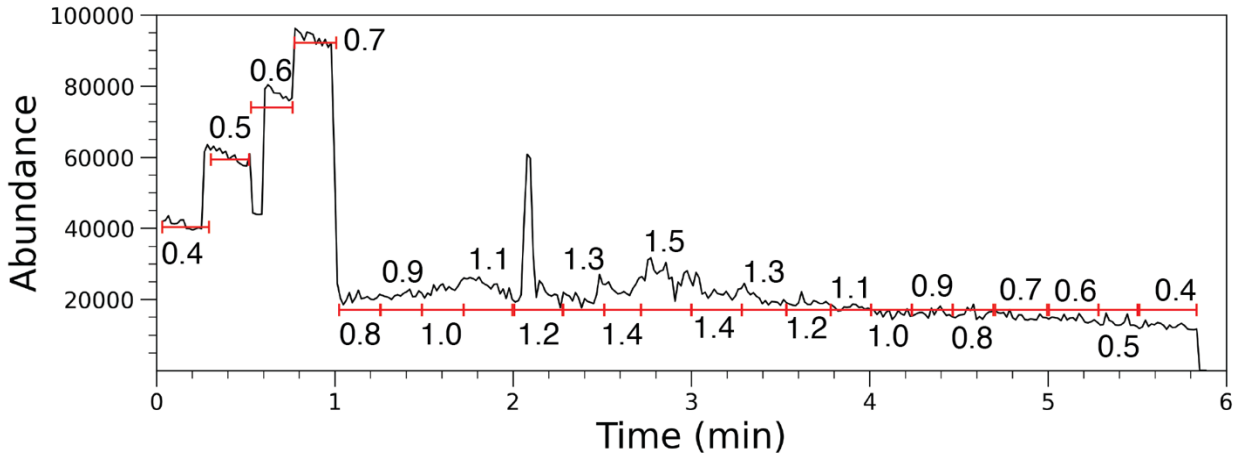

Supplemental Figure 6.2. The total ion current as a function of time from electrospray of a 10 mM CsI solution from an emitter with a ~608 nm diameter tip. The numbers above or below each time increment indicate the spray voltage in kV. Corona discharge occurred between time periods labeled 0.7 and 0.8. The onset voltage for ion formation is the same (0.4 kV) before and after corona discharge.

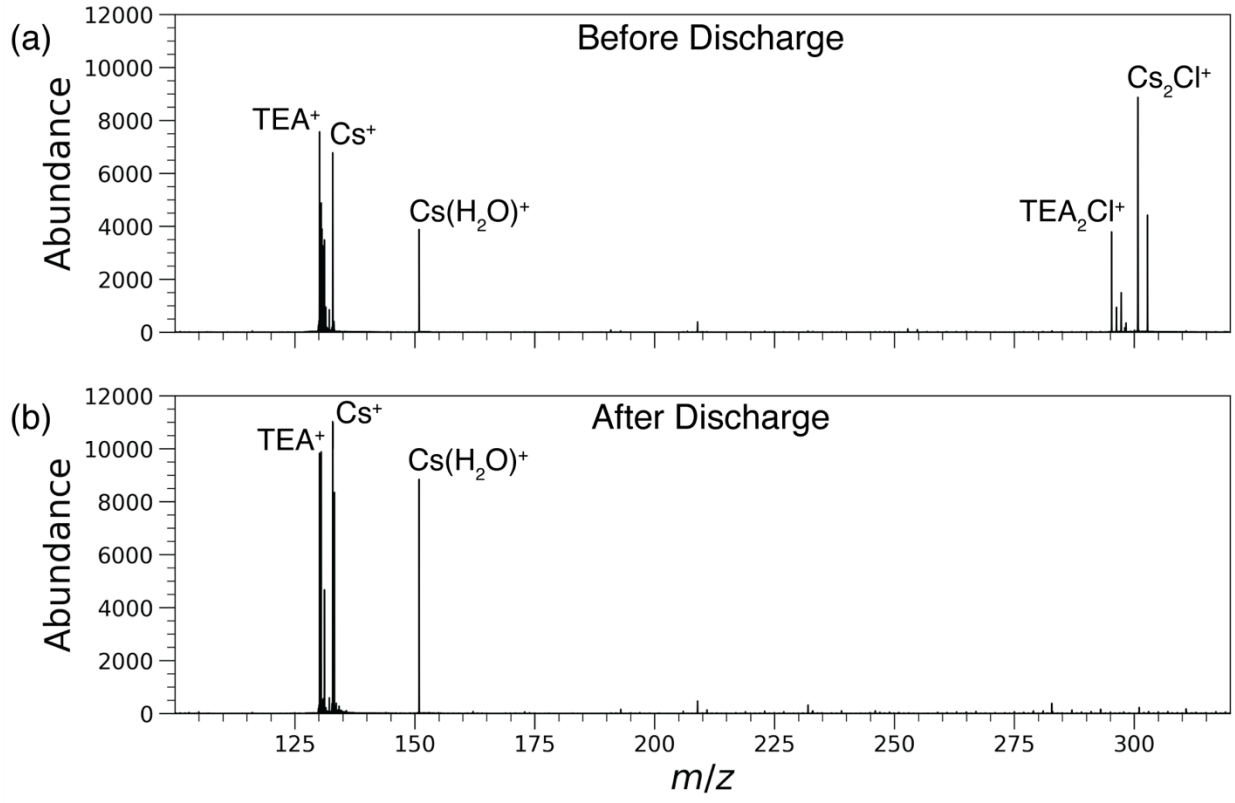

Supplemental Figure 6.3. nESI mass spectra of a 10 mM 1:1 TEACl:CsCl solution (5 mM each) (a) before and (b) after corona discharge.

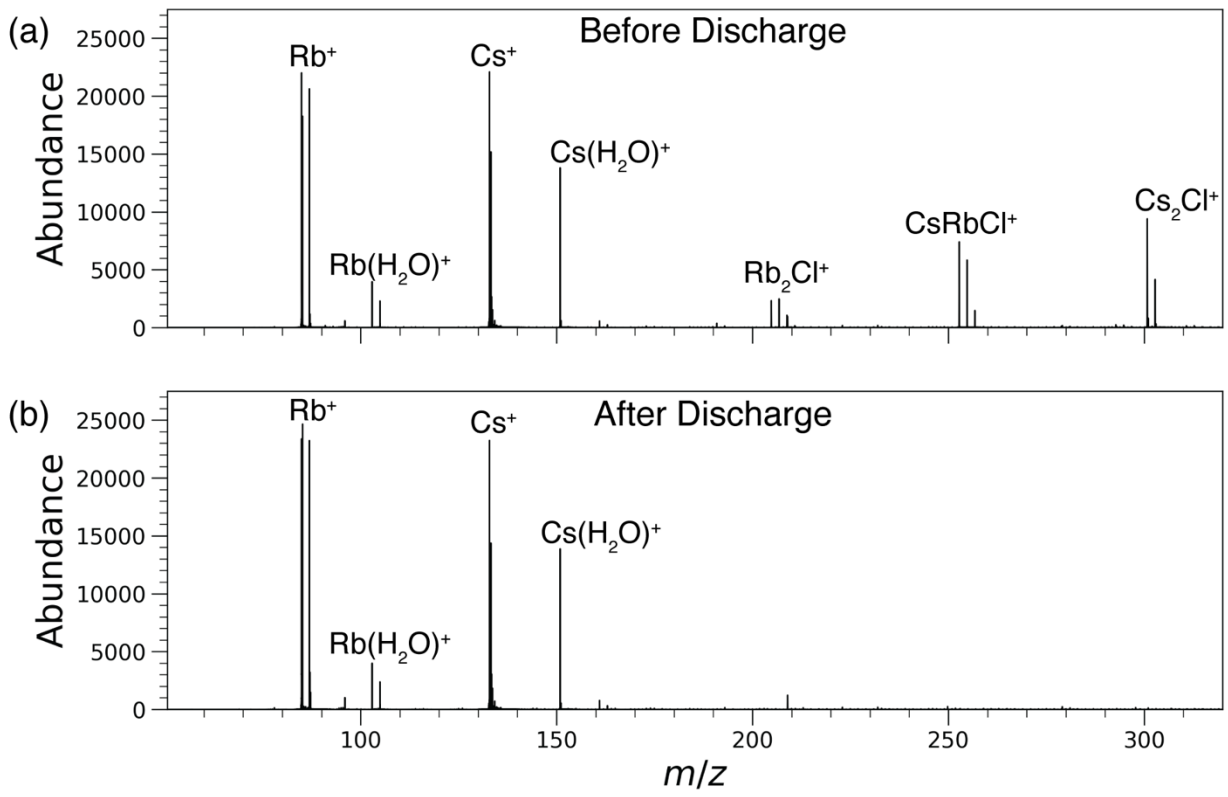

Supplemental Figure 6.4. nESI mass spectra of a 10 mM 1:1 RbCl:CsCl solution (5 mM each) (a) before and (b) after corona discharge.

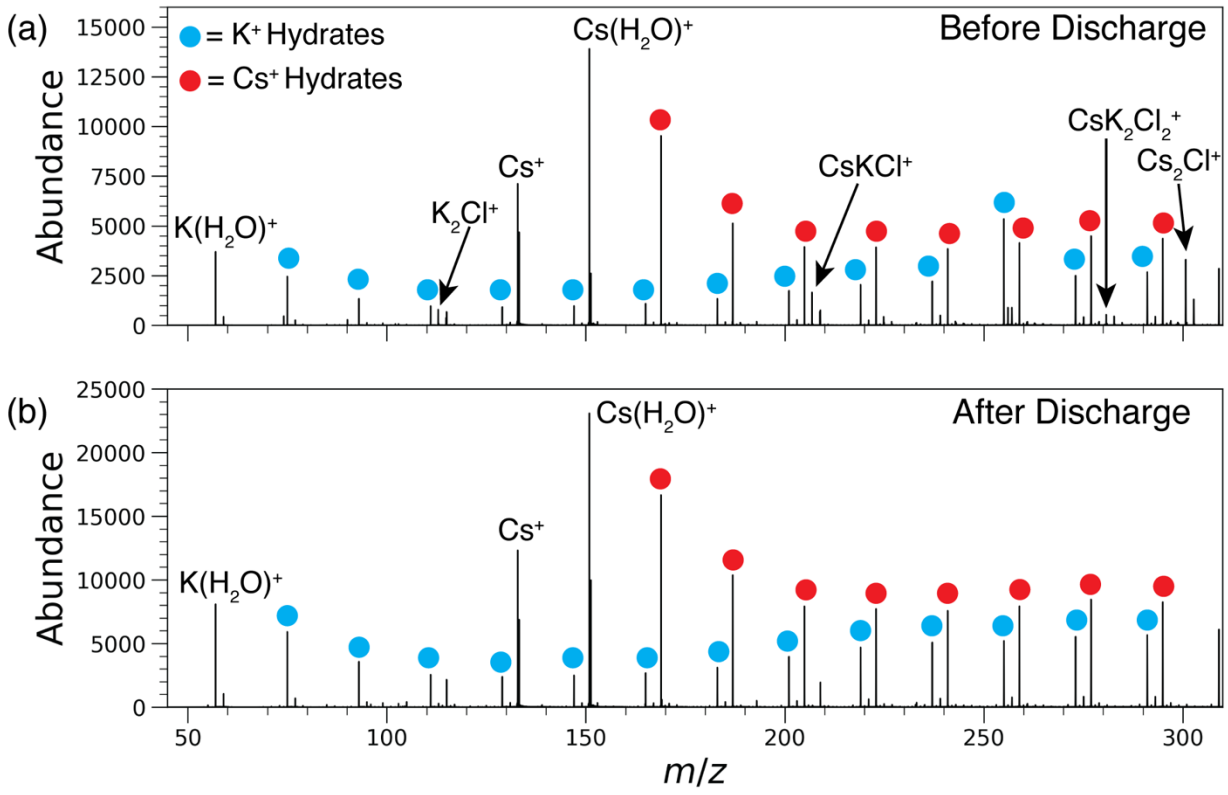

Supplemental Figure 6.5. nESI mass spectra of a 10 mM 1:1 KCl:CsCl solution (5 mM each) (a) before and (b) after corona discharge.

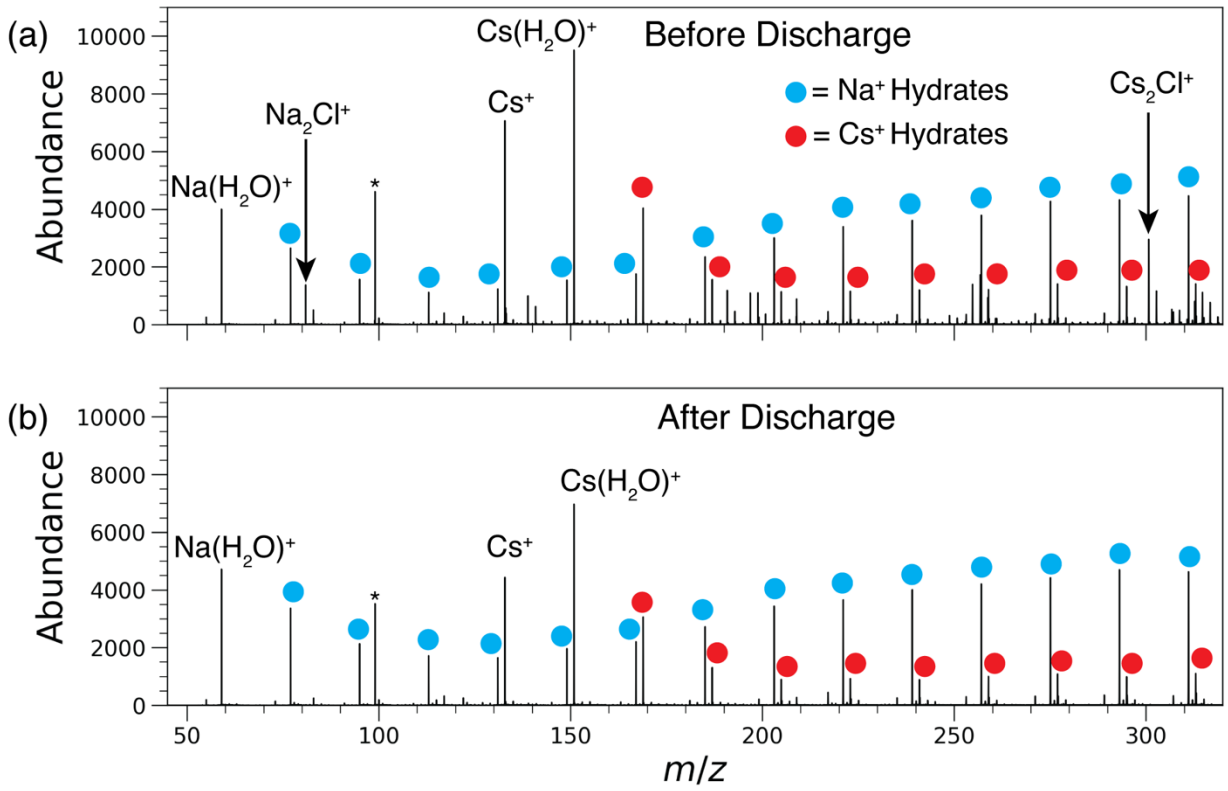

Supplemental Figure 6.6. nESI mass spectra of a 10 mM 1:1 NaCl:CsCl solution (5 mM each) (a) before and (b) after corona discharge. Asterisk indicates an organic contaminant present in the sample at *m*/*z* ~99.

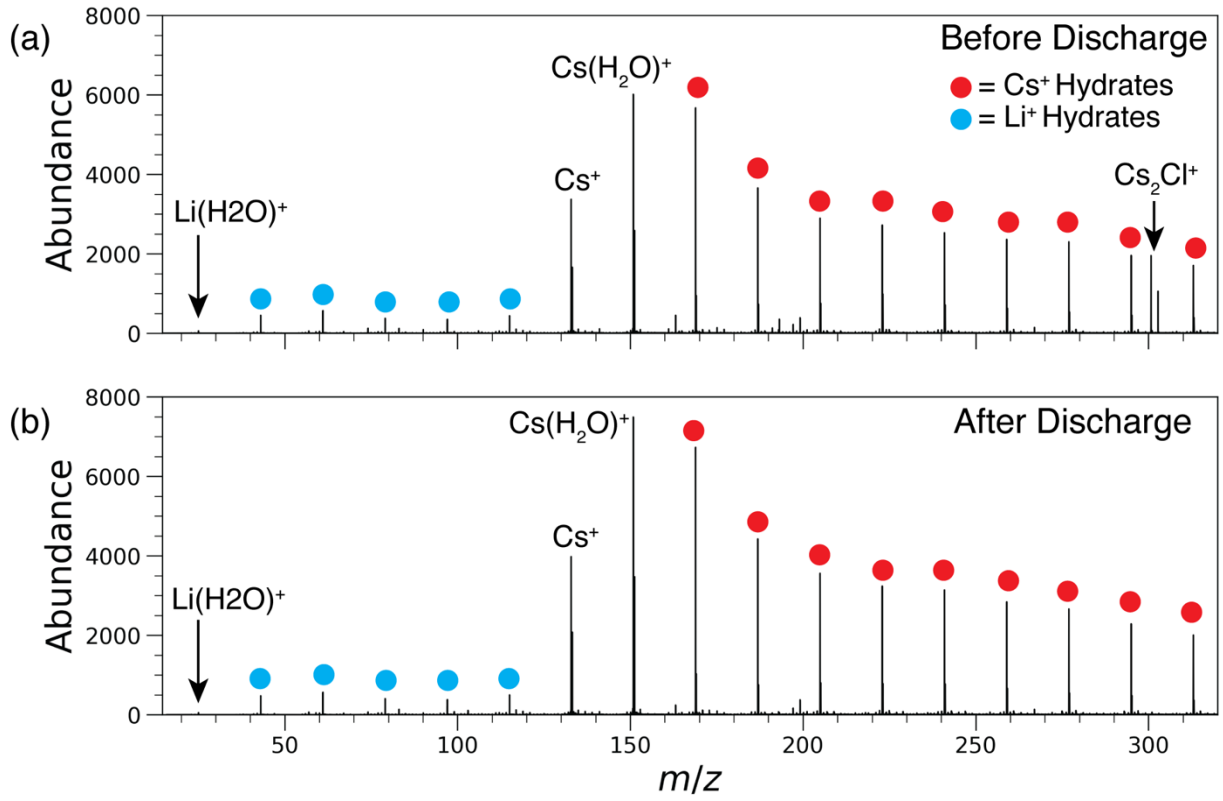

Supplemental Figure 6.7. nESI mass spectra of a 10 mM 1:1 LiCl:CsCl solution (5 mM each) (a) before and (b) after corona discharge.

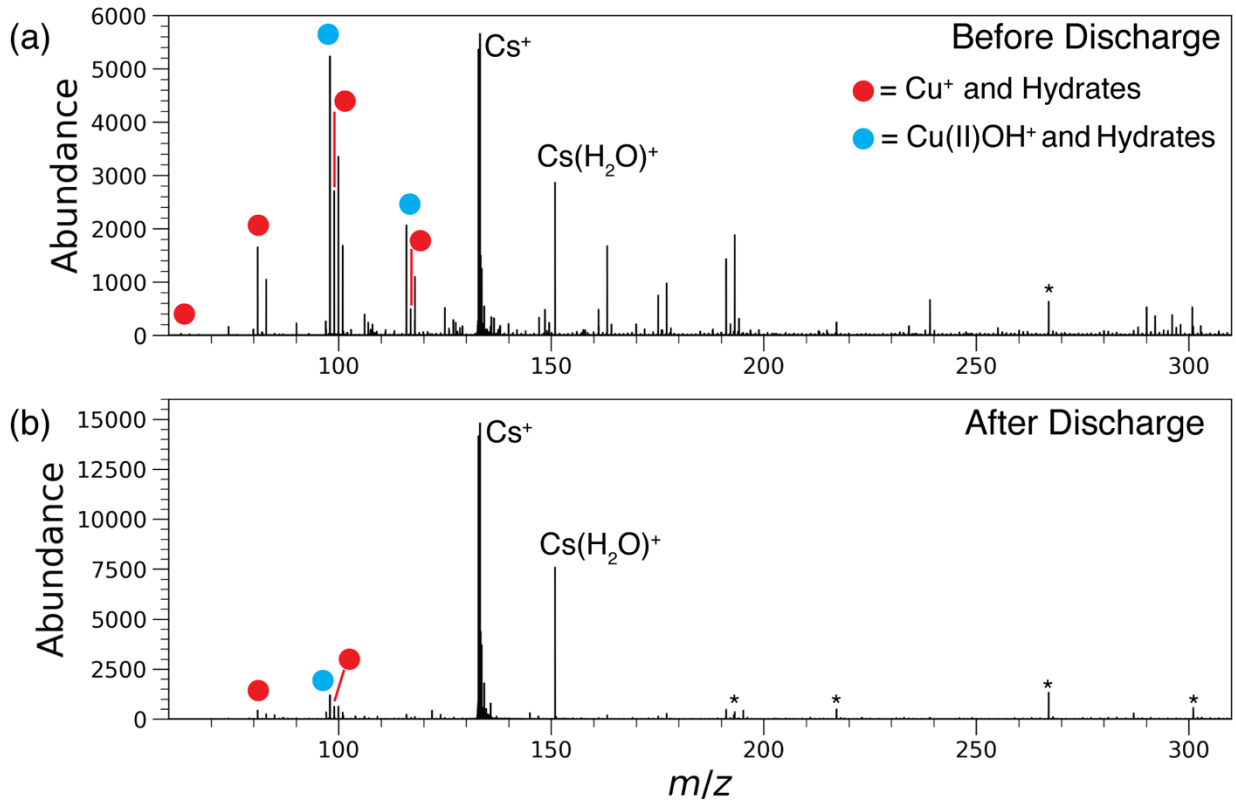

Supplemental Figure 6.8. nESI mass spectra of a 1:1 mixture of saturated CuCl and 5 mM CsCl (a) before and (b) after corona discharge. Asterisk indicates Cs-adducted organic contaminants that were confirmed by MS/MS.

Supplementary Table 6.1. *m/z* Values of Recurring Organic Contaminant Ions

m/z	**Charge**
99.046	+1
106.229	+1
177.177	+1
195.192	+1
217.123	+1
267.018	+1
301.041	+1
327.082	+1
348.999	+1
355.077	+1
381.132	+1
475.038	+1
502.995	+1
523.197	+1
551.220	+1
577.009	+1
591.072	+1
607.173	+1
651.038	+1
665.069	+1
725.047	+1
739.100	+1
873.077	+1
887.141	+1

Chapter 7

Laser Heating Nanoelectrospray Emitters for Fast Protein Melting Measurements with Mass Spectrometry

This chapter is reproduced with permission from:

Jacob S. Jordan, Evan R. Williams

"Laser Heating Nanoelectrospray Emitters for Fast Protein Melting Measurements with Mass Spectrometry"

Analytical Chemistry, **2022**, *94*(48):16894-16900

7.1 Abstract

Temperature-controlled nanoelectrospray ionization has been used to measure heat-induced conformational changes of biomolecules by mass spectrometry, but long thermal equilibration times associated with heating or cooling an entire emitter limits how fast these data can be acquired. Here, the tip of a borosilicate electrospray emitter is heated using 10.6 μm light from an unfocused CO_2 laser. At 1.2 W, the solution inside the emitter tip can be heated from room temperature to a steady state temperature of 78.2 ± 2.5 °C in less than 0.5 s and cools from 82.6 ± 0.6 °C back to room temperature within 4 s. The time required to establish a steady state temperature is more than 100-fold faster than that required for a resistively heated emitter due to the low thermal mass. Protein unfolding curves measured as a function of laser power can be acquired in ~40 s compared to a resistively heated apparatus that required ~21 min. to acquire similar data. Laser power is calibrated to temperature by comparisons of the average charge state of the protein cytochrome *c* measured with laser heating and with resistive heating. This laser heating method is applied to a three-component protein mixture to demonstrate the ability to rapidly acquire melting temperatures of proteins in mixtures. The ability to rapidly assess the thermal stabilities of multiple proteins simultaneously shows significant promise for coupling temperature-controlled ESI to separations techniques, providing a high-throughput method for determining the effects of solution composition, drug-binding, or sequence mutations on protein thermal stability.

7.2 Introduction

The thermodynamic stabilities of the native states of proteins and macromolecular complexes are fundamental properties that influence conformational diversity, solubility, and function. The stability of a protein native state can be measured using a variety of different methods, including chemically induced or thermally induced protein unfolding.[1] Temperature-induced unfolding data can be used to obtain a melting temperature (T_m) and other useful thermochemical information.[2] Thermal stabilities depend on solution composition and pH,[3] sequence mutations[4,5] and ligand/drug-binding,[3,6] making T_m values a useful metric when studying the stabilizing effect of formulation buffers[3] or identifying small molecule ligand binding in drug development workflows.[7] A variety of standard techniques are used to measure protein melting temperatures, including circular dichroism (CD) spectroscopy,[2,8] fluorescence/UV-Vis spectrophotometry[9,10] and differential scanning calorimetry (DSC).[11,12] These techniques generally require purified protein samples in order to avoid overlapping signals or transitions that lead to uncertainties in measured T_m values. Mass spectrometry (MS) has also been used to measure protein melting temperatures and has the advantage that purified samples are not required if proteins have different masses.[13,14] MS-based methods of determining T_m values also have the advantage of high sensitivity with little sample required, and changes in protein conformation, including folding/unfolding intermediate structures that are kinetically trapped during the ionization process,[15–17] can be identified based on either the abundance of each charge state[18–20] or by using ion mobility spectrometry.[16,20–23]

Several different variable-temperature electrospray ionization (vT-ESI) sources have been developed to change solution temperature during electrospray.[8] Resistively heated devices are most common, but heating or cooling has also been done with Peltier devices.[8] vT-ESI has been used to measure protein,[8,12,19–21,24–27] protein complex,[22,23,25,28–30] and DNA complex unfolding pathways and kinetics,[6,31] determine thermochemical values of protein[18,23,32–34] and peptide stability,[35] and to determine binding energetics of small molecule ligands.[32,36,37] Recently, El-Baba *et al.* determined T_m values of seven proteins from a mixture of ribosomal proteins using vT-ESI, illustrating the advantage of this technique for multiplexed measurements.[19]

Heating/cooling devices differ in the accessible temperature ranges and the rates at which the temperature can be changed.[8] However, a common characteristic of these devices is a relatively large thermal mass associated with heating the entire apparatus. A high thermal mass necessitates long thermal equilibration times of between 1 – 3 minutes before measuring mass spectra at each temperature.[8,12,18,20,24,28,36,37] Cooling the source between melting replicates can take >10 minutes, significantly reducing the throughput of this technique.

One alternative technique to measure protein melting by mass spectrometry is "laser-spray" in which a laser is used to heat the analyte solution. Initial laser-spray experiments by Hiraoka and coworkers using a 10.6 μm CO_2 laser were performed with the laser beam pointed down the barrel (coaxial orientation) of a stainless steel capillary with an inner diameter of 100 μm.[38–42] With a laser power of 0 W and 1.6 W, the relative abundance of the folded forms of cytochrome *c* at pH 3.5, determined by a change in the average charge state, was ~81 % and ~15 %, respectively.[38] These data fit well to a sigmoidal curve from which a melting power was determined from the inflection point of the curve.[38] Laser-spray has been utilized to study the effects of laser power on stabilities of proteins,[43] protein-DNA,[44] and DNA-drug complexes.[45]

A focused 10.6 μm laser has also been used to heat nanodroplets produced from electrospray emitters.[15,21] El-Baba *et al.* reported an increase in the weighted average charge state of ubiquitin with increasing laser power, similar to that reported for vT-ESI experiments, indicating that this technique is also applicable for the study of protein thermal denaturation.[15] Changing the

diameter of the tip of the electrospray emitter and hence the initial droplet size distribution produced by electrospray[46–48] resulted in a different extent of unfolding. These experiments indicate that thermally induced protein unfolding kinetics and structural intermediates can be investigated by producing droplets that have different initial sizes and hence lifetimes. Woodall *et al.* reported different extents of myoglobin unfolding by vT-ESI and nanodroplet heating with this same apparatus.[21] The weighted average charge state of holo-myoglobin increased by +4.0 charges during vT-ESI experiments at pH 9, but only by +1.5 and +2.5 from heating droplets produced by emitters with 4 μm and 24 μm diameter tips, respectively. Because equilibration times in vT-ESI experiments are typically on the order of one minute or more when the temperature of a solution is changed, conformational changes that occur likely reflect equilibrium conditions. In contrast, the time scale for protein folding/unfolding in droplets depends on the lifetime of the droplet[48,49] that can be readily varied between ~1 μs to ~50 μs.[47,49]

Here, a laser heated electrospray ionization (LH-ESI) source that uses a 10.6 μm CO_2 laser to heat only the tip of a borosilicate nanoelectrospray ionization emitter was constructed. Strong absorption of 10.6 μm light by borosilicate enables low laser fluences to be used to reach solution temperatures >80 °C. By rapidly changing laser power, protein melting curves can be acquired in less than 45 s. This method shows significant potential for rapidly determining protein melting temperatures by mass spectrometry, including the ability to acquire data on a separations time scale.

7.3 Experimental Methods

A laser-heated ESI (LH-ESI) source (Figure 1) was constructed by aligning the beam of a Synrad F48-2 10.6 μm CO_2 laser (Synrad Corporation, Mukilteo, WA) perpendicular to the inlet of an Orbitrap Elite mass spectrometer (ThermoFisher Corporation, Waltham, MA). Borosilicate emitters were aligned with the laser beam and the tip length that was irradiated with the laser was controlled by a beam block that prevents the rest of the capillary from being heated (Figure 1, inset). An IR power meter head (Ophir-Spiricon, North Logan, UT) after the capillary was used to measure laser power in real time. An Arduino microcontroller (Uno R3, Somerville, MA) with an Adafruit MCP4725 DAC (New York, NY) was programmed to read and change the laser power during the experiment via Arduino and Python code. Emitters were positioned in the beam path using a 3-axis stage using both a Dino-Lite digital microscope to visualize the distance from the MS inlet to the emitter and a 633 nm Helium-Neon laser (ThorLabs, Newton, NJ) that was co-aligned with the CO_2 laser beam. The variability between replicates reflects variations in tip morphology and tip positioning in addition to other variations typical in nano-ESI-MS experiments. An electrospray voltage (1.0 – 1.5 kV) was supplied via a 0.127 mm diameter platinum wire inserted into the back of the capillary and in contact with the solution.

Borosilicate nanoelectrospray capillaries (1.0 mm outer diameter, 0.78 mm inner diameter, Sutter Instrument, Novato, CA) were pulled to an inner diameter of ~1.3 ± 0.1 μm and a taper length of 3.5 ± 0.1 mm using a Sutter Instrument P-87 capillary puller.[50] Emitters were periodically imaged using a Hitachi TM-1000 scanning electron microscope (Tokyo, Japan) at the University of California, Berkeley Electron Microscopy Lab.

For calibration purposes, a vT-ESI source similar to that described by Sterling *et al.* was constructed.[51] In brief, the source consists of an aluminum cylinder wrapped in resistive heating

wire. The temperature of the apparatus was measured using a J-type thermocouple positioned within the metal heating jacket and was controlled using an Omega CNi3222 temperature controller (Stamford, CT). Borosilicate capillaries were inserted through the aluminum cylinder until the emitter tip was at the end of the heating jacket. A thermocouple placed inside the borosilicate capillary was used to confirm that the thermocouple in the heating jacket reflected the temperature inside the capillary. The temperature of the device was allowed to equilibrate for ~70 s at each temperature prior to starting electrospray and ~6 mass spectra (~3 s) were averaged at each temperature during analysis.

For cytochrome *c* (cyt *c*) melting experiments, 10 μM equine cyt *c* was prepared in 20 mM ammonium acetate at pH 6.8. The laser power was increased from 0 W to ~1.3 W in increments of ~75 mW and ~6 spectra were averaged at each laser power (~3 s). The instrument resolution was set to 60000 with a maximum injection time of 10 ms, resulting in a mass spectrum acquisition rate of ~0.42 s. To determine the effect of emitter position on protein melting, the tip position was adjusted in all three axes using micron adjusts and spectra were acquired for 15 s at a constant laser power of ~600 mW. To achieve higher spectral acquisition rates in experiments where the rate of heating was measured, the instrument resolution was set to 15000, resulting in a mass spectrum acquisition rate of 0.25 s. Solutions containing a mixture of cyt *c*, equine heart myoglobin, and pseudo-wildtype barstar were prepared (3 μM each) in 20 mM ammonium acetate (pH 6.8). Cyt *c* and equine heart myoglobin were obtained from Sigma-Aldrich (Burlington, MA) and were used without further purification. Pseudo-wildtype barstar (C40/82 replaced by Ala) was obtained as previously described.[52]

7.4 Results and Discussion

7.4.1 Performance of Laser Heated NanoESI

Borosilicate capillaries often used in nanoESI have tip diameters that are typically in the low tens of micron range, although emitter tips with diameters of a few microns or lower can be advantageous for native MS measurements.[53,54] Borosilicate absorbs strongly at the 10.6 μm output of a CO_2 laser and the emitter tips have low thermal mass. Because laser power can be changed quickly, laser irradiation of just the emitter tip should lead to a rapid change in solution temperature, which can induce protein unfolding. An apparatus was constructed (Figure 1) to accurately position an emitter tip in the beam of a CO_2 laser (~3.5 mm beam diameter) and to block laser light so that only the tip of the emitter is exposed to the laser beam. Factors that affect the heating of solution in an emitter tip with this apparatus were investigated using a solution of 10 μM cytochrome *c* (cyt *c*) in 20 mM ammonium acetate. The weighted average charge state was used as an indicator of protein conformation in solution.

The emitter position was adjusted along three axes at a constant laser power (~600 mW) in order to determine how the position affects solution heating during laser irradiation. An emitter tip was centered ~2.5 mm distant to the heated metal capillary interface of the mass spectrometer, and the final ~0.5 mm of the emitter tip was exposed to the laser beam. Under these conditions, the weighted average charge state for cyt *c* was 9.94 ± 0.08 (Figure S1), corresponding to half of the

protein in an unfolded form, compared to a value of 6.93 ± 0.02 when the emitter tip was not heated and the protein is fully folded.

With the emitter tip behind the beam block, there is no change in the average charge state of cyt *c* when the laser is on, even though nanodroplets formed by ESI pass through the ~600 mW laser beam before entering the mass spectrometer. This indicates that the nanodroplets are not significantly heated by the relatively low power of the unfocused laser beam, consistent with earlier CO_2 laser heated droplet experiments that required higher laser power (up to 17 W) focused to a 500 μm spot size to induce protein unfolding.[15,21] Exposing the emitter tip to more laser irradiation by positioning it ~1.5 mm in front of the beam block increased the weighted average charge state of cyt *c* to 10.8 ± 0.1, which is significantly higher than the value of 9.94 ± 0.08 when the tip is positioned only ~0.5 mm in front of the beam block. This indicates that exposing more of the emitter tip to the laser beam leads to higher solution temperature, either as a result of greater thickness of the borosilicate material further from the emitter tip leading to more absorption of the laser light or relatively lower conductive heat loss either to the surrounding air or to the rest of the capillary.

Adjustment of the emitter tip position along the *y*-axis (up or down with respect to the laser beam) also affects the average charge state of cyt *c* ions (Figure S1). The weighted average charge state varied from 7.06 ± 0.09 to 9.94 ± 0.08 over the distance ± 1 mm from the center. In contrast, adjustment of the emitter position ~0.5 mm left or right along the *z*-axis (axis of beam propagation) resulted in an average change in the weighted average charge state of only 0.2 (Figure S1), consistent with the low divergence of the laser along the direction of propagation. The ion signal is similar at each emitter position, indicating the differences in the observed charge-state distribution are due to different extents of heating and not differences in ion collection efficiency. These results indicate that careful positioning of the emitter with respect to the length exposed to laser light and the centering of the emitter within the beam is necessary in order to obtain reproducible heating of the solution inside the emitter. In subsequent experiments, the emitter was positioned so that the +12 charge state of cyt *c* was at ~50% relative abundance to the +7 charge state at ~600 mW of laser power to ensure reproducible tip positioning.

7.4.2 Rate of Laser Heating and Conductive Heat Loss

The rate of solution heating and cooling with LH-ESI was compared to that obtained using a resistively heated ESI emitter based on an earlier design.[51] With the latter device, changing the temperature of 20 μL of solution from ~79.5 °C to ~85 °C requires ~70 s (Figure S2). This time is consistent with that reported for other devices where thermal equilibration times at each temperature of ~1 – 3 minutes have been reported.[8,12,18,20,24,28,36,37]

In contrast, the solution inside the tip of an electrospray emitter can be rapidly heated using a laser. Changing the laser power from 0.0 W (ambient temperature) to ~1.2 W results in a change in the average charge state of cyt *c* from 6.92 ± 0.03 to 10.3 ± 0.3 within the duration of two mass spectral acquisitions (~0.5 s) and remains nearly the same with continued irradiation, indicating that the solution temperature has reached a steady state in less than 0.5 s (Figure 2, right axis). An exponential fit to the data results in a time constant of 0.11 s^{-1}. These data indicate that the time required to establish a steady state temperature upon heating an emitter tip with a laser (<0.5 s) is more than a factor of 100 less than that required for conventional vT-ESI sources. The rapid heating

and thermal steady state is likely due to the small volume of liquid that is heated inside the emitter tip and the low thermal mass of the emitter tip.

The absorption coefficient at 10.6 μm for Corning 7740 borosilicate glass used in Sutter Instrument capillaries has been reported to be 4893 cm^{-1} and 7812 cm^{-1} by the KBr pellet technique and the reflection method,[55] respectively, compared to a value of ~832 cm^{-1} for water.[31] Thus, the capillary absorbs light at a rate that is ~6 – 9 times greater than the aqueous solution itself. This indicates that the temperature of the borosilicate glass is higher than that of the solution, but the fast thermal steady state in solution indicates that heat conduction from the capillary to the aqueous solution occurs rapidly.

To investigate how rapidly the solution inside the electrospray emitter cools upon turning off the laser, the same cyt *c* solution was irradiated at 1.3 W, the highest laser power used in these experiments. The average charge state was 10.92 ± 0.03 prior to turning off the laser, upon which time, the average charge state decreased over the course of four seconds and returned to a steady state value of 6.95 ± 0.01, the same as that prior to turning on the laser (6.92 ± 0.03) (Figure 2, right axis). These data show that conductive heat loss from the emitter to the surrounding air is rapid and indicates that temperature melting data can be cycled from high to low temperature within four seconds.

7.4.3 Rapid Protein Melting Measurements

The performance of the LH-ESI apparatus for rapid protein melting measurements was evaluated by acquiring mass spectra of a solution of 10 μM cyt *c* in 20 mM ammonium acetate (pH 6.8) as a function of laser power from 0 W to 1.3 W. Upon increasing the laser power from 0 W to 1.3 W, the weighted average charge state of cyt *c* ions increased from ~6.93 ± 0.02 to ~10.85 ± 0.03, indicating that the protein population transitions from entirely folded to ~77% unfolded (Figure 3, red curve). The average charge state as a function of laser power was fit to a 7-parameter sigmoidal function. This resulted in a melting power, P_m, of ~0.60 ± 0.02 W obtained from three replicate measurements in which different electrospray emitters were used. The deviation in P_m between replicates is likely due to minor differences in positioning each emitter. Each of the replicate melting curves has the same shape, so a small linear power adjustment (<5%) can be done to make the melting powers for each curve match. This reduces the effects of minor differences in emitter positioning. The resulting P_m after these adjustments was 0.599 ± 0.001 W.

Protein thermal denaturation has also been observed by "laser-spray" ESI and by heating nanodroplets using a focused 10.6 μm laser beam. Shi *et al.* observed denaturation of cyt *c* in 1 mM ammonium acetate during laser-spray ESI using a 100 μm diameter stainless steel emitter at similar laser powers to those reported here.[38] At laser powers >1.6 W, cyt *c* dimers were observed. The authors proposed that the dimer signal is due to solvent evaporation at higher temperatures that increased concentration of cyt *c* at the emitter tip. Cyt *c* dimer signal is not observed at any laser power in the LH-ESI experiments reported here, likely due to the relatively small surface area exposed at the end of the borosilicate emitters, which reduces solvent evaporation. Nanodroplet heating experiments by El-Baba *et al*. required much higher laser fluences (up to 17 W and a beam focus of 500 μm) due to the low absorbance cross-section of water at this wavelength.[15] In our LH-ESI experiments, an unfocused laser at a power of only 1.3 W was sufficient to achieve complete melting of cyt *c* (T_m = 73.5 ± 0.5 °C) owing to the high absorbance

of borosilicate at this wavelength. At laser powers between 6 – 10 W, significantly higher than those used for LH-ESI experiments, emitters were observed to melt, disrupting the electrospray process.

In a separate experiment, the laser beam was focused to ~1 mm diameter in front of the emitter tip using a 50 mm focal length lens. There is no change in the average charge state when the laser power is changed from 0 W to ~17 W (Figure 3, left inset). These results indicate that a higher power is required to heat the nanodroplets to sufficient temperatures to initiate cyt *c* unfolding and that droplet heating is negligible in the LH-ESI experiments. The lower power required to achieve complete melting of a relatively stable protein with LH-ESI is an advantage of heating the emitter directly compared to heating the nanodroplets at 10.6 μm.

Because the solution temperature in LH-ESI experiments reaches a steady state in <0.5 s upon a large change in laser power, the laser power can be varied rapidly in order to measure protein melting curves. The LH-ESI melting curve of cyt *c* shown in Figure 3 required only ~40 s of total acquisition time per replicate to obtain. The acquisition speed is ultimately limited by the signal-to-noise ratio obtained in the mass spectral data. These spectra have high S/N (Figure 3, left inset) indicating the potential for these data to be acquired more quickly.

In contrast, the resistively heated vT-ESI source required much longer time to acquire temperature melts owing to the time necessary to establish a steady state at each set temperature. Data obtained for cyt *c* from ~27 °C to ~90 °C is shown in Figure 3. Over this temperature range, the average charge state increased from ~7.00 ± 0.03 to ~11.1 ± 0.3 (Figure 3, blue curve). An average charge state of 11.1 at ~90 °C from vT-ESI is similar to the value of 10.9 obtained at 1.3 W from LH-ESI, indicating that a similar temperature is achieved between these two methods. Increasing the solution temperature beyond ~90 °C resulted in a loss of signal due to bubble formation in the emitter tip that stopped the spray. A sigmoidal fit to the data results in a T_m of 73.5 ± 0.5 °C, matching well with prior reported values.[25,56] Because a minimum of 70 s between temperature points was needed to ensure a steady state temperature, the vT-ESI experiments required approximately 21 minutes per replicate. Consequently, >1 hour was required to acquire the three replicates shown in Figure 3 using vT-ESI. These results indicate that protein thermal denaturation data can be acquired 30 times faster with LH-ESI than resistively heated vT-ESI. However, the laser-heated method requires calibration in order to convert laser power to solution temperature.

7.4.4 Calibrating Laser Power to Solution Temperature

Melting powers determined from LH-ESI can be converted into melting temperatures by comparison to vT-ESI data. The change in the average charge state of cyt *c* for both LH-ESI and vT-ESI experiments was normalized between 0 and 1 (Δq). The Δq value at each laser power from LH-ESI was compared to that at each temperature from vT-ESI to determine an effective solution temperature within the tip during laser irradiation. When the Δq values are equal between these two experiments, then the temperatures within the tip should be the same. By finding each point where the normalized values are equal, a calibration curve was constructed to convert the measured laser power to temperature (Figure S3).

The laser power to temperature conversion makes it possible to determine how the solution *temperature* changes after the laser is turned on or off from the change in the average charge state

as a function of time. Upon turning the laser power on to ~1.2 W, the average charge state of cyt *c* increases from the ambient temperature value of 6.92 ± 0.03 to 10.33 ± 0.32 in <0.5 s, corresponding to a solution temperature of ~78.2 ± 2.5 °C (Figure 2, left axis; steady state temperature of ~77.4 ± 1.4 °C at later times). The data were fit to an exponential function with a time constant of 0.07 ± 0.01 s^{-1}.

A laser power of 1.3 W results in an average charge state of cyt *c* of 10.92 ± 0.03 corresponding to a solution temperature of 82.6 ± 0.6 °C (Figure 2, left axis). Upon turning off the laser, the average charge state of cyt *c* decreased to 7.30 ± 0.04 within the acquisition time of a single mass spectrum (~0.42 s), corresponding to a temperature of ~56 ± 3 °C. The solution temperature returns to ~28.5 °C (ambient temperature, the ESI emitter is close to the heated electrospray interface of the mass spectrometer) within four seconds. The data were fit to a single exponential function with a decay rate of 1.0 ± 0.1 s^{-1}. These experiments confirm that the solution temperature inside the ESI emitter rapidly reaches a steady state upon turning on the laser, cools quickly once the laser is turned off and that measurements in LH-ESI can be made within 0.5 s provided that the temperature is not reduced by more than 25 °C within this time. In contrast, emitters heated with the vT-ESI source required ~13 minutes on average to cool to room temperature after acquisition of a single melting curve as a result of the larger thermal mass associated with the aluminum heating jacket. Although this time could be reduced by actively cooling the emitters, either using Peltier devices or forced air-cooling for example, the cooling time between replicates poses a significant barrier to making vT-ESI techniques high-throughput.

This laser power to temperature conversion can be used to determine the T_m values of other proteins that have not been characterized by vT-ESI. However, positioning of the tip is critical (Figure S1) in order for this same calibration data to be used. To reduce the uncertainties in tip positioning, cyt *c* was used as an internal calibrant of temperature to more accurately measure the melting temperatures of other proteins in a solution.

7.4.5 Determining T_m Values with LH-ESI

In order to investigate the accuracy of LH-ESI for measuring T_m values of other proteins using cyt *c* as an internal calibrant, LH-ESI and vT-ESI data were obtained for a solution containing cyt *c*, equine heart myoglobin, and pseudo-wild type barstar (Ψbar*) at 3 μM each (Figure 4). The weighted average charge of cyt *c* increases from 6.9 ± 0.1 to 11.0 ± 1.0 upon an increase in temperature from ~29 °C to ~90 °C, comparable to the change from 7.05 ± 0.02 to 10.28 ± 0.09 upon increasing the laser power from 0 W to ~900 mW. Further increases in laser power resulted in unstable spray. The population abundance of apo-myoglobin ions (myoglobin that has lost a noncovalently bound heme) increased from 1.0 % ± 1.0 % to 100 % ± 0 % and 1.6 % ± 2.8% to 98.3 % ± 0.3 % across the same ranges of temperature and laser power, respectively. The protein Ψbar* undergoes a much smaller change in the weighted average charge state from 5.4 ± 0.1 to 6.4 ± 0.1 between ~29 °C and ~68 °C in vT-ESI experiments. Above 68 °C, Ψbar* ions are not observed in the vT-ESI mass spectra. However, during LH-ESI Ψbar* ions are observed at the highest laser powers and the weighted average charge state increases from 5.4 ± 0.1 at 0 W to 6.6 ± 0.1 at ~900 mW. The observation of Ψbar* ions at a higher temperature with LH-ESI may be related to the different experimental time scales. Formation of nonspecific aggregates of denatured

Ψbar* may occur during the long thermal equilibration times in vT-ESI, whereas aggregates may not form as quickly during LH-ESI due to the rapid measurement (<45 s). LH-ESI data for Ψbar* at low laser powers has significant scatter, which may be related to variations in laser power near the threshold for lasing. These data highlight an advantage of MS-based measurements of thermal stability – the capacity to measure the thermal denaturation of multiple proteins from the same solution simultaneously.

The Δq values were determined from these data and a temperature calibration using cyt *c* was applied to the LH-ESI data to generate the melting curves shown in Figure 4. A sigmoidal fit to the vT-ESI data resulted in T_m values for cyt *c*, myoglobin, and Ψbar* of 76.3 ± 4.2 °C, 71.6 ± 0.5 °C, and 58.2 ± 1.5 °C, respectively (Figure 4, dashed lines). T_m values determined from temperature-recalibrated LH-ESI measurements were 73.1 ± 1.2 °C, 71.5 ± 0.9 °C, and 63.1 ± 4.7 °C for cyt *c*, myoglobin, and Ψbar*, respectively, which agree well with values obtained by vT-ESI (Figure 4, solid lines).

The temperature calibration is most sensitive when there is a large change in average charge state with increasing temperature. The change in average charge state of cyt *c* is small at low temperature leading to greater uncertainty in the low temperature region. The larger difference in T_m values for Ψbar* obtained with the two methods may in part be attributed to this effect. More reproducible positioning of the emitter tips and calibrating the laser power using multiple proteins that have different T_m values should increase the accuracy and precision of the LH-ESI method. Combined, these experiments demonstrate the potential of LH-ESI for the high-throughput measurement of protein thermal stabilities by nESI-MS and elucidate the practical considerations for performing LH-ESI measurements of protein melting temperatures.

7.5 Conclusions

A CO_2 laser can rapidly change the temperature of solution inside the tip of a borosilicate glass electrospray emitter. A change in laser power from zero (ambient temperature) to 1.2 W results in a steady state solution temperature of 78 °C within less than 0.5 s. The fast heating time is a result of high absorption of borosilicate and the low thermal mass of the emitter tip that enables rapid energy transfer into the aqueous solution. The time necessary to return from a steady state temperature of 83 °C to ambient temperature after turning off the laser is about four seconds. The longer time for cooling reflects the slow thermal transfer rate from the tip of the capillary to the rest of the capillary as well as to the surrounding air, which could be improved by forced air cooling. Heating and cooling with LH-ESI is more than 100x faster than a thermally heated apparatus that was constructed for comparison.

This high heating/cooling rate makes it possible to acquire data as a function of laser power at least 31 times quicker than a conventional vT-ESI device. Laser powers can be calibrated to solution temperatures using the melting curves of proteins measured with both LH-ESI and vT-ESI. This calibration works well for proteins that have similar melting temperatures as the calibrant, but is most sensitive where there is the greatest change in the average charge with temperature. The ideal laser power-temperature calibrant would have a steady change in the average charge state over a large temperature range and would not undergo aggregation or degradation. An advantage of using a laser to heat the emitter tip vs heating nanodroplets directly is that >2000x lower laser fluence can be used. The laser power needed for LH-ESI could be

reduced by focusing the laser at the emitter tip and should enable low powered lasers to be used in these experiments. Alternative wavelengths, such as 2.9 μm, which is the maximum in the absorption for liquid water in the infrared region, could mitigate the power differences in heating the emitter vs. the droplets directly.

LH-ESI shows significant promise for coupling with separation techniques. Native capillary electrophoretic separations often have peak widths <1 minute, which is less than the typical thermal equilibration time in vT-ESI. In contrast, an entire melting curve could be acquired with LH-ESI within this time. These thermal stability measurements would add an extra dimension of information to native MS coupled to separations. Rapidly heating just the end of the borosilicate emitter also has the potential to mitigate aggregation processes that occur above the T_m of a protein, which can be an issue with vT-ESI due to the significantly longer measurement times at high temperature. As a result of the quick thermal equilibration, LH-ESI may enable the analysis of the thermal stability of aggregation-prone proteins above the T_m before oligomerization disrupts the electrospray process. Protein desalting using submicron borosilicate emitters has enabled the study of protein structures from biochemically relevant buffers.[53,54] LH-ESI with submicron emitters could potentially be used for high-throughput thermal stability screens of proteins, macromolecular complexes, and antibodies directly from formulation buffers, quickly identifying candidates for further investigation during the development of novel biotherapeutics.

7.6 Acknowledgments

The authors thank Dr. Anthony T. Iavarone and Dr. Conner C. Harper for insightful discussions, Dr. Sanjay R. Krishnaswamy for sample preparation of pseudo-wild type barstar and reviewers for their helpful comments and suggestions. This material is based upon work supported by the National Science Foundation Division of Chemistry under grant number CHE-1609866, CHE-2203907, a Graduate Research Fellowship (DGE-2146752), CALSOLV, as well as the Merck DBL SEEDS program. The authors thank the staff at the University of California, Berkeley Electron Microscopy Laboratory for advice on electrospray emitter imaging.

7.7 References

(1) Ibarra-Molero, B.; Loladze, V. V.; Makhatadze, G. I.; Sanchez-Ruiz, J. M. Thermal versus Guanidine-Induced Unfolding of Ubiquitin. An Analysis in Terms of the Contributions from Charge-Charge Interactions to Protein Stability. *Biochemistry* **1999**, *38*, 8138–8149.
(2) Norma J. Greenfield. Using Circular Dichroism Collected as a Function of Temperature to Determine the Thermodynamics of Protein Unfolding and Binding Interactions. *Nat. Protoc.* **2006**, *1*, 2527–2535.
(3) Huynh, K.; Partch, C. L. Analysis of Protein Stability and Ligand Interactions by Thermal Shift Assay. *Curr. Protoc. Protein Sci.* **2015**, *79*, 28.9.1-28.9.14.
(4) Schultz, D. A.; Baldwin, R. L. Cis Proline Mutants of Ribonuclease A. I. Thermal Stability. *Protein Sci.* **1992**, *1*, 910–916.

(5) Shih, P.; Kirsch, J. F.; Holland, D. R. Thermal Stability Determinants of Chicken Egg-White Lysozyme Core Mutants: Hydrophobicity, Packing Volume, and Conserved Buried Water Molecules. *Protein Sci.* **1995**, *4*, 2050–2062.
(6) Marchand, A.; Rosu, F.; Zenobi, R.; Gabelica, V. Thermal Denaturation of DNA G-Quadruplexes and Their Complexes with Ligands: Thermodynamic Analysis of the Multiple States Revealed by Mass Spectrometry. *J. Am. Chem. Soc.* **2018**, *140*, 12553–12565.
(7) Lo, M. C.; Aulabaugh, A.; Jin, G.; Cowling, R.; Bard, J.; Malamas, M.; Ellestad, G. Evaluation of Fluorescence-Based Thermal Shift Assays for Hit Identification in Drug Discovery. *Anal. Biochem.* **2004**, *332*, 153–159.
(8) Harrison, J. A.; Pruška, A.; Oganesyan, I.; Bittner, P.; Zenobi, R. Temperature-Controlled Electrospray Ionization: Recent Progress and Applications. *Chem. Eur. J.* **2021**, *27*, 18015–18028.
(9) Wen, J.; Lord, H.; Knutson, N.; Wikström, M. Nano Differential Scanning Fluorimetry for Comparability Studies of Therapeutic Proteins. *Anal. Biochem.* **2020**, *593*, 113581.
(10) Poklar, N.; Vesnaver, G. Thermal Denaturation of Proteins Studied by UV Spectroscopy. *J. Chem. Educ.* **2000**, *77*, 380.
(11) Kresheck, G. C.; Erman, J. E. Calorimetric Studies of the Thermal Denaturation of Cytochrome c Peroxidase. *Biochemistry* **1988**, *27*, 2490–2496.
(12) Wang, G.; Bondarenko, P. V.; Kaltashov, I. A. Multi-Step Conformational Transitions in Heat-Treated Protein Therapeutics Can Be Monitored in Real Time with Temperature-Controlled Electrospray Ionization Mass Spectrometry. *Analyst* **2018**, *143*, 670–677.
(13) Jarzab, A.; Kurzawa, N.; Hopf, T.; Moerch, M.; Zecha, J.; Leijten, N.; Bian, Y.; Musiol, E.; Maschberger, M.; Stoehr, G.; Becher, I.; Daly, C.; Samaras, P.; Mergner, J.; Spanier, B.; Angelov, A.; Werner, T.; Bantscheff, M.; Wilhelm, M.; Klingenspor, M.; Lemeer, S.; Liebl, W.; Hahne, H.; Savitski, M. M.; Kuster, B. Meltome Atlas—Thermal Proteome Stability across the Tree of Life. *Nat. Methods* **2020**, *17*, 495–503.
(14) Vallejo, D. D.; Rojas Ramírez, C.; Parson, K. F.; Han, Y.; Gadkari, V. V.; Ruotolo, B. T. Mass Spectrometry Methods for Measuring Protein Stability. *Chem. Rev.* **2022**, *122*, 7690–7719.
(15) El-Baba, T. J.; Fuller, D. R.; Woodall, D. W.; Raab, S. A.; Conant, C. R.; Dilger, J. M.; Toker, Y.; Williams, E. R.; Russell, D. H.; Clemmer, D. E. Melting Proteins Confined in Nanodroplets with 10.6 μm Light Provides Clues about Early Steps of Denaturation. *Chem. Commun.* **2018**, *54*, 3270–3273.
(16) Wyttenbach, T.; Bowers, M. T. Structural Stability from Solution to the Gas Phase: Native Solution Structure of Ubiquitin Survives Analysis in a Solvent-Free Ion Mobility-Mass Spectrometry Environment. *J. Phys. Chem. B* **2011**, *115*, 12266–12275.
(17) Gross, D. S.; Zhao, Y.; Williams, E. R. Dissociation of Heme-Globin Complexes by Blackbody Infrared Radiative Dissociation: Molecular Specificity in the Gas Phase? *J. Am. Soc. Mass Spectrom.* **1997**, *8*, 519–524.
(18) Brown, C. J.; Woodall, D. W.; El-Baba, T. J.; Clemmer, D. E. Characterizing Thermal Transitions of IgG with Mass Spectrometry. *J. Am. Soc. Mass Spectrom.* **2019**, *30*, 2438–2445.
(19) El-Baba, T. J.; Raab, S. A.; Buckley, R. P.; Brown, C. J.; Lutomski, C. A.; Henderson, L. W.; Woodall, D. W.; Shen, J.; Trinidad, J. C.; Niu, H.; Jarrold, M. F.; Russell, D. H.; Laganowsky, A.; Clemmer, D. E. Thermal Analysis of a Mixture of Ribosomal Proteins by vT-ESI-MS: Toward a Parallel Approach for Characterizing the Stabilitome. *Anal. Chem.* **2021**, *93*, 8484–8492.
(20) El-Baba, T. J.; Woodall, D. W.; Raab, S. A.; Fuller, D. R.; Laganowsky, A.; Russell, D. H.; Clemmer, D. E. Melting Proteins: Evidence for Multiple Stable Structures upon Thermal

Denaturation of Native Ubiquitin from Ion Mobility Spectrometry-Mass Spectrometry Measurements. *J. Am. Chem. Soc.* **2017**, *139*, 6306–6309.
(21) Woodall, D. W.; Henderson, L. W.; Raab, S. A.; Honma, K.; Clemmer, D. E. Understanding the Thermal Denaturation of Myoglobin with IMS-MS: Evidence for Multiple Stable Structures and Trapped Pre-Equilibrium States. *J. Am. Soc. Mass Spectrom.* **2021**, *32*, 64–72.
(22) Woodall, D. W.; El-Baba, T. J.; Fuller, D. R.; Liu, W.; Brown, C. J.; Laganowsky, A.; Russell, D. H.; Clemmer, D. E. Variable-Temperature ESI-IMS-MS Analysis of Myohemerythrin Reveals Ligand Losses, Unfolding, and a Non-Native Disulfide Bond. *Anal. Chem.* **2019**, *91*, 6808–6814.
(23) El-Baba, T. J.; Clemmer, D. E. Solution Thermochemistry of Concanavalin A Tetramer Conformers Measured by Variable-Temperature ESI-IMS-MS. *Int. J. Mass Spectrom.* **2019**, *443*, 93–100.
(24) Benesch, J. L. P.; Sobott, F.; Robinson, C. V. Thermal Dissociation of Multimeric Protein Complexes by Using Nanoelectrospray Mass Spectrometry. *Anal. Chem.* **2003**, *75*, 2208–2214.
(25) Wang, G.; Abzalimov, R. R.; Kaltashov, I. A. Direct Monitoring of Heat-Stressed Biopolymers with Temperature-Controlled Electrospray Ionization Mass Spectrometry. *Anal. Chem.* **2011**, *83*, 2870–2876.
(26) Shirzadeh, M.; Poltash, M. L.; Laganowsky, A.; Russell, D. H. Structural Analysis of the Effect of a Dual-FLAG Tag on Transthyretin. *Biochemistry* **2020**, *59*, 1013–1022.
(27) Jeanne Dit Fouque, K.; Fernandez-Lima, F. Following Structural Changes by Thermal Denaturation Using Trapped Ion Mobility Spectrometry-Mass Spectrometry. *J. Phys. Chem. B* **2020**, *124*, 6257–6265.
(28) Geels, R. B. J.; Calmat, S.; Heck, A. J. R.; van der Vies, S. M.; Heeren, R. M. A. Thermal Activation of the Co-Chaperonins GroES and Gp31 Probed by Mass Spectrometry. *Rapid Commun. Mass Spectrom.* **2008**, *22*, 3633–3641.
(29) Harrison, J. A.; Pruška, A.; Bittner, P.; Muck, A.; Cooper-Shepherd, D. A.; Zenobi, R. Advancing Cyclic Ion Mobility Mass Spectrometry Methods for Studying Biomolecules: Toward the Conformational Dynamics of Mega Dalton Protein Aggregates. *Anal. Chem.* **2022**, *94*, 12435–12443.
(30) Kostelic, M. M.; Ryan, J. P.; Brown, L. S.; Jackson, T. W.; Hsieh, C.; Zak, C. K.; Sanders, H. M.; Liu, Y.; Chen, V. S.; Byrne, M.; Aspinwall, C. A.; Baker, E. S.; Marty, M. T. Stability and Dissociation of Adeno-Associated Viral Capsids by Variable Temperature-Charge Detection-Mass Spectrometry. *Anal. Chem.* **2022**, *94*, 11723–11727.
(31) Marchand, A.; Czar, M. F.; Eggel, E. N.; Kaeslin, J.; Zenobi, R. Studying Biomolecular Folding and Binding Using Temperature-Jump Mass Spectrometry. *Nat. Commun.* **2020**, *11*, 566.
(32) Cong, X.; Liu, Y.; Liu, W.; Liang, X.; Russell, D. H.; Laganowsky, A. Determining Membrane Protein-Lipid Binding Thermodynamics Using Native Mass Spectrometry. *J. Am. Chem. Soc.* **2016**, *138*, 4346–4349.
(33) Qiao, P.; Schrecke, S.; Walker, T.; McCabe, J. W.; Lyu, J.; Zhu, Y.; Zhang, T.; Kumar, S.; Clemmer, D.; Russell, D. H.; Laganowsky, A. Entropy in the Molecular Recognition of Membrane Protein-Lipid Interactions. *J. Phys. Chem. Lett.* **2021**, *12*, 12218–12224.
(34) Raab, S. A.; El-Baba, T. J.; Woodall, D. W.; Liu, W.; Liu, Y.; Baird, Z.; Hales, D. A.; Laganowsky, A.; Russell, D. H.; Clemmer, D. E. Evidence for Many Unique Solution Structures for Chymotrypsin Inhibitor 2: A Thermodynamic Perspective Derived from vT-ESI-IMS-MS Measurements. *J. Am. Chem. Soc.* **2020**, *142*, 17372–17383.

(35) Pruška, A.; Marchand, A.; Zenobi, R. Novel Insight into Proximal DNA Domain Interactions from Temperature-Controlled Electrospray Ionization Mass Spectrometry. *Angew. Chemie Int. Ed.* **2021**, *60*, 15390–15398.
(36) McCabe, J. W.; Shirzadeh, M.; Walker, T. E.; Lin, C. W.; Jones, B. J.; Wysocki, V. H.; Barondeau, D. P.; Clemmer, D. E.; Laganowsky, A.; Russell, D. H. Variable-Temperature Electrospray Ionization for Temperature-Dependent Folding/Refolding Reactions of Proteins and Ligand Binding. *Anal. Chem.* **2021**, *93*, 6924–6931.
(37) Walker, T. E.; Shirzadeh, M.; Sun, H. M.; McCabe, J. W.; Roth, A.; Moghadamchargari, Z.; Clemmer, D. E.; Laganowsky, A.; Rye, H.; Russell, D. H. Temperature Regulates Stability, Ligand Binding (Mg^{2+} and ATP), and Stoichiometry of GroEL-GroES Complexes. *J. Am. Chem. Soc.* **2022**, *144*, 2667–2678.
(38) Shi, X.; Takamizawa, A.; Nishimura, Y.; Hiraoka, K.; Akashi, S. Thermal Unfolding of Proteins Probed by Laser Spray Mass Spectrometry. *Rapid Commun. Mass Spectrom.* **2008**, *22*, 1430–1436.
(39) Nakamura, M.; Takamizawa, A.; Yamada, H.; Hiraoka, K.; Akashi, S. Denaturation of α-Lactalbumin and Ubiquitin Studied by Electrospray and Laser Spray. *Rapid Commun. Mass Spectrom.* **2007**, *21*, 1635–1643.
(40) Hiraoka, K.; Saito, S.; Katsuragawa, J.; Kudaka, I. A New Liquid Chromatography/Mass Spectrometry Interface: Laser Spray. *Rapid Commun. Mass Spectrom.* **1998**, *12*, 1170–1174.
(41) Kudaka, I.; Kojima, T.; Saito, S.; Hiraoka, K. A Comparative Study of Laser Spray and Electrospray. *Rapid Commun. Mass Spectrom.* **2000**, *14*, 1558–1562.
(42) Hiraoka, K. Laser Spray: Electric Field-Assisted Matrix-Assisted Laser Desorption/Ionization. *J. Mass Spectrom.* **2004**, *39*, 341–350.
(43) Takamizawa, A.; Itoh, Y.; Osawa, R.; Iwasaki, N.; Nishimura, Y.; Akashi, S.; Hiraoka, K. Selective Dissociation of Non-Covalent Bonds in Biological Molecules by Laser Spray. *J. Mass Spectrom.* **2004**, *39*, 1053–1058.
(44) Shi, X.; Nishimura, Y.; Akashi, S.; Takamizawa, A.; Hiraoka, K. Evaluation of Binding Affinity of Protein-Mutant DNA Complexes in Solution by Laser Spray Mass Spectrometry. *J. Am. Soc. Mass Spectrom.* **2006**, *17*, 611–620.
(45) Shi, X.; Takamizawa, A.; Nishimura, Y.; Hiraoka, K.; Akashi, S. Stability Analysis for Double-Stranded DNA Oligomers and Their Noncovalent Complexes with Drugs by Laser Spray. *J. Mass Spectrom.* **2006**, *41*, 1086–1095.
(46) Mortensen, D. N.; Williams, E. R. Ultrafast (1 μs) Mixing and Fast Protein Folding in Nanodrops Monitored by Mass Spectrometry. *J. Am. Chem. Soc.* **2016**, *138*, 3453–3460.
(47) Mortensen, D. N.; Williams, E. R. Investigating Protein Folding and Unfolding in Electrospray Nanodrops upon Rapid Mixing Using Theta-Glass Emitters. *Anal. Chem.* **2015**, *87*, 1281–1287.
(48) Mortensen, D. N.; Williams, E. R. Theta-Glass Capillaries in Electrospray Ionization: Rapid Mixing and Short Droplet Lifetimes. *Anal. Chem.* **2014**, *86*, 9315–9321.
(49) Xia, Z.; Williams, E. R. Effect of Droplet Lifetime on Where Ions Are Formed in Electrospray Ionization. *Analyst* **2019**, *144*, 237–248.
(50) Jordan, J. S.; Xia, Z.; Williams, E. R. Tips on Making Tiny Tips: Secrets to Submicron Nanoelectrospray Emitters. *J. Am. Soc. Mass Spectrom.* **2022**, *33*, 607–611.
(51) Sterling, H. J.; Williams, E. R. Origin of Supercharging in Electrospray Ionization of Noncovalent Complexes from Aqueous Solution. *J. Am. Soc. Mass Spectrom.* **2009**, *20*, 1933–1943.

(52) Krishnaswamy, S. R.; Williams, E. R.; Kirsch, J. F. Free Energies of Protein-Protein Association Determined by Electrospray Ionization Mass Spectrometry Correlate Accurately with Values Obtained by Solution Methods. *Protein Sci.* **2006**, *15*, 1465–1475.
(53) Susa, A. C.; Xia, Z.; Williams, E. R. Small Emitter Tips for Native Mass Spectrometry of Proteins and Protein Complexes from Nonvolatile Buffers That Mimic the Intracellular Environment. *Anal. Chem.* **2017**, *89*, 3116–3122.
(54) Susa, A. C.; Xia, Z.; Williams, E. R. Native Mass Spectrometry from Common Buffers with Salts That Mimic the Extracellular Environment. *Angew. Chemie Int. Ed.* **2017**, *56*, 7912–7915.
(55) Sahba, N.; Rockett, T. J. Infrared Absorption Coefficients of Silica Glasses. *J. Am. Ceram. Soc.* **1992**, *75*, 209–212.
(56) Yang, F.; Zhou, B. R.; Zhang, P.; Zhao, Y. F.; Chen, J.; Liang, Y. Binding of Ferulic Acid to Cytochrome c Enhances Stability of the Protein at Physiological PH and Inhibits Cytochrome C-Induced Apoptosis. *Chem. Biol. Interact.* **2007**, *170*, 231–243.

7.8 Figures

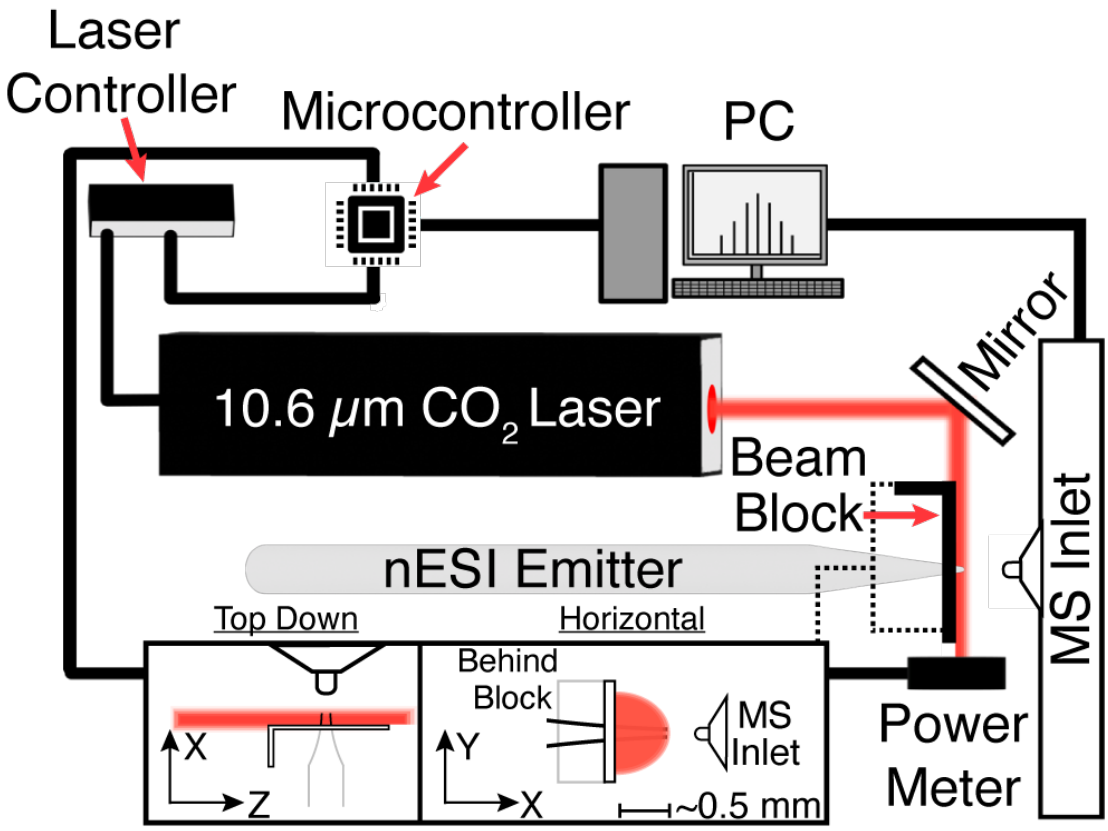

Figure 7.1. A schematic diagram of the laser heating device in combination with a mass spectrometer, where the tip of a borosilicate capillary is irradiated with 10.6 μm light from an unfocused CO_2 laser and laser power was measured and controlled with a microcontroller. The inset shows the emitter passing through the beam block.

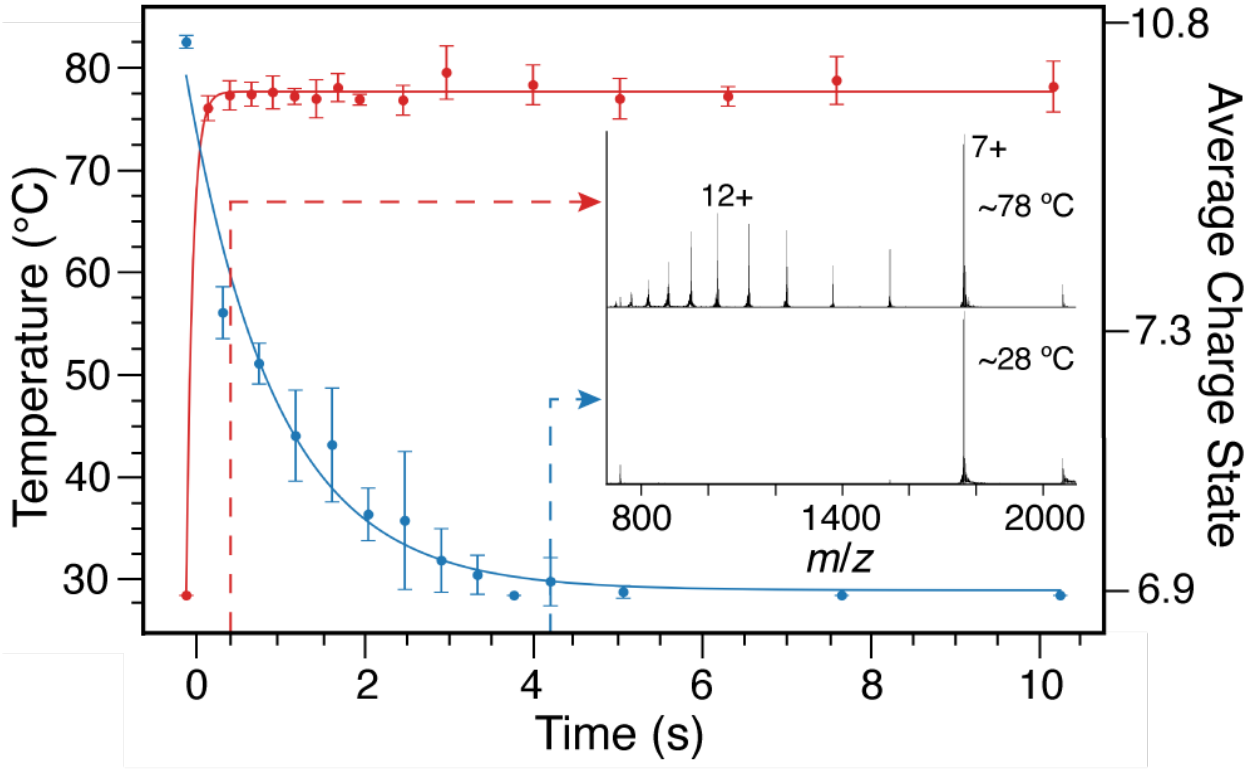

Figure 7.2. The average charge state of cyt *c* (right *y*-axis) as a function of time after the laser is turned on at a power of 1.2 W (red data) and after the laser is turned off at a marginally higher laser power (blue data). The inset shows mass spectra acquired 0.5 s after turning the laser on (top) and 4.2 s after turning the laser off (bottom). These data are converted to temperature (left *y*-axis) using the method described in the text. A blank spectrum shows that the peak at $m/z = 711$ is a contaminant.

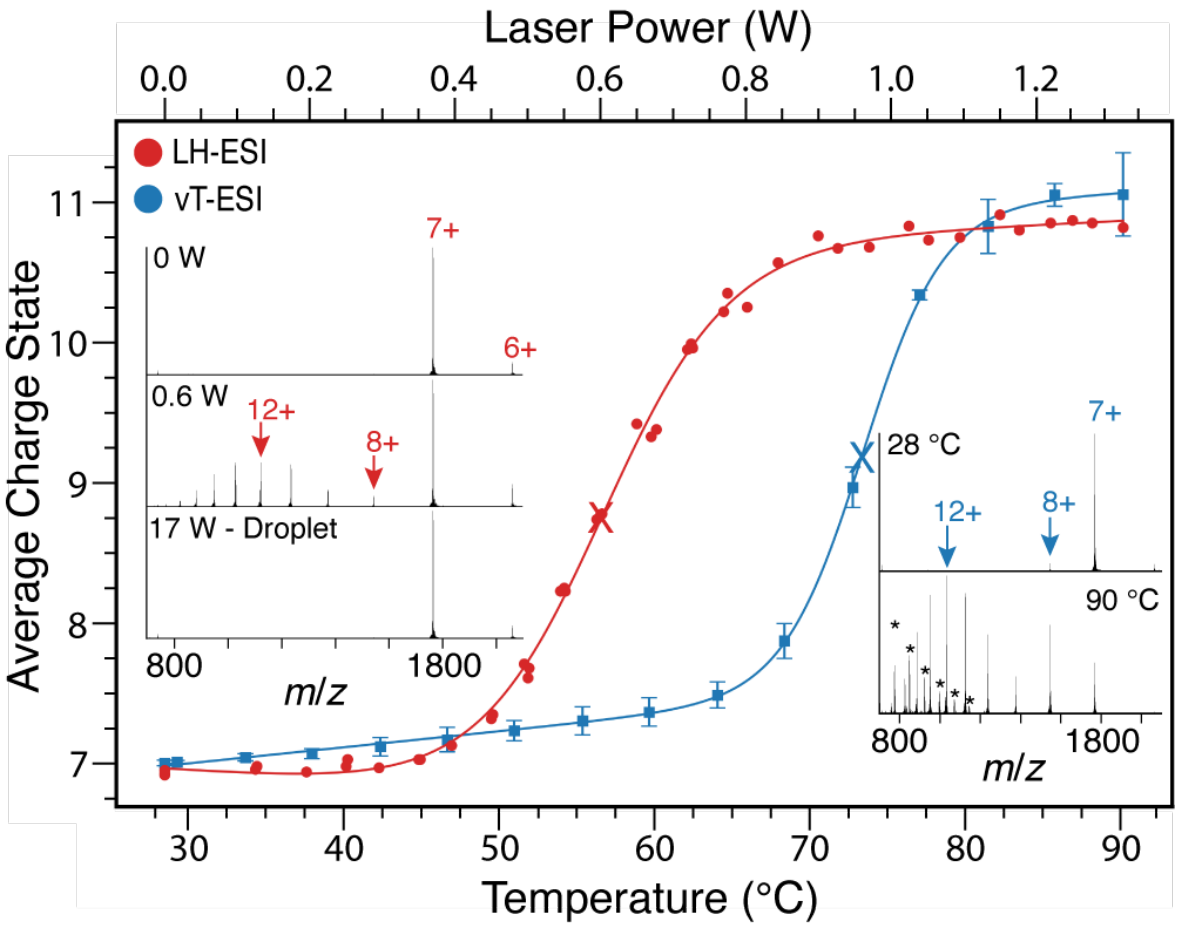

Figure 7.3. Melting curves for cyt *c* obtained by LH-ESI (red) and vT-ESI (blue). Data points from LH-ESI replicates are not typically at exactly the same laser power due to slight variations in laser power. A melting temperature and melting power of 73.5 ± 0.5 °C (blue cross) and 0.599 ± 0.001 W (red cross) are obtained from sigmoidal fits to the resistively heated and laser-heated data, respectively. Mass spectra of cyt *c* (left inset) acquired by emitter heating (middle) show a distribution at lower *m*/*z* indicating substantial protein unfolding at this power, but nanodroplet heating with a beam focused to ~1 mm (bottom) shows no evidence of protein unfolding. The right inset shows mass spectra acquired at different solution temperatures by vT-ESI. Asterisks indicate PDMS contaminant peaks.

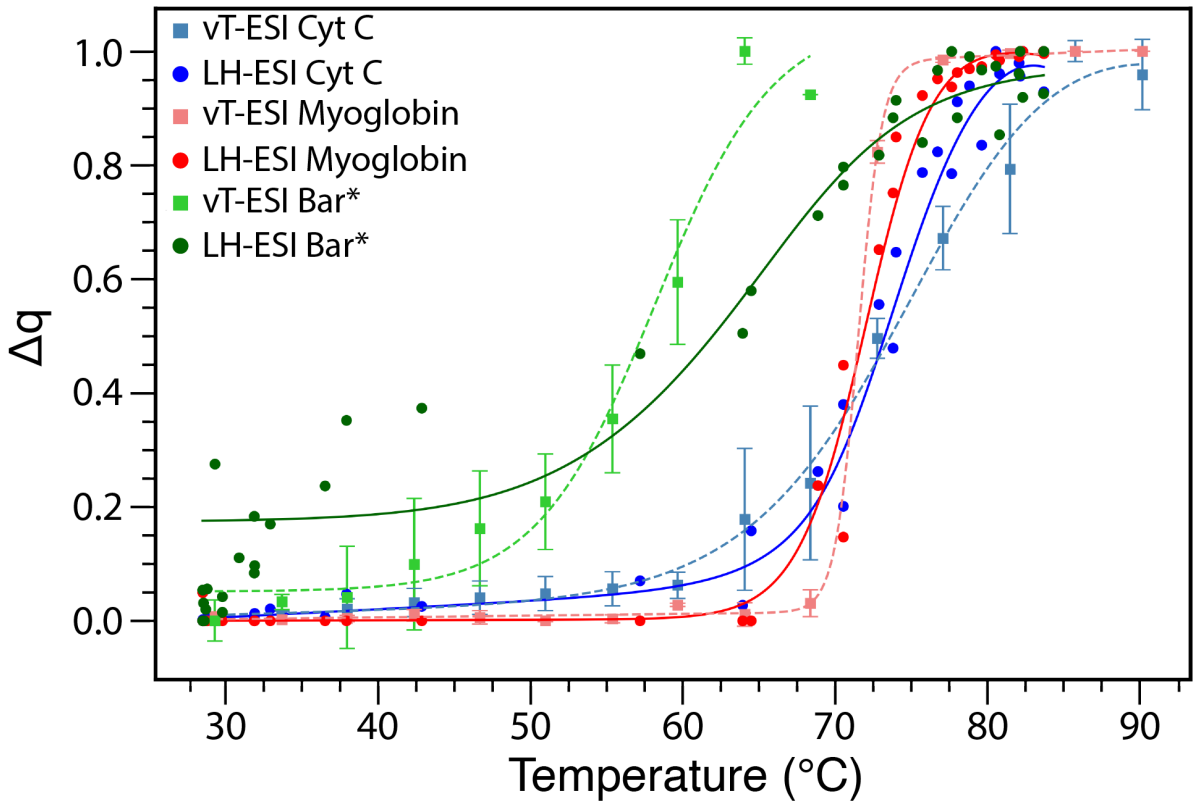

Figure 7.4. Temperature-calibrated melting curves for cyt *c*, myoglobin, and Ψbar* from LH-ESI (solid curves) and vT-ESI (dashed curves). The melting temperatures determined for myoglobin and Ψbar* from LH-ESI experiments agree with those obtained from vT-ESI.

7.9 Supplemental Information

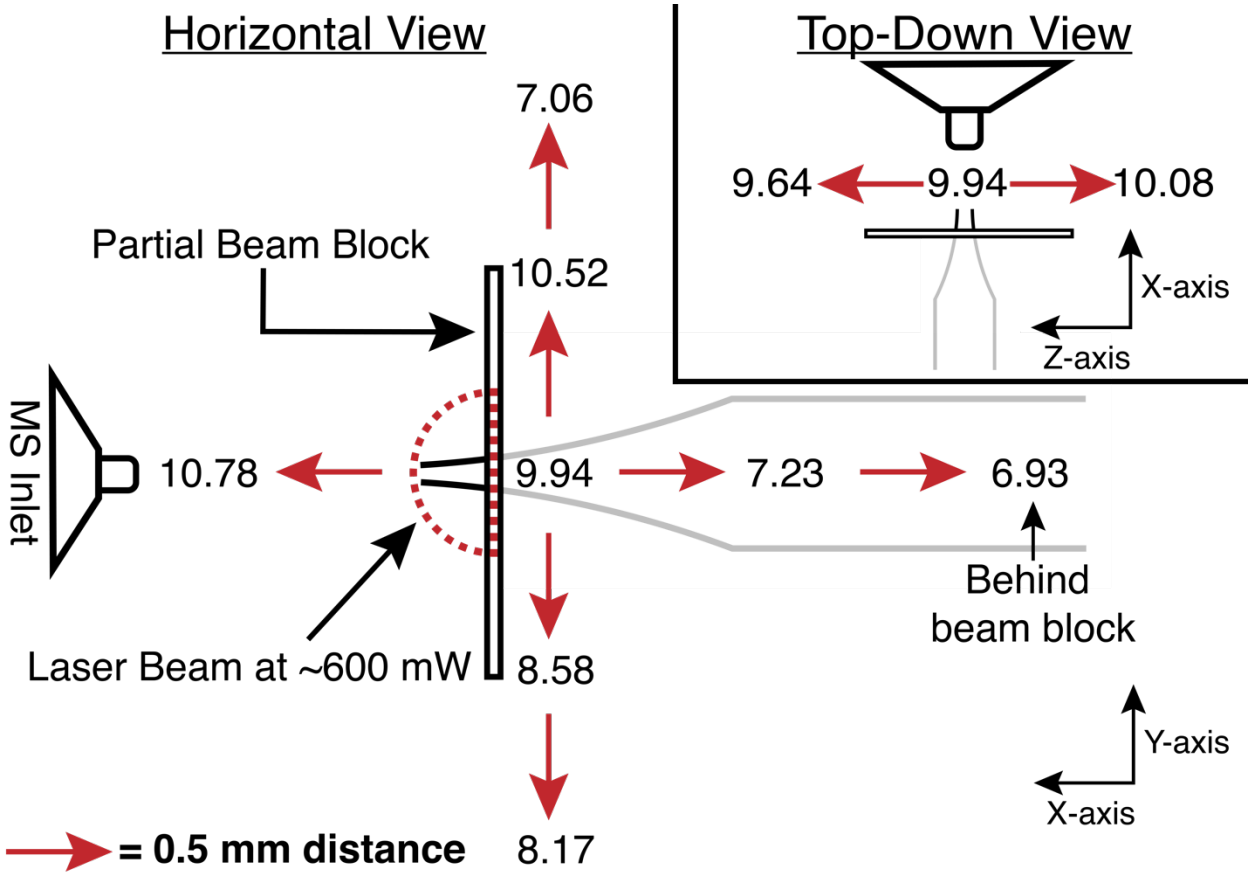

Supplemental Figure 7.1. Dependence of the weighted average charge state of cytochrome *c* on the position of the emitter within the LH-ESI source measured at a CO_2 laser power of 600 mW (unfocused laser beam). Each red arrow indicates the emitter was moved 0.5 mm in that direction.

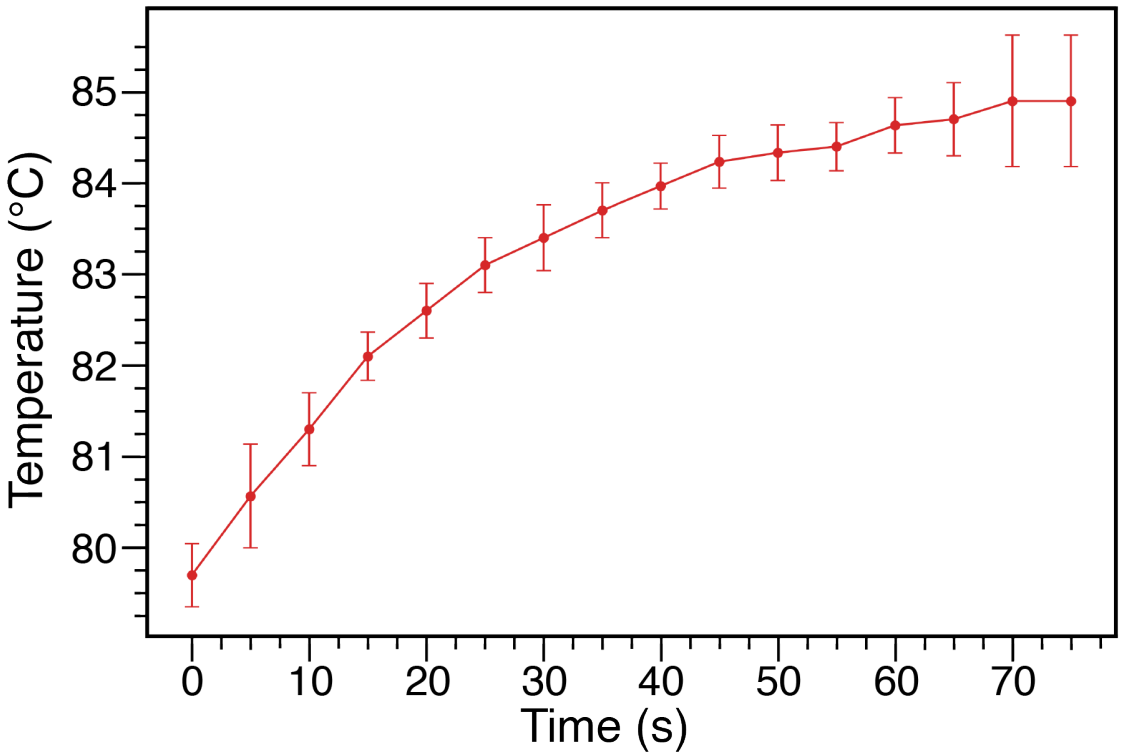

Supplemental Figure 7.2. The thermal equilibration time of the vT-ESI source for a change in temperature from ~79.5 °C to ~85 °C. Capillary was filled with 20 µL of cytochrome *c* in 20 mM ammonium acetate. Error bars represent the standard deviation from three replicate measurements using different emitters.

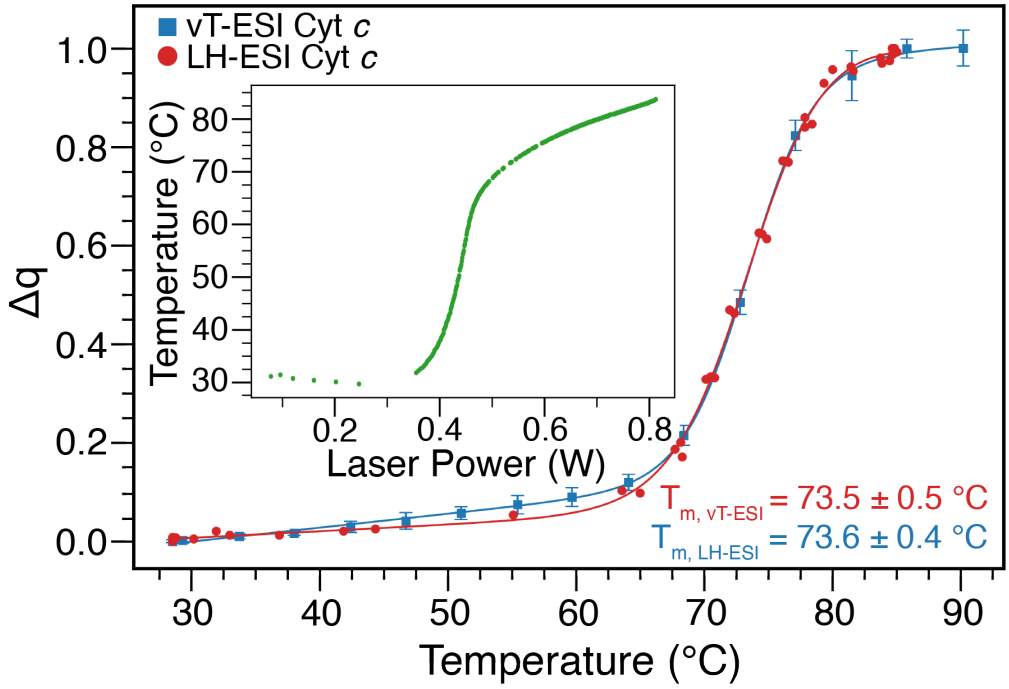

Supplemental Figure 7.3. Laser power calibration to solution temperature by normalizing both VT-ESI and LH-ESI charge state data and constructing a calibration function from each point where the Δq values are equal (inset). The melting temperature of cytochrome *c* determined from LH-ESI (73.6 ± 0.4 °C) matches well with the temperature determined by vT-ESI (73.5 ± 0.5 °C) as expected.

Chapter 8

Overcoming Aggregation with Laser Heated Nanoelectrospray Mass Spectrometry: Thermal Stability and Pathways for Loss of Bicarbonate from Carbonic Anhydrase II

This chapter is reproduced with permission from:

Jacob S. Jordan, Katherine J. Lee, Evan R. Williams

"Overcoming aggregation with laser heated nanoelectrospray mass spectrometry: thermal stability and pathways for loss of bicarbonate from carbonic anhydrase II"

Analyst, **2024**, *149*:2281-2290

8.1 Abstract

Variable temperature electrospray mass spectrometry is useful for multiplexed measurements of the thermal stabilities of biomolecules, but the ionization process can be disrupted by aggregation-prone proteins/complexes that have irreversible unfolding transitions. Resistively heating solutions containing a mixture of bovine carbonic anhydrase II (BCAII), a CO_2 fixing enzyme involved in many biochemical pathways, and cytochrome *c* leads to complete loss of carbonic anhydrase signal and a significant reduction in cytochrome *c* signal above ~72 °C due to aggregation. In contrast, when the tips of borosilicate glass nanoelectrospray emitters are heated with a laser, complete thermal denaturation curves for both proteins are obtained in <1 minute. The simultaneous measurements of the melting temperature of BCAII and BCAII bound to bicarbonate reveal that the bicarbonate stabilizes the folded form of this protein by ~6.4 °C. Moreover, the temperature dependences of different bicarbonate loss pathways are obtained. Although protein analytes are directly heated by the laser for only 140 ms, heat conduction further up the emitter leads to a total analyte heating time of ~41 s. Pulsed laser heating experiments could reduce this time to ~0.5 s for protein aggregation that occurs on a faster time scale. Laser heating provides a powerful method for studying the detailed mechanisms of cofactor/ligand loss with increasing temperature and promises a new tool for studying the effect of ligands, drugs, growth conditions, buffer additives, or other treatments on the stabilities of aggregation-prone biomolecules.

8.2 Introduction

Proteins typically function in one or more "native" conformations[1] that can be affected by solution properties including the pH,[2,3] ionic strength,[4–6] co-solutes such as ions,[6–8] other proteins or macromolecular crowding agents,[4,9,10] pressure,[11–13] and temperature.[14,15] Protein misfolding can result in aggregation-prone conformations, which are associated with a wide range of human diseases.[16] Thermal stability measurements or melting temperatures (T_m) are often used to determine how stable native protein complexes/conformations are relative to unfolded or misfolded states, which helps to predict how ligands may bind to certain structures, how enzymes may function under certain conditions, and how long protein therapeutics are stable when stored in different buffers. A number of biophysical assays are routinely used to study the thermal stabilities of proteins, protein complexes, and protein-ligand interactions, including circular dichroism,[14,17] differential scanning calorimetry,[17–19] differential scanning fluorimetry,[20,21] or ultraviolet/visible (UV/Vis)-spectrophotometry.[15,17] Fluorescence-based and calorimetric assays are routinely used to study the aggregation temperature of monoclonal antibodies and other biotherapeutic complexes from different buffer conditions.[21–24] However, all of these methods generally require purified samples and do not provide the type of detailed information that mass spectrometry (MS) can provide about solution conformers, unfolding intermediates, or ligand-binding.

Native MS is a well-established technique for measuring the stabilities of proteins and protein-ligand binding interactions.[25–29] It is possible to unambiguously identify ligand-binding from samples containing a single protein and thousands of potential ligands.[30] MS-based methods of measuring protein thermal stabilities have the advantage that they are sensitive and can be used to investigate protein mixtures as long as proteins have different masses that can be resolved.[31–33] Protein melting curves are obtained from MS data by monitoring the average charge state of each analyte or the relative abundance of conformers identified by ion mobility spectrometry. Variable-temperature electrospray ionization (vT-ESI), in which the solution temperature is varied during electrospray, has been used to determine the T_m values of proteins,[34–39] protein complexes,[19,34,40–46] protein as well as DNA complex unfolding pathways,[42,47–49] and the thermochemistry of ligand-binding to protein- and DNA-ligand complexes.[38,47,50,51] In combination with ion mobility spectrometry, thermochemical values can be determined for individual groups of closely related protein conformers.[36,38,40,52,53] The T_m values of 7 analyte molecules from a mixture of proteins was determined simultaneously, [54] clearly demonstrating the multiplexing capacity of this technique. Measurements with vT-ESI can be time consuming owing to the time necessary for thermal equilibration at each temperature. However, recent results demonstrate the acquisition of full melting curves for model proteins in <1 min.[39] Rapid heating of a solution on timescales between 0.8 ms – 4 minutes can also be done using theta glass emitters[55] or by rapidly flowing a solution through a resistively heated portion of an emitter.[35,47]

Protein melting has also been investigated using laser heating, either by irradiating the end of electrospray emitters[56–58] or by heating electrospray droplets directly.[38,59] Heating the end of a 100 μm diameter metal emitter led to protein unfolding and dissociation of noncovalent biomolecular complexes.[56,57,60] Heating the end of borosilicate emitters has the advantage that the solution temperature can be rapidly changed due to the small solution volume and rapid heat transfer to the surrounding atmosphere.[58] Solutions can be heated from room temperature to ~78 °C in less than 0.5 s and cooled from ~82 °C back to room temperature in <4 s.[58] The rapid equilibration enables

acquisition of protein melting curves in <40 s and laser power can be converted to solution temperature by calibration with vT-ESI data.[58] By laser heating electrospray droplets, unfolding intermediates were kinetically trapped and analyzed by ion mobility spectrometry.[38,59] Multiple time points along the unfolding process were measured using electrospray emitters with different diameters to produce droplets with different lifetimes. These laser-based heating techniques show great promise for rapidly characterizing protein T_m values, but to date, full melting curves have only been acquired for model proteins that have reversible unfolding transitions.

It is challenging to identify the T_m values of proteins that aggregate quickly with vT-ESI because of ion signal loss.[40,42] Here, the *rapid, localized* heating of laser-heated electrospray ionization (LH-ESI) enables, for the first time, detailed information about the thermal denaturation and bicarbonate loss mechanisms of bovine carbonic anhydrase II, a protein that rapidly aggregates at high temperatures, to be obtained. The effect of the bound bicarbonate reaction product on the thermal stability of the protein can also be obtained simultaneously from the same solution. The ability to measure melting transitions before aggregation can disrupt the electrospray process expands the multiplexing capacity of MS-based measurements of protein thermal stabilities to include mixtures containing aggregation-prone components, a class which includes monoclonal antibodies and other important biotherapeutics.

8.3 Experimental Methods

An LH-ESI source with a Synrad F48-2 10.6 μm CO_2 laser (Synrad Corporation, Mukilteo, WA) was used to heat the end of borosilicate glass electrospray emitters.[58] The length of the tip that was heated was limited with a metal beam block. Electrospray emitters were positioned in the beam using a 3-axis stage and a Dino-Lite digital microscope (Torrance, CA) such that either the final 300 μm or 500 μm of the tip was positioned past the beam block. An IR power meter head (Ophir-Spiricon, Logan, UT) was positioned downstream of the laser beam after the capillary to measure the laser power in real time. An Arduino Due microcontroller (Somerville, MA) was used to control and record the laser power during the experiment via Arduino and Python code. An electrospray voltage of +1.3 – 1.7 kV was applied to a platinum wire that was inserted into the back of the capillary and was in contact with the solution.

A vT-ESI source similar to that of Sterling et al.[61] was constructed for comparison to LH-ESI data. In brief, the source consists of an aluminum cylinder wrapped with resistive heating wire. The temperature of the apparatus is measured using a J-type thermocouple and an Omega CNi-3222 temperature controller (Stamford, CT). A thermocouple placed in the tip was used to calibrate the temperature measured inside of the heating jacket to a solution temperature. Electrospray emitters were inserted through the front end of the source until the emitter tip was aligned with the end of the heating jacket. The temperature of the apparatus was equilibrated for ~70 s at each temperature prior to starting electrospray at 1.3 kV. Data were acquired for ~10 s at each temperature for analysis. The custom LH-ESI or vT-ESI sources were aligned at the inlet of an Orbitrap Elite mass spectrometer (Thermo Fisher Corporation, Waltham, MA). Mass spectra were acquired between m/z = 500 – 4000 at a resolution setting of 15,000 to improve transmission of high m/z ions.

Nanoelectrospray emitters were pulled from borosilicate glass capillaries (1.0 mm outer diameter, 0.78 mm inner diameter, Sutter Instrument, Novato, CA, Part no. BF100-78-10) to a final

inner diameter of 2.45 ± 0.30 μm using a P-87 Flaming/Brown micropipette puller (Sutter Instrument).[62] Emitters were imaged using a Hitachi TM-1000 (Tokyo, Japan) scanning electron microscope at the Electron Microscopy Laboratory at the University of California, Berkeley.

Emitter flow rates were determined by measuring the mass of the emitter loaded with ~5-10 μL of solution using an Ohaus Analytical Plus balance (Parsippany, NJ) before and after electrospray at 1.3 kV for 5 minutes.[63,64] To determine the mass loss due to evaporation, the same emitter was placed in front of the mass spectrometer with no spray voltage applied and the mass was measured after 5 minutes. Mass loss due to solution flow during electrospray and evaporation were obtained using a density of 0.99821 g/mL for water at 20 °C.[65]

Bovine carbonic anhydrase II (BCAII) and cytochrome *c* (cyt *c*) solutions were prepared 7:3 in 50 mM ammonium acetate to a total protein concentration of 10 μM in Milli-Q water. All reagents were obtained from Sigma-Aldrich (St. Louis, MO) and were used without further purification. All reported melting curves, melting temperatures, and flow rates are the average of three replicate measurements using different ESI emitters.

8.4 Results and Discussion

8.4.1 Comparison of vT-ESI and LH-ESI for BCAII and Cyt c Melting Measurements

Bovine carbonic anhydrase II (BCAII) is a well-studied protein responsible for catalyzing the reversible hydration of CO_2 to ionic bicarbonate, a critical function in living organisms.[66] This protein is also a model system for understanding biochemical CO_2 reduction, knowledge that could lead to viable methods for converting CO_2 to useful chemical precursors.[67] However, industrial applications for BCAII are limited by the thermal stability of the enzyme,[67] which undergoes extensive aggregation in <5 min at 63 °C.[9] To gain insight into the stability of this important enzyme at elevated temperatures, vT-ESI was used to study the melting process of BCAII and the model protein cyt *c* that reversibly melts. A typical native mass spectrum acquired from a 50 mM aqueous ammonium acetate solution containing 7 μM BCAII and 3 μM cyt *c* is shown in Figure 1a. Both protonated (29,087.9 ± 0.8 Da)[68] and bicarbonate-bound (+61.1 ± 2.1 Da) BCAII with the native Zn^{2+} cofactor are formed (Figure 1a, inset). Ionic bicarbonate is a reaction product of BCAII catalytic activity and has previously been observed to be bound to BCAII in native MS experiments.[68] The tailing to higher *m/z* from the bicarbonate-bound form of BCAII is due to small nonspecific adducts that remain under the low inlet temperatures used in these experiments (100 °C) to prevent inadvertent heating of solution in the ESI emitters. The +6 - +8 charge states of cyt *c* are also formed, consistent with prior results.[35,58,69]

The melting of BCAII and cyt *c* was measured between solution temperatures of 27 °C and 86 °C using vT-ESI. At ~64 °C, there is a small population of higher charge states corresponding to unfolded BCAII (Figure 1b). No BCAII signal is observed at temperatures greater than ~72 °C (Figure 1d, data at 68 °C shown). There is an increase in light scattering intensity at 500 nm in <300 s when solutions of ~7 μM BCAII in 50 mM potassium phosphate buffer (pH 7) are incubated at 63 °C,[9] indicating that BCAII aggregates to form large oligomers at high temperatures. This indicates that the decrease in BCAII signal in these vT-ESI measurements above ~64 °C is due to

aggregation. Cyt *c* ions are still observed at temperatures >75 °C (Figure 1d, data at 68 °C shown), but remarkably, there are no high charge states of cyt *c* at 75 °C or even higher temperatures that are well above the melting temperature of this protein (T_m = ~74 °C).[35,70] Moreover, the abundances of the low charge states of cyt *c* are considerably lower at temperatures above 65 °C compared to when BCAII is not present in solution. The absence of unfolded monomers of cyt *c* indicate that these species may be co-aggregating with unfolded monomers of BCAII. Cyt *c* signal becomes highly variable above ~68 °C (Figure S1a). This suggests that aggregation may affect the ESI ion formation process at these relatively small emitter tip sizes. The complete loss of signal for BCAII, but not for cyt *c*, indicates that the aggregation process is rapid and produces large oligomers that are outside the mass or detection limits of the mass spectrometer.

LH-ESI is advantageous over vT-ESI due to rapid thermal equilibration times and localized heating at the very end of the emitter leading to less time for unfolded proteins to aggregate in solution. To investigate whether melting curves could be obtained before aggregation interferes with the electrospray process, the same BCAII/cyt *c* mixture was rapidly heated in the tip of the electrospray emitter using an LH-ESI source. Just the final 300 μm of the emitter tip was heated by using a beam block to limit the length of the capillary that was irradiated by the laser. The laser power was ramped between 0 W (laser off) and ~3.9 W. The laser powers used here are higher than those used in prior LH-ESI experiments due to irradiating a shorter, thinner volume at the end of the emitter tip.[58]

The mass spectra did not change with laser powers below ~1.8 W. At ~1.8 W, higher charge state ions (+11 - + 31) corresponding to denatured BCAII appear. These high charge state ions increase in abundance with increasing laser power (Figure 1c,e) and above ~3.3 W the abundances of all BCAII ions decrease (Figure 1e, S1b). The abundance of cyt *c* also increases with increasing laser power, reaching a maximum at the highest laser power of ~3.9 W used here (Figure S1b). Increased protein signal with increasing laser power was reported in "laser spray" experiments and was attributed to enhanced desolvation at the tip of the emitter at high solution temperatures.[56] The tailing baseline to higher *m/z* for the native charge states of BCAII at room temperature is largely eliminated at higher temperatures. This indicates that the adducts that cause the tailing are weakly bound to the protein. Solutions were prepared from lyophilized samples. During lyophilization, the concentration of material in solution, including salts and small molecules, increases and can lead to binding or adduction with the protein prior to or at the time the lyophilized powder is formed. Upon rehydration, these species may stay bound for a long period of time even in dilute solution. This adduction is not observed after turning the laser off and allowing the solution to cool back to room temperature (Figure S2a,b). At high solution temperatures, these weakly bound adducts may be lost from the protein and diffuse into the relatively dilute solution, preventing their rapid reassociation with the protein after the solution returns to room temperature. These results indicate that laser heating may be used to reduce adduction for more accurate and sensitive mass measurements.

At laser powers >3.7 W, there are no BCAII ions. We attribute the decrease in ion signal at higher laser power to rapid aggregation. Turning the laser off results in a return to a native charge state distribution and the re-appearance of peaks corresponding to BCAII in ~42 s resulting in spectra that are the same as that shown in Figure 1a (without adduction to BCAII ions, Figure S2b,c). These data indicate that fast heating with LH-ESI enables the analysis of the melting behavior of aggregation-prone proteins before aggregation can clog the spray or deplete the abundance of the monomer, expanding MS-based thermal stability measurements to a much wider range of biomolecular analytes.

8.4.2 Melting Curves for vT-ESI and LH-ESI Data

Melting curves are constructed from temperature dependent data by monitoring the change in the average charge state (ACS) or changes in the relative abundance of individual charge states/ion mobility identified conformers. For vT-ESI, the ACS of BCAII increases from 9.58 ± 0.08 to a maximum of 13.94 ± 0.54 between ~27 °C and ~72 °C (Figure 2a, blue data) after which no protein signal was obtained. The ACS of cyt *c* increases slightly from 6.96 ± 0.01 at ~27 °C to 7.38 ± 0.09 at ~86 °C (Figure 2a, orange data). The maximum ACS of cyt *c* in a mixture with BCAII at 86 °C is significantly lower than the maximum ACS obtained from solutions containing only cyt *c* (11.05 ± 0.30 at ~90 °C, Figure 2a, black data).[3] Essentially no information about the melting behavior of cyt *c* or BCAII can be obtained from these vT-ESI experiments due to the co-aggregation initiated by BCAII at ~64 °C.

Protein melting data acquired by LH-ESI can also be used to construct melting curves as a function of laser power. The ACS of BCAII increases from 9.76 ± 0.11 at 0 W to 17.62 ± 0.55 at ~3.6 W (Figure 2b, blue data). The ACS of cyt *c* increases from 6.97 ± 0.03 at 0 W to 8.69 ± 0.23 at ~3.9 W (Figure 2b, orange data). The maximum ACS of BCAII at ~3.6 W of laser power (17.62 ± 0.55) is significantly higher than the ACS at ~64 °C (13.94 ± 0.54) with vT-ESI, indicating that melting is not completed in vT-ESI before BCAII oligomerization interferes with the thermal stability measurements. The average charge state of cyt *c* at ~3.9 W is lower than the previously reported maximum average charge state for cyt *c* from vT-ESI experiments.[58] This is consistent with some population of denatured cyt *c* monomers co-aggregating with BCAII at very high laser powers, as was the case with vT-ESI, reducing the high charge population and reducing the ACS.

The average charge state versus laser power data were fit to a two-state model and resulted in melting power (P_m) values of ~2.6 W and ~3.3 W for BCAII and cyt *c,* respectively (Figure 2b). At high laser powers, the loss of BCAII ion signal indicates that the rate of aggregation is substantially higher and that aggregation occurs more rapidly than the residence time scale of solution in the heated portion of the emitter tip prior to electrospray droplet formation.

The unfolding transition of cyt *c* can be used to calibrate the laser power to solution temperature in LH-ESI experiments.[58] This method works best over the temperature range where the change in the average charge state versus temperature is highest. In the case of cyt *c*, this region (~3.0 - 3.6 W) does not have appreciable overlap with the melting transition of BCAII (~1.7 – 3.0 W). Therefore, a new calibration method was devised that uses the cyt *c* melting transition to determine the maximum temperature in the emitter tip before BCAII aggregation (Figure S3a,b). Then, the BCAII melting curve determined by LH-ESI was mapped between room temperature and this maximum value to generate a linear calibration function for converting laser power to solution temperature (Figure S3c,d). This two-protein calibration results in T_m values of 63.4 ± 0.6 °C and 73.9 ± 0.5 °C for BCAII and cyt *c* (Figure 2b, top axis), respectively, in agreement with the reported melting temperatures for these proteins (~63 °C[9,71] and ~74 °C,[35,54,58,70] respectively) obtained by circular dichroism and UV/Vis-spectrophotometry. Thermal stabilities of multiple proteins that have reversible unfolding transitions can be measured simultaneously using vT-ESI and LH-ESI.[54,58] Our data indicate that if one of the proteins in solution aggregates upon unfolding, it may not be possible to obtain melting temperatures even for proteins that have reversible unfolding

transitions and that adverse effects of aggregation and co-aggregation in protein mixtures can be overcome using LH-ESI.

8.4.3 Effect of the Bicarbonate Ion on BCAII Thermal Stability

MS-based measurements of protein melting have the advantage that the thermal stabilities of multiple forms of a protein with different masses, such as post-translational modifications and ligand- or cofactor-bound species, can be obtained simultaneously.[31] LH-ESI-MS results enable the concurrent analysis of the thermal stability of Zn-bound BCAII with and without a bound bicarbonate reaction product because the masses of these ions differ by ~61 Da (Figure 1a, inset).[68] With vT-ESI, there is a slight increase in the ACS of bicarbonate-bound BCAII species from 9.46 ± 0.08 at 27 °C to a maximum of 10.74 ± 0.84 at 64 °C (Figure 2a, red data), but the full melting behavior of this species cannot be tracked because there are no detectable BCAII ions above ~72 °C. The melting behavior of the apo- and bicarbonate-bound forms of the protein can be determined by LH-ESI. The ACS of bicarbonate-bound BCAII increases from 9.59 ± 0.22 at ~27 °C (0 W) to 16.92 ± 0.82 at ~79 °C (~3.6 W) (Figure 2b, red data). These data can be fit to a two-state model with a T_m of 69.8 ± 1.0 °C (P_m = 3.01 ± 0.07 W), which is higher than the T_m of the apo-protein (63.4 ± 0.6 °C, P_m = 2.55 ± 0.04 W). The 6.4 °C higher T_m value for bicarbonate-bound BCAII compared to the apo-protein indicates that the bicarbonate ion significantly stabilizes the folded conformation of BCAII.

Thermal denaturation of BCAII has been measured using a variety of biophysical characterization methods, including UV/Vis-spectrophotometry, differential scanning calorimetry, differential scanning fluorimetry, and circular dichroism. A T_m value of ~62 - 64 °C[66,71,72] obtained by these methods corresponds well with the measured T_m of apo-BCAII in the LH-ESI experiments. The thermal stability of an enzyme can also be measured by monitoring the enzymatic activity as a function of temperature. BCAII catalyzes the formation of a bicarbonate ion from CO_2 and the enzymatic activity can be assessed by monitoring the pH change in a slightly alkaline (pH ~8.1) CO_2-saturated solution to more neutral conditions (pH ~7) using a pH-sensitive dye or pH meter.[66,73,74] BCAII also exhibits esterase activity, which can be readily assessed by an increase in absorbance by the formation of *p*-nitrophenolate from the ester substrate *p*-nitrophenyl acetate.[66,75] Across a range of buffer conditions, a sharp decrease in both CO_2 hydration and esterase activity occurs at ~60 - 65 °C.[73–75] This is consistent with the thermal denaturation temperature of apo-BCAII and indicates that thermal denaturation is concomitant with loss of enzymatic activity. The residual activity of this enzyme at 70 °C has been reported to be between 0 – 30% at 25 °C,[72–75] consistent with some residual folded BCAII at this temperature. Conventional biophysical techniques used to measure protein thermal stability cannot distinguish between the apo- and holo-forms of the protein. Because LH-ESI-MS can independently monitor the unfolding of the apo- and bicarbonate-bound forms of BCAII by a difference in mass, this method is uniquely suited for studying the complex thermal denaturation and bicarbonate loss mechanisms of this enzyme.

8.4.4 Energetics and Mechanism for Loss of Bicarbonate from BCAII

Changes in the ACS vs temperature provide information about the difference between the thermal stabilities and T_m values of the bicarbonate-bound and apo-forms of BCAII, but do not provide mechanistic information about bicarbonate loss, the rate of interconversion between the two forms during heating, or the thermal stability of the protein-bicarbonate interaction. To investigate these properties of BCAII melting, the relative abundance of the folded (+8 - +10 charge states) and denatured (+11 - +31 charge states) forms of bicarbonate-bound and apo-BCAII were compared as a function of laser power. Unfolding of small proteins, such as BCAII, is typically fast on the time scale of these experiments. Under these conditions, mechanistic information about the ligand loss process can be derived from temperature-dependent measurements.

Changes in the ACS of the folded (F) and unfolded (U) forms of apo-BCAII measured by LH-ESI-MS show a melting temperature for the transition F → U of 63.4 ± 0.6 °C. Similarly, the ACS indicates a melting temperature for the transition of folded (BF) to unfolded (BU) bicarbonate-bound BCAII of 69.8 ± 1.0 °C. However, there are three pathways that can potentially occur for BF → U (Scheme 1). Information about these pathways can be obtained from analysis of the temperature dependance of the relative abundances of all the different forms of this protein. These data obtained with LH-ESI-MS are shown in Figure 3. Initially, folded apo- (F) and bicarbonate-bound BCAII species (BF) are predominant but their abundances decrease from 35.8 ± 1.7% and 58.1 ± 1.5% at room temperature (0 W) to ~1% at ~78 °C (~3.6 W), respectively (Figure 3, blue and red data, respectively). A two-state model fit to the data results in T_m (P_m) values of 65.1 ± 1.0 °C (2.68 ± 0.07 W) and 63.4 ± 0.5 °C (2.56 ± 0.04 W), respectively. The T_m for depletion of BF (63.4 ± 0.5 °C) is lower than the T_m determined for BF → BU from changes in the ACS (69.8 ± 1.0 °C). This is because the former includes both pathways for depletion of BF via BF → U and BF → BU → U whereas the latter is specific for BF → BU. The adequate fit of the F → U process to a sigmoidal curve and the absence of a measurable increase in F with temperature indicates that the process BF → F does not occur with F as a stable intermediate to any considerable extent. While this process may occur at temperatures above 63 °C, the lack of an increase in F indicates that F that is formed by bicarbonate loss at this elevated temperature is not stable on the time scale of our experiments.

The relative abundance of BU increases with temperature, reaches a maximum, and subsequently decreases at higher temperature indicating BU must go to U (Figure 3, green data). This is confirmed by the high abundance of U with increasing temperature which indicates that a substantial fraction of U must come from BF as well as F. The relative abundance of U increases from 2.8 ± 1.5% at ~27 °C to 85.9 ± 5.3% at ~80 °C with a formation temperature (T_f) of 65.8 ± 0.6 °C (Figure 3a, orange data). The BU data was fit to a sigmoid with sloped baselines to account for bicarbonate loss at high temperatures and a T_f of 63.8 ± 6.9 °C was obtained (Figure 3a, green data). This value is similar to the value obtained for F → U using the ACS method.

In order to separate the different pathways for formation of U from the LH-ESI melting curve data, the theoretical pathway BF → BU was modeled by assuming 100% conversion of BF to BU with no direct formation of U (Figure 3b, red dashed line). The difference between the theoretical and observed abundance of BU must be due to loss of bicarbonate from the unfolded bicarbonate-bound protein at high temperatures (BU → U) (Figure 3b, green dashed line). Fitting these data to a two-state model gives a T_m value for the BU → U process of ~65.9 °C (Scheme 1).

Formation of U can also proceed directly from BF (BF → U). U must also be formed from F (Figure 3b, blue dashed line, Figure S4) which may account for up to ~36% of U at the highest

temperature. The fraction of U that is formed by BF → U can be determined from the difference between the observed abundance of U and the sum of the other two formation pathways for U, F → U and BU → U (Figure S4). The difference between these two functions can be fit to a two-state model with a T_f of ~70.4 °C (Figure S4, black dashed line), indicating that BF → U is a minor, but clearly distinguishable pathway with ~6% relative abundance at ~80 °C. These data indicate that both BF → U and BF → BU are viable pathways for protein unfolding at solution temperatures near the T_m of the bicarbonate-bound protein.

Measuring the melting behavior of proteins using either the ACS or relative abundance of different species can probe different processes that occur during thermal denaturation and loss of a ligand from a protein. The T_m values determined for the F → U process are similar between the two analysis methods (63.4 ± 0.6 °C and 65.1 ± 1.0 °C for ACS and relative abundance quantification, respectively). This is expected because F → U is the only pathway for reducing the abundance of F. In contrast, BF has three potential pathways for loss of abundance. Analysis of temperature-dependent changes in the ACS of the bicarbonate-bound protein monitors *only* the thermal denaturation transition of BF → BU and, as a result, can provide a T_m value for this process. In contrast, the T_m value for the BF → BU process cannot be determined from changes in the relative abundance of BF due to additional dissociation and unfolding pathways that affect the observed abundances of BF, BU, and U (BF → BU → U and BF → U). The BU → U pathway (T_m = ~65.9 °C) influences the BF → BU equilibrium by reducing the abundance of BU at temperatures greater than ~65 °C. This process shifts more BF to BU, resulting in a lower T_m for BF determined from relative abundance data (T_m = 63.4 ± 0.5 °C) than from changes in the ACS (T_m = 69.8 ± 1.0 °C). This method for distinguishing pathways for loss of a ligand should work when the onset temperatures for the two processes are close, such as the ~4 °C difference measured here for the BU → U and BF → U pathways (T_m = ~65.9 °C and ~70.4 °C, respectively).

These LH-ESI-MS data reveal a complex melting behavior that would be challenging to measure with conventional biophysical characterization techniques that rely on a single spectroscopic or thermodynamic readout for an ensemble of molecules in a sample. The description of bicarbonate loss mechanisms outlined above can be elucidated by LH-ESI-MS due to the ability to distinguish between bicarbonate-bound and apo-forms of BCAII by mass and to measure melting behavior before substantial aggregation can occur. These data highlight the importance of analyzing both the ACS and relative abundance of protein species in MS-based analyses of protein thermal stabilities, which is uniquely suited for the detailed characterization of temperature-induced ligand loss and protein denaturation mechanisms.

8.4.5 Thermal Timescales of LH-ESI and vT-ESI

An important difference between vT-ESI and LH-ESI is that LH-ESI employs *fast*, *localized* heating at the tip of the emitter. Proteins are only heated for a short time prior to formation of electrospray droplets, which minimizes any aggregation that may occur upon protein unfolding. Once in the electrospray droplet, conditions where there is only one or zero molecules can be readily achieved with small emitter tips or lower protein concentration so that aggregation can be prevented entirely in the droplets.[76–79] In contrast, long thermal equilibration times typically used for vT-ESI can provide enough time for a protein to oligomerize. As noted by a reviewer, a rapid temperature rise could potentially be accompanied by an increase in pressure that can also affect

protein structure. However, the emitters are operated at and open to atmospheric pressure at both ends and the laser used in this study has a rise time of well over 1 μs. Thus, the solution pressure should not change during these laser heating experiments and the observed changes in protein structure should be due only to thermal effects.

In order to obtain an estimate of the time that a protein spends in the solution that is directly heated by the laser, the solution flow rate and volume in the heated portion of the emitter were measured. The flow rate was measured gravimetrically,[63,64] and the volume of the tip was approximated by a truncated cone. The inner diameter of the emitter tip and the inner diameter 300 μm away from the tip are ~2.4 μm and ~45 μm determined from scanning electron and optical light microscope images, respectively. The volume of solution in the final 300 μm of the emitter tip is ~170 pL. Solvent evaporation from 2.4 μm emitters occurs at a rate of 15.6 ± 5.9 nL min^{-1}. The flow rate during electrospray after accounting for solvent loss due to evaporation was 73.0 ± 19.0 nL min^{-1}. Based on these values, protein analytes are exposed to the solution that is directly heated by the laser for only ~140 ms prior to electrospray droplet formation. Increasing the heated length of the capillary to 500 μm leads to an increase in the solution volume that is directly heated to ~445 pL, resulting in a protein residence time of ~367 ms.

In addition to the small solution volume that is directly heated by the laser, heat transfer to solution that is not directly heated occurs. Heating the final 300 μm of the emitter to ~82 °C (~3.9 W) with the laser leads to loss of signal for BCAII. When the laser is turned off, native BCAII monomer signal returns within 41 ± 26 s (Figure S2c). Thus, a total solution volume of ~50 nL is heated. These results indicate that aggregation of BCAII occurs faster than ~41 s above ~80 °C, which is faster than has been previously reported for this protein. There are likely two contributing factors. A prior light scattering method could only detect aggregates larger than ~500 nm,[9] whereas depletion/formation of the different conformers of the protein monomer are measured with MS. Even small aggregates are well outside of the mass range and detection limits of the Orbitrap mass spectrometer used in this study. Another contributing factor may be that the rate of protein aggregation increases rapidly with increasing temperature,[80,81] and the laser heating experiments can take the protein well above its melting temperature.

Heating a longer length of the emitter (500 μm) results in all protein signal disappearing in <2 s at laser powers of ~0.6 W, indicating that proteins have sufficient time to undergo aggregation within the emitter before being ejected into electrospray droplets. When this larger solution volume is heated until protein signal disappears, native charge states return to the same intensities as before heating after ~74 ± 21 s, corresponding to a total heated volume of ~90 nL. Indirect heating affects a ~2x larger volume of solution when the final 500 μm of the tip is heated vs the final 300 μm. This in turns provides a correspondingly longer timescale for protein aggregation to occur before electrospray droplet formation. Pulsed laser heating can raise the solution temperature in less than 0.5 s,[58] and could extend these kinetic measurements to proteins that aggregate in under one second.

8.5 Conclusions

A laser can rapidly heat small volumes of solution at the end of a borosilicate ESI emitter, making it possible to measure the thermal denaturation of aggregation-prone proteins from which information about the thermal stabilities of protein-ligand interactions and ligand loss can be

obtained. These data show that at moderate solution temperatures where unfolding and ligand loss begins to occur, the rate at which aggregation occurs is slower than the time necessary for heating and droplet formation. This enables investigation into the melting behavior of BCAII in its bicarbonate-bound and apo-forms and the stability of both forms are obtained simultaneously from the same solution. Analysis of these data using both the average charge states of individual species as well as the relative abundances of all species makes it possible to obtain thermochemical information about various pathways for unfolding and ligand loss. The ability of the LH-ESI method to measure the thermal stability of biomolecules should be applicable to a wide range of proteins that are prone to aggregation, which includes important biopharmaceuticals, such as monoclonal antibodies and antibody-drug conjugates. LH-ESI may also be used to study aggregation kinetics at fast timescales by varying the length of the emitter heated by the laser beam, providing information about the earliest stages of protein aggregation and identifying stable intermediate structures amenable to disruption or therapeutic intervention along the pathway towards higher order oligomers.

LH-ESI also shows significant promise for coupling with solution-phase separations methods, such as capillary electrophoresis or size exclusion chromatography, where chromatographic peak widths are <1 minute and shorter than typical thermal equilibration times necessary to obtain vT-ESI data over a full range of temperatures. Obtaining LH-ESI melting curves on chromatographic timescales would add an additional dimension of information to native MS analyses of complex mixtures. In combination with autosampling instrumentation, LH-ESI may facilitate high-throughput measurements of protein, protein complex, and protein-ligand thermochemistry, paving the way towards proteome-wide screening of the effect of ligands/drugs, buffers, growth conditions, or other treatments on protein thermal stabilities.

8.6 Acknowledgements

This material is based upon work supported by the National Science Foundation Division of Chemistry under grant number CHE-2203907, an ACS Graduate Research Fellowship sponsored by Eli Lilly and Company (JSJ), and the Merck DBL SEEDS program.

8.7 References

(1) R. Lumry and H. Eyring, *J. Phys. Chem.*, 1954, **58**, 110–120.
(2) K. Huynh and C. L. Partch, *Curr. Protoc. Protein Sci.*, 2015, **79**, 28.9.1-28.9.14.
(3) S. K. Chowdhury, V. Katta and B. T. Chait, *J. Am. Chem. Soc.*, 1990, **112**, 9013–9015.
(4) Q. Wang, K.-C. Liang, A. Czader, M. N. Waxham and M. S. Cheung, *PLoS Comput. Biol.*, 2011, **7**, e1002114.
(5) O. G. Hampe, *Eur. J. Biochem.*, 1972, **31**, 32–37.
(6) R. L. Baldwin, *Biophys. J.*, 1996, **71**, 2056–2063.
(7) F. Hofmeister, *Arch. Exp. Path. Pharma.*, 1888, **25**, 1–30.
(8) F. Ahmad and C. C. Bigelow, *J. Protein Chem.*, 1986, **5**, 355–367.
(9) S. Mittal and L. R. Singh, *J. Biochem.*, 2014, **156**, 273–282.

(10) H. Dong, S. Qin and H. X. Zhou, *PLoS Comput. Biol.*, 2010, **6**, e1000833.
(11) J. Roche, J. A. Caro, D. R. Norberto, P. Barthe, C. Roumestand, J. L. Schlessman, A. E. Garcia, B. García-Moreno E. and C. A. Royer, *PNAS*, 2012, **109**, 6945–6950.
(12) G. Panick, R. Malessa, R. Winter, G. Rapp, K. J. Frye and C. A. Royer, *J. Mol. Biol.*, 1998, **275**, 389–402.
(13) C. A. Royer, *Bioch. Biophys. Acta, Protein Struct. Mol. Enzym.*, 2002, **1595**, 201–209.
(14) N. J. Greenfield, *Nat. Protoc.*, 2006, **1**, 2527–2535.
(15) N. Poklar and G. Vesnaver, *J. Chem. Ed.*, 2000, **77**, 380.
(16) C. A. Ross and M. A. Poirier, *Nat. Med.*, 2004, **10**, S10–S17.
(17) N. Poklar, N. Petrovčič, M. Oblak and G. Vesnaver, *Protein Sci.*, 2008, **8**, 832–840.
(18) G. C. Kresheck and J. E. Erman, *Biochemistry*, 1988, **27**, 2490–2496.
(19) G. Wang, P. V. Bondarenko and I. A. Kaltashov, *Analyst*, 2018, **143**, 670–677.
(20) J. Wen, H. Lord, N. Knutson and M. Wikström, *Anal. Biochem.*, 2020, **593**, 113581.
(21) S. H. Kim, H. J. Yoo, E. J. Park and D. H. Na, *Pharmaceuticals*, 2021, **15**, 29.
(22) T. O. C. Kwan, S. A. Kolek, A. E. Danson, R. I. Reis, I. S. Camacho, P. D. Shaw Stewart and I. Moraes, *Front. Mol. Biosci.*, 2022, **9**, 1–7.
(23) J. A. J. Housmans, G. Wu, J. Schymkowitz and F. Rousseau, *FEBS J.*, 2023, **290**, 554–583.
(24) J. J. Lavinder, S. B. Hari, B. J. Sullivan and T. J. Magliery, *J. Am. Chem. Soc.*, 2009, **131**, 3794–3795.
(25) G. T. H. Nguyen, T. N. Tran, M. N. Podgorski, S. G. Bell, C. T. Supuran and W. A. Donald, *ACS Cent. Sci.*, 2019, **5**, 308–318.
(26) G. T. H. Nguyen, W. Y. Leung, T. N. Tran, H. Wang, V. Murray and W. A. Donald, *Anal. Chem.*, 2020, **92**, 1130–1137.
(27) G. T. H. Nguyen, A. Nocentini, A. Angeli, P. Gratteri, C. T. Supuran and W. A. Donald, *Anal. Chem.*, 2020, **92**, 4614–4622.
(28) E. G. Báez Bolivar, D. T. Bui, E. N. Kitova, L. Han, R. B. Zheng, E. J. Luber, S. Y. Sayed, L. K. Mahal and J. S. Klassen, *Anal. Chem.*, 2021, **93**, 4231–4239.
(29) E. N. Kitova, A. El-Hawiet, P. D. Schnier and J. S. Klassen, *J. Am. Soc. Mass Spectrom.*, 2012, **23**, 431–441.
(30) G. T. H. Nguyen, J. L. Bennett, S. Liu, S. E. Hancock, D. L. Winter, D. J. Glover and W. A. Donald, *J. Am. Chem. Soc.*, 2021, **143**, 21379–21387.
(31) D. D. Vallejo, C. Rojas Ramírez, K. F. Parson, Y. Han, V. V. Gadkari and B. T. Ruotolo, *Chem. Rev.*, 2022, **122**, 7690–7719.
(32) A. Laganowsky, D. E. Clemmer and D. H. Russell, *Annu. Rev. Biophys.*, 2022, **51**, 63–77.
(33) P. Leuenberger, S. Ganscha, A. Kahraman, V. Cappelletti, P. J. Boersema, C. von Mering, M. Claassen and P. Picotti, *Science*, 2017, **355**, eaai7825.
(34) J. L. P. Benesch, F. Sobott and C. V. Robinson, *Anal. Chem.*, 2003, **75**, 2208–2214.
(35) G. Wang, R. R. Abzalimov and I. A. Kaltashov, *Anal. Chem.*, 2011, **83**, 2870–2876.
(36) T. J. El-Baba, D. W. Woodall, S. A. Raab, D. R. Fuller, A. Laganowsky, D. H. Russell and D. E. Clemmer, *J. Am. Chem. Soc.*, 2017, **139**, 6306–6309.
(37) K. Jeanne Dit Fouque and F. Fernandez-Lima, *J. Phys. Chem. B*, 2020, **124**, 6257–6265.
(38) D. W. Woodall, L. W. Henderson, S. A. Raab, K. Honma and D. E. Clemmer, *J. Am. Soc. Mass Spectrom.*, 2021, **32**, 64–72.
(39) J. Liu, Y. Wang, X. Wang, W. Qin and G. Li, *Int. J. Mass Spectrom.*, 2023, **494**, 117151.
(40) T. J. El-Baba and D. E. Clemmer, *Int. J. Mass Spectrom.*, 2019, **443**, 93–100.

(41) R. B. J. Geels, S. Calmat, A. J. R. Heck, S. M. van der Vies and R. M. A. Heeren, *Rapid Commun. Mass Spectrom.*, 2008, **22**, 3633–3641.
(42) C. J. Brown, D. W. Woodall, T. J. El-Baba and D. E. Clemmer, *J. Am. Soc. Mass Spectrom.*, 2019, **30**, 2438–2445.
(43) M. M. Kostelic, J. P. Ryan, L. S. Brown, T. W. Jackson, C. Hsieh, C. K. Zak, H. M. Sanders, Y. Liu, V. S. Chen, M. Byrne, C. A. Aspinwall, E. S. Baker and M. T. Marty, *Anal. Chem.*, 2022, **94**, 11723–11727.
(44) J. A. Harrison, A. Pruška, P. Bittner, A. Muck, D. A. Cooper-Shepherd and R. Zenobi, *Anal. Chem.*, 2022, **94**, 12435–12443.
(45) L. W. Henderson, E. M. Sharon, A. K. S. Gautam, A. J. Anthony, M. F. Jarrold, D. H. Russell, A. Matouschek and D. E. Clemmer, *J. Phys. Chem. Lett.*, 2023, **14**, 5014–5017.
(46) C. W. Lin, S. D. Oney-Hawthorne, S. T. Kuo, D. P. Barondeau and D. H. Russell, *Biochemistry*, 2022, **61**, 2733-2741.
(47) A. Marchand, M. F. Czar, E. N. Eggel, J. Kaeslin and R. Zenobi, *Nat. Commun.*, 2020, **11**, 566.
(48) A. Pruška, J. A. Harrison, A. Granzhan, A. Marchand and R. Zenobi, *Anal. Chem.*, 2023, **95**, 14384–14391.
(49) A. Marchand, F. Rosu, R. Zenobi and V. Gabelica, *J. Am. Chem. Soc.*, 2018, **140**, 12553–12565.
(50) X. Cong, Y. Liu, W. Liu, X. Liang, D. H. Russell and A. Laganowsky, *J. Am. Chem. Soc.*, 2016, **138**, 4346–4349.
(51) T. Walker, H. M. Sun, T. Gunnels, V. Wysocki, A. Laganowsky, H. Rye and D. Russell, *ACS Cent. Sci.*, 2023, **9**, 466–475.
(52) S. A. Raab, T. J. El-Baba, D. W. Woodall, W. Liu, Y. Liu, Z. Baird, D. A. Hales, A. Laganowsky, D. H. Russell and D. E. Clemmer, *J. Am. Chem. Soc.*, 2020, **142**, 17372–17383.
(53) H. Pan, S. A. Raab, T. J. El-Baba, S. R. Schrecke, A. Laganowsky, D. H. Russell and D. E. Clemmer, *J. Phys. Chem. A*, 2023, **127**, 9399–9408.
(54) T. J. El-Baba, S. A. Raab, R. P. Buckley, C. J. Brown, C. A. Lutomski, L. W. Henderson, D. W. Woodall, J. Shen, J. C. Trinidad, H. Niu, M. F. Jarrold, D. H. Russell, A. Laganowsky and D. E. Clemmer, *Anal. Chem.*, 2021, **93**, 8484–8492.
(55) F. Zhao, S. M. Matt, J. Bu, O. G. Rehrauer, D. Ben-Amotz and S. A. McLuckey, *J. Am. Soc. Mass Spectrom.*, 2017, **28**, 2001–2010.
(56) X. Shi, A. Takamizawa, Y. Nishimura, K. Hiraoka and S. Akashi, *Rapid Commun. Mass Spectrom.*, 2008, **22**, 1430–1436.
(57) X. Shi, A. Takamizawa, Y. Nishimura, K. Hiraoka and S. Akashi, *J. Mass Spectrom.*, 2006, **41**, 1086–1095.
(58) J. S. Jordan and E. R. Williams, *Anal. Chem.*, 2022, **94**, 16894–16900.
(59) T. J. El-Baba, D. R. Fuller, D. W. Woodall, S. A. Raab, C. R. Conant, J. M. Dilger, Y. Toker, E. R. Williams, D. H. Russell and D. E. Clemmer, *Chem. Commun.*, 2018, **54**, 3270–3273.
(60) A. Takamizawa, Y. Itoh, R. Osawa, N. Iwasaki, Y. Nishimura, S. Akashi and K. Hiraoka, *J. Mass Spectrom.*, 2004, **39**, 1053–1058.
(61) H. J. Sterling and E. R. Williams, *J. Am. Soc. Mass Spectrom.*, 2009, **20**, 1933–1943.
(62) J. S. Jordan, Z. Xia and E. R. Williams, *J. Am. Soc. Mass Spectrom.*, 2022, **33**, 607–611.
(63) D. N. Mortensen and E. R. Williams, *Anal. Chem.*, 2014, **86**, 9315–9321.
(64) J. S. Jordan, Z. M. Miller, C. C. Harper, E. Hanozin and E. R. Williams, *J. Am. Soc. Mass Spectrom.*, 2023, **34**, 1186–1195.

(65) M. L. Williams, *Occup. Environ. Med.*, 1996, **53**, 504–504.
(66) V. M. Krishnamurthy, G. K. Kaufman, A. R. Urbach, I. Gitlin, K. L. Gudiksen, D. B. Weibel and G. M. Whitesides, *Chem. Rev.*, 2008, **108**, 946–1051.
(67) A. Sharma, R. Chiang, M. Manginell, I. Nardi, E. N. Coker, J. M. Vanegas, S. B. Rempe and G. D. Bachand, *ACS Omega*, 2023, **8**, 37830–37841.
(68) L. F. Schachner, A. N. Ives, J. P. McGee, R. D. Melani, J. O. Kafader, P. D. Compton, S. M. Patrie and N. L. Kelleher, *J. Am. Soc. Mass Spectrom.*, 2019, **30**, 1190–1198.
(69) H. Zhang, W. Cui and M. L. Gross, *Int. J. Mass Spectrom.*, 2013, **354–355**, 288–291.
(70) F. Yang, B. R. Zhou, P. Zhang, Y. F. Zhao, J. Chen and Y. Liang, *Chem. Biol. Interact.*, 2007, **170**, 231–243.
(71) N. S. Sarraf, A. A. Saboury, B. Ranjbar and A. A. Moosavi-Movahedi, *Acta Biochim. Pol.*, 2004, **51**, 665–671.
(72) F. Azari and M. Nemat-Gorgani, *Biotechnol. Bioeng.*, 1999, **62**, 193–199.
(73) S. Bhattacharya, M. Schiavone, S. Chakrabarti and S. K. Bhattacharya, *Biotechnol. Appl. Biochem.*, 2003, **38**, 111.
(74) C. Capasso, V. De Luca, V. Carginale, P. Caramuscio, C. F. N. Cavalheiro, R. Cannio and M. Rossi, *Chem. Eng. Trans.*, 2012, **27**, 271–276.
(75) L. Alaei, A. A.Moosavi-Movahedi, H. Hadi, A. A. Saboury, F. Ahmad and M. Amani, *Protein Pept. Lett.*, 2012, **19**, 852–858.
(76) K. L. Davidson, D. R. Oberreit, C. J. Hogan and M. F. Bush, *Int. J. Mass Spectrom.*, 2017, **420**, 35–42.
(77) A. C. Susa, Z. Xia and E. R. Williams, *Anal. Chem.*, 2017, **89**, 3116–3122.
(78) J. S. Jordan and E. R. Williams, *Anal. Chem.*, 2021, **93**, 1725–1731.
(79) J. S. Jordan and E. R. Williams, *Analyst*, 2021, **146**, 6822–6830.
(80) M. F. Drenski, M. L. Brader, R. W. Alston and W. F. Reed, *Anal. Biochem.*, 2013, **437**, 185–197.
(81) V. A. Borzova, K. A. Markossian, N. A. Chebotareva, S. Y. Kleymenov, N. B. Poliansky, K. O. Muranov, V. A. Stein-Margolina, V. V. Shubin, D. I. Markov and B. I. Kurganov, *PLoS One*, 2016, **11**, e0153495.

8.8 Figures

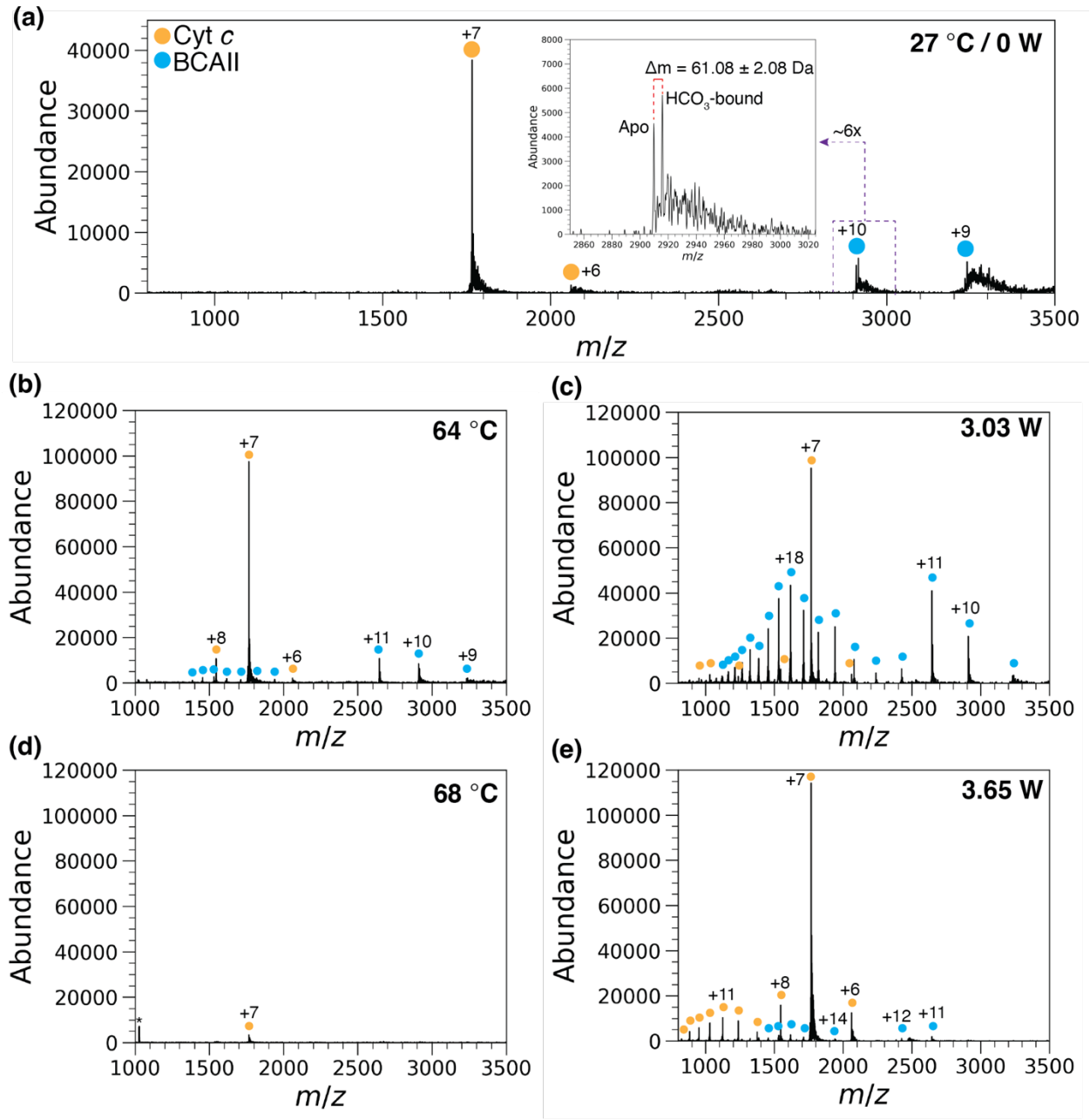

Figure 8.1. (a) Native ESI mass spectra of a 7:3 BCAII:Cyt *c* mixture (10 µM total protein concentration) in 50 mM ammonium acetate at room temperature. The inset shows the region between *m/z* = 2850 – 3025, highlighting apo-BCAII and bicarbonate-bound species. (b,d) vT-ESI mass spectra of the BCAII:Cyt *c* mixture acquired at solution temperatures of 64 °C and 68 °C. (c,e) LH-ESI mass spectra of the same sample acquired at laser powers of 3.03 W and 3.65 W by heating only the final 300 µm of the emitter.

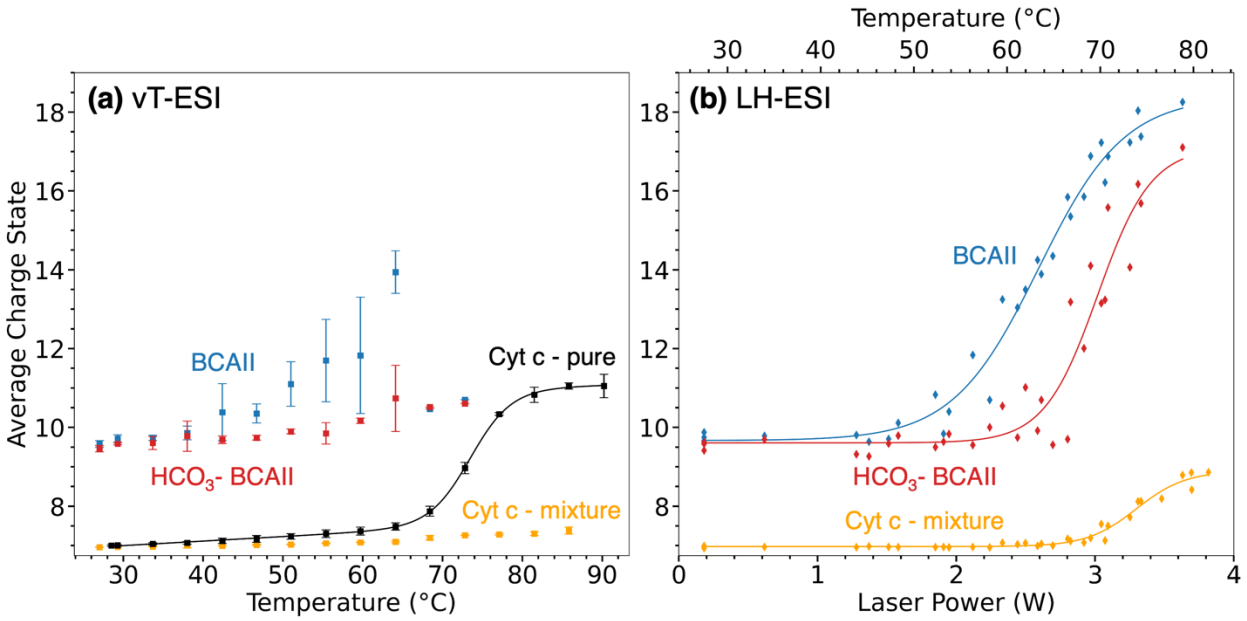

Figure 8.2. Average charge state of apo- and bicarbonate-bound BCAII (blue/red) and cyt *c* (orange/black) obtained by (a) vT-ESI or (b) LH-ESI from a solution containing 7:3 BCAII:cyt *c* in 50 mM ammonium acetate. LH-ESI data are shown as a function of laser power (bottom axis) and recalibrated temperature (top axis). BCAII signal above ~68 °C in (a) was observed in only one replicate. Data in black were obtained from a solution containing 10 μM cyt *c* in 20 mM ammonium acetate. There are no BCAII ions above ~72 °C in vT-ESI experiments due to irreversible aggregation, preventing the measurement of a full melting curve for this protein.

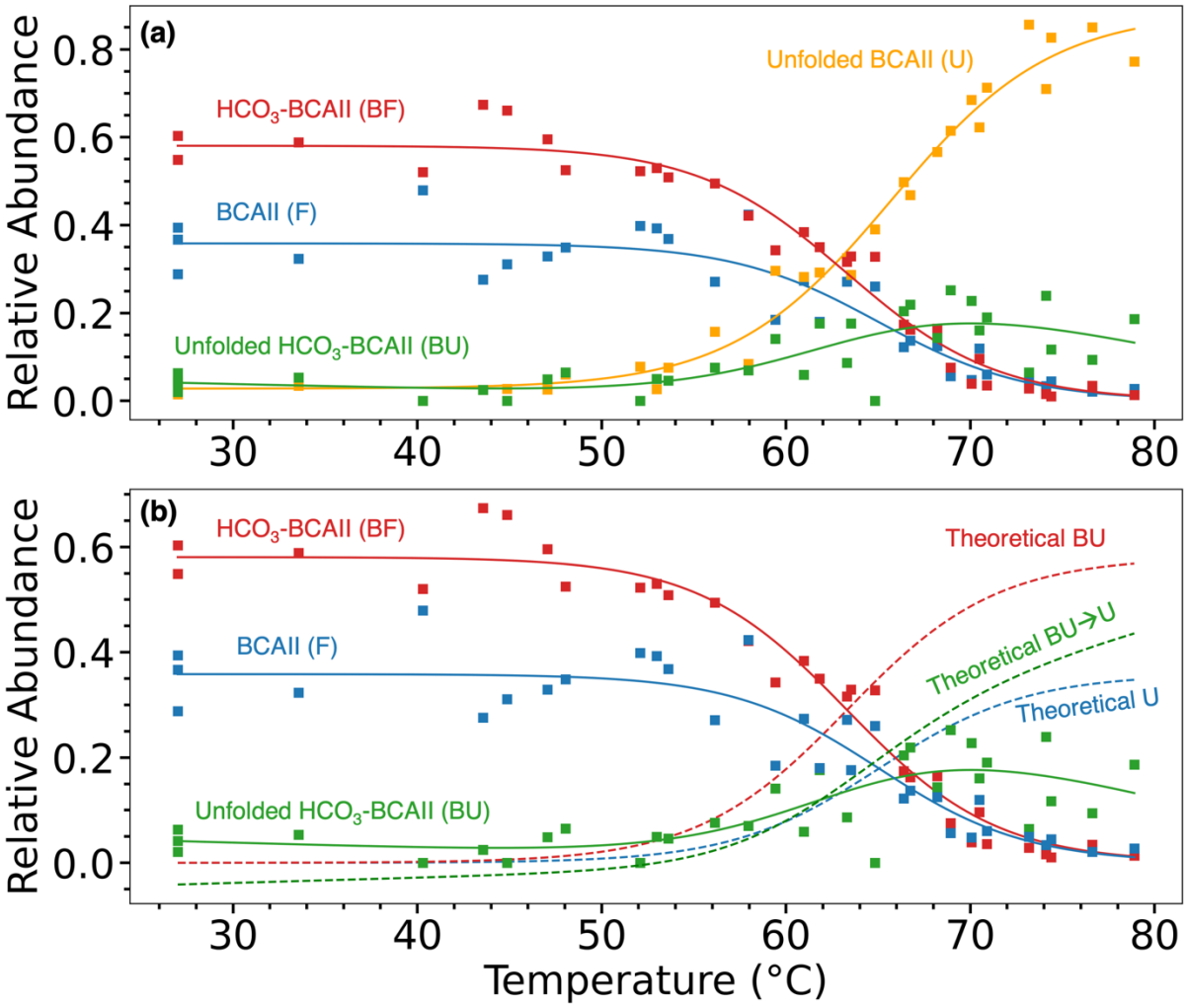

Figure 8.3. (a) LH-ESI melting curves of the native (charge states +8 - +10) and denatured (charge states +11 - +31) forms of bicarbonate-bound and apo-BCAII measured by the population abundances of the different forms and (b) including the modeled abundances (dashed lines) of BU, U, and U that is formed by loss of bicarbonate from BU (BU→U).

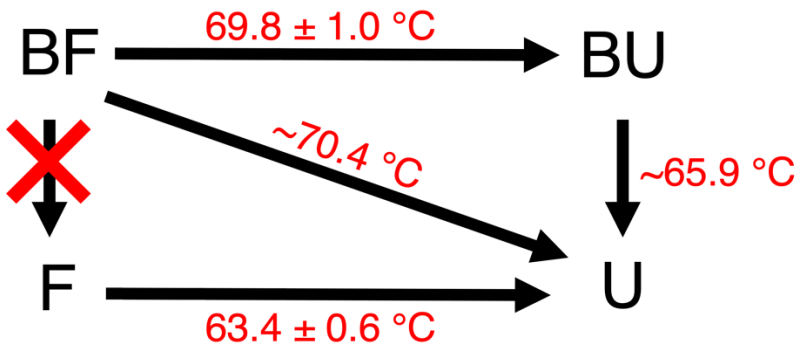

Scheme 8.1. Possible mechanisms of bicarbonate loss from BCAII and the associated T_m value for each of the processes (shown in red above each arrow). Conversion of the folded bicarbonate-bound protein to folded apo-protein is not observed. BF = bicarbonate-bound folded protein; BU = bicarbonate-bound unfolded protein; F = folded apo-protein; U = unfolded apo-protein.

8.9 Supplemental Information

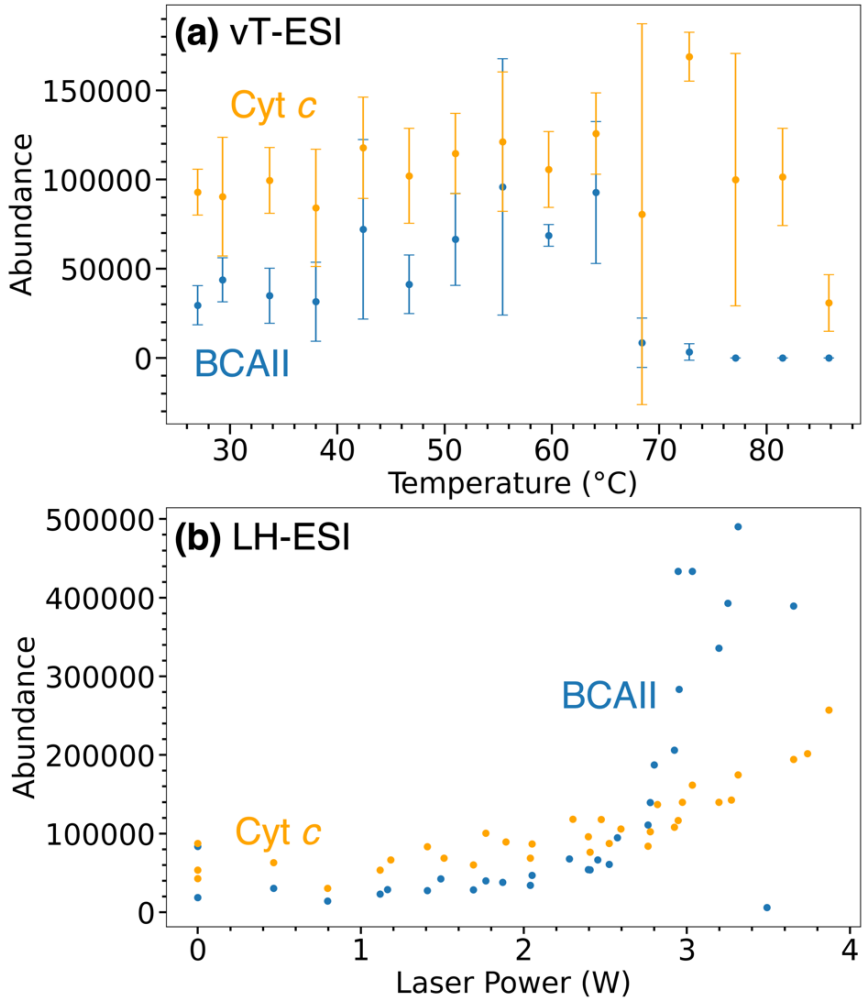

Supplemental Figure 8.1. The total ion abundances of BCAII (blue) and cyt *c* (orange) as a function of (a) solution temperature and (b) laser power. Aggregation above ~72 °C results in no BCAII signal and low cyt *c* signal in vT-ESI experiments, whereas high laser powers increase protein signal for both proteins before a sharp decrease in abundance of BCAII at laser powers >~3.3 W.

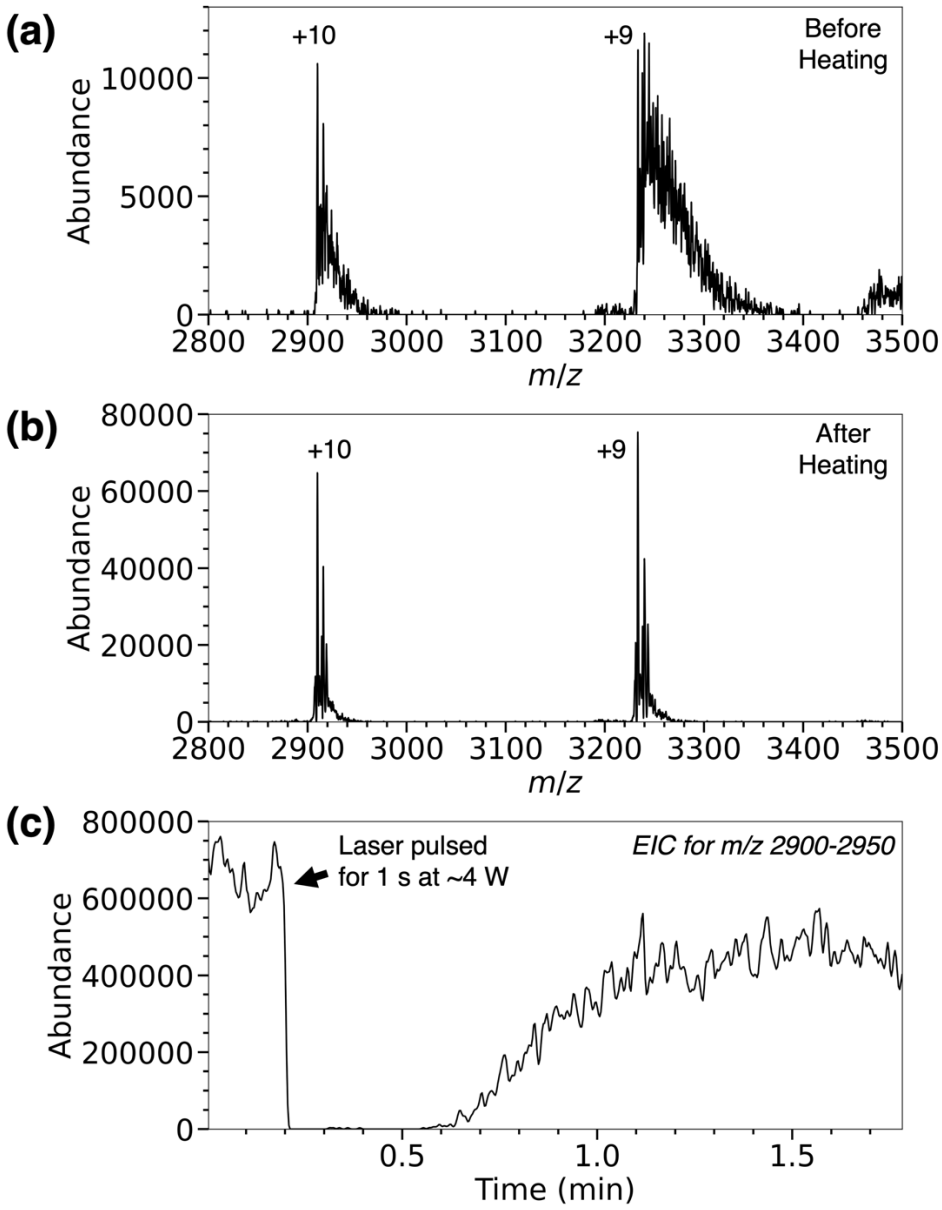

Supplemental Figure 8.2. Small molecule/ion adduction to BCAII results in (a) charge states that tail to higher *m*/*z* before heating, but (b) significantly narrower charge states after heating and a return of the solution to room temperature indicating that a thermal cycle can significantly reduce adduction. A typical (c) extracted ion chromatogram (EIC) for the region of 2900 – 2950 *m/z* (the +10 charge state) demonstrates the time required for aggregated material to be expelled from the heated portion of the emitter and signal to return after laser heating at ~4 W.

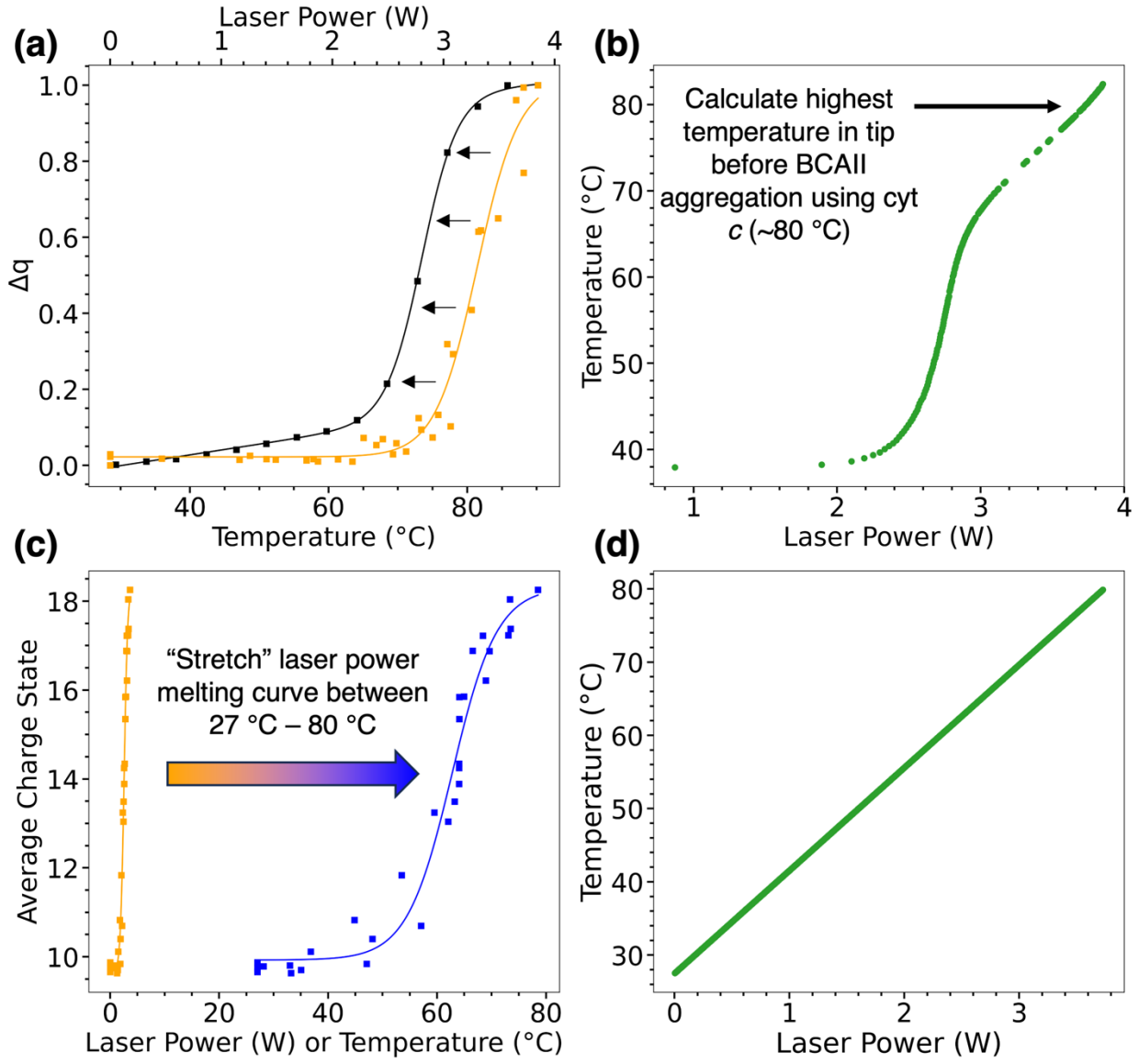

Supplemental Figure 8.3. The two-protein calibration procedure consists of (a) aligning the normalized change in the weighted average charge state of cyt *c* measured by vT-ESI and LH-ESI to (b) determine the temperature in the tip at high laser powers. The BCAII melting curve (c) determined by LH-ESI (in yellow) was then mapped between room temperature and ~80 °C (mapped function in blue) to generate (d) a linear calibration function for converting laser power to solution temperature. In contrast to a prior LH-ESI report where cyt *c* was used to establish a relationship between laser power and solution temperature,[1] a linear temperature calibration is generated here by "stretching" the sigmoidal fit for BCAII determined by LH-ESI between room temperature (27 °C) and the maximum temperature in the tip before BCAII aggregation determined using cyt *c* unfolding (~80 °C). The T_m values determined for BCAII and cyt *c* using this method are 63.4 ± 0.6 °C and 73.9 ± 0.5 °C, in excellent agreement with literature T_m values for these proteins.

Chapter 9

Temperature Induced Unfolding *and* Folding of Cytochrome *c* in the Same Aqueous Solutions

9.1 Abstract

The biochemical function, catalytic activity, and ligand-binding affinity of a protein is largely determined by the "native" folded structure. The native conformation can be disrupted by changes in pH, buffer identity, or temperature, which typically results in unfolding to form elongated structures. Characterizing the many conformations present during the protein unfolding process can provide information applicable to the development of drugs/ligands, the engineering of more stable native structures for biotherapeutics, and to fundamental biophysical research on protein stability thermodynamics, but ensemble measurement methods are often analyzed using a "two state" (folded vs. unfolded) model that does not provide information about individual conformers. Herein, we use variable-temperature electrospray ionization ion mobility mass spectrometry to investigate the thermally induced unfolding of a model protein cytochrome *c*. While a majority of the conformers formed at high temperature have an elongated structure, there is one conformer that is more compact than the native state of the protein that increases in abundance up to 95 °C. Rapid mixing and collision-induced gas-phase unfolding experiments demonstrate that the formation of this compact conformer is not an artifact of rapid refolding during the ESI process or structural rearrangement in the gas-phase and that ions with low charge states formed from high temperatures have similar shapes to, but are structurally distinct from, the native conformers of cyt *c*. These experiments demonstrate the utility of mass and mobility measurements for investigating protein conformational landscapes and provide the first evidence of structural rearrangements that result in many compact protein conformers in a solution where a majority of the protein has unfolded.

9.2 Experimental Methods

Ion mobility mass spectrometry experiments were performed using a Waters Synapt G2-Si quadrupole time-of-flight mass spectrometer (Waters Corporation, Milford, MA). The sampling cone and source offset voltages were 30 V and 5 V, respectively, and the instrument inlet temperature was 80 °C. Pressures in the trap, helium cell, and IMS cell were ~0.03 mbar, ~4.3 mbar, and ~3.2 mbar, respectively. Collision induced unfolding (CIU) experiments were performed by varying the trap collision energy from 0 – 100 V. Ion mobility arrival time distributions and mass spectra were analyzed using MassLynx V4.1 (Waters Corporation) and two dimensional CIU data were analyzed using CIUSuite 2.

Variable-temperature electrospray ionization (vT-ESI) experiments were performed using a homebuilt resistively heated source similar to that developed by Sterling *et al.* Briefly, the source consists of an aluminum jacket wrapped in nichrome heating wire. The temperature in the jacket was controlled using an Omega CNi-3222 temperature controller (Stamford, CT) and measured using a K-type thermocouple embedded in the heating jacket (Omega). A second thermocouple was placed in the tip to calibrate the temperature in the jacket to the temperature in the tip. The source was allowed to equilibrate at each temperature for ~70 seconds and mass spectra were averaged for ~30 s at temperatures between 27 °C and 90 °C.

Single barrel and theta capillary electrospray emitters were pulled to inner diameters of ~1.3 ± 0.1 μm and 1.8 ± 0.1 μm (long dimension), respectively, using a P-87 Flaming/Brown micropipette puller (Sutter Instrument, Novato, CA).[1] Emitter diameters were imaged using a Hitachi TM-1000 scanning electron microscope at the Electron Microscopy Lab at the University of California, Berkeley. Electrospray ionization was initiated by applying 0.7 – 1.4 kV to a platinum wire inserted into the emitter and in contact with the solution. Protein solutions were prepared to a final concentration of 10 μM in 20 mM ammonium acetate and titrated to pH values of 7, 3.3, or 2.9 using acetic acid. Cyt *c,* ammonium acetate, and acetic acid were obtained from Sigma-Aldrich and were used without further purification.

9.3 Results and Discussion

9.3.1 A Melting Curve for Cytochrome *c* from Mass Spectrometry

Melting curves of cyt *c* (10 μM) in 20 mM aqueous ammonium acetate at pH 7 and at pH 3.3 at temperatures between 27 °C and 90 °C were measured using a variable-temperature nanoelectrospray source and are shown in Figure 1. The average charge state of the protein was used as an indicator of conformational changes in solution, with low charge states indicative of a folded compact form of the protein and higher charge states indicating more open or extended forms. At pH 7, the +7 charge state of cyt *c* is the dominant ion (~95% total ion signal) at 27 °C, consistent with a native folded structure in this solution (Figure 2a). There is also a peak at *m/z* 711 corresponding to a peptide contaminant from the cyt *c* sample. At 90 °C, a significant abundance of this charge state remains, but there is also a broad distribution of higher charge states between +8 and +18 indicative of more unfolded structures (Figure 2c). The average charge increases from 6.98 ± 0.03 at 27 °C to 11.44 ± 0.26 at ~90 °C. These solution-phase unfolding data can be fit to a two-state model from which a melting temperature (T_m) of 73.1 ± 0.2 °C is obtained, in agreement with prior reports (Figure 1, blue data).[2–4] Although the melting curve measured using average charge states fit a two-state model, the "native' charge states of cyt *c* (+6 - +8) are still abundant at ~90 °C, a value that is well above the melting temperature of this protein (Figure 2c). Moreover, there is little change in the average charge state above 80 °C, indicating that the distribution of unfolded and folded protein conformers has reached a steady state. In a two-state model, a plateau at temperatures above the melting transition indicates that all of the folded protein has unfolded so that only the unfolded form of the protein is present in solution. However, mass spectrometry data indicate that some folded forms of the protein remain and are unaffected by temperatures well above the melting transition. These data indicate the presence of

a different folded structure that has much higher thermal stability or that there is some refolding that occurs in the electrospray droplets prior to gaseous ion formation.

The native structure of cyt *c* is destabilized at low pH.[5] A melting curve obtained from an acidified solution (pH 3.3) is show in Figures 1 (in red) and mass spectral data at low and high temperature are shown in Figure 2b,d. At 27 °C, the average charge state is 7.13 ± 0.05, just slightly higher than that at pH 7 indicating that there may be a slight opening of the native structure at this more acidic pH. The peptide contaminant at *m/z* = 711 is lower relative abundance at this pH, suggesting that the ionization efficiency of cyt *c* is higher at lower pH. At 90 °C, very little of these native charge states remain and most of the ions are highly charged, indicative of unfolded structures, with an average charge state of 13.44 ± 0.13. Fitting the melting curve data to a two-state model results in a T_m value of 44.2 ± 0.3 °C. The ~30 °C lower T_m value obtained at pH 3.3 compared to pH 7.0 is consistent with native structure being less stable at this low pH.

Remarkably, low charge states corresponding to a compact structure remain at the highest temperature (Figure 2d) and do not change in abundance from 55 °C to 90 °C (Figure 1). If refolding inside the droplet was the origin of the persistence of this low charge state, less refolding should occur with increasing droplet temperature, resulting in a slight increase in the average charge state above 55 °C, which is not observed (Figure 1, red data). Moreover, the low charge-state ions corresponding to folded cyt *c* are significantly less abundant at pH 3.3 than they are at pH 7.0. This indicates that the low charge states at pH 7.0 are not formed by refolding in the droplets since this should have also occurred at pH 3.3. These results again suggest the presence of a compact folded form of cyt *c* in solution that is either formed at higher temperature or persists at all temperatures.

9.3.2 Ion Mobility and Cyt *c* Conformations

Information about conformations of cyt *c* in the gas phase can be obtained from ion mobility measurements from which information about solution-phase conformations can be inferred. Ion mobility arrival time distributions of each charge state were measured as a function of temperature and these data were converted to collision cross sections using protein ion calibrants that have known mass and cross section.[6] An ion mobility collision cross section distribution (CCSD) for the native +7 charge state at 27 °C is shown in Figure 2e and 2f for pH 7 and pH 3.3 solutions, respectively. The number of conformers was estimated by fitting a minimum number of Gaussian curves to the data at each temperature to achieve a cumulative fit with $R^2 > 0.9$ and ensuring that all distinct features were accounted for in these fits.[7–10] A library of ions with unique CCS values and fitted widths was generated. These data were iteratively fit allowing abundances to vary. Thus, peaks that are present only at high temperatures were also fit to low temperature data. The CCSD of the +7 charge state was fit to 6 distinct peaks and has a general shape that is similar to prior reports at ~27 °C.[11–14] These distinct ion species may reflect different conformations of cyt c in solution, or these conformers may be formed as a result of the electrospray process prior to gaseous ion formation. These data are similar to other traveling wave ion mobility data for the cyt *c* +7 charge state acquired by Barran and coworkers in which the CCSD of the cyt *c* +7 charge state had four resolved conformations.[12] However, Jarrold and coworkers report only a single conformer for this charge state using ion mobility measurements in a drift tube.[11,14] In these prior reports, conformers at higher CCS (up to ~2100 Å^2) are formed upon

activation in the source, the collision cell, or in the drift cell. These data indicate that the conformers at CCS values >~1400 Å^2 may have originated from activation in the gas-phase rather than in solution. At 90 °C, an additional compact peak appears at a lower CCS value of 1243 ± 37 Å^2 and other peaks in the CCSD are shifted by ~25 Å^2 towards larger CCS values, consistent with a slight expansion of these protein conformers at higher solution temperatures (Figure 2g). The more compact conformer that is a distinct feature at high temperatures may also be present at 27 °C but the abundance is too low to be resolved/detected.

A more compact conformer is only observed in the CCSD of the +7 charge state. The higher abundance of this compact sub-population of cyt *c* structures indicate that not only are they stable, but they are *stabilized* at high temperatures. Compaction of the +7 charge state of cyt *c* that has undergone oxidative modifications [15] or bound to a cardiolipin ligand[16] has been reported, indicating that a more compact version of this protein is accessible in solution. However, these data are the first evidence of cyt *c* forming both more unfolded structures and a more compact structure with increasing solution temperature. We are unaware of any other data for this or other well studied proteins commonly fit to a two-state folding model that indicate that *both unfolded and more compact forms can be stabilized with increasing temperature for the same protein in the same aqueous solution.*

CCSDs for the +7 charge state acquired from pH 3.3 solutions also show evidence of 6 distinct conformations, with a general shift towards larger CCS values at higher solution temperatures (Figure 2f,h). The compact conformer is undetectable at 27 °C but increases in abundance with increasing solution temperature. The relative abundance of the compact conformer at 90 °C is lower than it is at pH 7, indicating that acidification preferentially destabilizes this more compact conformer. The relative abundances of the two least compact structures also increases consistent with acidification destabilizing all of the more compact conformers. The pH dependence indicates that this change from more compact to less compact structures must reflect different conformations in solution and are not an artifact of the electrospray ionization process. Both the steady state average charge state at temperatures above 55 °C (Figure 1, pH 3.3 data) and the increasing abundance of the most compact conformer with increasing temperature, indicate that the compact conformer is not formed as a result of protein refolding within the electrospray droplet prior to gaseous ion formation.

9.3.3 Rapid Mixing and Protein Refolding in Droplets

To further rule out the possibility that the compact conformer of the +7 ion formed at higher temperatures is formed by refolding in droplets, rapid mixing experiments were performed using theta glass electrospray emitters. In these experiments, an acidified cyt c solution is mixed with a buffer to cause a pH jump to induce protein folding in the electrospray droplets.[17,18] Mass spectra acquired from an acidified (pH 2.9) solution show a bimodal charge-state distribution with both low (+5-+9) and high (+13-+20) charge states (Figure 3a). Assuming that the +6 and +7 charge states are folded conformations, the +8 is an unfolding intermediate, and the higher charge state correspond to more highly unfolded structures, these data indicate that only ~1% of the protein remains folded at this low pH (Figure 3a). Results using the theta glass emitters where a solution consisting of 100 mM ammonium acetate (pH 7) is mixed with the acidified 2.9 pH solution containing cyt c are shown in Figure 3b. The +7 charge state is by far the most abundant (ACS =

7.60) with only a minor abundance of high charge states corresponding to unfolded structures. These data indicate that ~79% of the protein population is folded and the majority of this folding occurs in the electrospray droplets. The lifetime of these droplets can be estimated using the known refolding time constant of cyt *c* (57 μs)[19] and the percent of folded protein in a 1:1 mixture of the two solutions at equilibrium. Mass spectra of a 1:1 equilibrium mixture (pH 4.4) show only the +6 - +8 charge states of cyt *c* (Figure S1a). Based on these data, the lifetime of droplets produced from the ~1.8 μm tip size used here is ~89 μs. This lifetime is larger than that reported for similar sized emitters on different instruments (~27 μs) and may result from the gentle conditions of the instrument interface, i.e., less rapid desolvation in the heated interface region.[18,20,21] Information about the conformers that are formed in these rapid folding experiments was obtained from the CCSD of the +7 ion. The CCSD obtained after mixing is indistinguishable from that obtained at room temperature from neutral pH solutions and that obtained from the equilibrium mixture (pH ~4.4) (Figure 3c). These data indicate that a return to a native conformation can occur within the lifetime of the droplet (~89 μs), but clearly shows that the compact conformer is not formed by kinetically trapping of a transient structure during fast refolding of the protein within the electrospray droplet. Thus, we conclude that the more compact form that increases in abundance with increasing temperature must exist in solution simultaneously with more unfolded structures that also increase in abundance with increasing temperature.

9.3.4 Collision-Induced Unfolding of Compact and Extended Conformers

The stabilities of the compact forms of the +7 charge state of cyt *c* in the gas phase was probed using collision-induced unfolding (CIU). Ions were formed from 90 °C pH 7 solutions to maximize the extent of the compact conformer, which is ~29% abundance at 0 V collision voltage. The abundance of conformer 1 decreases with increasing collision energy until it is <1% abundance at 12 V with a CIU_{50} value of 8.3 ± 0.3 V (Figure 4a, blue data). The abundance of the predominant native conformer stays relatively constant from 0 – 5 V before gradually decreasing to <1% at 20 V with a CIU_{50} value of 9.8 ± 0.2 V (Figure 4a, orange data). Neither the native nor the compact conformer increase in abundance with increasing collision energy and both conformers convert into more elongated species, indicating that the compact conformer is not formed via gas-phase structural rearrangement.

9.3.5 Are the Same Native Conformers Retained at High Temperatures?

Each of the 5 native conformers of the +7 charge state are observed to increase in drift time by ~0.1 – 0.2 ms between ~27 °C and 90 °C. This increase in drift time could be due to a slight expansion of the protein structure at higher temperatures or could be due to the formation of different conformers that are not resolved by IMS. The CIU fingerprint can be used to distinguish between conformers that cannot be resolved by IMS alone so long as they have differences in their gas-phase stability.

At 27 °C, the CIU_{50} values for the 5 resolved conformers of the +7 charge state are 11.2 ± 0.2 V (orange data), 15.2 ± 0.6 V (green data), 11.7 ± 0.2 V and 15.6 ± 0.8 V (red data), 15.9 ± 0.1

V (purple data), and 13.6 ± 0.9 V (brown data) (Figure 4b). The data in red, which represent the conformer with a drift time of ~8.7 ms, is a clear intermediate in the gas-phase unfolding process. When produced from 90 °C solutions, the CIU_{50} values of these same conformers are 9.8 ± 0.2 V (orange data), 12.7 ± 0.3 V (green data), 10.2 ± 0.3 V and 13.8 ± 0.6 V (red data), 13.3 ± 0.1 V (purple data), and 13.1 ± 0.6 V (brown data, Figure 4a). Except for the most extended conformer depicted in brown, these CIU_{50} values are ~12-16% lower than for ions with similar drift times at room temperature. These data indicate the ions produced from high temperature are less stable against gas-phase activation compared to their room temperature analogues.

Two dimensional plots of drift time versus collision voltage are helpful for monitoring how conformers interconvert with increasing collision energy. For the +7 charge state at 90 °C, there are 2 major unfolding transitions from the predominant native conformer (~6.5 ms) to an intermediate conformer (~8.7 ms) at 9.5 V and from this intermediate conformer to a more elongated conformer (~9.8 ms) at 12.5 V (Figure 4c). At 27 °C, there are two similar transitions with midpoints at 10.5 V and 15.5 V (Figure 4d). The lower midpoint voltages of these transitions when produced from high temperatures is in agreement with the differences in CIU_{50} values for individual species and could be due to the ions having higher energy retained from the hotter solution or due to the conformers formed from higher temperature solutions having a different structure. Ions entering the collision cell with higher energies would result in lower voltages required for unfolding, but the higher energy 15.5 V transition should be less affected than the lower energy 10.5 V transition. The opposite trend is observed in the data in Figure 4 indicating that ions are not entering the IMS cell with significantly higher energy when produced from the 90 °C solution. The shift to lower transition voltages is consistent with the formation of different protein conformations at high temperature with similar overall shapes and lower resistance to gas-phase unfolding than those present at room temperature. CIU of the +6 charge state results in one major transition from a conformer at ~6.9 ms to ~8.3 ms (Figure S2). The CIU_{50} of this transition is 14.5 V at 27 °C and 12.5 V at 90°C (Figure S2). The shift to lower voltages at higher temperature is in agreement with the data for the +7 charge state and indicates that the +6 charge state may also form into different conformations above the melting temperature.

Protein thermal denaturation data obtained from circular dichroism or fluorescence/UV-Vis spectrophotometry experiments is often fit to a two-state model that considers the “folded” protein structure to be depleted at high solution temperatures by conversion into more elongated, “unfolded” species.[22–24] From vT-ESI data acquired over a wide range of solution conditions and on a number of model proteins, low charge state ions in mass spectra acquired at high solution temperatures indicate that compact species are present in solution well above the melting temperature.[2,3,7,8,10,25–30] To date, the identity of these compact ions formed from heated solutions has not been investigated using IMS, despite the apparent contrast of this data with nearly all existing literature on protein melting. The IMS-MS data presented here is in agreement with existing literature on protein melting that indicates the native form of a protein is significantly destabilized by higher temperatures, but indicates that this can proceed via the formation of conformations that are elongated, more compact, or of similar shape to native conformers. The high abundance of these compact, low charge state conformers at 90 °C indicates a high thermal stability, but the relatively low CIU_{50} voltages for gas-phase unfolding suggests that solvent interactions likely play a significant role in stabilizing these structures.

9.4 Conclusions

Temperature-dependent mass spectrometry data on the model protein cyt *c* reveals the surprising formation of a low abundance compact conformer at elevated temperatures in the same solution where the majority of the protein population unfolds. The ability to measure distinct conformational states from solution using both charge-state and ion mobility information makes it possible to observe unusual phenomenon that have not been observed previously using more conventional techniques that measure changes in a physical property from folded to unfolded structures. Collision induced unfolding experiments indicate that ions with low charge states formed from solutions at high temperature are similarly shaped, but structurally distinct from the native conformers present at room temperature. To our knowledge, these results are the first evidence of both unfolding and compaction of a protein in response to elevated temperatures in the same solution. This method is promising for the high resolution characterization of protein unfolding landscapes, and in combination with fast laser-heating experiments, could pave the way for high throughput thermochemistry measurements on the LC timescale. A brief survey of other model proteins, including lysozyme and ubiquitin, has not shown evidence of compaction at elevated temperatures. Whether multiple pathways for both protein folding and unfolding at high temperatures is unique to cyt *c* or is more general remains to be determined.

9.5 Acknowledgements

This work was supported by the National Science Foundation Division of Chemistry (grant number CHE-2203907), an ACS Graduate Research Fellowship sponsored by Eli Lilly and Company (JSJ), and Merck & Co., Inc., San Francisco, CA, USA, through their Discovery Biologics SEEDS program.

9.6 References

(1) Jordan, J. S.; Xia, Z.; Williams, E. R. Tips on Making Tiny Tips: Secrets to Submicron Nanoelectrospray Emitters. *J. Am. Soc. Mass Spectrom.* **2022**, *33* (3), 607–611.
(2) Jordan, J. S.; Williams, E. R. Laser Heating Nanoelectrospray Emitters for Fast Protein Melting Measurements with Mass Spectrometry. *Anal. Chem.* **2022**, *94* (48), 16894–16900.
(3) Wang, G.; Abzalimov, R. R.; Kaltashov, I. A. Direct Monitoring of Heat-Stressed Biopolymers with Temperature-Controlled Electrospray Ionization Mass Spectrometry. *Anal. Chem.* **2011**, *83* (8), 2870–2876.
(4) Yang, F.; Zhou, B.-R.; Zhang, P.; Zhao, Y.-F.; Chen, J.; Liang, Y. Binding of Ferulic Acid to Cytochrome c Enhances Stability of the Protein at Physiological PH and Inhibits Cytochrome C-Induced Apoptosis. *Chem. Biol. Interact.* **2007**, *170* (3), 231–243.
(5) Kuroda, Y.; Kidokoro, S.; Wada, A. Thermodynamic Characterization of Cytochrome c at Low PH. *J. Mol. Biol.* **1992**, *223* (4), 1139–1153.

(6) Bush, M. F.; Hall, Z.; Giles, K.; Hoyes, J.; Robinson, C. V.; Ruotolo, B. T. Collision Cross Sections of Proteins and Their Complexes: A Calibration Framework and Database for Gas-Phase Structural Biology. *Anal. Chem.* **2010**, *82* (22), 9557–9565.
(7) Raab, S. A.; El-Baba, T. J.; Woodall, D. W.; Liu, W.; Liu, Y.; Baird, Z.; Hales, D. A.; Laganowsky, A.; Russell, D. H.; Clemmer, D. E. Evidence for Many Unique Solution Structures for Chymotrypsin Inhibitor 2: A Thermodynamic Perspective Derived from vT-ESI-IMS-MS Measurements. *J. Am. Chem. Soc.* **2020**, *142* (41), 17372–17383.
(8) Woodall, D. W.; Henderson, L. W.; Raab, S. A.; Honma, K.; Clemmer, D. E. Understanding the Thermal Denaturation of Myoglobin with IMS-MS: Evidence for Multiple Stable Structures and Trapped Pre-Equilibrium States. *J. Am. Soc. Mass Spectrom.* **2021**, *32* (1), 64–72.
(9) Pan, H.; Raab, S. A.; El-Baba, T. J.; Schrecke, S. R.; Laganowsky, A.; Russell, D. H.; Clemmer, D. E. Variation of CI-2 Conformers upon Addition of Methanol to Water: An IMS-MS-Based Thermodynamic Analysis. *J. Phys. Chem. A* **2023**, *127* (45), 9399–9408.
(10) El-Baba, T. J.; Woodall, D. W.; Raab, S. A.; Fuller, D. R.; Laganowsky, A.; Russell, D. H.; Clemmer, D. E. Melting Proteins: Evidence for Multiple Stable Structures upon Thermal Denaturation of Native Ubiquitin from Ion Mobility Spectrometry-Mass Spectrometry Measurements. *J. Am. Chem. Soc.* **2017**, *139* (18), 6306–6309.
(11) Mao, Y.; Woenckhaus, J.; Kolafa, J.; Ratner, M. A.; Jarrold, M. F. Thermal Unfolding of Unsolvated Cytochrome c : Experiment and Molecular Dynamics Simulations. *J. Am. Chem. Soc.* **1999**, *121* (12), 2712–2721.
(12) Jhingree, J. R.; Beveridge, R.; Dickinson, E. R.; Williams, J. P.; Brown, J. M.; Bellina, B.; Barran, P. E. Electron Transfer with No Dissociation Ion Mobility–Mass Spectrometry (ETnoD IM-MS). The Effect of Charge Reduction on Protein Conformation. *Int. J. Mass Spectrom.* **2017**, *413*, 43–51.
(13) Dickinson, E. R.; Jurneczko, E.; Pacholarz, K. J.; Clarke, D. J.; Reeves, M.; Ball, K. L.; Hupp, T.; Campopiano, D.; Nikolova, P. V.; Barran, P. E. Insights into the Conformations of Three Structurally Diverse Proteins: Cytochrome c, P53, and MDM2, Provided by Variable-Temperature Ion Mobility Mass Spectrometry. *Anal. Chem.* **2015**, *87* (6), 3231–3238.
(14) Shelimov, K. B.; Clemmer, D. E.; Hudgins, R. R.; Jarrold, M. F. Protein Structure in Vacuo : Gas-Phase Conformations of BPTI and Cytochrome c. *J. Am. Chem. Soc.* **1997**, *119* (9), 2240–2248.
(15) Chea, E. E.; Deredge, D. J.; Jones, L. M. Insights on the Conformational Ensemble of Cyt C Reveal a Compact State during Peroxidase Activity. *Biophys. J.* **2020**, *118* (1), 128–137.
(16) Szymkowicz, L.; Lento, C.; Wilson, D. J. Impact of Cardiolipin and Phosphatidylcholine Interactions on the Conformational Ensemble of Cytochrome c. *Biochemistry* **2019**, *58* (34), 3617–3626.
(17) Mortensen, D. N.; Williams, E. R. Theta-Glass Capillaries in Electrospray Ionization: Rapid Mixing and Short Droplet Lifetimes. *Anal. Chem.* **2014**, *86* (18), 9315–9321.
(18) Mortensen, D. N.; Williams, E. R. Investigating Protein Folding and Unfolding in Electrospray Nanodrops upon Rapid Mixing Using Theta-Glass Emitters. *Anal. Chem.* **2015**, *87* (2), 1281–1287.
(19) Shastry, M. C. R.; Luck, S. D.; Roder, H. A Continuous-Flow Capillary Mixing Method to Monitor Reactions on the Microsecond Time Scale. *Biophys. J.* **1998**, *74* (5), 2714–2721.
(20) Xia, Z.; Williams, E. R. Effect of Droplet Lifetime on Where Ions Are Formed in Electrospray Ionization. *Analyst* **2019**, *144* (1), 237–248.

(21) Chen, C. J.; Williams, E. R. The Role of Analyte Concentration in Accelerated Reaction Rates in Evaporating Droplets. *Chem. Sci.* **2023**, *14* (18), 4704–4713.
(22) Norma J. Greenfield. Using Circular Dichroism Collected as a Function of Temperature to Determine the Thermodynamics of Protein Unfolding and Binding Interactions. *Nat. Protoc.* **2006**, *1* (6), 2527–2535.
(23) Wen, J.; Lord, H.; Knutson, N.; Wikström, M. Nano Differential Scanning Fluorimetry for Comparability Studies of Therapeutic Proteins. *Anal. Biochem.* **2020**, *593*, 113581.
(24) Kresheck, G. C.; Erman, J. E. Calorimetric Studies of the Thermal Denaturation of Cytochrome c Peroxidase. *Biochemistry* **1988**, *27* (7), 2490–2496.
(25) Jeanne Dit Fouque, K.; Fernandez-Lima, F. Following Structural Changes by Thermal Denaturation Using Trapped Ion Mobility Spectrometry–Mass Spectrometry. *J. Phys. Chem. B* **2020**, *124* (29), 6257–6265.
(26) El-Baba, T. J.; Raab, S. A.; Buckley, R. P.; Brown, C. J.; Lutomski, C. A.; Henderson, L. W.; Woodall, D. W.; Shen, J.; Trinidad, J. C.; Niu, H.; Jarrold, M. F.; Russell, D. H.; Laganowsky, A.; Clemmer, D. E. Thermal Analysis of a Mixture of Ribosomal Proteins by VT-ESI-MS: Toward a Parallel Approach for Characterizing the Stabilitome. *Anal. Chem.* **2021**, *93* (24), 8484–8492.
(27) Benesch, J. L. P.; Sobott, F.; Robinson, C. V. Thermal Dissociation of Multimeric Protein Complexes by Using Nanoelectrospray Mass Spectrometry. *Anal. Chem.* **2003**, *75* (10), 2208–2214.
(28) Jordan, J. S.; Lee, K. J.; Williams, E. R. Overcoming Aggregation with Laser Heated Nanoelectrospray Mass Spectrometry: Thermal Stability and Pathways for Loss of Bicarbonate from Carbonic Anhydrase II. *Analyst* **2024**, *149* (8), 2281–2290.
(29) El-Baba, T. J.; Clemmer, D. E. Solution Thermochemistry of Concanavalin A Tetramer Conformers Measured by Variable-Temperature ESI-IMS-MS. *Int. J. Mass Spectrom.* **2019**, *443*, 93–100.
(30) Woodall, D. W.; El-Baba, T. J.; Fuller, D. R.; Liu, W.; Brown, C. J.; Laganowsky, A.; Russell, D. H.; Clemmer, D. E. Variable-Temperature ESI-IMS-MS Analysis of Myohemerythrin Reveals Ligand Losses, Unfolding, and a Non-Native Disulfide Bond. *Anal. Chem* **2019**, *91* (10), 6808–6814.

9.7 Figures

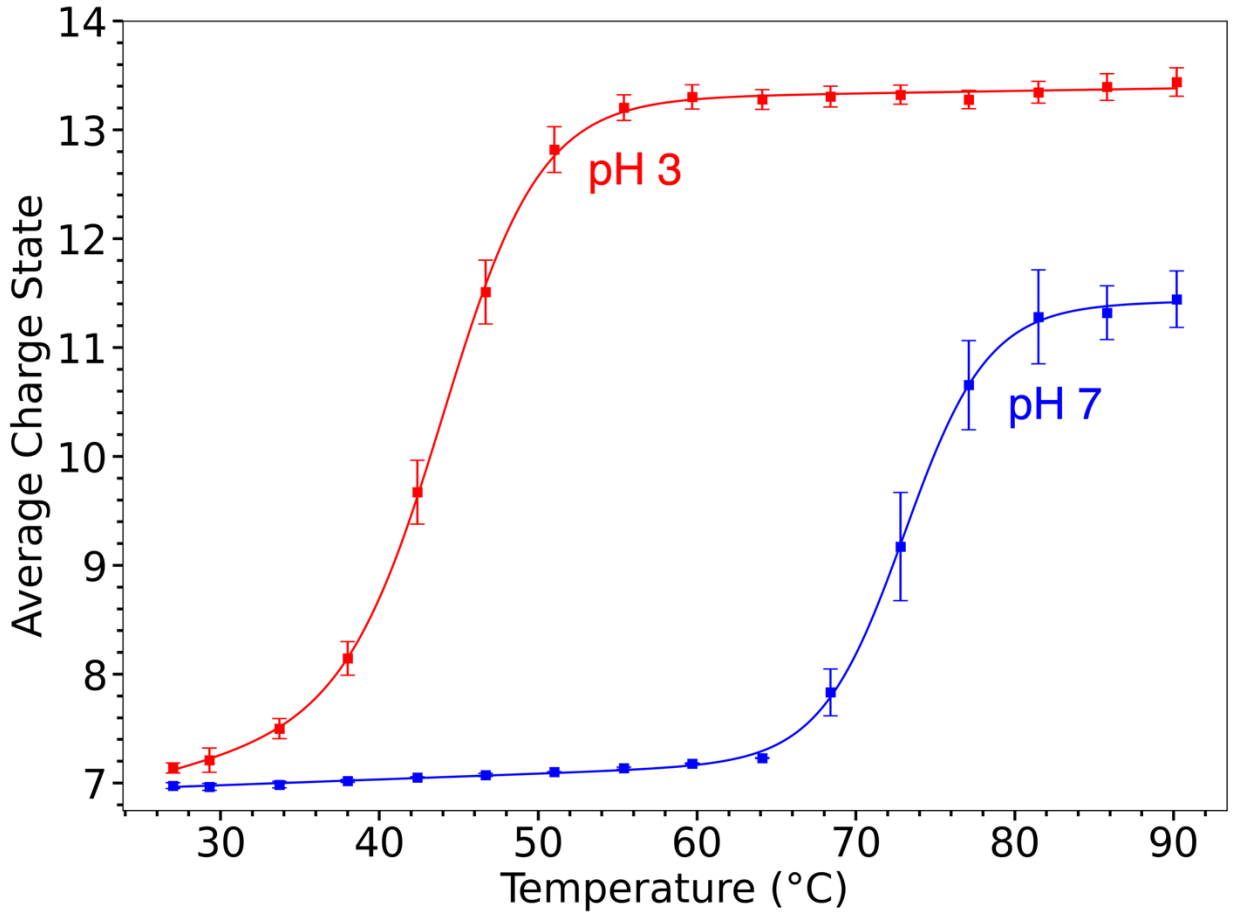

Figure 9.1. Melting curves for cyt *c* determined at (blue) pH 7 and (red) pH 3 on the basis of the change in the average charge state versus temperature. Two state models fit to the data result in T_m values of 73.1 ± 0.2 °C and 44.2 ± 0.3 °C at pH 7 and pH 3.3, respectively.

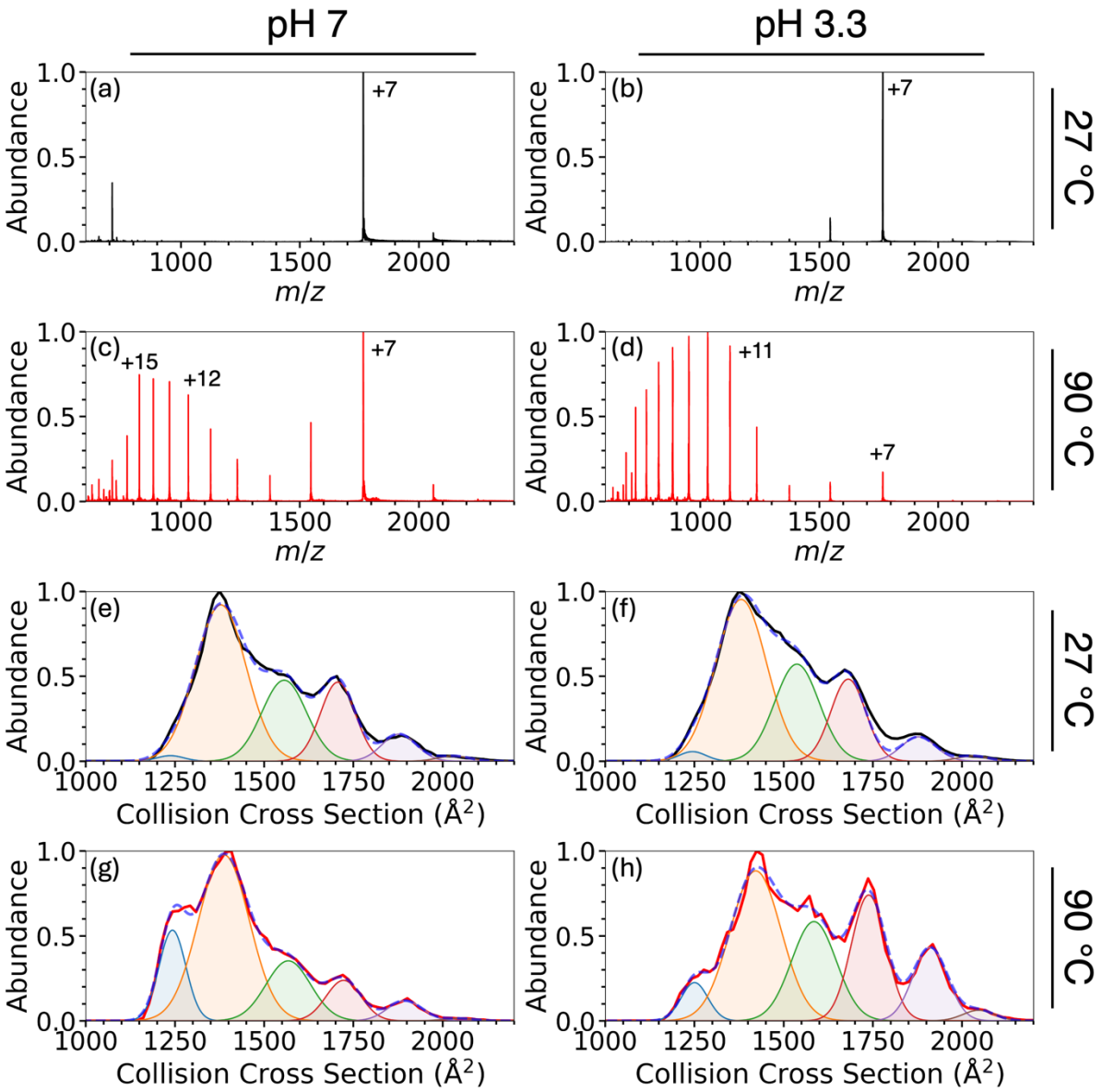

Figure 9.2. (a-d) Mass spectra and (e-h) collision-cross section distributions for the +7 charge state of 10 μM cyt *c* in (a,c,e,g) pH 7 or (b,d,f,h) pH 3.3 at solution temperatures of (a,b,e,f) ~27 °C or (c,d,g,h) 90 °C with fitted gaussians to represent individual cyt *c* conformers. The dashed blue lines in (e-h) represent the sum of the individual gaussian fits to the data.

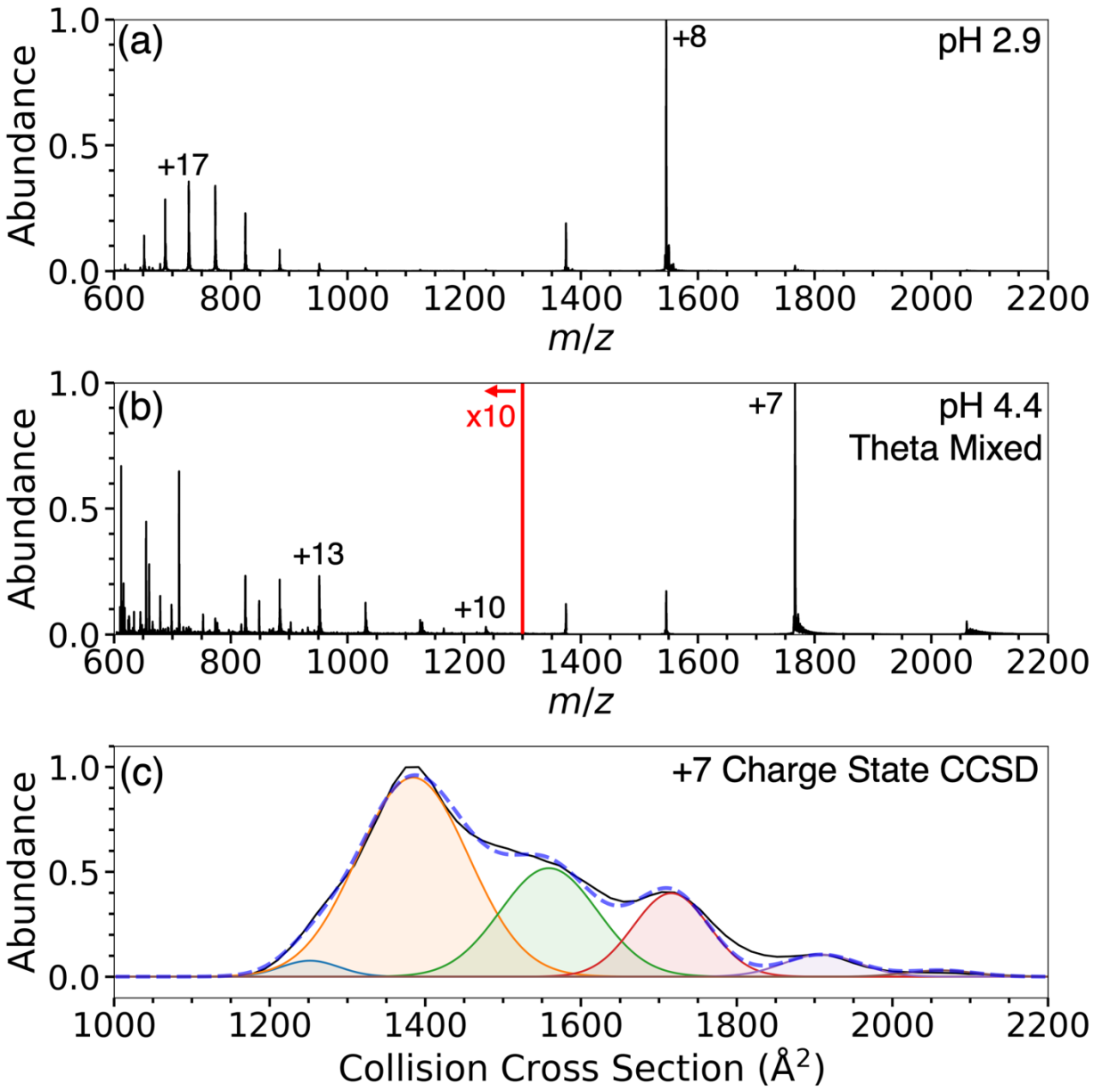

Figure 9.3. (a) Mass spectrum acquired from an acidifed cyt *c* solution (pH 2.9) (a) before and (b) after theta mixing with a neutralizing solution of 100 mM ammonium acetate (pH 7). Protein refolding in the droplet results in a significantly lower abundance of high charge states after theta mixing. The CCS distribution in (c) demonstrates that the compact conformer of the +7 charge state is not formed by rapid protein refolding in the droplet.

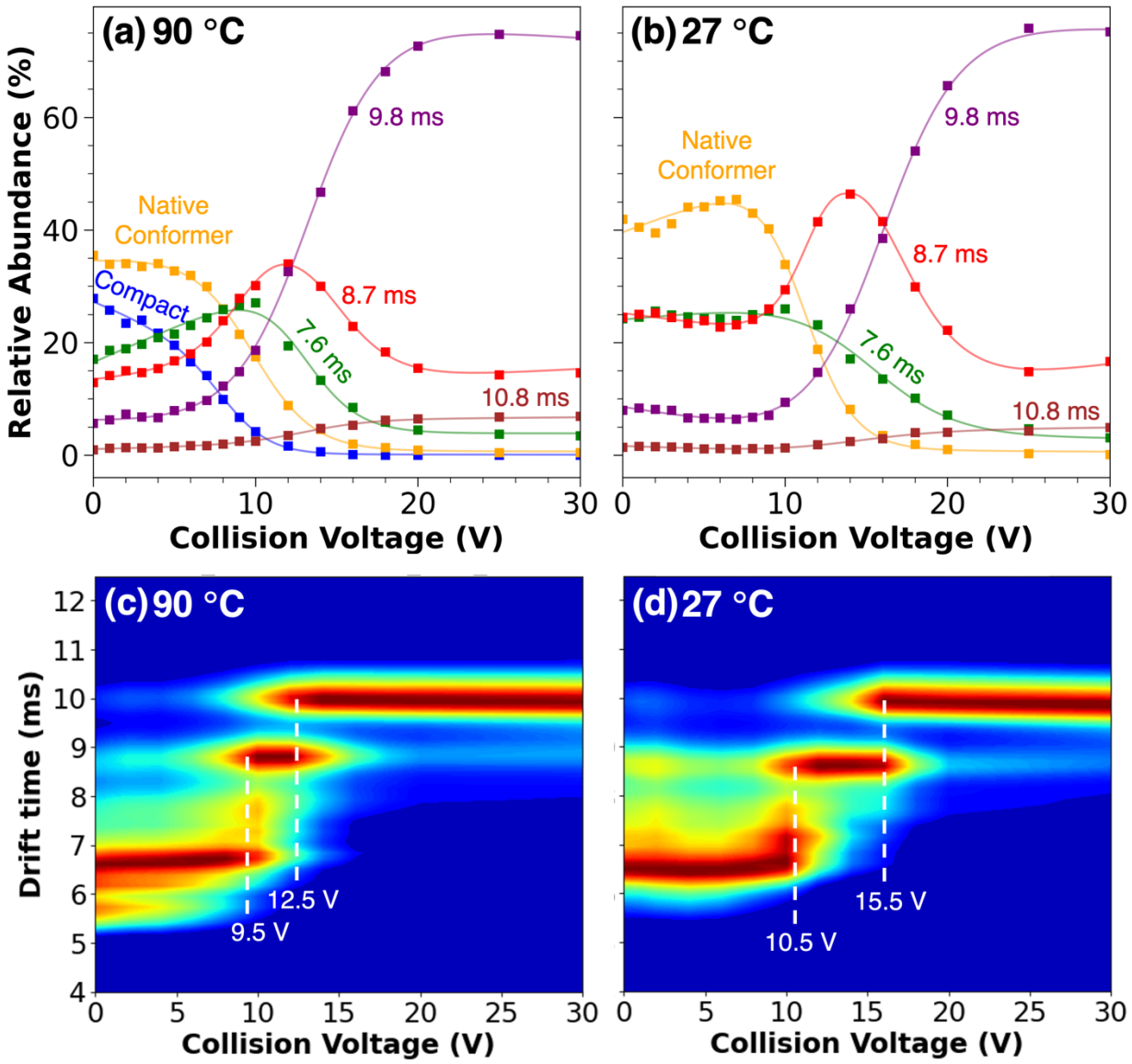

Figure 9.4. (a,b) The relative abundance of different conformers of the +7 charge state at (a) 90 °C and (b) 27 °C. The numbers next to each curve denote the drift time of the ion. Interconversion between conformers is visualized using a (c,d) two dimension plot of drift time versus collision voltage. White dashed lines in (c) and (d) are used to denote the CIU_{50} values for each transition determined using CIUSuite 2.

9.8 Supplemental Information

9.8.1 Calculation of Droplet Lifetimes

The maximum droplet lifetime was determined based on the extent of cyt *c* refolding after theta mixing an acidified cyt *c* solution (pH 2.9) and a neutralizing solution at pH 7. The percent of unfolded protein was determined based on the population abundance of charge states >+8. Droplet lifetimes were calculated using the integrated rate law for a two-state folding reaction:

$$t = \tau * \ln\left(\frac{A_e - A_0}{A_e - A_t}\right)$$

Where *t* is the reaction time, τ is the protein refolding time constant (~57 μs for cyt *c*), and A_e, A_t, and A_0 are the percent abundances of unfolded protein at equilibrium, at time *t* (after mixing), and at time 0 (before mixing), respectively.

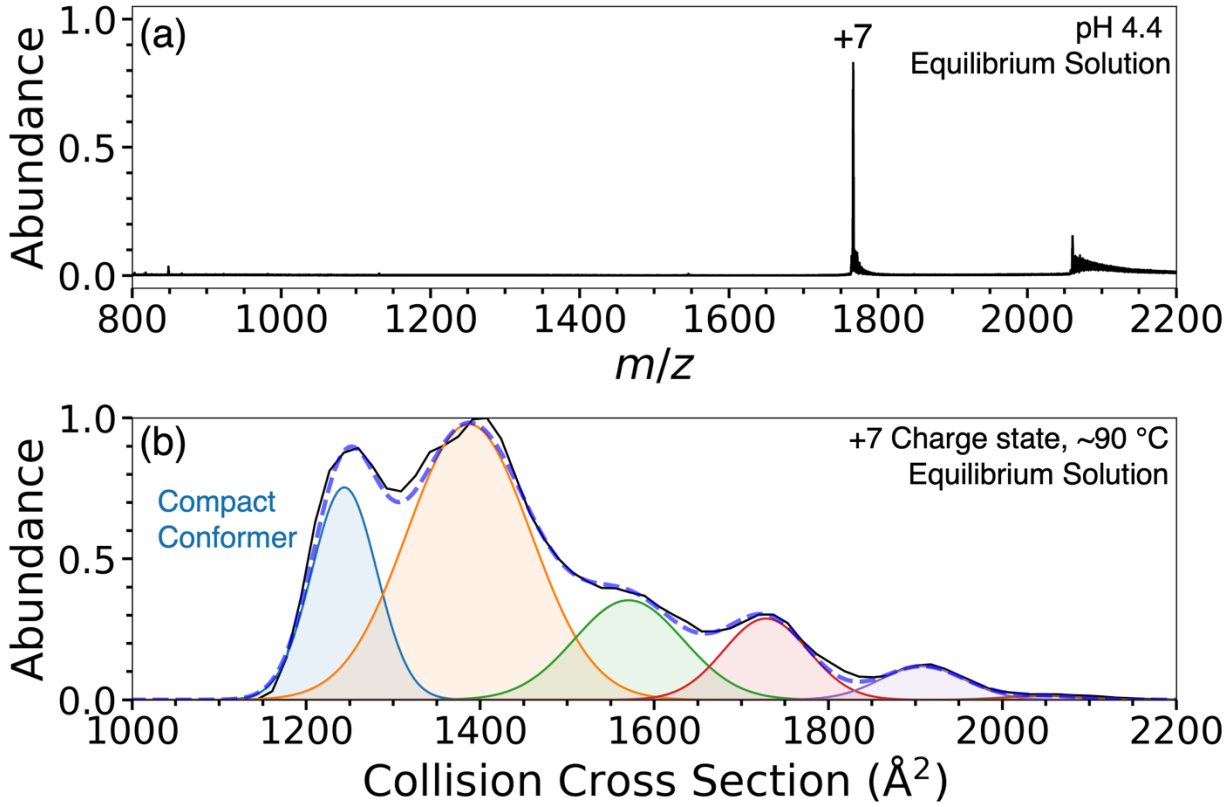

Supplemental Figure 9.1. (a) Mass spectrum of a 1:1 mixture of an acidified cyt *c* solution (pH 2.9) and a 100 mM ammonium acetate solution (pH 7) at equilibrium (pH 4.4). (b) The compact conformer (blue peak) still appears in the CCS distribution of the +7 charge state of cyt *c* at high temperatures from this equilibrium mixture.

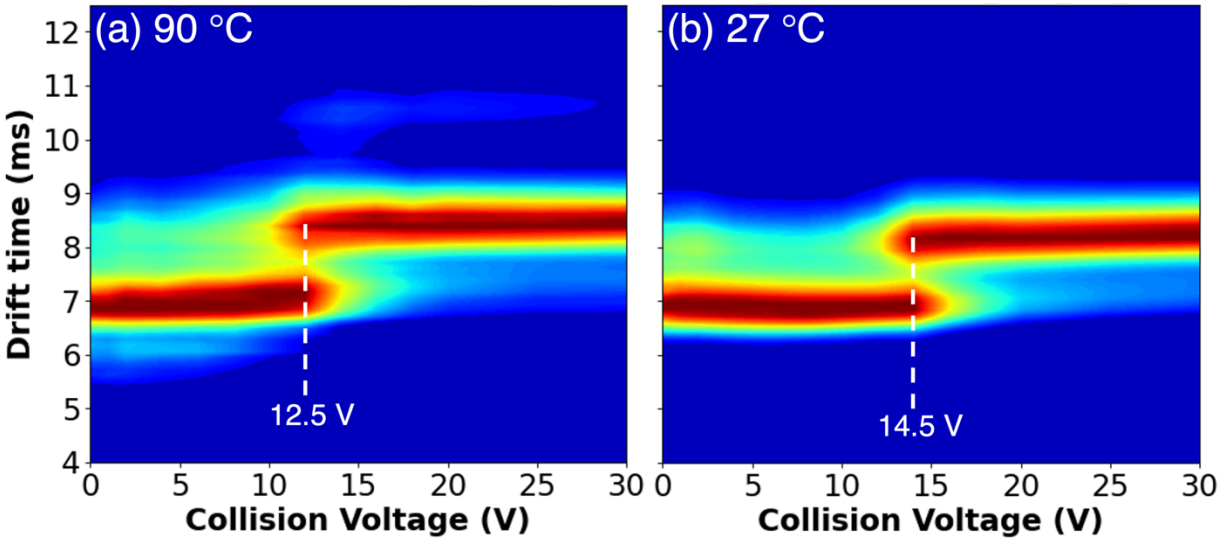

Supplemental Figure 9.2. Two dimensional drift time versus collision voltage plots for the +6 charge state produced from solutions at (a) 90 °C and (b) 27 °C.

Chapter 10

Charge Detection Mass Spectrometry Reveals Conformational Heterogeneity in MegaDalton-Sized Monoclonal Antibody Aggregates

This chapter is reproduced with permission from:

Jacob S. Jordan, Conner C. Harper, Fan Zhang, Esther Kofman, Mandy Li, Karthik Sathiyamoorthy, Jan Paulo Zaragoza, Laurence Fayadat-Dilman, and Evan R. Williams

"Charge Detection Mass Spectrometry Reveals Conformational Heterogeneity in MegaDalton-Sized Monoclonal Antibody Aggregates"

Journal of the American Chemical Society, **2024**, *146*:23297-23305.

10.1 Abstract

Aggregation of protein-based therapeutics can occur during development, production, or storage and can lead to loss of efficacy and potential toxicity. Native mass spectrometry of a covalently linked pentameric monoclonal antibody complex with a mass of ~800 kDa reveals several distinct conformations, smaller complexes, and abundant higher-order aggregates of the pentameric species. Charge detection mass spectrometry (CDMS) reveals individual oligomers up to the pentamer mAb trimer (15 individual mAb molecules; ~2.4 MDa) whereas intermediate aggregates composed of 6 – 9 mAb molecules and aggregates larger than the pentameric dimer (1.6 MDa) were not detected/resolved by standard mass spectrometry, size exclusion chromatography (SEC), capillary electrophoresis (CE-SDS), or by mass photometry. Conventional QTOF MS, mass photometry, SEC, and CE-SDS did not resolve partially or more fully unfolded conformations of each oligomer that were readily identified using CDMS by their significantly higher extent of charging. Trends in the charge-state distributions of individual oligomers provides detailed insight into how the structures of compact and elongated mAb aggregates change as a function of aggregate size. These results demonstrate the advantages of CDMS for obtaining accurate masses and information about the conformations of large antibody aggregates despite extensive overlapping m/z values. These results open up the ability to investigate structural changes that occur in small, soluble oligomers during the earliest stages of aggregation for antibodies or other proteins.

10.2 Introduction

Protein aggregation is a common factor in many devastating human diseases, including Alzheimer's disease, Parkinson's disease, and Huntington's disease among many others.[1,2] Many protein therapeutics are also prone to aggregation, which can degrade their efficacy and may lead to adverse patient outcomes.[3–5] Understanding factors that affect protein aggregation are important for the development, storage, and shipment of biopharmaceuticals. The effects of thermal and freeze/thaw stress on the aggregation of biotherapeutics are routinely characterized for FDA approval of new pharmaceuticals.[6] Characterization is typically done using methods such as optical, fluorescence, or electron microscopy, size-exclusion chromatography, capillary electrophoresis, and dynamic or multi-angle light scattering.[7] While these methods can often quantify changes in the abundances of higher order, visible aggregates or protein monomers and dimers, the resolution at intermediate aggregate sizes (>10 nm - <100 nm) may be limited so that individual oligomeric states are not distinguished.

Native mass spectrometry (MS) is routinely used for characterizing proteins, DNA, and the stoichiometry and structures of macromolecular complexes owing to the inherent high sensitivity and speed of analysis. Native MS has been extensively used to characterize the masses, stoichiometries, and stabilities of monoclonal antibody therapeutics (mAbs) and drug-antibody complexes.[8–11] However, characterizing higher order aggregates with conventional MS instruments can be challenging because of detection and resolution limitations associated with high *m/z* measurements and the heterogeneity of large molecular complexes. Heterogeneity can be intrinsic to the sample itself, but also can be the result of adduction of non-volatile salts, molecules, and solvent to gaseous ions that are formed directly from solution by electrospray ionization.[12,13] Adducts broaden peaks in a charge-state distribution, an effect that can ultimately prevent individual charge states from being resolved. Under these circumstances, little information about masses is obtained directly from a mass spectrum. The extent of heterogeneity typically increases with analyte mass, but limitations on resolving power as a result of sample heterogeneity are sample dependent.[14] The lack of a robust method for measuring the masses and stoichiometries of higher molecular weight analytes using conventional MS instrumentation often precludes the characterization of the distribution of higher order oligomers for many biomolecules of pharmaceutical interest, especially when analyte masses extend into the MDa range.

Charge detection mass spectrometry (CDMS), in which the *m/z* and charge of individual ions are measured independently, overcomes the high mass limitations of conventional MS instruments. CDMS has been used to measure the masses of a diverse array of analytes, including intact viruses,[14–19] virus-like particles,[11,20,21] large protein complexes,[22,23] cellular replication and folding machinery,[24,25] synthetic polymers,[21,23,26–29] large salt clusters,[30] aqueous nanodroplets,[31,32] and synthetic nanoparticles with masses extending into the high MDa and even GDa range.[33–35] The advantage of individual ion measurements is that chemical noise is eliminated – the mass of each ion is measured independently of other ions. This makes it possible to obtain accurate masses for even highly heterogeneous analytes.[14,18] More recently, Orbitrap instruments have been used to make individual ion measurements as well.[36–41] Mass measurements of individual large biomolecules can also be made with mass photometry, which relies upon the scattering of incident light as biomolecules interact with a glass surface,[42–44] and nanoelectromechanical sensor mass spectrometry, which measures the change in the resonant frequency of a nanofabricated sensor upon landing of a particle.[45–47] CDMS has been compared to mass photometry and size exclusion chromatography for the characterization of small, heavily glycosylated antibody therapeutics[40] and recent differential ion mobility separations show this method can provide information about mAb

oligomers as large as ~1.2 MDa.[48] CDMS has advantages for investigating antibody aggregation and aggregation-induced conformational changes, including the ability to measure molecular complexes with masses well into the 100's of MDa range. Here, we compare conventional native MS, mass photometry, size exclusion chromatography, capillary electrophoresis, and CDMS for characterizing the oligomeric distribution of a covalently bound complex consisting of five identical mAb molecules.[40]

10.3 Experimental

A representative humanized IgG1 antibody heavy chain (HC) was designed with an appended, slightly modified human cartilage oligomeric matrix protein (COMP) motif (Uniprot: P49747, pos29-73, DLAPQMLRELQETNAALQDVRELLRQQVKEITFLKNTVMECDACG) following a $(G_3S)_4$ flexible linker at its C-terminus to promote pentameric assembly through disulfide and coiled-coil formation. This engineered HC and the corresponding kappa light chain (LC) were cloned separately for co-transfection into *in-house* mammalian expression vectors with signal peptides to promote secretion of the recombinant pentameric antibody. Plasmids for HC and LC were transiently transfected at 1:1 DNA ratio into a 293 cell expression system in suspension using serum-free defined media (Invitrogen Corporation, Carlsbad, CA). Cell culture supernatants were harvested after 4-days. High-throughput Protein-A based MabSelect affinity chromatography using miniature columns (Repligen/Cytiva, Waltham, MA) enabled 1-step purification of recombinant antibodies from the harvested clarified cell culture fluid (CCCF) to generate purified material.

Size exclusion chromatography (SEC) was performed using a Waters Acquity BEH450 column (2.5 μm, 4.6 x 150 mm, Milford, MA**)** using an isocratic flow of 100 mM sodium phosphate, 200 mM sodium chloride, and 0.02% sodium azide (pH 7). Chromatograms were acquired using both 214 and 280 nm wavelengths, and integration of the absorption at 280 nm was performed using EMPOWER 3 (Waters Corporation). The molecular weights of unknowns were calculated based on the retention time of standards with known molecular weights between 112 Da and ~1.3 MDa analyzed using the same SEC conditions.

Capillary electrophoresis sodium dodecyl sulfate (CE-SDS) was done using a MauriceFlex instrument and CE-SDS PLUS cartridge (Bio-Techne, Minneapolis, MN) under non-reducing conditions. The CE-SDS PLUS molecular weight (MW) marker was supplemented with thyroglobulin to extend the range to 660 kDa. The sample was diluted in CE-SDS PLUS 1X sample buffer to make a 50 μL solution of 0.5 mg/mL protein. Iodoacetamide (IAA) was used as the alkylation reagent. 2 μL of CE-SDS PLUS 25X Internal Standard and 2.5 μL of 250 mM IAA were added to the sample and the sample was heated for 10 min at 70 °C. The MW marker and sample were run with injection at 4600 V over 20 s and separation at 5750 V for 90 min. Analysis of the acquired data was performed using the Compass for iCE software (Bio-Techne).

Mass photometry (MP) was performed using a Refeyn TwoMP instrument (Refeyn Ltd., Oxford, UK). Thyroglobulin and phosphate-buffered saline were used as a calibrant and as a blank, respectively. The sample was diluted in phosphate buffered saline (PBS) to a final concentration within an ideal working range of 10-50 nM. For data acquisition, 18 μL of buffer was added to a well, followed by the addition of 2 μL of the diluted sample. The well contents were mixed

thoroughly, and measurements were started within a duration of 60 s. Analysis of the acquired data was performed using the DiscoverMP software (Refeyn Ltd.).

For mass spectrometry measurements, covalently linked pentameric mAb complexes were buffer exchanged into aqueous 163 mM ammonium acetate (pH 6.8) using a Micro Bio-Spin 6 column (Bio-Rad Laboratories, Hercules, CA). Ions were formed by electrospray (ESI) from borosilicate emitters that are pulled to a 1.1 ± 0.1 μm tip diameter. Emitters were fabricated in-house from borosilicate capillaries (1.0 mm outer diameter, 0.78 mm inner diameter, Sutter Instrument, Novato, CA, Part No. BF100-78-10) using a P-87 Flaming/Brown micropipette puller (Sutter Instrument).[49] Tip diameters were measured using a Hitachi TM-1000 scanning electron microscope (Tokyo, Japan) at the Electron Microscopy Laboratory at the University of California, Berkeley.

Data were acquired using a quadrupole time-of-flight (QTOF) Premier mass spectrometer (Waters Corporation, Milford, MA). The source temperature was 80 °C, and the extraction cone, sampling cone, and ion guide voltages were 3 V, 100 V, and 2 V, respectively. The backing pressure in the source was 5-10 mbar to assist desolvating larger ions. The collision gas flow rate was 0.75 mL min^{-1}, resulting in a final argon gas pressure of ~0.002 mbar in the collision cell. Ions were formed by applying a voltage of ~0.7 – 1.3 kV to a 0.127 mm platinum wire inserted into the back of nESI emitters and in contact with the solution.

Charge detection mass spectrometry experiments were performed using an instrument and data analysis methods that are described in detail elsewhere.[19,33,50] The instrument consists of a heated ion transfer tube maintained at 140 °C, three RF-only quadrupole ion guides, and an electrostatic cone trap.[33] To enable transmission over a wide range of *m/z* values (*m/z* = ~2,000 – 20,000), data were acquired by sweeping across five different tuning conditions by varying the voltages and frequencies of the RF-only quadrupoles and ion funnel. Reported relative abundances are based on the peak height (in counts) of each species. These data were analyzed with a 10 ms short time Fourier transform window length. All mass spectrometry experiments were performed at the University of California, Berkeley. All other experiments were performed at Merck & Co., Inc., San Francisco, CA, USA.

10.4 Results and Discussion

10.4.1 QTOF MS and CDMS Characterization of the Pentamer mAb Sample

A covalent pentameric IgG1 complex (valency = 10) was produced through disulfide bond linkage and non-covalent interactions through a coiled-coil motif at the C-terminus of the heavy chain (HC) of a conventional mAb. This pentamer form could induce clustering of specific membrane receptors favoring functional downstream cell signaling pathways. An electrospray mass spectrum of the pentamer mAb complex acquired with a QTOF mass spectrometer shows a variety of highly charged species, including two elongated forms of the pentamer mAb with measured masses of 800.3 ± 0.2 kDa (*m/z* values between 4,000 and 5,500; charge states +140 – +185) and 800.7 ± 0.4 kDa (*m/z* values between 6,500 and 7,500; charge states +104 - +124), as well as a 400.1 ± 0.1 kDa ion (*m/z* values between 4,000 and 5,000; charge states +69 - +102) that does not correspond to a complex with an integer number of mAb molecules (Figure 1a). The

extent of protein charging from electrospray ionization is related to the conformation or shape of proteins in solution.[51] Higher charge ions are produced from proteins with more elongated conformations, indicating that the predominant species in the sample are elongated pentamer mAbs.

There are also many compact species observed in the QTOF mass spectrum, including a compact monomeric form of the pentamer mAb complex with a measured mass of 799.6 ± 0.8 kDa) (*m/z* values between 12,000 and 14,000; charge states between +57 and +67) (Figure 1a). There is also signal for the mAb heavy chain (*m/*z = 3100 – 3600, 47.1 ± 0.1 kDa) and the mAb monomer (*m/z* = 5900 – 6500, 160.1 ± 0.1 kDa). Charge-state distributions between *m/z* 8,000 – 11,000 correspond to ions with masses of 320.7 ± 0.1 kDa, 488.1 ± 0.6 kDa, and 384.2 ± 0.2 kDa. The first two correspond to a dimer and trimer mAb complex, respectively, whereas the third may correspond to an aggregate or ion consisting of a mAb dimer and a heavy chain. The broad peaks and elevated baseline between *m/z* 3,000 and 11,000 clearly indicate the presence of other species that are unresolved. Although masses can be obtained for the dimer and trimer in this region, other components contributing to the signal underneath these distributions cannot be obtained directly.

There is a broad, unresolved peak at *m/z* = 16,000 – 19,000 (Figure 1a). Because charge-state resolution was not achieved, a mass was not obtained, but it almost certainly corresponds in part to a dimer of the pentamer complex (~1.6 MDa) based on the *m*/*z* range. The pentamer appears to be relatively homogenous based on the resolved charge-state distributions, but salt or solvent adduction as well as binding of smaller species to high mass ions can lead to broad, overlapping peaks in a *m*/*z* spectrum that are not resolved, making it more difficult to characterize MDa-sized complexes. There is no identifiable signal for oligomers larger than the dimer of the pentamer complex.

The same pentamer sample was analyzed using CDMS and these data are shown in the form of a mass histogram (Figure 1b) and a two-dimensional representation of the same mass and charge data (Figure 1c). The mass histogram (Figure 1b) is analogous to a deconvolved mass spectrum obtained with conventional mass spectrometers. The two-dimensional plot (Figure 1c) provides information about the extent of charging or shape of the complexes.[18] Both highly elongated and compact species are observed. The different structures can be distinguished based on the differing number of charges even for ions that have the exact same mass. Highly elongated forms of the monomer (161.1 ± 0.5 kDa), dimer (324.1 ± 0.9 kDa), trimer (478.8 ± 1.2 kDa), tetramer (647.1 ± 2.0 kDa), and pentamer mAbs (799.2 ± 0.9 kDa) are abundant. There is also an ion at 402.8 ± 2.6 kDa that does not correspond to an integer number of mAbs that was also observed in the QTOF data. The masses determined from the highly charged forms of these species are in good agreement with the masses obtained from the QTOF mass spectra. There are also a number of highly charged oligomers consisting of the pentamer mAb and and smaller mAb oligomers. The largest oligomer is a highly charged form of the pentamer mAb trimer (15 mAbs, 2.40 ± 0.01 MDa). Each of the high charge forms of these aggregates span a similar *m/z* range (~4,000 – 6,000) and are likely present in the QTOF mass spectrum but are not resolved underneath the distribution for the abundant, elongated form of the pentamer. These data demonstrate that CDMS can quantify low abundance species when there are many ions of similar and overlapping *m/z*, making it possible to identify the composition of biotherapeutic samples that contain multiple species.

In addition to the high charge state forms of the complexes, lower charge distributions are also observed for each oligomer in the CDMS data, consistent with more compact conformations. The most abundant low charge species is the pentamer mAb (825.0 ± 2.6 kDa) with an average

charge of +64, similar to that in the QTOF data (+62). In the QTOF data, the higher charged forms of this complex are the most abundant form of the pentamer mAb whereas the more compact form is more abundant in the CDMS data. This difference in abundance may be due to lower ion transmission and/or lower detection efficiency of high *m/z* ions in the QTOF instrument. The compact dimer of the pentamer complex (1.61 ± 0.01 MDa) consisting of a total of 10 mAb molecules is ~16% abundance relative to the compact monomer. Other low charge, lower mass species are also observed, including the mAb monomer (173.1 ± 5.2 kDa, at low abundance), dimer (344.4 ± 5.1 kDa), trimer (492.7 ± 5.1 kDa), and tetramer (657.1 ± 4.3 kDa), as well as a 420.8 ± 12.1 kDa complex corresponding to a non-integer number of mAbs (Figure 1c). The CDMS masses for these compact species are ~2-8% higher than the masses obtained from the QTOF data and from the higher charge forms of these oligomers in the CDMS data. Higher protein charge states retain fewer adducts compared to lower charge states,[52–54] indicating that the overweight masses obtained for the compact forms of these oligomers is likely caused by adduction of small molecules, including water, as a result of the gentle conditions of the CDMS instrument. Additional activation of the ions prior to CDMS detection should reduce this mass discrepancy as is often done with conventional MS instruments. The mAb tetramer was not observed in the QTOF MS data, but the low abundance of this ion in CDMS data indicates that it may contribute to the heterogeneity between *m/z* = 10,000 – 11,000 in the QTOF mass spectrum. The abundance of the pentameric dimer is significantly higher in the CDMS data than in the QTOF data. CDMS indicates that the higher charged forms of the pentameric dimer are ~5.9 times greater in abundance than that of the lower, more compact form. These ions appear in a similar range of *m/z* as the elongated pentamer. These are not resolved in the QTOF data but would contribute to signal intensity attributed to the pentamer in this region. This same phenomenon of overlapping *m/z* distributions is true for other more extended forms of the large oligomers. Another contributing factor to differences in signal abundances between the QTOF and CDMS data at high mass is that there is not a detection mass bias in CDMS once the number of charges on an ion exceeds the detection limit,[33] but sensitivity decreases at high *m/z* in QTOF instruments. We conclude that the abundance of pentameric dimer measured in CDMS is more reflective of the solution composition.

Some aggregation can occur as a result of analyte concentration during electrospray droplet evaporation.[13,54] To determine if that is possible here, the average number of molecules per droplet was estimated from the droplet size formed from an emitter with a tip diameter of 1.1 μm and ~1 μM analyte concentration.[13,55–57] Under these conditions, there is on average one analyte molecule per twelve droplets, indicating that significant aggregation in the electrospray process is unlikely and that the oligomers must originate from solution. Because the *m/z* and *z* are determined independently with CDMS, it is possible to resolve a broad variety of species that have overlapping *m/z* values, but different extents of charging. As a result, CDMS shows significant promise as a technique for measuring the relative abundances of compact and elongated species with sufficient resolution to identify and characterize different forms of individual antibody oligomers.

10.4.2 Comparing MS-Based Characterization with Conventional Techniques

Aggregation in biopharmaceutical products is typically characterized using methods such as size exclusion chromatography (SEC), capillary electrophoresis sodium dodecyl sulfate (CE-SDS), and more recently, mass photometry. A mass photometry histogram was acquired on the

same pentamer mAb sample (Figure 2a). There are peaks at 819 ± 32 kDa and 1.64 ± 0.06 MDa that correspond to the pentameric mAb complex and its dimer. The few counts between 2.3 MDa and 2.7 MDa may indicate the presence of a pentamer mAb trimer, but the mass spread in these data indicate that the signal is due to background noise or conformational heterogeneity of the higher order aggregates (Figure 2a). Mass photometry also indicates the presence of several lower mass species (80 ± 23 kDa, 326 ± 24 kDa and 485 ± 25 kDa) which may correspond to a mAb heavy chain, as well as two and three mAb complexes (Figure 2a). There is also a broad peak centered at 1.29 ± 0.10 MDa that may correspond to aggregates of the pentamer mAb and other smaller mAb species (Figure 2a). The mass photometry data do not provide any indication of the different forms of the pentameric complex that are clearly distinguished in the mass spectrometry datasets.

The same pentamer mAb sample was analyzed using a standard SEC workflow for antibody analysis. The SEC data for the pentamer mAb sample has three predominant peaks at 3.00 min (621 kDa), 2.63 min (1.28 MDa), and 2.42 min (1.80 MDa) (Figure 2b). These masses do not correspond to any of the species observed by QTOF MS, CDMS, or by mass photometry. SEC separates analytes based on hydrodynamic radius, but samples containing multiple oligomers that each have conformational heterogeneity can result in ambiguous assignments of masses and identities to peaks in the SEC trace. Column interactions may also play a role in the ambiguous assignment of peak identities. Fractions were collected for each these three peaks and characterized using QTOF MS and CDMS. Both QTOF and CDMS mass spectra of the main peak fraction (2.63 min) show approximately equal abundances of the compact and elongated form of the pentamer mAb monomer as well as the smaller mAb dimer, trimer and a ~400 kDa species that does not correspond to an integer number of mAb monomers (Figure S1a,b). A low abundance of compact pentamer mAb dimer was also detected. No protein signal was resolved in fractions collected from other peaks in the SEC trace. These data indicate that standard SEC workflows for mAb characterization do not sufficiently separate the individual oligomeric forms of the pentamer mAb. While additional fraction collections with MS analysis and optimization of the SEC separations would likely lead to improved separation and information, a standard workflow for mAb characterization was chosen as being most representative of the information that is obtained from a standard analysis as was done for the other methods.

This sample was also characterized using nonreducing CE-SDS separations, which resulted in 8 peaks. The most abundant peak at 3.28 min likely corresponds to the pentamer mAb. The molecular weight determined by CE-SDS for the pentamer is 674 kDa, which is 15.8% lower than the mass determined by mass spectrometry. There are several sources of error in determining the molecular weight of proteins using CE-SDS, making identification of the other peaks ambiguous.[58] The presence of species both larger and smaller than the pentamer mAb is consistent with the data obtained by mass spectrometry and mass photometry. In contrast to these conventional methods, CDMS provides information about the mass and conformation of individual antibody oligomers from a single measurement, and these data make it possible to unambiguously identify species based on their mass and charge.

10.4.3 Characterizing the Conformational Heterogeneity of mAb Oligomers with CDMS

The ability to clearly resolve different conformations from the charge-state distribution of each oligomeric state of the mAb monomer can provide insight into how the structure of successive oligomers evolves with their increasing size. There are both compact and more elongated forms of all of the oligomers observed in the CDMS data. The charge-state distribution of the compact and elongated species for each oligomer are shown as a function of the number of mAb molecules in the oligomer in Figure 3. The abundances of both forms are normalized separately so that they can be more clearly seen on the combined plot. The average charge of the most compact structures (charged near the Rayleigh limit) gradually increases from ~32 *e* to ~95 *e* as the oligomer size increases from the $n = 1$ to $n = 9$, where n refers to the number of mAb molecules in the oligomer (Figure 3, compact conformations shown in red). The $n = 9$ oligomer clearly has two conformations at lower (~85 *e*) and higher (~95 *e*) charge. This trend in charging with increasing size (shown by a gray arrow) indicates that at $n = 10$, only the lower charge conformer exists (shifted to slightly higher charge (~97 e) owing to the higher mass). These data indicate that a more compact conformational state is strongly favored for the $n = 10$ species. It is more difficult to distinguish individual peaks corresponding to different conformations in the charge plots for higher order oligomers due to the heterogeneity inherent to MDa-sized complexes and their lower overall abundance, but there is a clear overall shift of the elongated species towards forming more compact structures at larger sizes.

The same analysis was performed for the highly charged ions above the Rayleigh line (Figure 1c and Figure 3 black data). The broader range of charging shows that the higher charged species have more conformational heterogeneity than the compact forms, and that this heterogeneity increases with increasing oligomer size. There is a difference of ~+50 *e* between the most elongated conformation of each oligomer between $n = 1$ and $n = 5$. This approximately linear increase in charge indicates that these species are highly elongated. However, beginning at $n = 3$, the abundance of lower charge (~71 *e* and ~107 *e*) peaks are indicative of the formation of more compact, partially elongated structures. These peaks may arise from the aggregation of both elongated and compact conformers or from the structural rearrangement of larger elongated species into more compact structures. Three distinct peaks are also observed for the $n = 4$ oligomer (~75 *e*, ~142 *e*, and ~189 *e*), which are mostly consolidated into two peaks at intermediate charges of ~122 *e* and ~180 *e* for the $n = 5$ predominant pentameric species (Figure 3), consistent with the two less compact structures observed in the QTOF data (Figure 1a). The fully elongated species of the pentamer mAb (~240 *e*) appears to be heavily disfavored compared to the two more compact, but still elongated, species. These data demonstrate that small oligomers can have considerable conformational heterogeneity and that the structures and conformational ensemble of each successive oligomer can change significantly.

For aggregates larger than the pentamer mAb, the extent of charging for the elongated forms decreases suddenly. The charge-state distribution for the $n = 6$ oligomer has two peaks for elongated conformations that are both ~30 *e* lower charge than the two peaks for elongated species of the $n = 5$ oligomer. Larger aggregates show a gradual increase in the extent of charging until the $n = 10$ oligomer. The peaks at ~184 *e* and ~203 *e* for the $n = 10$ oligomer are significantly lower in abundance for the $n = 11$ oligomer whereas the lower charge ~157 *e* peak remains abundant, indicative of a preference for a more compact structure despite the increase in mass and oligomeric state. Resolution of distinct peaks in the charge-state distribution is lost with increasing oligomer size due to the increasing inherent heterogeneity of these larger complexes. However, the overall distribution of charge states for the less compact oligomers between $n = 11$ and $n = 15$ increases at a rate similar to that of the compact forms. This suggests that the elongated forms of successively

larger mAb oligomers progressively tend toward more globular structures. These data clearly show that the pentamer mAb (n = 5) and pentamer mAb dimer (n = 10) have distinct conformations that are important in the aggregation process. The oligomeric states subsequent to these key species yield ions with lower charge, suggesting more compact structures are formed via structural rearrangement. These data demonstrate that CDMS can clearly track conformational changes associated with the oligomerization processes of large proteins and also indicate that mAb oligomers possess unique conformations that are not merely amorphous aggregates of monomer subunits.

CDMS appears to be uniquely suited for characterizing the aggregation process of species with masses extending into the MDa range due to the ability to readily resolve individual oligomers both by mass and by conformation. The ability to readily resolve many different conformers of the same mass ion based on resolved charge-state distributions irrespective of overlapping m/z values with other ions is analogous to the ability of ion mobility combined with mass spectrometry to resolve different conformers based on differences in collisional cross sections.[59] These features of CDMS show significant promise as a characterization technique to investigate antibody aggregation during the development, storage, and shipment of pharmaceuticals, as well as early stage, transient protein oligomers implicated in neurodegenerative diseases.

10.5 Conclusions

Information about the masses and conformations of large macromolecular complexes can be readily obtained using CDMS even for highly heterogeneous mixtures, making it a promising technique for studying monoclonal antibody aggregation and degradation products. Protein charge-state distributions generated from ESI reflect solution-phase conformations. The presence of multiple resolved charge-state distributions for the same size oligomer indicates that these different structures exist in solution and are preserved through the ionization process under the soft mass spectrometry interface conditions that were used.[31,60] Many aggregates of a mAb and pentamer mAb complex that are detected and resolved by CDMS are not detected by other methods often used to measure the extent of aggregation. The pentamer mAb and dimers are observed with mass photometry, conventional native MS, and SEC, as are species corresponding to the mAb heavy chain, and dimer and trimer mAb complexes. In addition to these species, the CDMS data clearly shows the presence of oligomers with up to 15 mAb molecules and masses up to ~2.4 MDa. CDMS measurements enable the analysis of the charge-state distribution for each oligomer, providing insights into the conformational heterogeneity of the oligomerization/aggregation process. In this respect, the CDMS data provide both mass and shape information comparable to that obtained by ion mobility spectrometry, but at a much larger molecular size. This type of information should prove useful for characterizing aggregation-prone proteins associated with neurodegenerative disease and for the design of drugs or buffer additives that inhibit protein aggregation because specific forms of the aggregates can be targeted and readily analyzed. Aggregates of mAb therapeutics can be formed during development, purification, formulation, and storage and may have unwanted side-effects in patients. CDMS appears to be well-suited for characterizing protein conformations and aggregation products at the level of individual oligomers that could prove beneficial at different stages of drug development, for quality control, and for optimizing formulations for biopharmaceutical stability.

10.6 Acknowledgements

This material is based upon work supported by the National Science Foundation Division of Chemistry under grant number CHE-2203907, an ACS Graduate Research Fellowship sponsored by Eli Lilly and Company (J.S.J.), the Arnold and Mabel Beckman Foundation Postdoctoral Fellowship in Chemical Instrumentation (C.C.H.), Merck & Co., Inc., San Francisco, CA, USA, Inc. through their Discovery Biologics SEEDS program, and the National Institutes of Health (grant 5R01GM139338) for the development and construction of the charge detection mass spectrometer used in this research.

10.7 References

(1) Ross, C. A.; Poirier, M. A. Protein Aggregation and Neurodegenerative Disease. *Nat. Med.* **2004**, *10* (S7), S10–S17.
(2) Stefani, M.; Dobson, C. M. Protein Aggregation and Aggregate Toxicity: New Insights into Protein Folding, Misfolding Diseases and Biological Evolution. *J. Mol. Med.* **2003**, *81* (11), 678–699.
(3) Ratanji, K. D.; Derrick, J. P.; Dearman, R. J.; Kimber, I. Immunogenicity of Therapeutic Proteins: Influence of Aggregation. *J. Immunotoxicol.* **2014**, *11* (2), 99–109.
(4) Swanson, M. D.; Rios, S.; Mittal, S.; Soder, G.; Jawa, V. Immunogenicity Risk Assessment of Spontaneously Occurring Therapeutic Monoclonal Antibody Aggregates. *Front. Immunol.* **2022**, *13* (July), 1–11.
(5) Wang, W.; Singh, S. K.; Li, N.; Toler, M. R.; King, K. R.; Nema, S. Immunogenicity of Protein Aggregates—Concerns and Realities. *Int. J. Pharm.* **2012**, *431* (1–2), 1–11.
(6) United States Food and Drug Administration. *Guidance for Industry Q6B Specifications: Test Procedures and Acceptance Criteria for Biotechnological/Biological Products*; 1999.
(7) den Engelsman, J.; Garidel, P.; Smulders, R.; Koll, H.; Smith, B.; Bassarab, S.; Seidl, A.; Hainzl, O.; Jiskoot, W. Strategies for the Assessment of Protein Aggregates in Pharmaceutical Biotech Product Development. *Pharm. Res.* **2011**, *28* (4), 920–933.
(8) Rosati, S.; Yang, Y.; Barendregt, A.; Heck, A. J. R. Detailed Mass Analysis of Structural Heterogeneity in Monoclonal Antibodies Using Native Mass Spectrometry. *Nat. Protoc.* **2014**, *9* (4), 967–976.
(9) Villafuerte-Vega, R. C.; Li, H. W.; Slaney, T. R.; Chennamsetty, N.; Chen, G.; Tao, L.; Ruotolo, B. T. Ion Mobility-Mass Spectrometry and Collision-Induced Unfolding of Designed Bispecific Antibody Therapeutics. *Anal. Chem.* **2023**, *95* (17), 6962–6970.
(10) Campuzano, I. D. G.; Netirojjanakul, C.; Nshanian, M.; Lippens, J. L.; Kilgour, D. P. A.; Van Orden, S.; Loo, J. A. Native-MS Analysis of Monoclonal Antibody Conjugates by Fourier Transform Ion Cyclotron Resonance Mass Spectrometry. *Anal. Chem.* **2018**, *90* (1), 745–751.
(11) Tamara, S.; den Boer, M. A.; Heck, A. J. R. High-Resolution Native Mass Spectrometry. *Chem. Rev.* **2022**, *122* (8), 7269–7326.
(12) Susa, A. C.; Xia, Z.; Williams, E. R. Native Mass Spectrometry from Common Buffers with Salts That Mimic the Extracellular Environment. *Angew. Chem. Int. Ed.* **2017**, *56* (27), 7912–7915.
(13) Susa, A. C.; Xia, Z.; Williams, E. R. Small Emitter Tips for Native Mass Spectrometry of Proteins and Protein Complexes from Nonvolatile Buffers That Mimic the Intracellular Environment. *Anal. Chem.* **2017**, *89* (5), 3116–3122.

(14) Harper, C. C.; Miller, Z. M.; Lee, H.; Bischoff, A. J.; Francis, M. B.; Schaffer, D. V.; Williams, E. R. Effects of Molecular Size on Resolution in Charge Detection Mass Spectrometry. *Anal. Chem.* **2022**, *94* (33), 11703–11712.
(15) Grande, A. E.; Li, X.; Miller, L. M.; Zhang, J.; Draper, B. E.; Herzog, R. W.; Xiao, W.; Jarrold, M. F. Antibody Binding to Recombinant Adeno Associated Virus Monitored by Charge Detection Mass Spectrometry. *Anal. Chem.* **2023**, *95* (29), 10864–10868.
(16) Barnes, L. F.; Draper, B. E.; Jarrold, M. F. Analysis of Recombinant Adenovirus Vectors by Ion Trap Charge Detection Mass Spectrometry: Accurate Molecular Weight Measurements beyond 150 MDa. *Anal. Chem.* **2022**, *94* (3), 1543–1551.
(17) Barnes, L. F.; Draper, B. E.; Kurian, J.; Chen, Y. T.; Shapkina, T.; Powers, T. W.; Jarrold, M. F. Analysis of AAV-Extracted DNA by Charge Detection Mass Spectrometry Reveals Genome Truncations. *Anal. Chem.* **2023**, *95* (9), 4310–4316.
(18) Bischoff, A. J.; Harper, C. C.; Williams, E. R.; Francis, M. B. Characterizing Heterogeneous Mixtures of Assembled States of the Tobacco Mosaic Virus Using Charge Detection Mass Spectrometry. *J. Am. Chem. Soc.* **2022**, *144* (51), 23368–23378.
(19) Miller, Z. M.; Harper, C. C.; Lee, H.; Bischoff, A. J.; Francis, M. B.; Schaffer, D. V.; Williams, E. R. Apodization Specific Fitting for Improved Resolution, Charge Measurement, and Data Analysis Speed in Charge Detection Mass Spectrometry. *J. Am. Soc. Mass Spectrom.* **2022**, *33* (11), 2129–2137.
(20) Miller, L. M.; Bond, K. M.; Draper, B. E.; Jarrold, M. F. Characterization of Classical Vaccines by Charge Detection Mass Spectrometry. *Anal. Chem.* **2021**, *93* (35), 11965–11972.
(21) Harper, C. C.; Avadhani, V. S.; Hanozin, E.; Miller, Z. M.; Williams, E. R. Dynamic Energy Measurements in Charge Detection Mass Spectrometry Eliminate Adverse Effects of Ion–Ion Interactions. *Anal. Chem.* **2023**, *95* (26), 10077–10086.
(22) Harper, C. C.; Elliott, A. G.; Oltrogge, L. M.; Savage, D. F.; Williams, E. R. Multiplexed Charge Detection Mass Spectrometry for High-Throughput Single Ion Analysis of Large Molecules. *Anal. Chem.* **2019**, *91* (11), 7458–7465.
(23) Harper, C. C.; Williams, E. R. Enhanced Multiplexing in Fourier Transform Charge Detection Mass Spectrometry by Decoupling Ion Frequency from Mass to Charge Ratio. *J. Am. Soc. Mass Spectrom.* **2019**, *30* (12), 2637–2645.
(24) El-Baba, T. J.; Raab, S. A.; Buckley, R. P.; Brown, C. J.; Lutomski, C. A.; Henderson, L. W.; Woodall, D. W.; Shen, J.; Trinidad, J. C.; Niu, H.; Jarrold, M. F.; Russell, D. H.; Laganowsky, A.; Clemmer, D. E. Thermal Analysis of a Mixture of Ribosomal Proteins by vT-ESI-MS: Toward a Parallel Approach for Characterizing the *Stabilitome*. *Anal. Chem.* **2021**, *93* (24), 8484–8492.
(25) Anthony, A. J.; Gautam, A. K. S.; Miller, L. M.; Ma, Y.; Hardwick, A. G.; Sharma, A.; Ghatak, S.; Matouschek, A.; Jarrold, M. F.; Clemmer, D. E. CDMS Analysis of Intact 19S, 20S, 26S, and 30S Proteasomes: Evidence for Higher-Order 20S Assemblies at a Low pH. *Anal. Chem.* **2023**, *95* (33), 12209–12215.
(26) Elliott, A. G.; Harper, C. C.; Lin, H.-W.; Williams, E. R. Effects of Individual Ion Energies on Charge Measurements in Fourier Transform Charge Detection Mass Spectrometry (FT-CDMS). *J. Am. Soc. Mass Spectrom.* **2019**, *30* (6), 946–955.
(27) Elliott, A. G.; Harper, C. C.; Lin, H. W.; Williams, E. R. Mass, Mobility and MS^n Measurements of Single Ions Using Charge Detection Mass Spectrometry. *Analyst* **2017**, *142* (15), 2760–2769.
(28) Harper, C. C.; Elliott, A. G.; Lin, H. W.; Williams, E. R. Determining Energies and Cross Sections of Individual Ions Using Higher-Order Harmonics in Fourier Transform Charge Detection Mass Spectrometry (FT-CDMS). *J. Am. Soc. Mass Spectrom.* **2018**, *29* (9), 1861–1869.
(29) Halim, M. A.; Clavier, C.; Dagany, X.; Kerleroux, M.; Dugourd, P.; Dunbar, R. C.; Antoine, R. Infrared Laser Dissociation of Single Megadalton Polymer Ions in a Gated Electrostatic Ion Trap: The Added Value of Statistical Analysis of Individual Events. *Phys. Chem. Chem. Phys.* **2018**, *20* (17), 11959–11966.

(30) McPartlan, M. S.; Harper, C. C.; Hanozin, E.; Williams, E. R. Ion Emission from 1–10 MDa Salt Clusters: Individual Charge State Resolution with Charge Detection Mass Spectrometry. *Analyst* **2024**, *149* (3), 735-744.
(31) Hanozin, E.; Harper, C. C.; McPartlan, M. S.; Williams, E. R. Dynamics of Rayleigh Fission Processes in ∼100 nm Charged Aqueous Nanodrops. *ACS Cent. Sci.* **2023**, *9* (8), 1611–1622.
(32) Harper, C. C.; Brauer, D. D.; Francis, M. B.; Williams, E. R. Direct Observation of Ion Emission from Charged Aqueous Nanodrops: Effects on Gaseous Macromolecular Charging. *Chem. Sci.* **2021**, *12* (14), 5185–5195.
(33) Harper, C. C.; Miller, Z. M.; McPartlan, M. S.; Jordan, J. S.; Pedder, R. E.; Williams, E. R. Accurate Sizing of Nanoparticles Using a High-Throughput Charge Detection Mass Spectrometer without Energy Selection. *ACS Nano* **2023**, *17* (8), 7765–7774.
(34) Doussineau, T.; Bao, C. Y.; Antoine, R.; Dugourd, P.; Zhang, W.; D'Agosto, F.; Charleux, B. Direct Molar Mass Determination of Self-Assembled Amphiphilic Block Copolymer Nanoobjects Using Electrospray-Charge Detection Mass Spectrometry. *ACS Macro Lett.* **2012**, *1* (3), 414–417.
(35) Doussineau, T.; Désert, A.; Lambert, O.; Taveau, J. C.; Lansalot, M.; Dugourd, P.; Bourgeat-Lami, E.; Ravaine, S.; Duguet, E.; Antoine, R. Charge Detection Mass Spectrometry for the Characterization of Mass and Surface Area of Composite Nanoparticles. *J. Phys. Chem. C* **2015**, *119* (20), 10844–10849.
(36) Kostelic, M. M.; Ryan, J. P.; Brown, L. S.; Jackson, T. W.; Hsieh, C.; Zak, C. K.; Sanders, H. M.; Liu, Y.; Chen, V. S.; Byrne, M.; Aspinwall, C. A.; Baker, E. S.; Marty, M. T. Stability and Dissociation of Adeno-Associated Viral Capsids by Variable Temperature-Charge Detection-Mass Spectrometry. *Anal. Chem.* **2022**, *94* (34), 11723–11727.
(37) Lai, S. H.; Tamara, S.; Heck, A. J. R. Single-Particle Mass Analysis of Intact Ribosomes by Mass Photometry and Orbitrap-Based Charge Detection Mass Spectrometry. *iScience* **2021**, *24* (11), 103211.
(38) Kafader, J. O.; Melani, R. D.; Durbin, K. R.; Ikwuagwu, B.; Early, B. P.; Fellers, R. T.; Beu, S. C.; Zabrouskov, V.; Makarov, A. A.; Maze, J. T.; Shinholt, D. L.; Yip, P. F.; Tullman-Ercek, D.; Senko, M. W.; Compton, P. D.; Kelleher, N. L. Multiplexed Mass Spectrometry of Individual Ions Improves Measurement of Proteoforms and Their Complexes. *Nat. Methods* **2020**, *17* (4), 391–394.
(39) McGee, J. P.; Melani, R. D.; Yip, P. F.; Senko, M. W.; Compton, P. D.; Kafader, J. O.; Kelleher, N. L. Isotopic Resolution of Protein Complexes up to 466 KDa Using Individual Ion Mass Spectrometry. *Anal. Chem.* **2021**, *93* (5), 2723–2727.
(40) den Boer, M. A.; Lai, S. H.; Xue, X.; van Kampen, M. D.; Bleijlevens, B.; Heck, A. J. R. Comparative Analysis of Antibodies and Heavily Glycosylated Macromolecular Immune Complexes by Size-Exclusion Chromatography Multi-Angle Light Scattering, Native Charge Detection Mass Spectrometry, and Mass Photometry. *Anal. Chem.* **2022**, *94* (2), 892–900.
(41) Du, C.; Cleary, S. P.; Kostelic, M. M.; Jones, B. J.; Kafader, J. O.; Wysocki, V. H. Combining Surface-Induced Dissociation and Charge Detection Mass Spectrometry to Reveal the Native Topology of Heterogeneous Protein Complexes. *Anal. Chem.* **2023**, *95* (37), 13889–13896.
(42) Hundt, N.; Cole, D.; Hantke, M. F.; Miller, J. J.; Struwe, W. B.; Kukura, P. Direct Observation of the Molecular Mechanism Underlying Protein Polymerization. *Sci. Adv.* **2022**, *8* (35), eabm7935.
(43) Young, G.; Hundt, N.; Cole, D.; Fineberg, A.; Andrecka, J.; Tyler, A.; Olerinyova, A.; Ansari, A.; Marklund, E. G.; Collier, M. P.; Chandler, S. A.; Tkachenko, O.; Allen, J.; Crispin, M.; Billington, N.; Takagi, Y.; Sellers, J. R.; Eichmann, C.; Selenko, P.; Frey, L.; Riek, R.; Galpin, M. R.; Struwe, W. B.; Benesch, J. L. P.; Kukura, P. Quantitative Mass Imaging of Single Biological Macromolecules. *Science,* **2018**, *360* (6387), 423–427.
(44) Liebthal, M.; Kushwah, M. S.; Kukura, P.; Dietz, K. J. Single Molecule Mass Photometry Reveals the Dynamic Oligomerization of Human and Plant Peroxiredoxins. *iScience* **2021**, *24* (11), 103258.
(45) Lai, S. H.; Reynaud, A.; Zhang, N. N.; Kwak, M.; Vysotskyi, B.; Dominguez-Medina, S.; Fortin, T.; Clement, K.; Defoort, M.; Lee, T. G.; Liu, K.; Hentz, S.; Masselon, C. D. Characterizing Nanoparticle Mass Distributions Using Charge-Independent Nanoresonator Mass Spectrometry. *J. Phys. Chem. C* **2022**, *126* (49), 20946–20953.

(46) Dominguez-Medina, S.; Fostner, S.; Defoort, M.; Sansa, M.; Stark, A. K.; Halim, M. A.; Vernhes, E.; Gely, M.; Jourdan, G.; Alava, T.; Boulanger, P.; Masselon, C.; Hentz, S. Neutral Mass Spectrometry of Virus Capsids above 100 Megadaltons with Nanomechanical Resonators. *Science* **2018**, *362* (6417), 918–922.
(47) Kaynak, B. E.; Alkhaled, M.; Kartal, E.; Yanik, C.; Hanay, M. S. Atmospheric-Pressure Mass Spectrometry by Single-Mode Nanoelectromechanical Systems. *Nano Lett.* **2023**, *23* (18), 8553–8559.
(48) Wörner, T. P.; Thurman, H. A.; Makarov, A. A.; Shvartsburg, A. A. Expanding Differential Ion Mobility Separations into the MegaDalton Range. *Anal. Chem.* **2024**.
(49) Jordan, J. S.; Xia, Z.; Williams, E. R. Tips on Making Tiny Tips: Secrets to Submicron Nanoelectrospray Emitters. *J. Am. Soc. Mass Spectrom.* **2022**, *33* (3), 607–611.
(50) Harper, C. C.; Miller, Z. M.; Williams, E. R. Combined Multiharmonic Frequency Analysis for Improved Dynamic Energy Measurements and Accuracy in Charge Detection Mass Spectrometry. *Anal. Chem.* **2023**, *95* (45), 16659–16667.
(51) Chowdhury, S. K.; Katta, V.; Chait, B. T. Probing Conformation Changes in Proteins by Mass Spectrometry. *J. Am. Chem. Soc.* **1990**, *112* (24), 9012–9013.
(52) Cassou, C. A.; Williams, E. R. Desalting Protein Ions in Native Mass Spectrometry Using Supercharging Reagents. *Analyst* **2014**, *139* (19), 4810–4819.
(53) Iavarone, A. T.; Udekwu, O. A.; Williams, E. R. Buffer Loading for Counteracting Metal Salt-Induced Signal Suppression in Electrospray Ionization. *Anal. Chem.* **2004**, *76* (14), 3944–3950.
(54) Flick, T. G.; Merenbloom, S. I.; Williams, E. R. Anion Effects on Sodium Ion and Acid Molecule Adduction to Protein Ions in Electrospray Ionization Mass Spectrometry. *J. Am. Soc. Mass Spectrom.* **2011**, *22* (11), 1968-1977.
(55) Jordan, J. S.; Williams, E. R. Effects of Electrospray Droplet Size on Analyte Aggregation: Evidence for Serine Octamer in Solution. *Anal. Chem.* **2021**, *93* (3), 1725–1731.
(56) Jordan, J. S.; Williams, E. R. Homochiral Preference of Serine Octamer in Solution and Formed by Dissociation of Large Gaseous Clusters. *Analyst* **2021**, *146* (22), 6822–6830.
(57) Davidson, K. L.; Oberreit, D. R.; Hogan, C. J.; Bush, M. F. Nonspecific Aggregation in Native Electrokinetic Nanoelectrospray Ionization. *Int. J. Mass Spectrom.* **2017**, *420*, 35–42.
(58) Wiesner, R.; Scheller, C.; Krebs, F.; Wätzig, H.; Oltmann-Norden, I. A Comparative Study of CE-SDS, SDS-PAGE, and Simple Western: Influences of Sample Preparation on Molecular Weight Determination of Proteins. *Electrophoresis* **2021**, *42* (3), 206–218.
(59) Bleiholder, C.; Bowers, M. T. The Solution Assembly of Biological Molecules Using Ion Mobility Methods: From Amino Acids to Amyloid β-Protein. *Annu. Rev. Anal. Chem.* **2017**, *10* (1), 365–386.
(60) Mortensen, D. N.; Williams, E. R. Ultrafast (1 μs) Mixing and Fast Protein Folding in Nanodrops Monitored by Mass Spectrometry. *J. Am. Chem. Soc.* **2016**, *138*, 3453-3460.

10.8 Figures

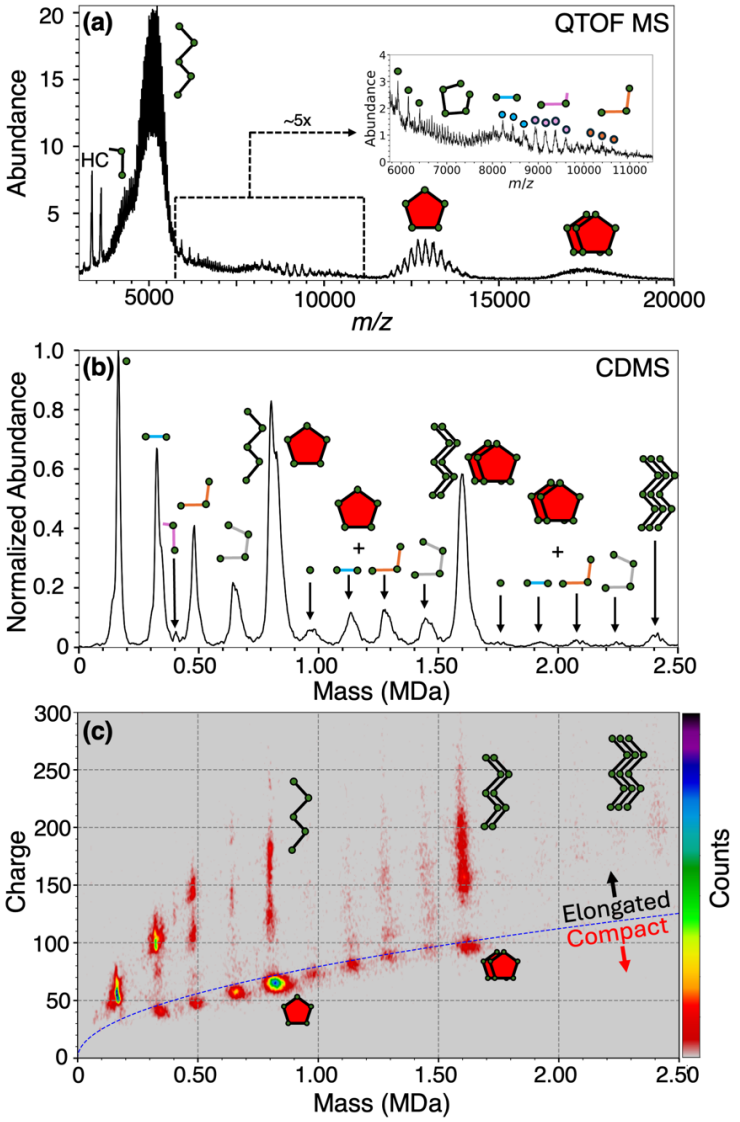

Figure 10.1. Mass spectral data from a pentameric mAb sample acquired using (a) native mass spectrometry with a QTOF mass spectrometer and (b,c) charge detection mass spectrometry using a custom built instrument. The inset in (a) is an expansion of the region from *m/z* 5,500 – 12,000 and shows the overlapping charge-state distributions in this region that indicate the presence of unresolved species. The CDMS 1D mass histogram in (b) is analogous to a deconvolved mass spectrum obtained by conventional native MS, whereas the CDMS 2D histogram in (c) disperses ion signal based on mass (*x*-axis) and charge (*y*-axis) with abundance indicated by the color code to the right of the plot. The blue dashed line in (c) corresponds to the Rayleigh limit for an aqueous droplet as a function of mass. Distributions above the Rayleigh line in (c) correspond to ions with an elongated conformation, whereas ions below this line have more compact structures that are more spherical.

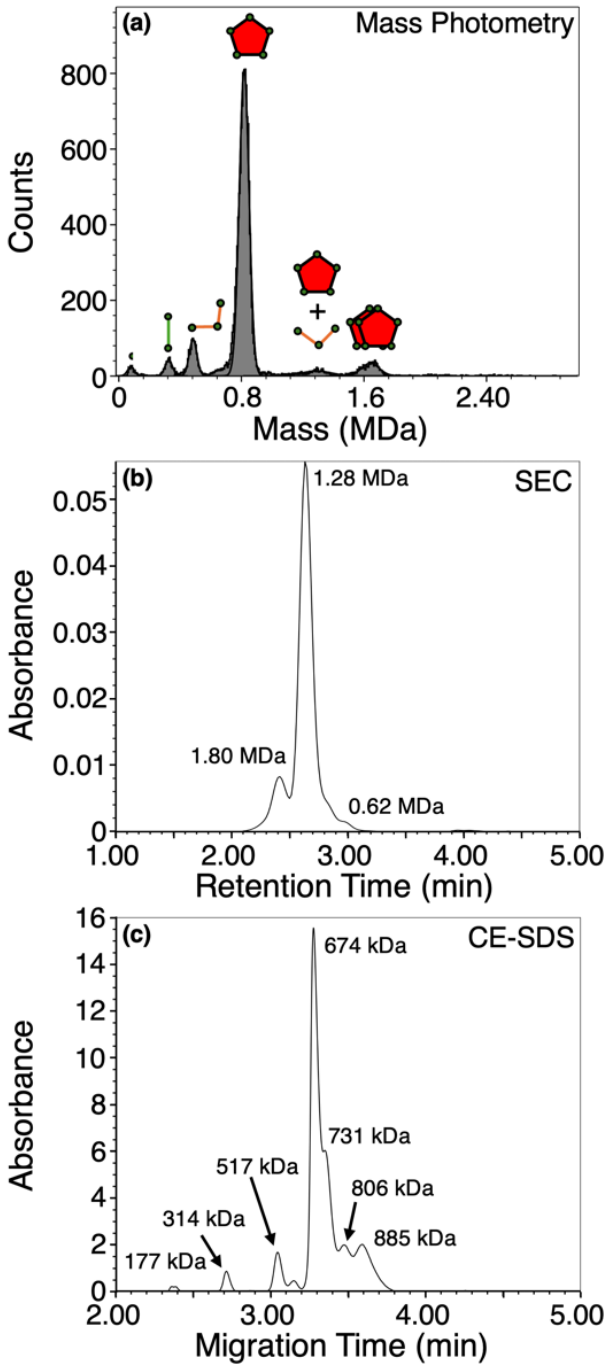

Figure 10.2. (a) Mass photometry histogram, (b) a SEC trace, and (c) a CE-SDS trace of the same pentameric mAb sample. Mass photometry signal for the pentamer mAb monomer and dimer is observed along with smaller species corresponding to a mAb heavy chain, as well as a mAb dimer and trimer. The molecular weights assigned to peaks in the SEC and CE-SDS traces in (b) and (c) were calculated based on the retention time or migration time of molecular weight standards with masses between 112 Da and 1.3 MDa. These masses and abundances do not directly correspond to species observed in the QTOF, CDMS, or mass photometry data, making assignments of these peaks ambiguous.

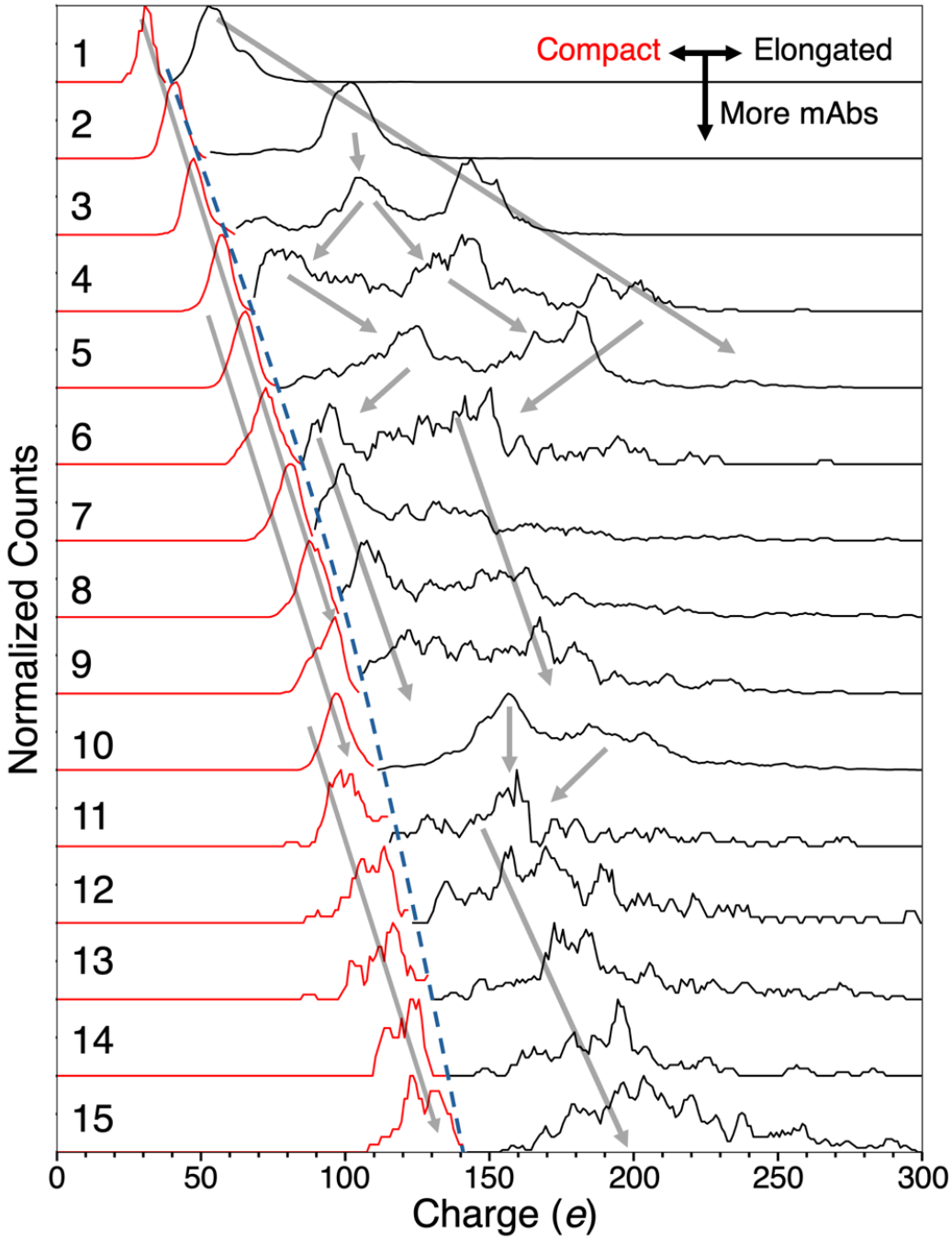

Figure 10.3. CDMS data shown in Figure 1c is replotted as a function of charge (*x*-axis) vs. the normalized abundances of each observed oligomeric species (*y*-axis) and shows the evolution of the structures of compact forms of the oligomers (charged near or below the Rayleigh limit; data in red) and the more elongated forms of the oligomers (charges above the Rayleigh limit; data in black). The numbers progressing down the *y*-axis correspond to the increasing number of mAb molecules in each oligomer. Data to the left and right of the blue dashed line are normalized separately so that the compact and elongated conformers can more clearly be compared on the same figure. Arrows show trends in conformational heterogeneity as a function of oligomer size.

10.9 Supplemental Information

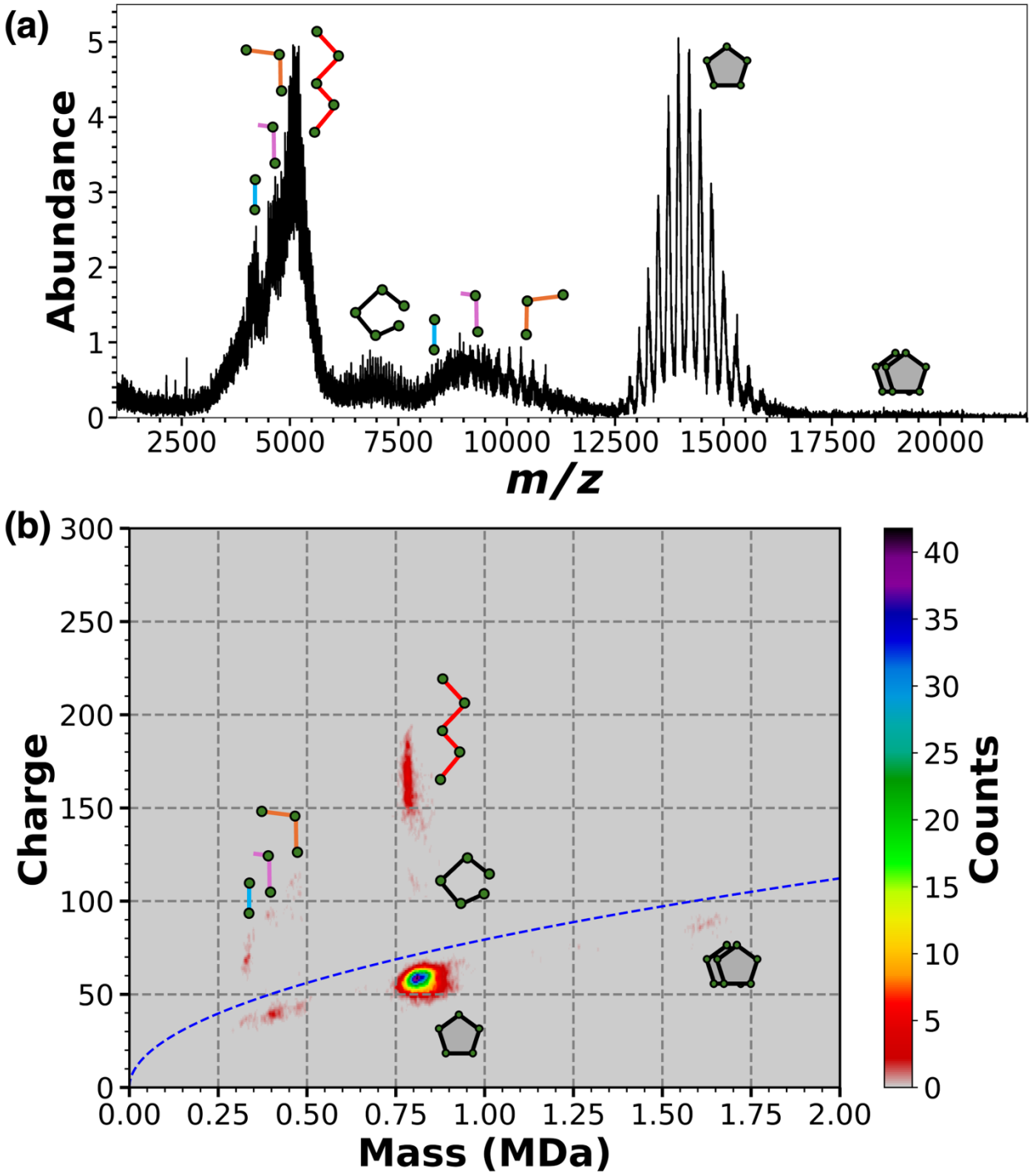

Supplemental Figure 10.1. An (a) QTOF MS mass spectrum and a (b) CDMS 2D mass-charge histogram of a fraction collected from the predominant peak in the SEC trace at ~2.63 min. The majority of this peak is composed of both elongated and folded forms of the pentamer mAb monomer

Chapter 11

High-Throughput Single Particle Characterization of Aggregation Pathways and the Effects of Inhibitors for Large (MegaDalton) Protein Oligomers

11.1 Abstract

Protein aggregation is involved in many human diseases, but rapidly characterizing the sizes and shapes of intermediate oligomers (~10 – 100 nm) important to the formation of macroscale aggregates like amyloid fibrils is a significant analytical challenge. Here, charge detection mass spectrometry (CDMS) is used to characterize individual conformational states of bovine serum albumin oligomers with up to ~225 molecules (15 MDa). Elongated, partially folded, and globular conformational families for each oligomer can be readily distinguished based on the extent of charging. The abundances of individual conformers vary with changes in the monomer concentration or by adding aggregation inhibitors, such as SDS, heparin, or $MgCl_2$. These results show the potential of CDMS for rapidly investigating intermediate oligomers in protein aggregation processes that are important for understanding aggregate formation and inhibition mechanisms and could accelerate formulation buffer development to prevent the aggregation of biotherapeutics.

11.2 Introduction

Protein aggregation is involved in many human diseases including Alzheimer's, Parkinsons', and Huntingtons' disease, dementia, amyotrophic lateral sclerosis (ALS), type-2 diabetes, and transmissible spongiform encephalopathies.[1] Understanding aggregation mechanisms and pathways is important for developing effective drugs and treatments for inhibiting the progression of disease. Protein-based therapeutics also aggregate under a wide range of stress conditions which can cause inefficacy and toxicity *in vivo*.[2] Developing buffer systems to prevent aggregate formation for the effective transport and storage of biotherapeutics is a critical part of any drug development workflow and requires the characterization of aggregates formed after stress in many different solution conditions.

Small proteinaceous oligomers can be characterized by many different methods, including size-exclusion chromatography,[3] mass photometry,[4–8] and mass spectrometry.[9] Information about the average size of much larger complexes formed after extensive aggregation occurs can be obtained from light scattering methods.[10] A variety of different microscopy techniques can provide individual particle data from which distributions of particle size and shape can be determined.[11] However, little is known about intermediate size aggregates that have masses in the MDa range. This is due in part to molecular complexity and the short-lived nature of what can be transient species that are challenging to measure using existing methods.

Native mass spectrometry has significant advantages for characterizing smaller oligomeric states of proteins. In combination with ion mobility spectrometry (IMS), information about the abundances and shapes of individual oligomers has been obtained for different proteins and peptides implicated as precursors in human disease, including Aβ42,[12–15] Tau,[16–18] TDP-43,[19,20] and α-synuclein.[21–23] Information about the secondary structure elements of aggregate forming peptide oligomers has been obtained through the combination of gas-phase infrared spectroscopy with IMS-MS.[24–26] However, characterizing full length proteins or higher order aggregates using these techniques is hampered by the mass range of conventional MS instruments that measure ensembles of ions. Complex mixtures of high molecular mass species can lead to charge-state distributions with overlapping *m/z* values that prevents information about ion charge and hence mass from being obtained.[27]

Charge detection mass spectrometry, in which the *m/z* and charge of individual analyte ions are measured simultaneously, overcomes the mass and charge limitations of conventional MS instruments. CDMS instruments have been used to investigate large protein complexes[28–30] and molecular machines,[31,32] intact viruses[33–36] and virus-like particles,[37,38] salt clusters,[39] synthetic polymers,[40,41] as well as aqueous nanodroplets[42,43] and nanoparticles with masses that extend into the GDa range.[44,45] The high mass capabilities of CDMS are well suited to measuring a broad mass range of oligomers formed by aggregation in solution.[46,47] Here, aggregates of the model protein bovine serum albumin (BSA) are formed during heat stress under a variety of solution conditions. CDMS measurements of these complex mixtures with and without aggregation inhibitors demonstrates the advantages of CDMS for rapidly characterizing the sizes and conformations of protein oligomers in a mass range that has not been previously accessible using conventional analysis methods.

11.3 Experimental Methods

Aqueous solutions of 0.1 – 37 mg/mL (~1.5 – 550 μM) bovine serum albumin (BSA) with 50 mM ammonium acetate (pH 6.8) were heated to 75 °C for 20 minutes using a dry bath incubator (Fisher Scientific, Hampton, NH). After heat stress, samples were vortexed and filtered through a 0.22 μm syringe filter (Thermofisher Scientific, Waltham, MA) to remove insoluble aggregates. For inhibition experiments, sodium dodecyl sulfate (SDS) and heparin (5 kDa average molecular weight) were added in molar equivalent ratios of 1:4 and 1:1 to 5 mg/mL aqueous BSA solutions containing 50 mM ammonium acetate. 5 mg/mL BSA in 50 mM ammonium acetate and 200 mM $MgCl_2$ were used to test the inhibitory effect of $MgCl_2$. BSA, $MgCl_2$, and ammonium acetate were obtained from Sigma-Aldrich (St. Louis, MO). Heparin and SDS were obtained from Fisher Scientific. All reagents were used without further purification.

Ions were formed by electrospray ionization from borosilicate nanoelectrospray emitters fabricated in-house from borosilicate capillaries (0.78 mm inner diameter, 1.00 mm outer diameter, Sutter Instrument, Novato, CA) pulled to a final inner diameter of 1.3 ± 0.1 μm using a Sutter Instrument P-87 Flaming/Brown micropipette puller.[55] Emitter tip diameters were imaged using a Hitachi TM-1000 microscope (Tokyo, Japan) at the University of California, Berkeley - Electron Microscopy Laboratory. Charge detection mass spectrometry experiments were performed using a custom-built instrument. Both this instrument and the data analysis methods are described in detail elsewhere.[44,45,56,57] This instrument consists of a heated ion transfer tube (140 °C), three RF-

only quadrupole ion guides, and an electrostatic cone trap. Ion transmission over a wide range of *m/z* values was achieved by varying the RF voltages and frequencies applied to the quadrupoles and ion funnel.

11.4 Results and Discussion

11.4.1 Soluble Protein Oligomer Size and Conformation

Bovine serum albumin (BSA) can form both fibrillar and amorphous aggregates within minutes at temperatures higher than ~60 °C. The performance of CDMS for characterizing protein oligomers in the MDa size range was evaluated by measuring mass and charge data from solutions containing 5 mg/mL (~75 μM) bovine serum albumin (BSA) before and after heating at 75 °C for 20 minutes. A CDMS mass histogram (Figure 1a) obtained from an unheated solution shows resolved oligomers up to hexamers (~405 kDa) and unresolved oligomers with masses between 0.5 – 2.5 MDa (7 – 37 molecules). The low signal for oligomers with masses between 300 kDa and 500 kDa, as well as the observation that the higher mass aggregates disappear upon addition of a small molecule (see below), indicate that these aggregates exist in solution and are not an artifact of the electrospray process. QTOF mass spectra of this solution shows low-charge forms of abundant monomer up to a low abundance hexamer, corresponding to compact, folded structures in solution (Figure S1). The baseline at *m/z* >10,000 is slightly elevated, and this is likely due to larger, unresolved globular aggregates that are clearly detected by CDMS. After heating the solution at 75 °C for 20 minutes, individual BSA oligomers up to the 23-mer are well-resolved by CDMS (Figure 1b) and there is unresolved signal up to ~15 MDa (~225 molecules) (Figure S2). The appearance of these oligomers from the heated sample, but not from the unheated sample, indicate that these aggregates were formed due to solution heating. The lower resolution obtained for the larger aggregates without heating is likely due to adducting salts and small molecules that can be dissociated from the protein when a solution is heated.[48]

An advantage of CDMS analysis is that because both the mass and charge of an ion are measured simultaneously, data can be plotted as a two-dimension histogram. A 2D histogram for the heated sample of BSA in Figure 1b shows four distinct conformer families, indicated by the different colored regions in Figure 2a, that extend over a wide range of both mass and charge. These conformer families, denoted as **I**, **II**, **III**, and **IV**, are distinguished based on different extents of charging for ions that have the same mass. The blue dashed line in Figure 2a is the calculated Rayleigh charge limit for a spherical water nanodrop with a given mass and charge. In native mass spectrometry, proteins and protein complexes typically charge to ~80% of the Rayleigh limit, consistent with compact forms associated with native structures.[49] In contrast, highly elongated ions charge significantly above the Rayleigh limit. Oligomers in conformer family **I**, indicated by the green shaded region, are charged close to the Rayleigh limit (Figure 2a). A mass histogram of just this green region (Figure 2b) shows a monomer and oligomers as large as the 14-mer (~1 MDa). Conformer family **II** contains aggregates charged well below the Rayleigh limit (Figure 2a, purple region) that span from 1.0 MDa (~15 molecules) up to ~15 MDa (~225 molecules) in size (Figure 2c). The lower charge compared to the Rayleigh limit is consistent with more compact globular structures. The maximum oligomer size of conformer family **I** overlaps in mass with the

minimum oligomer size of conformer family **II**, indicating that conformer family **I** may convert into conformer family **II** in this overlapping oligomer size range.

Conformer family **III** (Figure 2a, blue region) consists of highly charged oligomers that start at the trimer and are well-resolved to the 24-mer, although ion signals up to ~2 MDa (~30 BSA molecules, Figure 2d) are observed. These conformers are charged well above the Rayleigh limit and show a near linear increase in charge with increasing mass, indicating that these structures must be highly elongated in solution. Conformer family **IV** (Figure 2a, orange region) has charge states between those of the highly extended (**III**) and compact forms (**I** and **II**) of BSA oligomers. The range of charge states is broader than it is for the other conformer families indicating that this family of structures can take on a range of conformations between those of the compact and highly extended forms. The abundance of small oligomers (<5 BSA molecules) charged above the Rayleigh limit in unheated solutions is very low (Figure S3), indicating that the vast majority of the two extended conformer families are formed in solution after heating (Figure 2a) and are not an artifact of the electrospray ionization process. Individual conformers are mass resolved up to ~1 MDa (~15 BSA molecules). Oligomers above this mass are not individually resolved, likely due to salt or other small molecule adducts that broaden peaks. The BSA monomer and dimer have compact structures and there are no higher charged forms present. This indicates that unfolding of both of these species at 75 °C is reversible. In contrast, the extended structures of the unfolded trimer and higher order aggregates indicates that their formation is irreversible and produces long-lived aggregates that are stable at room temperature. Thus, it appears that the unfolded trimer is critical to the formation of larger aggregates that have highly unfolded structures.

These data demonstrate the advantage of CDMS to resolve distinct conformation families of individual protein oligomers formed during heat stress based on the ability to measure both mass and charge. The oligomers readily resolved in the 2D mass-charge histogram in Figure 2a are completely unresolved in *m/z* space (Figure S4), highlighting the advantage of the simultaneous measurements of mass and charge of individual ions for samples containing highly heterogenous analytes that overlap significantly in *m/z*.

11.4.2 Aggregation Pathways Depend on Initial Monomer Concentration

Protein aggregation and the types of structures (amorphous, fibrils, etc.) generated upon stress depend on concentration. To investigate how the initial monomer concentration affects the abundance of the conformational families identified in Figure 2a, solutions containing 0.1 – 37 mg/mL (~1.5 – 550 μM) BSA were heat-stressed for 20 min at 75 °C and the resulting aggregation products characterized using CDMS. From unheated solutions containing 0.1 mg/mL BSA, there are compact oligomers up to the hexamer with little higher order aggregates (Figure S5a). After heating, there is abundant monomer and dimer as well as compact aggregates of conformer family **II** with masses up to 2.0 MDa (30 molecules) (Figure S5b). The absence of solution turbidity after heating indicate that these aggregates are sufficiently small to remain soluble (Figure S6).

At concentrations $\geq$ 1 mg/mL, there are both elongated and compact higher-order oligomers after heat stress (Figure 3). At 1 mg/mL, oligomers in compact conformer family **I** extend past 30-mers (2 MDa) and overlap in size with conformer family **II**, which extends from ~22-mers (~1.5 MDa) to 119-mers (~8 MDa) (Figure 3a). At 5 – 15 mg/mL, the average molecular mass of conformer family **I** are reduced with increasing concentration (Figure 3a-c). whereas both

the average molecular mass and the abundances of conformer family **II** increase between 1 - 5 mg/mL before decreasing at higher concentrations. The abundance of conformers **III** and **IV** is higher at 5 and 10 mg/mL compared to 1 mg/mL. Above 10 mg/mL, the abundance of conformer families **I**, **II**, and **III** is reduced. This is likely due to the rapid formation of larger, insoluble aggregates that are filtered out prior to the CDMS measurement (Figure S7). Samples with BSA concentrations >10 mg/mL have higher turbidity and viscosity after heating than lower concentration samples, consistent with the formation of large, insoluble aggregates (Figure S6).

Increasing the concentration and monitoring the abundances of the conformational families provides information about the kinetics of different aggregation pathways. Decreased abundance for any family indicates the formation of higher order, insoluble aggregates of the same family that deplete the population of small oligomers or conversion to a different conformer family. Less kinetically favored pathways require higher monomer concentrations for formation and depletion of small oligomers. The compact families **I** and **II** decrease in abundance above 1 mg/mL and 5 mg/mL, respectively, indicating that the formation of large, amorphous aggregates is the most kinetically favored pathway. The increase in abundance of the elongated conformers **III** and **IV** at 5 mg/mL and subsequent decrease in abundance at concentrations above 5 mg/mL and 10 mg/mL, respectively, indicate that the formation of elongated aggregates is less kinetically favored than the compact aggregates of conformer families **I** and **II**. These data are consistent with prior work on different amyloid-forming proteins, wherein forming amorphous aggregates proceeds without a lag-phase and is kinetically favored over the formation of amyloid fibrils, which require significant changes to protein secondary and tertiary structure and the formation of specific, fibril-competent structures to initiate fibrillation.[50] The compact oligomers form into larger molecular weight aggregates that are not observed between concentrations of 5 mg/mL and 10 mg/mL but there is no change in the turbidity of samples in this concentration range. In contrast, at concentrations >10 mg/mL where conformations **III** and **IV** are reduced in abundance, there are significant changes in turbidity and viscosity. These data indicate that large amorphous/globular aggregates formed from conformer family **I** and **II** are more soluble than elongated/fibril-like aggregates formed from conformer families **III** and **IV**. These results show the promise of CDMS for investigating aggregation kinetics in a size range where other biophysical techniques cannot resolve individual oligomer conformations.

11.4.3 Aggregation Inhibitors Decrease the Formation of Specific Conformations

Aggregation inhibitors can affect the distributions and conformations of aggregates that are formed upon heat stress. Solutions containing 5 mg/mL BSA and 4 molar eq. sodium dodecyl sulfate (SDS) detergent were heated to 75 °C for 20 min. Only compact monomer, dimer and a low abundance of trimer were observed, indicating that SDS prevents formation of all higher order aggregates irrespective of their structure (Figure 4b compared to the reference solution without SDS shown in Figure 4a). This result indicates that SDS interferes with the oligomerization process by preventing the formation of the elongated trimer. The absence of conformer family **II** in these data confirms that these species exist in both unheated (Figure 1a) and heated solutions (Figure 3a) and are dissociated upon addition of SDS. There were no changes in turbidity after heating in the presence of SDS, indicating that the absence of signal for small oligomers in these data is due to inhibition of the aggregation process rather than acceleration to form higher order oligomers.

These data indicate that SDS prevents the formation of elongated (fibril-like) BSA aggregates, consistent with prior transmission electron microscopy results.[51]

Heating a 5 mg/mL BSA solution at 75 °C for 20 min with 1 molar eq. heparin (average MW ~5 kDa) resulted in the formation of compact oligomers (**I**) as large as the 10-mer and partially elongated species (**IV**) (Figure 4c). Globular aggregates (**II**) that range from 1 – 6 MDa (15 – 89 molecules) were also formed compared to up to ~15 MDa (~222 molecules) in samples without heparin. Heparin prevents the formation of elongated (highly charged) forms of each oligomer, consistent with the reported anti-amyloid behavior of this MW heparin.[52] The absence of conformer family **II** between 6 and 15 MDa with heparin (Figure S8) indicates that heparin also inhibits the self-association of compact forms of BSA, consistent with prior reports using higher molecular weight heparins (~15 kDa) at lower pH and ionic strengths.[53] The intermediate charged oligomers (**IV**) observed in the presence of heparin may be aggregating via a different mechanism that utilizes a portion of the protein that heparin does not strongly interact with. Their lower abundance compared to the sample without heparin indicates they are destabilized in the presence of heparin, suggesting that heparin is partially inhibiting the oligomerization process along this pathway as well. These data indicate that heparin effectively combats amyloid formation by preventing the formation of fully elongated oligomers and destabilizing partially elongated oligomers and high mass globular aggregates.

CDMS 2D mass-charge histograms of 5 mg/mL BSA with 200 mM $MgCl_2$ acquired after heat-stress show compact (**I**) and partially elongated (**IV**) oligomers, as well as a low abundance of elongated (**III**) oligomers (Figure 4d). Compact oligomers up to the tetramer are formed in the presence of $MgCl_2$ compared to the 11-mer without $MgCl_2$. Higher charge oligomers are more difficult to resolve in these data, likely due to extensive adduction of $MgCl_2$. There is no evidence for "magic" number clusters above 0.5 MDa, so loss of individual oligomer resolution does not adversely affect conclusions drawn from these data. These data indicate that $MgCl_2$ stabilizes oligomers with a partially elongated structure, preventing the formation of large amorphous aggregates as well as highly extended aggregates and provides additional evidence that partially elongated BSA oligomers are formed via a different mechanism than globular or fully elongated, amyloid-like conformers. There was no increase in the hydrodynamic radius determined from light scattering data from 80 °C heat-stressed BSA (0.1 mg/mL) in the presence of 200 mM Mg^{2+} compared to a ~50 nm increase in the average hydrodynamic radius without Mg^{2+}, indicating that aggregation was inhibited.[54] Conformer **IV** aggregates detected after heat stress in the presence of Mg^{2+} by CDMS are low abundance and dispersed over a wide mass range and may not have been detected by the earlier ensemble dynamic light scattering measurements. These data indicate CDMS has significant advantages for characterizing the masses and shapes of oligomers in the hundreds of kDa to 10+ MDa size range. The three inhibitors used here demonstrate three different mechanisms of action for inhibiting the formation of larger oligomers that can be readily distinguished by their "aggregation footprint" in mass and charge space.

11.5 Conclusions

CDMS measurements of oligomer size and conformation are enabled through simultaneous measurements of both *m*/*z* and charge for each individual ion. For BSA, information about oligomers consisting of over 200 protein molecules with masses up to 15 MDa was obtained. Four

distinct conformer families of oligomers are resolved based on the extent of charging at a given size. The abundances of these families depend on the initial protein concentration and is affected by the presence of inhibitors. SDS, heparin and $MgCl_2$ all reduce aggregation and information about which aggregation pathways are inhibited is obtained from the sizes and abundances of each resolved conformational family. The ability to monitor the kinetics of amyloid fibril or amorphous aggregate formation makes CDMS a promising technique for obtaining information at the earliest stages of the aggregation process without the need for microscopy methods that require extensive sample preparation or the need to wait until much larger aggregates that can be optically detected are formed.

The information about the oligomer shape obtained from the extent of charging is analogous to that obtained from ion mobility measurements albeit at much lower resolution. However, CDMS has the advantage that it can be applied to much larger proteins making it possible to obtain information about size and shape in a size range (100's of MDa – GDa) that is difficult to measure using more conventional biophysical methods. Characterizing oligomers involved in the earliest stages of aggregation for full length Tau (~45 kDa), TDP-43 (~43 kDa), or even Huntington protein (~350 kDa) would provide insight into the molecular mechanisms of aggregation involved in neurological disease. Aggregation inhibition assays often require long periods of time (~hrs – days) to assay the formation of light-scattering particles under different solution conditions. CDMS measurements could accelerate these workflows by assaying the earliest stages of the aggregation process, providing quick feedback on the stabilizing effect of solution conditions or inhibitors that may significantly aid the development of formulation/storage buffers for biopharmaceuticals or the discovery of novel compounds for inhibiting the aggregation of disease-causing amyloid-forming proteins.

11.6 Acknowledgements

This work was supported by the National Science Foundation Division of Chemistry (grant number CHE-2203907), the National Institutes of Health (grant number 5R01GM139338) for development and construction of the CDMS instrument and data analysis methods used in this work, an ACS Graduate Research Fellowship sponsored by Eli Lilly and Company (JSJ), the Arnold and Mabel Beckman Foundation Postdoctoral Fellowship in Chemical Instrumentation (CCH), and Merck & Co., Inc., San Francisco, CA, USA, through their Discovery Biologics SEEDS program.

11.7 References

(1) Ross, C. A.; Poirier, M. A. Protein Aggregation and Neurodegenerative Disease. *Nat. Med.* **2004**, *10* (S7), S10–S17.
(2) Ratanji, K. D.; Derrick, J. P.; Dearman, R. J.; Kimber, I. Immunogenicity of Therapeutic Proteins: Influence of Aggregation. *J. Immunotoxicol.* **2014**, *11* (2), 99–109.

(3) Fekete, S.; Beck, A.; Veuthey, J. L.; Guillarme, D. Theory and Practice of Size Exclusion Chromatography for the Analysis of Protein Aggregates. *J. Pharm. Biomed. Anal.* **2014**, *101*, 161–173.
(4) Ray, S.; Mason, T. O.; Boyens-Thiele, L.; Farzadfard, A.; Larsen, J. A.; Norrild, R. K.; Jahnke, N.; Buell, A. K. Mass Photometric Detection and Quantification of Nanoscale α-Synuclein Phase Separation. *Nat. Chem.* **2023**, *15* (9), 1306–1316.
(5) Wu, D.; Piszczek, G. Measuring the Affinity of Protein-Protein Interactions on a Single-Molecule Level by Mass Photometry. *Anal. Biochem.* **2020**, *592* (November 2019), 113575.
(6) Hundt, N.; Cole, D.; Hantke, M. F.; Miller, J. J.; Struwe, W. B.; Kukura, P. Direct Observation of the Molecular Mechanism Underlying Protein Polymerization. *Sci. Adv.* **2022**, *8* (35), eabm7935.
(7) Liebthal, M.; Kushwah, M. S.; Kukura, P.; Dietz, K. J. Single Molecule Mass Photometry Reveals the Dynamic Oligomerization of Human and Plant Peroxiredoxins. *iScience* **2021**, *24* (11), 103258.
(8) Paul, S. S.; Lyons, A.; Kirchner, R.; Woodside, M. T. Quantifying Oligomer Populations in Real Time during Protein Aggregation Using Single-Molecule Mass Photometry. *ACS Nano* **2022**, *16* (10), 16462–16470.
(9) Pukala, T. L. Mass Spectrometric Insights into Protein Aggregation. *Essays Biochem.* **2023**, *67* (2), 243–253.
(10) Mehalebi, S.; Nicolai, T.; Durand, D. Light Scattering Study of Heat-Denatured Globular Protein Aggregates. *Int. J. Biol. Macromol.* **2008**, *43* (2), 129–135.
(11) Kundel, F.; Tosatto, L.; Whiten, D. R.; Wirthensohn, D. C.; Horrocks, M. H.; Klenerman, D. Shedding Light on Aberrant Interactions – a Review of Modern Tools for Studying Protein Aggregates. *FEBS J.* **2018**, *285* (19), 3604–3630.
(12) Bernstein, S. L.; Wyttenbach, T.; Baumketner, A.; Shea, J. E.; Bitan, G.; Teplow, D. B.; Bowers, M. T. Amyloid β-Protein: Monomer Structure and Early Aggregation States of Aβ42 and Its Pro19 Alloform. *J. Am. Chem. Soc.* **2005**, *127* (7), 2075–2084.
(13) Bernstein, S. L.; Dupuis, N. F.; Lazo, N. D.; Wyttenbach, T.; Condron, M. M.; Bitan, G.; Teplow, D. B.; Shea, J. E.; Ruotolo, B. T.; Robinson, C. V.; Bowers, M. T. Amyloid-β Protein Oligomerization and the Importance of Tetramers and Dodecamers in the Aetiology of Alzheimer's Disease. *Nat. Chem.* **2009**, *1* (4), 326–331.
(14) Bleiholder, C.; Dupuis, N. F.; Wyttenbach, T.; Bowers, M. T. Ion Mobility–Mass Spectrometry Reveals a Conformational Conversion from Random Assembly to β-Sheet in Amyloid Fibril Formation. *Nat. Chem.* **2011**, *3* (2), 172–177.
(15) Österlund, N.; Moons, R.; Ilag, L. L.; Sobott, F.; Graslund, A. Native Ion Mobility-Mass Spectrometry Reveals the Formation of B-barrel Shaped Amyloid-β Hexamers in a Membrane-Mimicking Environment. *J. Am. Chem. Soc.* **2019**, *141* (26), 10440–10450.
(16) Shahpasand-Kroner, H.; Portillo, J.; Lantz, C.; Seidler, P. M.; Sarafian, N.; Loo, J. A.; Bitan, G. Three-repeat and Four-repeat Tau Isoforms Form Different Oligomers. *Protein Sci.* **2022**, *31* (3), 613–627.
(17) Stroganova, I.; Willenberg, H.; Tente, T.; Depraz Depland, A.; Bakels, S.; Rijs, A. M. Exploring the Aggregation Propensity of PHF6 Peptide Segments of the Tau Protein Using Ion Mobility Mass Spectrometry Techniques. *Anal. Chem.* **2024**, *96* (13), 5115–5124.
(18) Stroganova, I.; Toprakcioglu, Z.; Willenberg, H.; Knowles, T. P. J.; Rijs, A. M. Unravelling the Structure and Dynamics of Ac-PHF6-NH 2 Tau Segment Oligomers. **2024**. Preprint at https://doi.org/10.26434/chemrxiv-2024-hzclg.

(19) Depraz Depland, A.; Stroganova, I.; Wootton, C. A.; Rijs, A. M. Developments in Trapped Ion Mobility Mass Spectrometry to Probe the Early Stages of Peptide Aggregation. *J. Am. Soc. Mass Spectrom.* **2023**, *34* (2), 193–204.
(20) Laos, V.; Do, T. D.; Bishop, D.; Jin, Y.; Marsh, N. M.; Quon, B.; Fetters, M.; Cantrell, K. L.; Buratto, S. K.; Bowers, M. T. Characterizing TDP-43 307–319 Oligomeric Assembly: Mechanistic and Structural Implications Involved in the Etiology of Amyotrophic Lateral Sclerosis. *ACS Chem. Neurosci.* **2019**, *10* (9), 4112–4123.
(21) Frimpong, A. K.; Abzalimov, R. R.; Uversky, V. N.; Kaltashov, I. A. Characterization of Intrinsically Disordered Proteins with Electrospray Ionization Mass Spectrometry: Conformational Heterogeneity of α-synuclein. *Proteins: Struct., Func., Bioinf.* **2010**, *78* (3), 714–722.
(22) Moons, R.; Konijnenberg, A.; Mensch, C.; Van Elzen, R.; Johannessen, C.; Maudsley, S.; Lambeir, A.-M.; Sobott, F. Metal Ions Shape α-Synuclein. *Sci. Rep.* **2020**, *10* (1), 16293.
(23) Phillips, A. S.; Gomes, A. F.; Kalapothakis, J. M. D.; Gillam, J. E.; Gasparavicius, J.; Gozzo, F. C.; Kunath, T.; MacPhee, C.; Barran, P. E. Conformational Dynamics of α-Synuclein: Insights from Mass Spectrometry. *Analyst* **2015**, *140* (9), 3070–3081.
(24) Hoffmann, W.; Folmert, K.; Moschner, J.; Huang, X.; von Berlepsch, H.; Koksch, B.; Bowers, M. T.; von Helden, G.; Pagel, K. NFGAIL Amyloid Oligomers: The Onset of Beta-Sheet Formation and the Mechanism for Fibril Formation. *J. Am. Chem. Soc.* **2018**, *140* (1), 244–249.
(25) Seo, J.; Hoffmann, W.; Warnke, S.; Huang, X.; Gewinner, S.; Schöllkopf, W.; Bowers, M. T.; von Helden, G.; Pagel, K. An Infrared Spectroscopy Approach to Follow β-Sheet Formation in Peptide Amyloid Assemblies. *Nat. Chem.* **2017**, *9* (1), 39–44.
(26) Bakels, S.; Daly, S.; Doğan, B.; Baerenfaenger, M.; Commandeur, J.; Rijs, A. M. Probing High-Order Transient Oligomers Using Ion Mobility Mass Spectrometry Coupled to Infrared Action Spectroscopy. **2024**. Preprint at https://doi.org/10.26434/chemrxiv-2024-3gdw8.
(27) Bischoff, A. J.; Harper, C. C.; Williams, E. R.; Francis, M. B. Characterizing Heterogeneous Mixtures of Assembled States of the Tobacco Mosaic Virus Using Charge Detection Mass Spectrometry. *J. Am. Chem. Soc.* **2022**, *144* (51), 23368–23378.
(28) Harper, C. C.; Elliott, A. G.; Oltrogge, L. M.; Savage, D. F.; Williams, E. R. Multiplexed Charge Detection Mass Spectrometry for High-Throughput Single Ion Analysis of Large Molecules. *Anal. Chem.* **2019**, *91* (11), 7458–7465.
(29) McGee, J. P.; Melani, R. D.; Yip, P. F.; Senko, M. W.; Compton, P. D.; Kafader, J. O.; Kelleher, N. L. Isotopic Resolution of Protein Complexes up to 466 KDa Using Individual Ion Mass Spectrometry. *Anal. Chem.* **2021**, *93* (5), 2723–2727.
(30) Du, C.; Cleary, S. P.; Kostelic;, M. M.; Jones, B. J.; Kafader, J. O.; Wysocki, V. H. Combining Surface-Induced Dissociation and Charge Detection Mass Spectrometry to Reveal the Native Topology of Heterogeneous Protein Complexes. *Anal. Chem.* **2023**, *95* (37), 13889-13896.
(31) Anthony, A. J.; Gautam, A. K. S.; Miller, L. M.; Ma, Y.; Hardwick, A. G.; Sharma, A.; Ghatak, S.; Matouschek, A.; Jarrold, M. F.; Clemmer, D. E. CDMS Analysis of Intact 19S, 20S, 26S, and 30S Proteasomes: Evidence for Higher-Order 20S Assemblies at a Low PH. *Anal. Chem.* **2023**, *95* (33), 12209–12215.
(32) Lai, S. H.; Tamara, S.; Heck, A. J. R. Single-Particle Mass Analysis of Intact Ribosomes by Mass Photometry and Orbitrap-Based Charge Detection Mass Spectrometry. *iScience* **2021**, *24* (11), 103211.

(33) Harper, C. C.; Miller, Z. M.; Lee, H.; Bischoff, A. J.; Francis, M. B.; Schaffer, D. V.; Williams, E. R. Effects of Molecular Size on Resolution in Charge Detection Mass Spectrometry. *Anal. Chem.* **2022**, *94* (33), 11703–11712.
(34) Barnes, L. F.; Draper, B. E.; Jarrold, M. F. Analysis of Recombinant Adenovirus Vectors by Ion Trap Charge Detection Mass Spectrometry: Accurate Molecular Weight Measurements beyond 150 MDa. *Anal. Chem.* **2022**, *94* (3), 1543–1551.
(35) Kostelic, M. M.; Ryan, J. P.; Brown, L. S.; Jackson, T. W.; Hsieh, C.; Zak, C. K.; Sanders, H. M.; Liu, Y.; Chen, V. S.; Byrne, M.; Aspinwall, C. A.; Baker, E. S.; Marty, M. T. Stability and Dissociation of Adeno-Associated Viral Capsids by Variable Temperature-Charge Detection-Mass Spectrometry. *Anal. Chem.* **2022**, *94* (34), 11723–11727.
(36) Pierson, E. E.; Keifer, D. Z.; Selzer, L.; Lee, L. S.; Contino, N. C.; Wang, J. C. Y.; Zlotnick, A.; Jarrold, M. F. Detection of Late Intermediates in Virus Capsid Assembly by Charge Detection Mass Spectrometry. *J. Am. Chem. Soc.* **2014**, *136* (9), 3536–3541.
(37) Tamara, S.; den Boer, M. A.; Heck, A. J. R. High-Resolution Native Mass Spectrometry. *Chem. Rev.* **2022**, *122* (8), 7269–7326. https://doi.org/10.1021/acs.chemrev.1c00212.
(38) Miller, L. M.; Bond, K. M.; Draper, B. E.; Jarrold, M. F. Characterization of Classical Vaccines by Charge Detection Mass Spectrometry. *Anal. Chem.* **2021**, *93* (35), 11965–11972.
(39) McPartlan, M. S.; Harper, C. C.; Hanozin, E.; Williams, E. R. Ion Emission from 1–10 MDa Salt Clusters: Individual Charge State Resolution with Charge Detection Mass Spectrometry. *Analyst* **2024**, *149* (3), 735–744.
(40) Doussineau, T.; Bao, C. Y.; Antoine, R.; Dugourd, P.; Zhang, W.; D'Agosto, F.; Charleux, B. Direct Molar Mass Determination of Self-Assembled Amphiphilic Block Copolymer Nanoobjects Using Electrospray-Charge Detection Mass Spectrometry. *ACS Macro Lett.* **2012**, *1* (3), 414–417.
(41) Doussineau, T.; Désert, A.; Lambert, O.; Taveau, J. C.; Lansalot, M.; Dugourd, P.; Bourgeat-Lami, E.; Ravaine, S.; Duguet, E.; Antoine, R. Charge Detection Mass Spectrometry for the Characterization of Mass and Surface Area of Composite Nanoparticles. *J. Phys. Chem. C* **2015**, *119* (20), 10844–10849.
(42) Hanozin, E.; Harper, C. C.; McPartlan, M. S.; Williams, E. R. Dynamics of Rayleigh Fission Processes in ∼100 nm Charged Aqueous Nanodrops. *ACS Cent. Sci.* **2023**, *9* (8), 1611–1622.
(43) Harper, C. C.; Brauer, D. D.; Francis, M. B.; Williams, E. R. Direct Observation of Ion Emission from Charged Aqueous Nanodrops: Effects on Gaseous Macromolecular Charging. *Chem. Sci.* **2021**, *12* (14), 5185–5195.
(44) Harper, C. C.; Jordan, J. S.; Papanu, S.; Williams, E. R. Characterization of Mass, Diameter, Density, and Surface Properties of Colloidal Nanoparticles Enabled by Charge Detection Mass Spectrometry. *ACS Nano* **2024**, *18* (27), 17806–17814.
(45) Harper, C. C.; Miller, Z. M.; McPartlan, M. S.; Jordan, J. S.; Pedder, R. E.; Williams, E. R. Accurate Sizing of Nanoparticles Using a High-Throughput Charge Detection Mass Spectrometer without Energy Selection. *ACS Nano* **2023**, *17* (8), 7765–7774.
(46) den Boer, M. A.; Lai, S. H.; Xue, X.; van Kampen, M. D.; Bleijlevens, B.; Heck, A. J. R. Comparative Analysis of Antibodies and Heavily Glycosylated Macromolecular Immune Complexes by Size-Exclusion Chromatography Multi-Angle Light Scattering, Native Charge Detection Mass Spectrometry, and Mass Photometry. *Anal. Chem.* **2022**, *94* (2), 892–900.
(47) Wörner, T. P.; Thurman, H. A.; Makarov, A. A.; Shvartsburg, A. A. Expanding Differential Ion Mobility Separations into the MegaDalton Range. *Anal. Chem.* **2024**, *96* (14), 5392-5398.

(48) Jordan, J. S.; Lee, K. J.; Williams, E. R. Overcoming Aggregation with Laser Heated Nanoelectrospray Mass Spectrometry: Thermal Stability and Pathways for Loss of Bicarbonate from Carbonic Anhydrase II. *Analyst* **2024**, *149* (8), 2281–2290.
(49) Susa, A. C.; Xia, Z.; Tang, H. Y. H.; Tainer, J. A.; Williams, E. R. Charging of Proteins in Native Mass Spectrometry. *J. Am. Soc. Mass Spectrom.* **2017**, *28* (2), 332–340.
(50) Yoshimura, Y.; Lin, Y.; Yagi, H.; Lee, Y. H.; Kitayama, H.; Sakurai, K.; So, M.; Ogi, H.; Naiki, H.; Goto, Y. Distinguishing Crystal-like Amyloid Fibrils and Glass-like Amorphous Aggregates from Their Kinetics of Formation. *Proc. Natl. Acad. Sci.* **2012**, *109* (36), 14446–14451.
(51) Ma, X. J.; Zhang, Y. J.; Zeng, C. M. Inhibition of Amyloid Aggregation of Bovine Serum Albumin by Sodium Dodecyl Sulfate at Submicellar Concentrations. *Biochemistry (Mosc.)* **2018**, *83* (1), 60–68.
(52) Zhu, H.; Yu, J.; Kindy, M. S. Inhibition of Amyloidosis Using Low-Molecular-Weight Heparins. *Mol. Med.* **2001**, *7* (8), 517–522.
(53) Minsky, B. B.; Zheng, B.; Dubin, P. L. Inhibition of Antithrombin and Bovine Serum Albumin Native State Aggregation by Heparin. *Langmuir* **2014**, *30* (1), 278–287.
(54) Liu, X.; Zhang, W.; Liu, J.; Pearce, R.; Zhang, Y.; Zhang, K.; Ruan, Q.; Yu, Y.; Liu, B. Mg^{2+} Inhibits Heat-Induced Aggregation of BSA: The Mechanism and Its Binding Site. *Food Hydrocoll.* **2020**, *101*, 105450.
(55) Jordan, J. S.; Xia, Z.; Williams, E. R. Tips on Making Tiny Tips: Secrets to Submicron Nanoelectrospray Emitters. *J. Am. Soc. Mass Spectrom.* **2022**, *33* (3), 607–611.
(56) Miller, Z. M.; Harper, C. C.; Lee, H.; Bischoff, A. J.; Francis, M. B.; Schaffer, D. V.; Williams, E. R. Apodization Specific Fitting for Improved Resolution, Charge Measurement, and Data Analysis Speed in Charge Detection Mass Spectrometry. *J. Am. Soc. Mass Spectrom.* **2022**, *33* (11), 2129–2137.
(57) Harper, C. C.; Miller, Z. M.; Williams, E. R. Combined Multiharmonic Frequency Analysis for Improved Dynamic Energy Measurements and Accuracy in Charge Detection Mass Spectrometry. *Anal. Chem.* **2023**, *95* (45), 16659–16667.

11.8 Figures

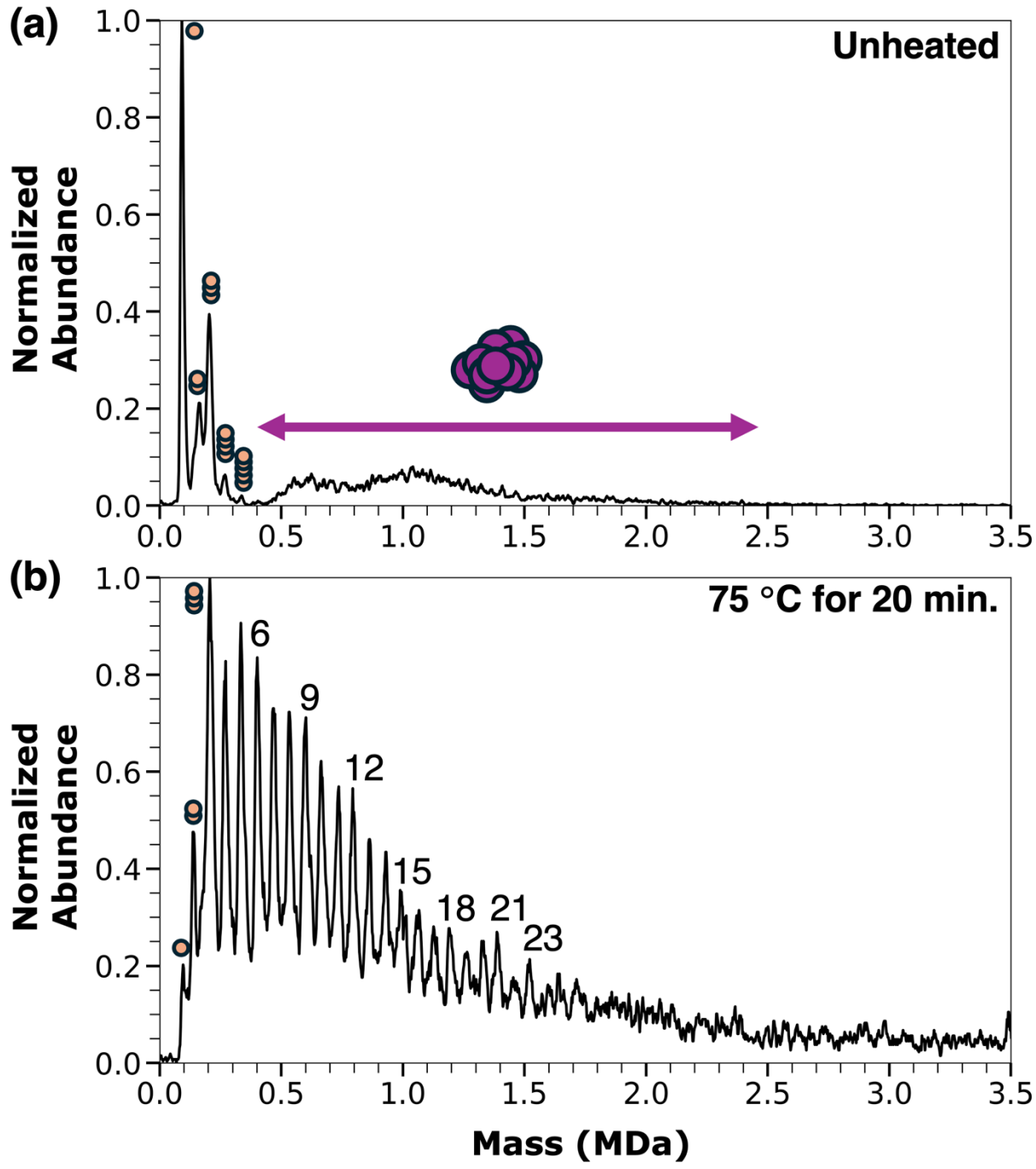

Figure 11.1. CDMS mass histograms of 5 mg/mL aqueous BSA solutions with 50 mM ammonium acetate (pH 6.8) (a) unheated and (b) heated at 75 °C for 20 min prior to cooling and filtering. The labels in (b) correspond to the number of BSA molecules in each oligomer.

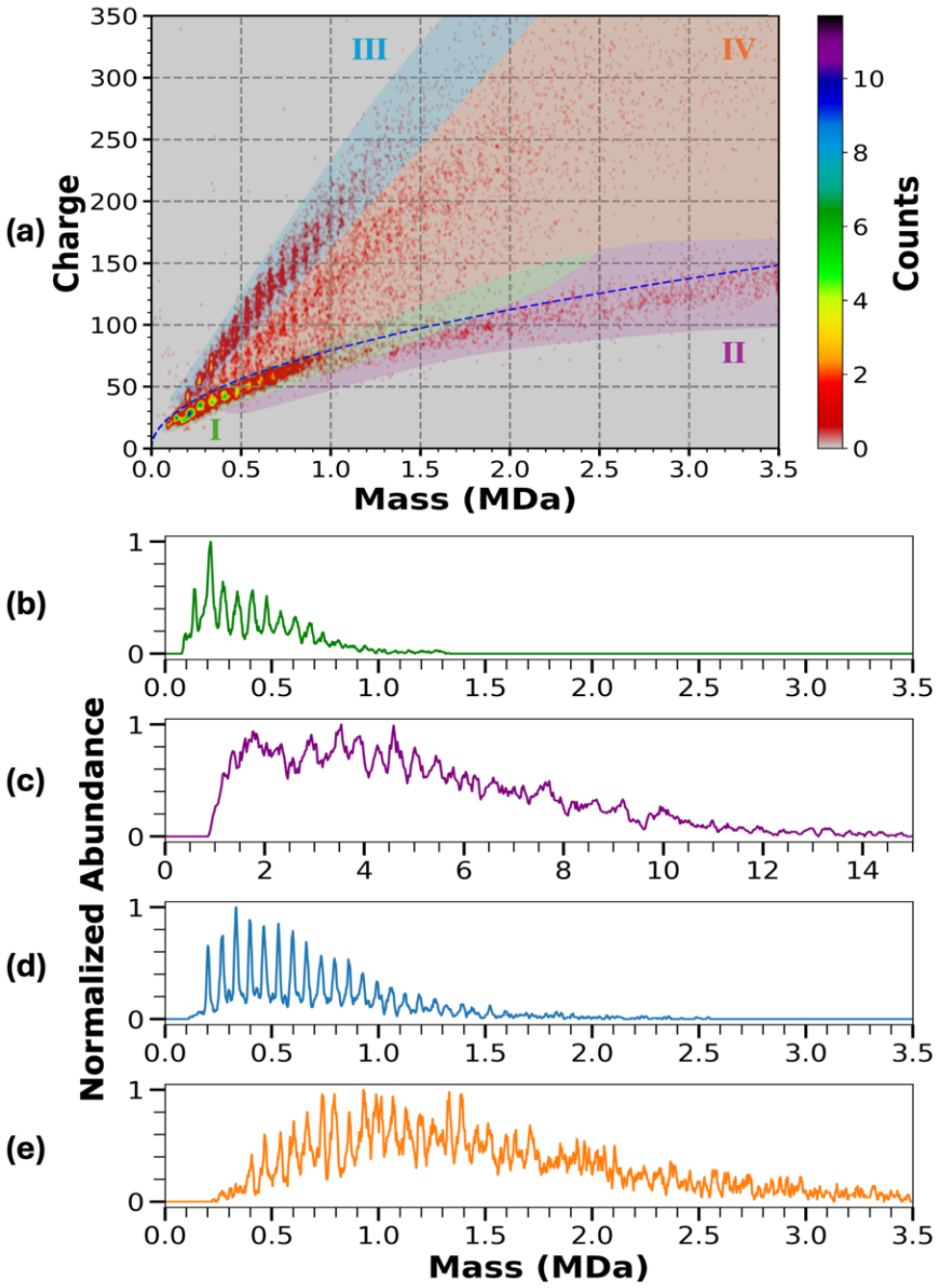

Figure 11.2. (a) 2-dimensional CDMS mass-charge data obtained from a 5 mg/mL aqueous solution of BSA (with 50 mM ammonium acetate, pH 6.8) heat stressed at 75 °C for 20 min. By selecting the individual families of conformers distinguished by the extent of oligomer charging, 1D mass histograms were extracted to show the different distributions of aggregate size for the (b) compact conformer family I (green), (c) higher mass and density conformer family II (purple), (d) elongated conformer family III (blue), and (d) partially elongated conformer family IV (orange). The blue dashed line represents the Rayleigh limit of an aqueous droplet as a function of mass.

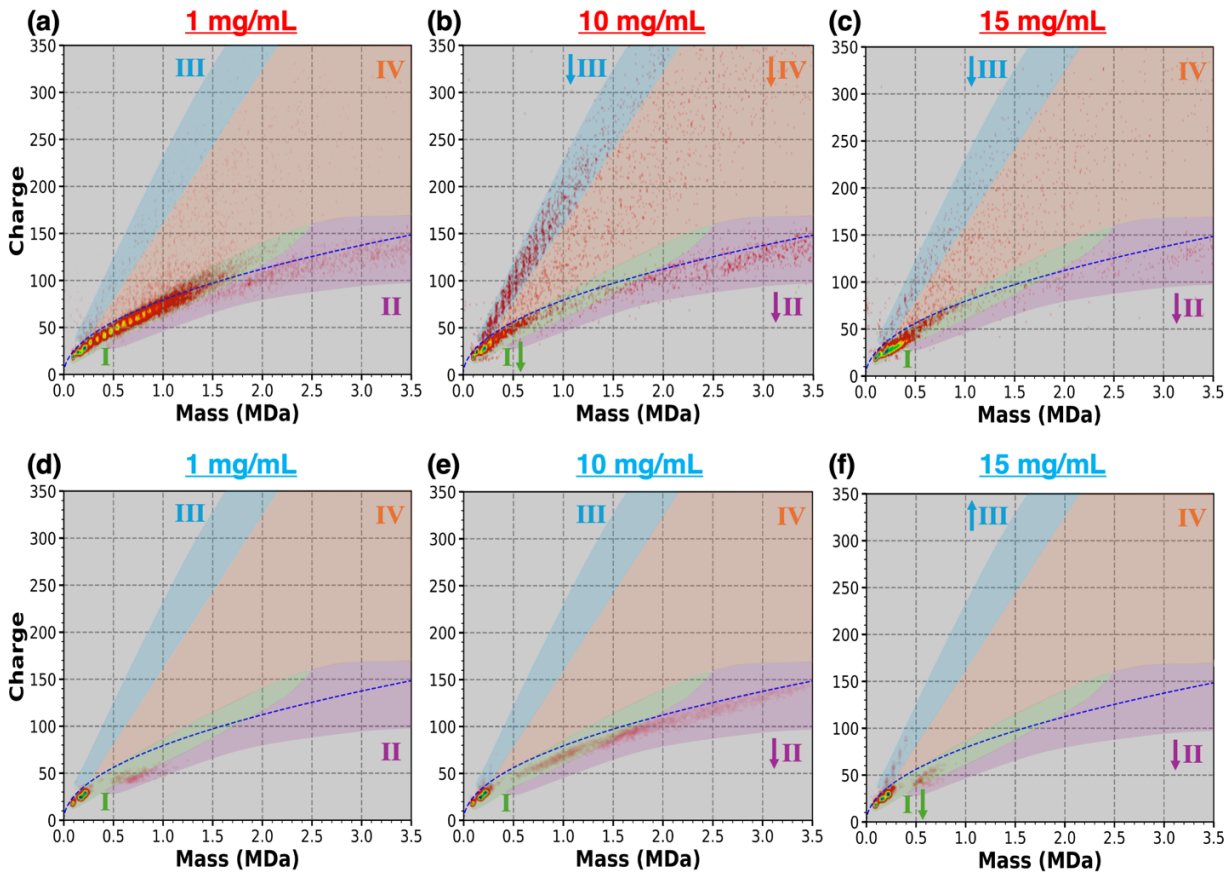

Figure 11.3. 2D mass-charge data obtained from aqueous BSA solutions (with 50 mM ammonium acetate, pH 6.8) at an initial BSA concentration of (a,d) 1 mg/mL, (b,e) 10 mg/mL, and (c,f) 15 mg/mL after heating at 75 °C for 20 min (a,b,c) and before heating (d,e,f). Shaded regions correspond to the same conformational families identified in Figure 2a. Arrows depict the increase or decrease in both abundance and size distribution for each conformational family relative to the lower concentrations. The arrows for the 10 mg/mL data depict the change in abundance and size distribution of each family relative to the 5 mg/mL data in Figures 10.2a and Supplementary Figure 10.3.

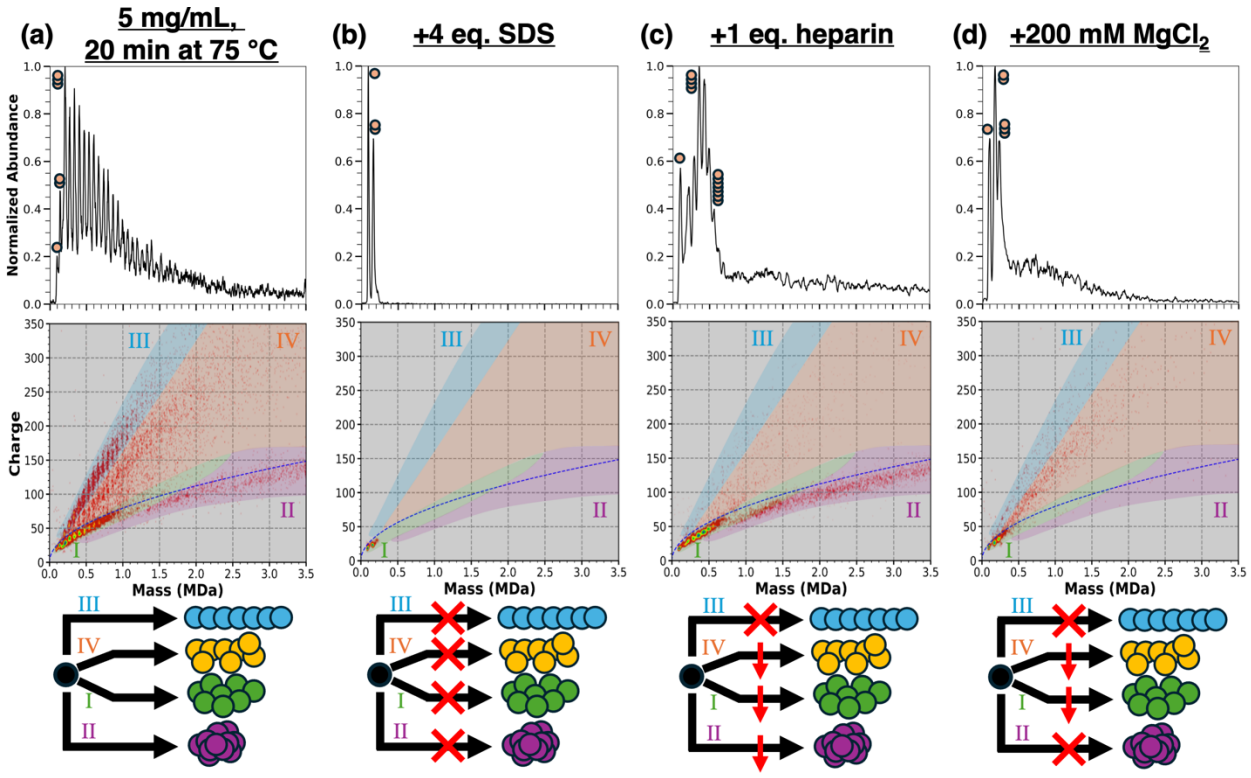

Figure 11.4. Mass histograms (top row) and 2D mass-charge data (middle row) of heat-stressed (75 °C for 20 min) BSA solutions (5 mg/mL BSA with 50 mM ammonium acetate, pH 6.8) containing (a) no inhibitor, (b) 4 molar eq. SDS, (c) 1 molar eq. heparin, or (d) 200 mM $MgCl_2$. The schemes in the bottom row indicate how each inhibitor affects the formation pathway for the four different conformational families. Shaded regions correspond to the same conformational families identified in Figure 10.2a.

11.9 Supplemental Information

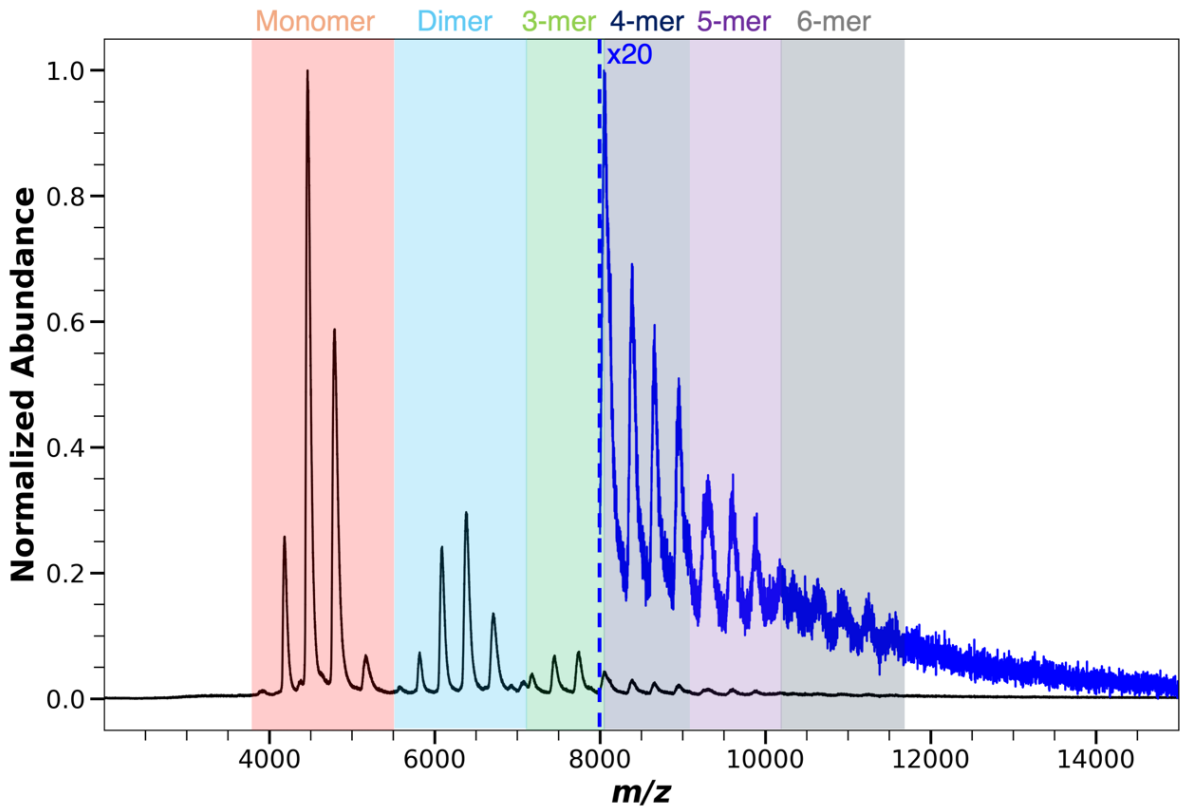

Supplemental Figure 11.1. Quadrupole Time-of-flight (QTOF) mass spectrum of 5 mg/mL BSA in 50 mM ammonium acetate. The abundances for the data in blue were expanded by ~20x to show the tail of unresolved signal that extends to ~15,000 *m/z*.

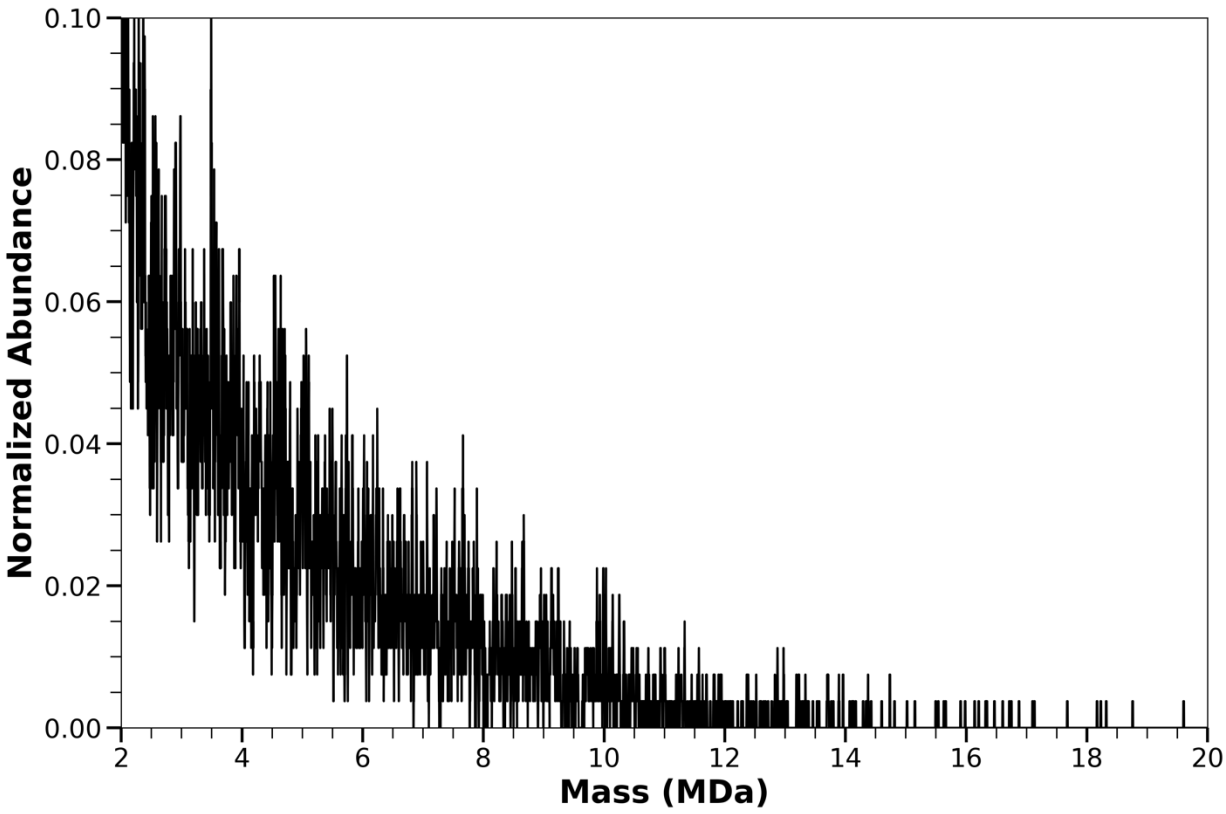

Supplemental Figure 11.2. Extended 1D mass histogram of the data shown in Figure 1b (unsmoothed), demonstrating the formation of low-abundance aggregates with masses extending to ~20 MDa.

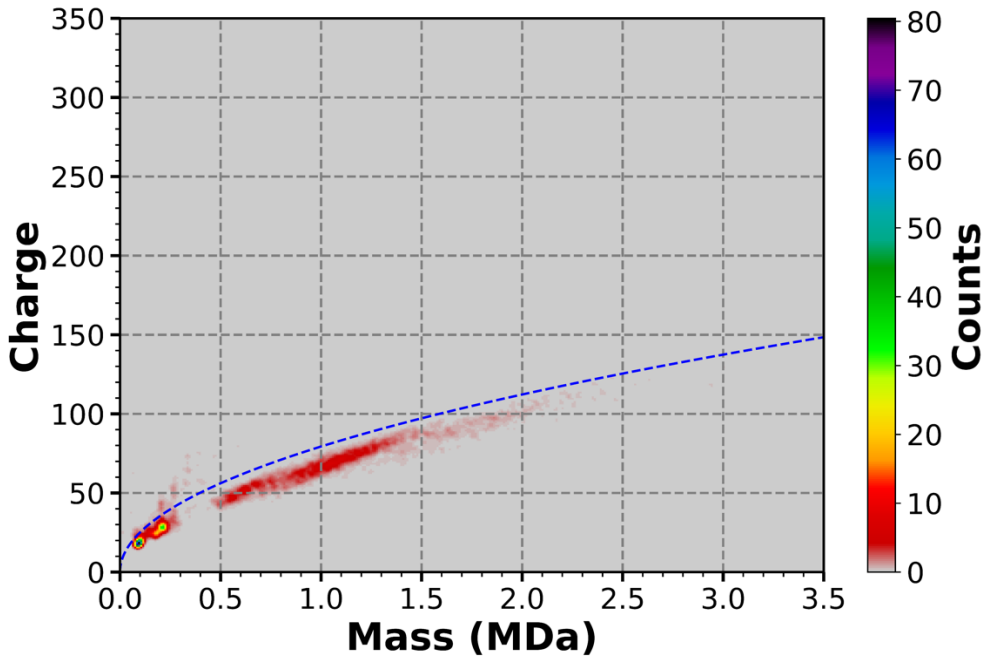

Supplemental Figure 11.3. 2D mass-charge histogram of a 5 mg/mL BSA solution that was not heat stressed. These data show that the higher order, high charge oligomers observed in heated samples are not present in solution before heat-stress.

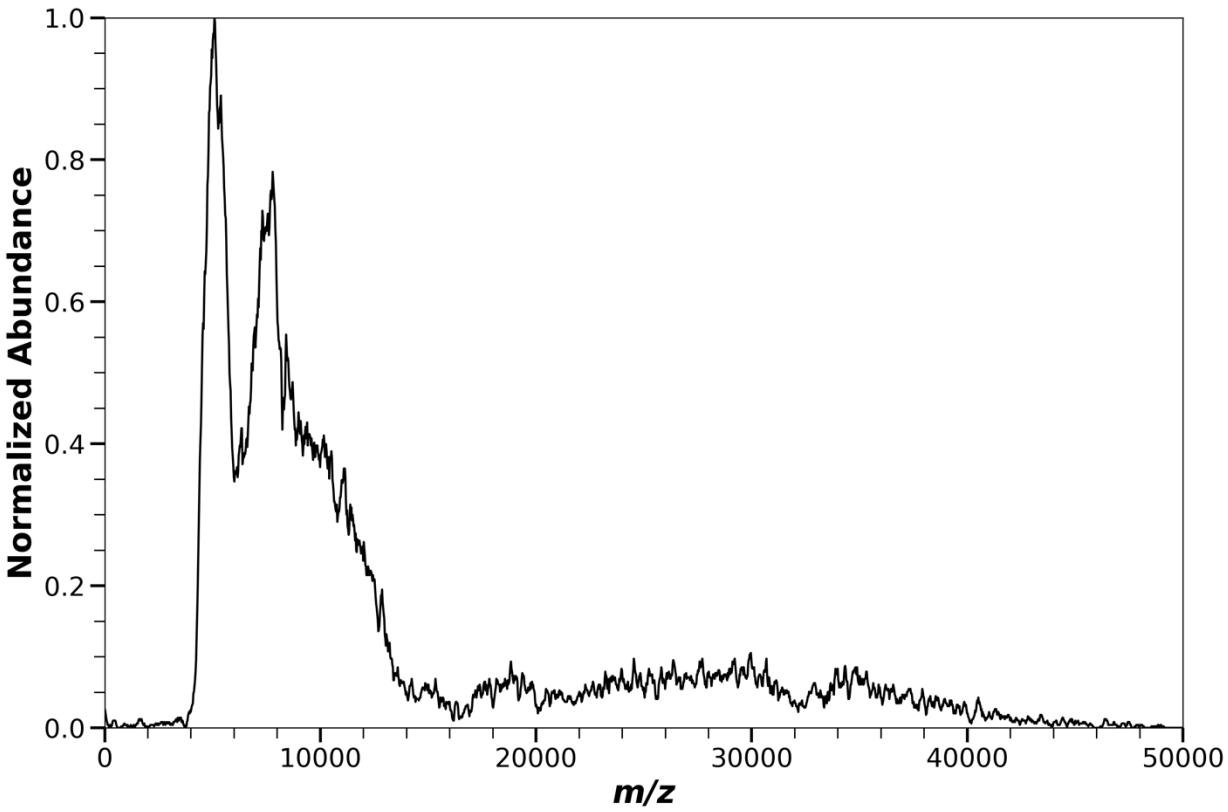

Supplemental Figure 11.4. Figure 2a data plotted in the form of a conventional mass spectrum, *i.e.,* as a function of *m/z*.

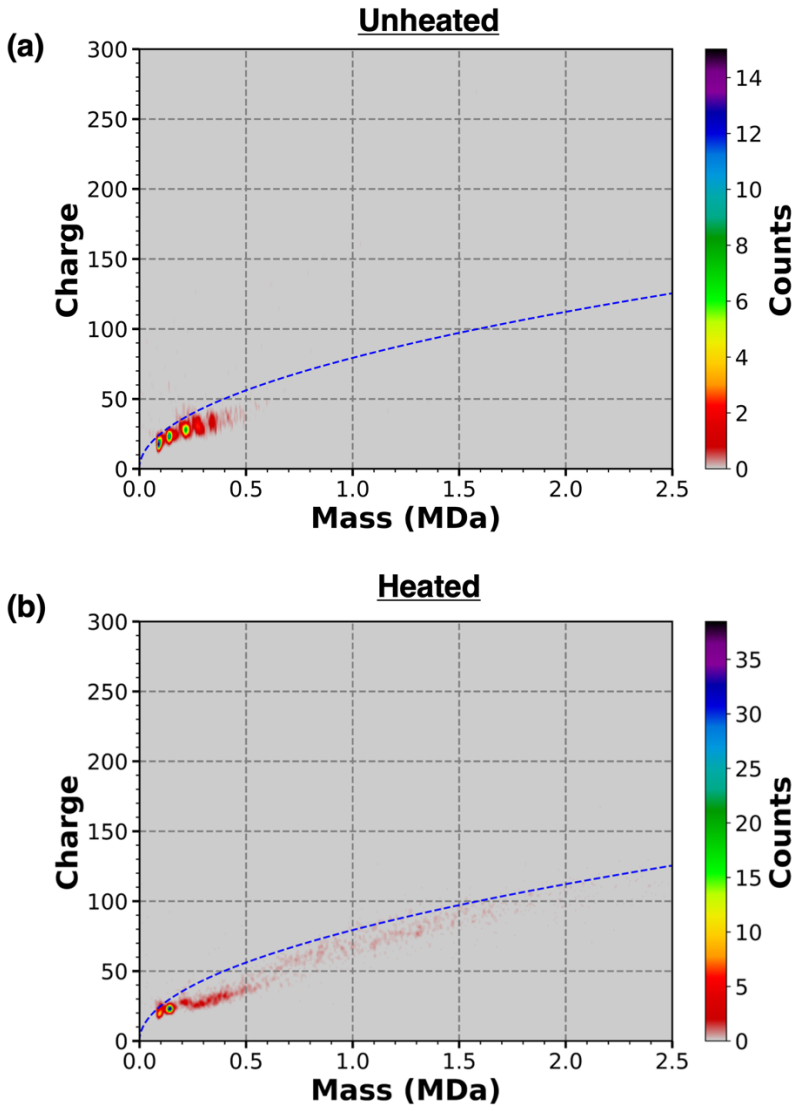

Supplemental Figure 11.5. 2D mass-charge histogram of 0.1 mg/mL BSA solution (a) without heating and (b) heated at 75 °C for 20 min.

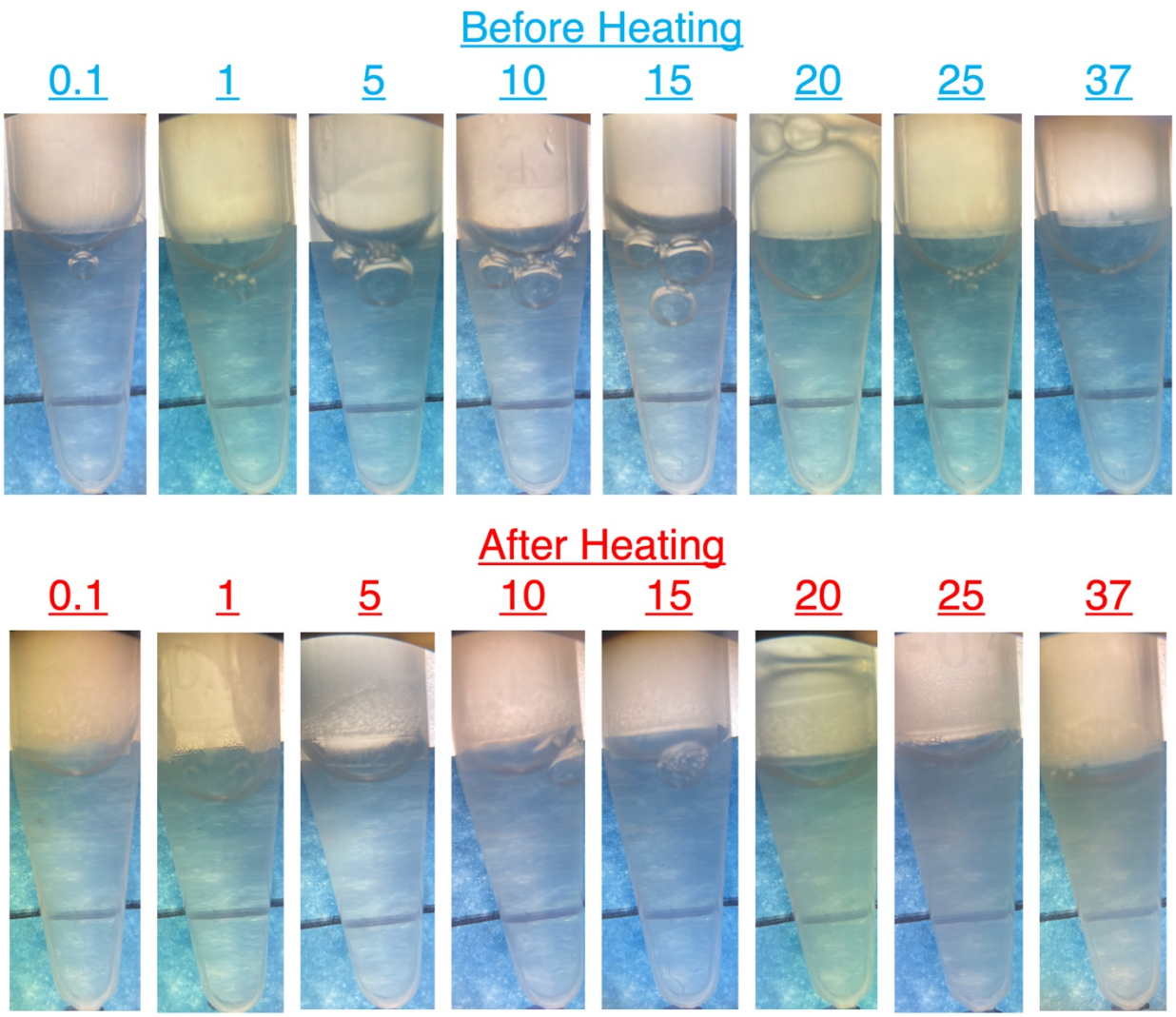

Supplemental Figure 11.6. Microscope images showing the turbidity of samples containing 0.1 – 37 mg/mL BSA (blue) before and (red) after heating at 75 °C for 20 minutes. The numbers above each photo are the concentration of BSA in the sample in mg/mL.

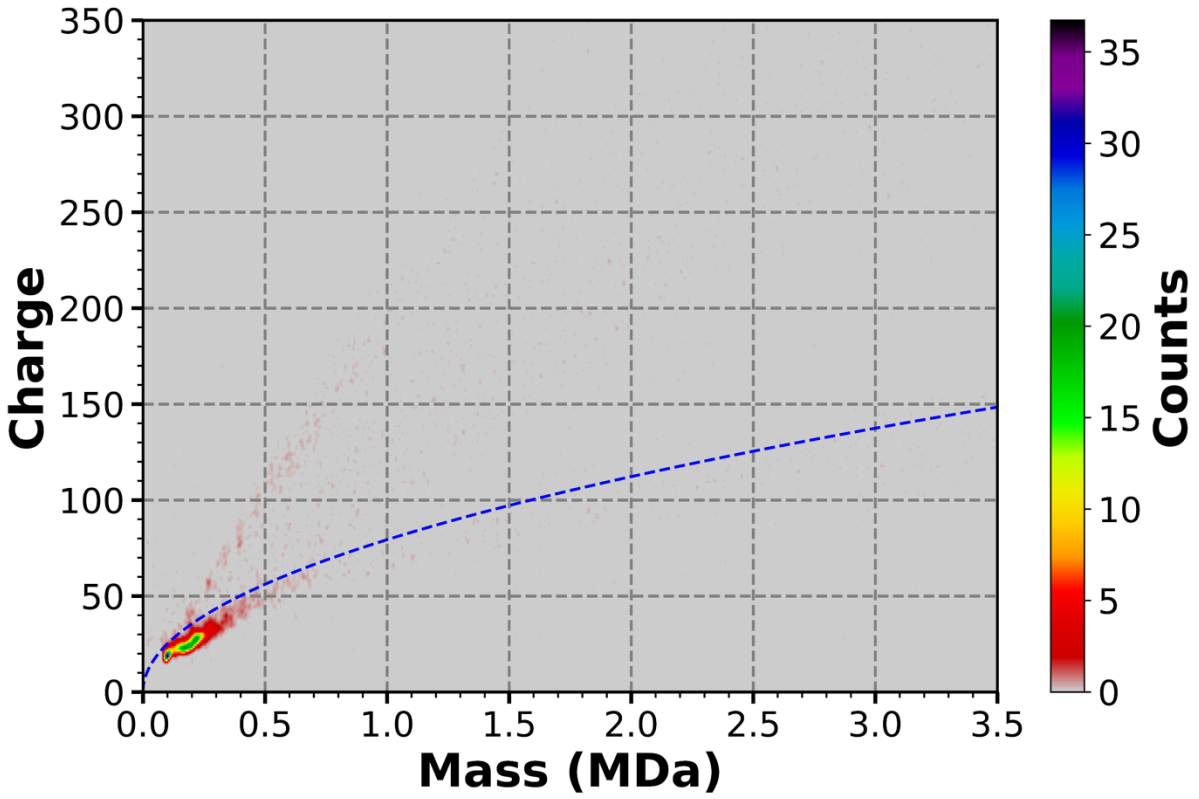

Supplemental Figure 11.7. CDMS 2D mass-charge histogram of 25 mg/mL BSA after heating at 75 °C for 20 min.

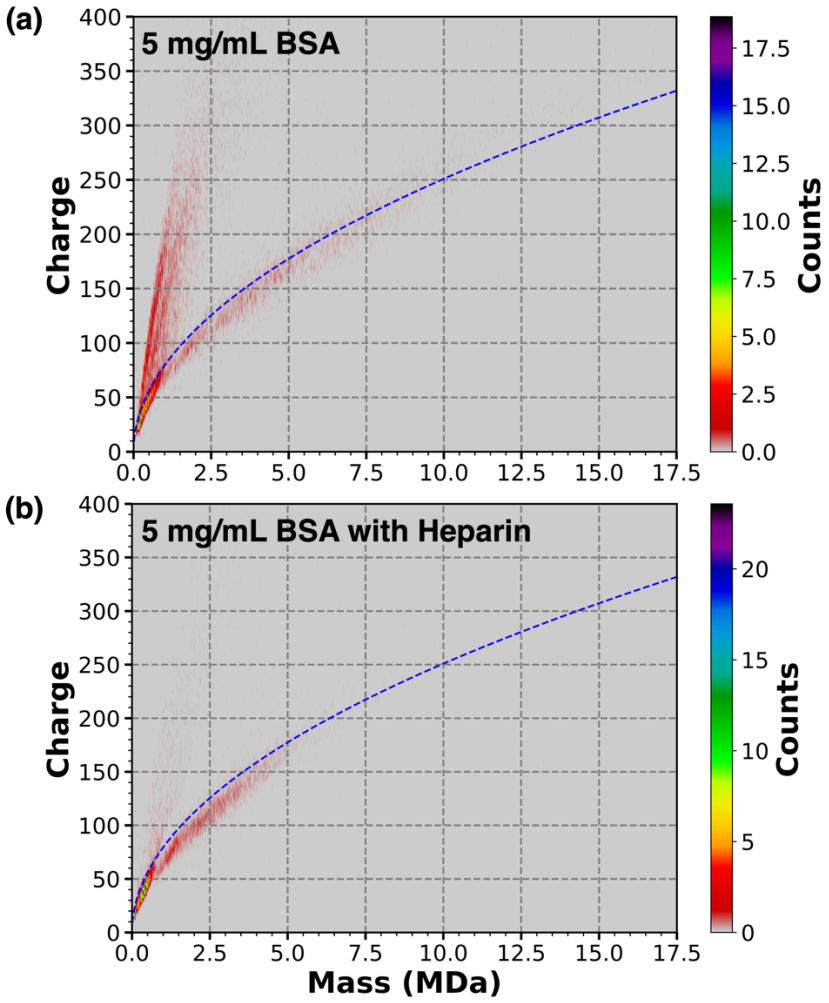

Supplemental Figure 11.8. CDMS 2D mass-charge histogram of 5 mg/mL BSA after heating at 75 °C for 20 min (a) without and (b) with 1 mol. eq. 5 kDa avg. molecular weight heparin.

Chapter 12

Characterizing Monoclonal Antibody Aggregation using Charge Detection Mass Spectrometry and Industry Standard Methods

12.1 Abstract

Protein aggregation in the human body contributes to a multitude of neurodegenerative diseases. Aggregation of protein-based biotherapeutics can cause toxicity in vivo and adverse patient outcomes. Samples of ~680 kDa monoclonal antibody (M) – fluorophore (F) complexes with four different antibody sequences were analyzed using size-exclusion chromatography (SEC) and mass spectrometry using both quadrupole-time-of-flight (QTOF) and charge detection mass spectrometry (CDMS). Higher order structures were not resolved using SEC, but species as large as the MF_2 complex and M_4F_4 were resolved and detected using QTOF and CDMS, respectively. Results from three freeze/thaw cycles and long term heat stress indicate that both aggregation and degradation occurs. Two of the antibodies form a critical M_2F complex that is sensitive to thermal stress, whereas the other two antibodies favor degradation and formation of the assembled MF_2 complex in response to freeze-thaw and thermal stressors, respectively. These data show that small differences in mAb sequence can result in significant changes to the aggregation and degradation pathways and highlight the promise of combined mass spectrometry approaches for characterizing how various stress factors affect mAbs.

12.2 Experimental Methods

Monoclonal antibodies were produced at Merck & Co., Inc., South San Francisco, CA, using Protein A purification protocols. Phycoerythrin conjugation was performed by AAT Bioquest using a protocol based on Buccutite-crosslinking chemistry. Freeze/thaw cycles of the PE-mAb samples were performed by thawing the samples at room temperature for 1 hr and incubating at -80 °C for 1 hr. This process was repeated 2x for a total of three freeze/thaw cycles. Elevated temperature incubations and controls were performed for 10 days at 37 °C and 4 °C, respectively.

To characterize aggregation by UP-SEC, the sample was prepared by diluting to a final concentration of 1 mg/ml and 5 µg was injected onto a Waters Acquity BEH 450 SEC column (1.7 µm, 4.6 × 150 mm, Waters Corporation, Milford, MA). An isocratic flow of mobile phase consisting of 100 mM sodium phosphate, 200 mM sodium chloride, and 0.02% sodium azide (pH 7) was used with a separation flow rate of 0.5 ml/min on a Waters H-Class UPLC. Chromatograms were collected at both 215 and 280 nm wavelengths and integration of the absorption at 280 nm was performed using EMPOWER 2 (Waters Corporation).

Native mass spectrometry was performed using nanoelectrospray emitters with inner diameters of ~1.3 ± 0.1 µm that were pulled using a Flaming/Brown P-87 pipette puller (Sutter Instrument, Novato, CA) from borosilicate capillaries (1.0 mm outer diameter, 0.78 mm inner

diameter, Sutter Instrument, Novato, CA).[1] Emitter diameters were imaged using a Hitachi TM-1000 scanning electron microscope (Tokyo, Japan) at the Electron Microscopy Laboratory at the University of California, Berkeley. Immediately prior to mass spectrometry measurements, PE-mAb samples were diluted to 1 mg/mL and buffer exchanged into 163 mM ammonium acetate (pH 7.2) (Sigma-Aldrich, Burlington, MA) using a Micro Bio 6 Spin column (Bio-Rad Laboratories, Hercules, CA). Conventional mass spectrometry experiments were performed using a Waters Q-TOF Premier quadrupole time-of-flight mass spectrometer (Waters Corporation, Milford, MA). The source temperature was 80 °C, and the extraction cone, sampling cone, and ion guide voltages were 3 V, 100 V, and 2 V, respectively. The backing pressure in the source was increased to 5-10 mbar to assist desolvating larger ions. The collision gas flow rate was 0.75 mL min^{-1}, resulting in a final gas (argon) pressure of ~1 x 10^{-2} mbar in the collision cell. Ions were formed by applying a voltage of ~0.7 – 1.3 kV to a 0.127 mm platinum wire inserted into the back of nESI emitters and in contact with the solution.

CDMS experiments were performed using a custom charge detection mass spectrometer and data analysis methods that are described in detail elsewhere.[2–5] In brief, the instrument consists of an electrospray ion source, a heated ion transfer tube maintained at 140 °C, three RF-only quadrupole ion guides, and an electrostatic cone trap. RF frequencies and voltages were varied across three different conditions to enable ion transmission and measurement over a range of *m/z* values between ~9,000 and ~20,000. Population abundances are based on the peak height (in counts) of each species. All mass spectrometry experiments were performed at the University of California, Berkeley and all other experiments were performed at Merck & Co., Inc., South San Francisco, CA.

12.3 Results and Discussion

12.3.1 Quantifying PE-mAb Oligomerization by Size-Exclusion Chromatography

Four phycoerythrin-mAb (PE-mAb) conjugates (denoted PE-mAb #1-#4) were analyzed using a standard SEC workflow for characterizing mAb aggregation to determine the relative abundance of fluorophore-conjugated species and higher molecular weight oligomers. Each conjugate contains the same fluorophore (PE) but have mAbs with differing amino acid sequences. In the following discussion, units of the PE fluorophore are denoted with F and mAbs are denoted M. Thus, the intact complex containing one mAb and two fluorophores is denoted as MF_2.

SEC chromatograms acquired for PE-mAb #1 contain peaks with retention times (RT) of 3.07 min, 3.25 min, 3.55 min, and 3.81 min (Figure 1a). These RTs can be converted into masses based on the RT of globular protein standards that have known molecular weights. The peak with the highest RT (3.81 min) corresponds to low mass components of the PE fluorophore with an average mass of ~23 kDa. Native PE is composed of six α (~19 kDa each), six β (~20 kDa each), and one γ subunit (~27.5 kDa) with a theoretical mass of ~269 kDa.[6] The peak at 3.55 min likely corresponds to the heavy chain of the non-conjugated mAb (~91 kDa) and the two subsequent lower RT peaks at 3.07 min and 3.25 min correspond to the PE fluorophore without the γ subunit (~243 kDa) and to the MF complex (~436 kDa). The large unresolved signal at even lower RT corresponds to higher order complexes or aggregates with masses greater than 500 kDa. The high

relative signal for this peak suggests that a significant concentration of higher order aggregates exist in solution, but their identity is not determined from these SEC measurements because of their similar elution times and broad peak widths that preclude the resolution of individual species. A similar chromatogram was obtained for PE-mAb #2 in which peaks corresponding to fluorophore subunits, mAb heavy chain, native fluorophore, and an MF complex are resolved, but higher order oligomers are not (Figure S1a).

SEC chromatograms for PE-mAbs #3 and #4 are significantly different than those of PE-mAbs #1 and #2, but are very similar to each other. There are peaks with RTs (masses) of 3.96 min (~10 kDa), 3.77 min (~28 kDa), 3.50 min (~91 kDa), 3.27 min (~228 kDa), and 3.10 min (~398 kDa) in both chromatograms (Figure 2a and S2a). The 10 kDa and 28 kDa species likely correspond to components of PE and are significantly lower abundance than in samples containing PE-mAbs #1 and #2. The lower RT peaks corresponding to masses of ~228 kDa and ~398 kDa are assigned to the F and the MF complex, but are broad and nearly unresolved which may result in some inaccuracy in determining the molecular weight of these components. Unresolved signal in the SEC trace for PE-mAbs #3 and #4 (<2.78 min and <2.42 min, respectively) indicate the presence of higher order oligomers in solution. Based on these SEC data, essentially no information can be obtained about the higher order aggregates of any of the PE-mAbs.

12.3.2 Quantifying PE-mAb Oligomers using QTOF Mass Spectrometry

SEC separates aggregates primarily by size in solution whereas mass spectrometry separates molecules based on differences in mass when *m*/*z* values of individual components are resolved. PE-mAb conjugates were buffer exchanged into 163 mM ammonium acetate and mass spectra were acquired using a Waters Q-TOF Premier mass spectrometer. There are charge-state distributions corresponding to a number of relatively low mass species below *m/z* ~6000 in QTOF mass spectra of PE-mAbs #1 and #2 with deconvolved masses of 18,864.9 ± 0.8 Da, 20,281.9 ± 0.4 Da, 39,283.8 ± 34.4 Da, and 117,664.7 ± 120.8 Da (Figure 1b and S1b). These ions are assigned as the α, β, αβ, and $\alpha_3\beta_3$ subunits of the PE fluorophore (F), respectively, based on observed masses of 18,977 Da, 20,327 Da, 39,304 Da, and 117,955 Da in prior reports (Figure 1b and S1b).[6] The slightly lower masses obtained here may be due to fewer solvent or small molecule adducts to these ions. Signal for the free γ subunit (~27.8 kDa) is not observed. There are additional low abundance charge-state distributions in the range of *m/z* = 6000 – 9000. The most abundant distribution in this region corresponds to ions with masses of 258.6 ± 0.2 kDa for mAb #1 and 276.9 ± 0.5 kDa for mAb #2, which we assign to the intact fluorophore (previously reported mass of 263.2 – 264.1 kDa).[6] The origin of this ~18 kDa difference in mass between these two samples is unclear, but may correspond to a fluorophore without and with one additional α subunit. Elevated signal baseline and low signal-to-noise prevents the characterization of other, slightly lower *m*/*z* distributions in this region that also appear to be present and may correspond to F with different numbers of bound bilin subunits (MW = ~583), which have been reported to bind to PE in prior native MS experiments.[6] The MF complex is also resolved at higher *m/z* with a mass of 417.7 ± 0.5 kDa for both samples (Figure 1b and S1b). This region contains a single charge state distribution corresponding to a mAb and the ~259 kDa form of the PE fluorophore. The absence of a second complex containing the ~277 kDa form of the PE fluorophore indicates that the MF complex forms specifically with the ~259 kDa form that is most abundant in the PE-mAb #1

sample. The origin of the high abundance of the ~277 kDa form of the PE fluorophore in the PE-mAb #2 sample is unclear. There is a tailing baseline to even higher *m/z,* from which the +47 - +49 charge states of the MF_2 complex (MW = 676.1 ± 1.4 kDa) can be resolved. QTOF measurements on samples containing mAb #1 and #2 do not show any resolved charge-state distributions for ions larger than the MF_2 complex.

Ions corresponding to the β and αβ subunits of the fluorophore are also present in QTOF mass spectra of PE-mAbs #3 and #4, but there is no signal for the $\alpha_3\beta_3$ subunit of F (Figure 2b and S2b). Dissociated mAb light chain and light chain degradation products are observed at low abundance with deconvoluted masses of 24,266 ± 147 Da and 12,182.7 ± 0.9 Da, respectively. In samples containing PE-mAb #3, there are two charge-state distributions at higher *m/z* values (6,000 – 9,000) corresponding to masses of 154.2 ± 0.6 kDa and 248.8 ± 0.2 kDa, which are attributed to free mAb and the PE fluorophore, respectively (Figures 2b and S2b). Charge-state distributions for the MF and MF_2 complexes are also resolved (MW = 405.9 ± 0.7 kDa and 686.4 ± 0.7 kDa, respectively) and there is an elevated baseline that tails to higher *m/z* indicative of unresolved higher order complexes. Different masses for the fluorophore (264.2 ± 0.3 kDa) and the MF complex (417.8 ± 0.9 kDa) are obtained from samples containing PE-mAb #4. These data indicate that the assembly of the PE fluorophore can be heterogeneous, consistent with prior reports that indicate heterogenous incorporation of γ and bilin subunits into this flourophore.[6] There is no resolved signal for ions larger than the MF_2 and MF complexes in the QTOF data for PE-mAbs #3 and #4, respectively (Figure 2b and S2b).

The high abundance of F subunits in samples containing PE-mAbs #1 and #2 and higher population of MF and MF_2 complexes in samples containing PE-mAbs #3 and #4 is consistent with the SEC results. The low abundance of higher order oligomers observed by QTOF MS compared to SEC may be due to lower ion transmission and detection efficiency of the QTOF mass spectrometer with increasing *m/z*, or due to increased heterogeneity of the analytes with higher mass, which yields broadened peaks and elevated baselines.

12.3.3 Characterizing PE-mAb Oligomerization using Charge Detection Mass Spectrometry

Several higher order complexes not identified with QTOF MS are detected using CDMS, including the MF (417.4 ± 1.0 kDa), M_2F (535.7 ± 1.8 kDa), and MF_2 (674.1 ± 1.4 kDa) complexes (Figure 1c, 2c, S1c, S2c). Higher order complexes are also well-resolved, but are lower abundance including M_2F_2 (821.4 ± 2.8 kDa), M_3F_2 (950.6 ± 4.7 kDa), M_2F_3 (1.08 ± 0.01 MDa), and M_3F_3 (1.24 ± 0.01 MDa) (Figures 1c, 2c,, S1c, S2c). The largest complex in CDMS mass spectra of PE-mAb samples #1 - #4 are the M_4F_5, M_3F_3, M_3F_4, and M_6F_6 complexes, respectively. There is also unresolved signal that extends to ~4 MDa. The resolution of the CDMS instrument used here increases with increasing molecular size and charge,[7] indicating that the unresolved signal here is due to the inherent heterogeneity of many possible combinations of M and F as well as other smaller species also in the sample, and it is not a limitation of the resolution of the CDMS instrument. In order to characterize higher order aggregates that are not detected by QTOF MS, an *m/z* cutoff of ~9000 *m/z* was used in these experiments which limits the smallest species detected to MF. These data indicate that a large number of high order oligomers of M and F can be resolved using CDMS that are unresolved using other conventional characterization methods.

CDMS mass spectra for each of the four PE-mAbs include a peak corresponding to the M_2F complex (~536 kDa). This species is not resolved by SEC or by QTOF MS. In the SEC traces, there is a broad baseline due to unresolved oligomers from ~2 – 3.5 min that overlaps with peaks corresponding to the MF and MF_2 complexes (Figure 1a, 2a, S1a, S2a). The M_2F complex likely contributes to this elevated baseline at ~3.1 min. In QTOF mass spectra, there are two resolvable charge state distributions that correspond to the F and MF molecules (Figure 1b, 2b, S1b, S2b. There is also a broad, unresolved signal that tails out from *m/z* ~12000 – 14000 which may correspond to the M_2F species. In contrast, the high sensitivity and resolution at high *m/z* values afforded by CDMS enables the MF, M_2F, MF_2 complexes and a number of higher order oligomers to be resolved and identified.

The high mass and low abundance of individual aggregates may explain why they are not observed or resolved by QTOF MS or SEC. The unresolved signal at lower RT values (0 - ~3 min) in the SEC chromatograms of all PE-mAbs indicate a high abundance of aggregates that are resolved at low abundance in CDMS mass spectra. The reason for this difference may be a result of the different detection methods. The PE-mAb aggregates likely absorb more light per aggregate particle than the corresponding number of free PE-mAbs. This effect could result in a large absorbance baseline arising from a relatively low abundance of higher order aggregates. In addition, aggregates that fall outside of the MW range of the SEC separation will elute at the same time and the overlap between many low abundance oligomers may result in a large signal in the chromatogram.

12.3.4 Quantifying Higher Order PE-mAb Aggregation after Freeze-Thaw Cycles

Freeze-thaw (FT) cycles can occur during cold-chain transport of biotherapeutics and have negative effects on long-term stability and storage.[8–10] In order to assess the effect of FT stress on PE-conjugated mAbs, samples were subjected to 3 FT cycles from -80 °C to ~26 °C. PE-mAb conjugates were stressed in phosphate buffered saline before buffer exchanging into 163 mM ammonium acetate immediately prior to MS measurements.

The most significant change after FT stress in CDMS mass spectra of PE-mAbs #1 and #2 is the abundance of the M_2F complex. This species increased in population abundance by ~12% and ~7%, respectively (Figure 3a,b,e,f). The abundance of the MF and MF_2 species decreases by ~8% and ~4% on average between the two samples. There are no significant changes in the abundance of the other higher order aggregates. PE-mAbs #3 and #4 have a significantly different response to FT stress. The abundance of the M_2F complex in CDMS mass spectra of these mAbs is low and remains unchanged after FT cycling (Figure 3c,d,g,h). The MF_2 decreases in abundance after FT from 32% to 21% and 43% to 31% for mAbs #3 and #4, respectively (Figure 3c,d,g,h). Besides a slight increase in the abundance of the M_2F_2 there is no significant change in the abundance of higher order aggregates larger than the MF_2. These data indicate a significantly different response to FT stress based on mAb sequence: mAbs #1 and #2 favor the formation of the M_2F complex, whereas mAbs #3 and #4 favored the degradation of MF_2. The increased abundance of the M_2F for mAbs #1 and #2 may be due to aggregation of MF with free M generated from breakdown of some of the MF complexes, suggesting that aggregation and degradation of this complex are competing pathways.

QTOF MS data provides insight into the effects of FT stress on lower molecular weight species in the samples. Representative QTOF mass spectra for PE-mAbs #1 and #3 before and after FT stress are shown in Figure 4. For PE-mAbs #1 and #2, there is a slight decrease in the abundance of F and MF and an increase in free F subunits, consistent with these molecules being degraded (Figure 4a,c and S3a,b). These data indicate that higher order aggregates, including M_2F, have a higher stability against FT stress than smaller species that are prone to degradation. PE-mAbs #3 and #4 show a higher abundance of F subunits after FT stress (Figure 4b,d and S4a,b). There is also elevated baseline between m/z = 2,500 – 6,000 that was not present for PE-mAbs #3 and #4 before FT, indicating the presence of unresolved lower molecular weight species. These QTOF MS data also indicate that the mAb primary sequence influences the FT stress response of lower molecular weight species: PE-mAbs #1 and #2 undergo some F degradation to form resolved F subunits, whereas in samples containing PE-mAbs #3 and #4 unresolved peaks at low m/z and a high abundance of F subunits is consistent with the formation of highly heterogeneous degradation products that may arise from fluorophore or degraded mAbs.

Combined, these CDMS and QTOF MS data provide a detailed view of the aggregation/degradation response of PE-mAbs as a result of FT stress that is challenging to obtained by other aggregate characterization techniques. The ability to discern changes in the concentration of low-abundance species, such as the M_2F complex and other higher order oligomers that cannot be resolved by SEC or QTOF MS, is a unique advantage of this CDMS-based approach for characterizing mAb aggregation and mAb responses to stressed conditions.

12.3.5 Effect of Thermal Stress on PE-mAb Aggregation

The U.S. FDA also recommends the characterization of aggregates formed after incubation at elevated temperatures that biotherapeutics may experience during storage, shipping, or in the human body. QTOF and CDMS mass spectra were acquired for all 4 PE-mAbs after incubation at 4 °C and 37 °C for 10 days. Cold incubation (4 °C) of PE-mAbs #1 and #2 for 10 days results in an increase in the abundance of the M_2F species by ~5% and ~14%, respectively, in agreement with the trends observed from FT stress (Figure 3a,b,e,f and Figure 5a,b,e,f). Unresolved aggregates between ~1 – 3 MDa also increase in abundance after cold incubation, suggesting that cold temperature favors the formation of larger oligomers (Figure 5e,f). Cold incubation of PE-mAbs #3 and #4 results in a drastic decrease in the abundance of MF, an increase in the abundance of MF_2, and no changes to the abundances of other resolved complexes or higher order aggregates (Figure 5c,d,g,h). These data indicate that the MF formed from mAbs #3 and #4 is unstable against cold temperatures and that higher order species, including the MF_2, are more stable under these conditions. Even for the relatively mild conditions used here (4 °C) there appears to be a significant difference in the stress response of these conjugates based on mAb identity.

Incubation at elevated temperatures can increase the rate of aggregation, degradation or both and can amplify minor differences in stability between species. Incubation of PE-mAbs #1 and #2 at 37 °C for 10 days results in the abundance of the M_2F complex being reduced by ~70% and no unresolved aggregates at masses >2 MDa (Figure 5a,b,i,j), consistent with degradation of these higher order oligomers. The drastic reduction in the abundance of the M_2F complex at high temperatures, as well as the increased abundance at low temperature incubation, indicate that this species may be a critical structure in the formation or degradation of higher order oligomers. For

PE-mAbs #3 and #4, the MF species decreases in abundance even more than that observed under cold stress conditions and the MF_2 complex is the predominant species in the sample (Figure 5c,d,k,l). CDMS mass spectra acquired after incubation of PE-mAb #3 at 37 °C show significant peak broadening and peaks at masses higher than ~800 kDa that do not align with the expected masses for any aggregates of F and M, indicative of the formation of very heterogeneous aggregates that may have incorporated smaller mAb degradation products (Figure 5c,k). These data further highlight the different stress responses that may arise as a result of different mAb sequences, even between mAbs #3 and #4 that share similar response patterns to all other stressing conditions but display very different spectra after incubation at 37 °C.

QTOF mass spectra were also acquired on all four PE-mAbs after 4 °C and 37 °C stress. The abundances of F amd MF in mass spectra of PE-mAbs #1 and #2 are very low before and after incubation at 4 °C, so subtle changes in the abundance of MF like those observed by CDMS may be difficult to detect from these data (Figure 6a,c and S5a,b). QTOF mass spectra of PE-mAb #2 show an increase in the ratio of F:MF from 1:1 before incubation to ~2:1 after incubation, consistent with a reduced abundance of MF observed in CDMS data (Figure S5a,b). Mass spectra acquired on PE-mAb #3 after cold incubation show a similar increase in the ratio of F:MF, a decreased population of F subunits, and increased resolution of the MF_2 that is consistent with the formation of higher order aggregates, including the MF_2 from smaller species (Figure 6b,d). The origin of the decrease in the abundance of the MF observed by CDMS for PE-mAb #4 is less clear, as there does not appear to be a similar change in the abundance of F, MF, or MF_2 in these mass spectra (Figure S6a,b).

After 37 °C incubation, there is no signal for the $\alpha_3\beta_3$ subunit in QTOF mass spectra for all mAbs, indicating that this species is not thermally stable (Figure 6e,f and S6a,c). There is also an increase in the abundance of F, in agreement with the decrease in MF population observed by CDMS for all PE-mAbs (Figure 5 and 6). For PE-mAbs #3 and #4, there is signal for the free mAb consistent with degradation of the MF to form lower molecular weight species. Ions with masses of ~44 kDa (in both PE-mAb #3 and #4) and ~98 kDa (PE-mAb #4) are also formed, which may correspond to the mAb heavy chain and a mAb molecule with no light chains (i.e. only composed of 2 heavy chains), respectively (Figure 6f and S6c). The QTOF data acquired after thermal incubation at various temperatures are consistent with the trends observed by CDMS, but provide less information about how temperature stress affects the formation and degradation of important structures along the pathway towards higher order oligomers.

12.4 Conclusions

Measuring the aggregation and degradation of large biotherapeutics can be challenging owing to their high molecular weight and heterogeneity. Native mass spectrometry shows significant promise as a tool to characterize the complicated aggregation and degradation pathways for mAbs and antibody-drug conjugates due to high sensitivity, resolution, and speed of analysis. The high mass range and single ion measurement capacity of CDMS enables the characterization of very low abundance, high mass oligomers that are not readily identified by either SEC or conventional QTOF MS. These benefits show significant promise for CDMS as a tool for quantifying and characterizing the formation or degradation of higher-order aggregates during the development, quality control, and manufacture of biopharmaceuticals. Measuring the kinetics of

aggregation or degradation processes at smaller timescales (1 day) and comparing to longer-term stress (10 days) could provide insight into the different processes that occur during storage and has the potential to accelerate mAb stability assays by reducing the incubation time required to obtain an understanding of the aggregation behavior of a given molecule/mAb.

CDMS also shows promise as a high-throughput method for determining the effects of mAb sequence or charge variation, as well as different formulation buffers, on the aggregation behavior and conformations formed under stressed conditions. CDMS can distinguish between different conformations based on different extents of charging, enabling the resolution of individual conformer families even for aggregates in the multi-MDa size range.[11] CDMS in combination with submicron diameter emitters, which enables the measurement of proteins directly from biochemically relevant nonvolatile buffers, may enable the study of how buffer conditions influence aggregation behavior, reducing the time required for formulation buffer development and shortening the time-to-approval for novel biopharmaceuticals.

12.5 Acknowledgements

This work was supported by the National Science Foundation Division of Chemistry (grant number CHE-2203907), the National Institutes of Health (grant number 5R01GM139338) for development and construction of the CDMS instrument and data analysis methods used in this work, an ACS Graduate Research Fellowship sponsored by Eli Lilly and Company (JSJ), the Arnold and Mabel Beckman Foundation Postdoctoral Fellowship in Chemical Instrumentation (CCH), and Merck & Co., Inc., San Francisco, CA, USA, through their Discovery Biologics SEEDS program.

12.6 References

(1) Jordan, J. S.; Xia, Z.; Williams, E. R. Tips on Making Tiny Tips: Secrets to Submicron Nanoelectrospray Emitters. *J. Am. Soc. Mass Spectrom.* **2022**, 33 (3), 607–611.
(2) Harper, C. C.; Jordan, J. S.; Papanu, S.; Williams, E. R. Characterization of Mass, Diameter, Density, and Surface Properties of Colloidal Nanoparticles Enabled by Charge Detection Mass Spectrometry. *ACS Nano* **2024**, 18 (27), 17806–17814.
(3) Harper, C. C.; Miller, Z. M.; McPartlan, M. S.; Jordan, J. S.; Pedder, R. E.; Williams, E. R. Accurate Sizing of Nanoparticles Using a High-Throughput Charge Detection Mass Spectrometer without Energy Selection. *ACS Nano* **2023**, 17 (8), 7765–7774.
(4) Miller, Z. M.; Harper, C. C.; Lee, H.; Bischoff, A. J.; Francis, M. B.; Schaffer, D. V.; Williams, E. R. Apodization Specific Fitting for Improved Resolution, Charge Measurement, and Data Analysis Speed in Charge Detection Mass Spectrometry. *J. Am. Soc. Mass Spectrom.* **2022**, 33 (11), 2129–2137.
(5) Harper, C. C.; Miller, Z. M.; Williams, E. R. Combined Multiharmonic Frequency Analysis for Improved Dynamic Energy Measurements and Accuracy in Charge Detection Mass Spectrometry. *Anal. Chem.* **2023**, 95 (45), 16659–16667.

(6) Leney, A. C.; Tschanz, A.; Heck, A. J. R. Connecting Color with Assembly in the Fluorescent B-phycoerythrin Protein Complex. *FEBS J*. **2018**, 285 (1), 178–187.
(7) Harper, C. C.; Miller, Z. M.; Lee, H.; Bischoff, A. J.; Francis, M. B.; Schaffer, D. V.; Williams, E. R. Effects of Molecular Size on Resolution in Charge Detection Mass Spectrometry. *Anal. Chem.* **2022**, 94 (33), 11703–11712.
(8) Kueltzo, L. A.; Wang, W.; Randolph, T. W.; Carpenter, J. F. Effects of Solution Conditions, Processing Parameters, and Container Materials on Aggregation of a Monoclonal Antibody during Freeze-Thawing. *J. Pharm. Sci.* **2008**, 97 (5), 1801–1812.
(9) Roberts, C. J. Protein Aggregation and Its Impact on Product Quality. *Curr. Opin. Biotechnol.* **2014**, 30, 211–217.
(10) Rayfield, W. J.; Kandula, S.; Khan, H.; Tugcu, N. Impact of Freeze/Thaw Process on Drug Substance Storage of Therapeutics. *J. Pharm. Sci.* **2017**, 106 (8), 1944–1951.
(11) Jordan, J. S.; Harper, C. C.; Zhang, F.; Kofman, E.; Li, M.; Sathiyamoorthy, K.; Zaragoza, J. P.; Fayadat-Dilman, L.; Williams, E. R. Charge Detection Mass Spectrometry Reveals Conformational Heterogeneity in Megadalton-Sized Monoclonal Antibody Aggregates. *J. Am. Chem. Soc.* **2024**, 146 (33), 23297–23305.

12.7 Figures

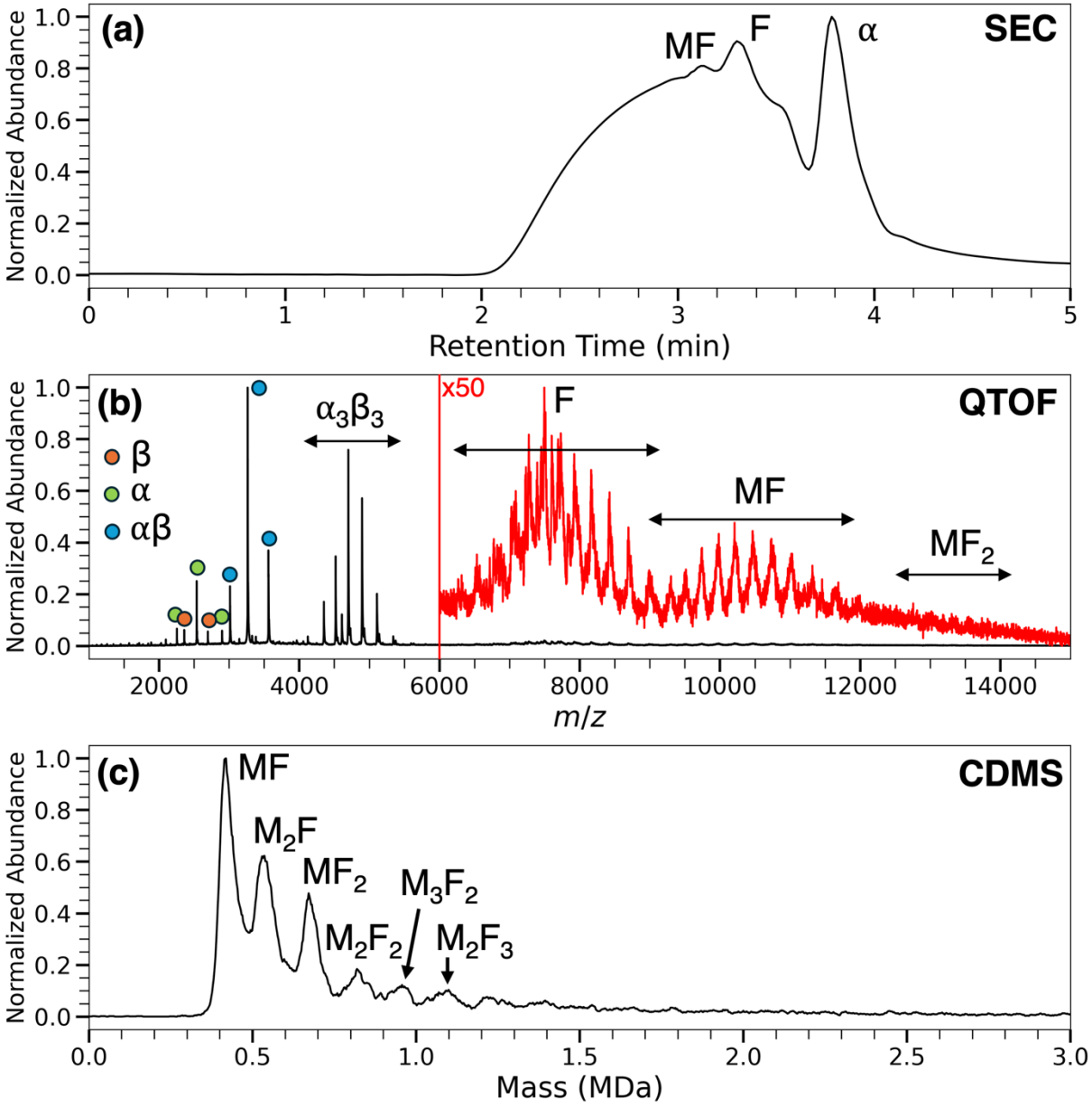

Figure 12.1. Data for PE-conjugate mAb #1 obtained using (a) SEC, (b) QTOF MS, and (c) CDMS.

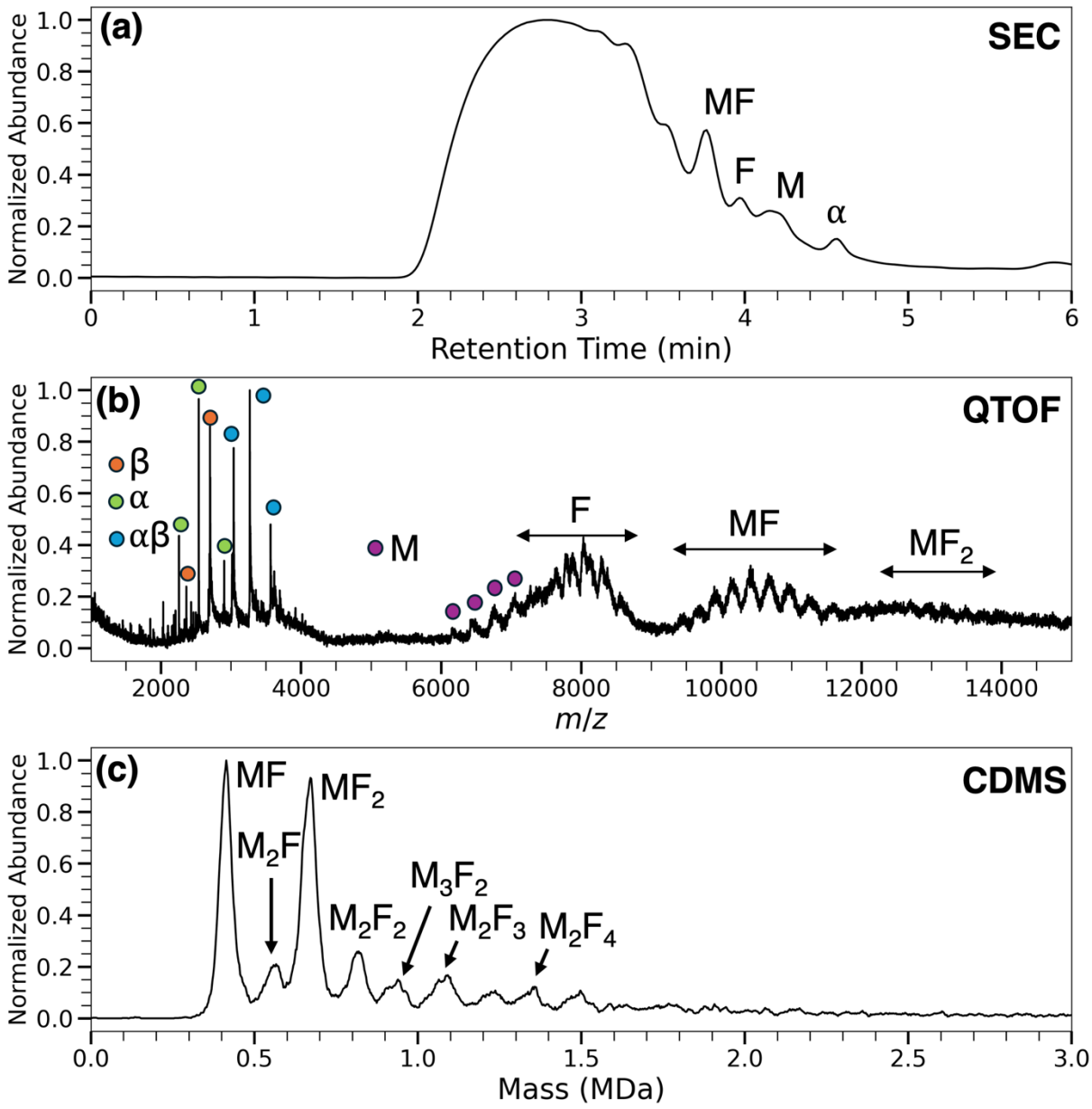

Figure 12.2. Data for PE-conjugate mAb #3 obtained using (a) SEC, (b) QTOF MS, and (c) CDMS.

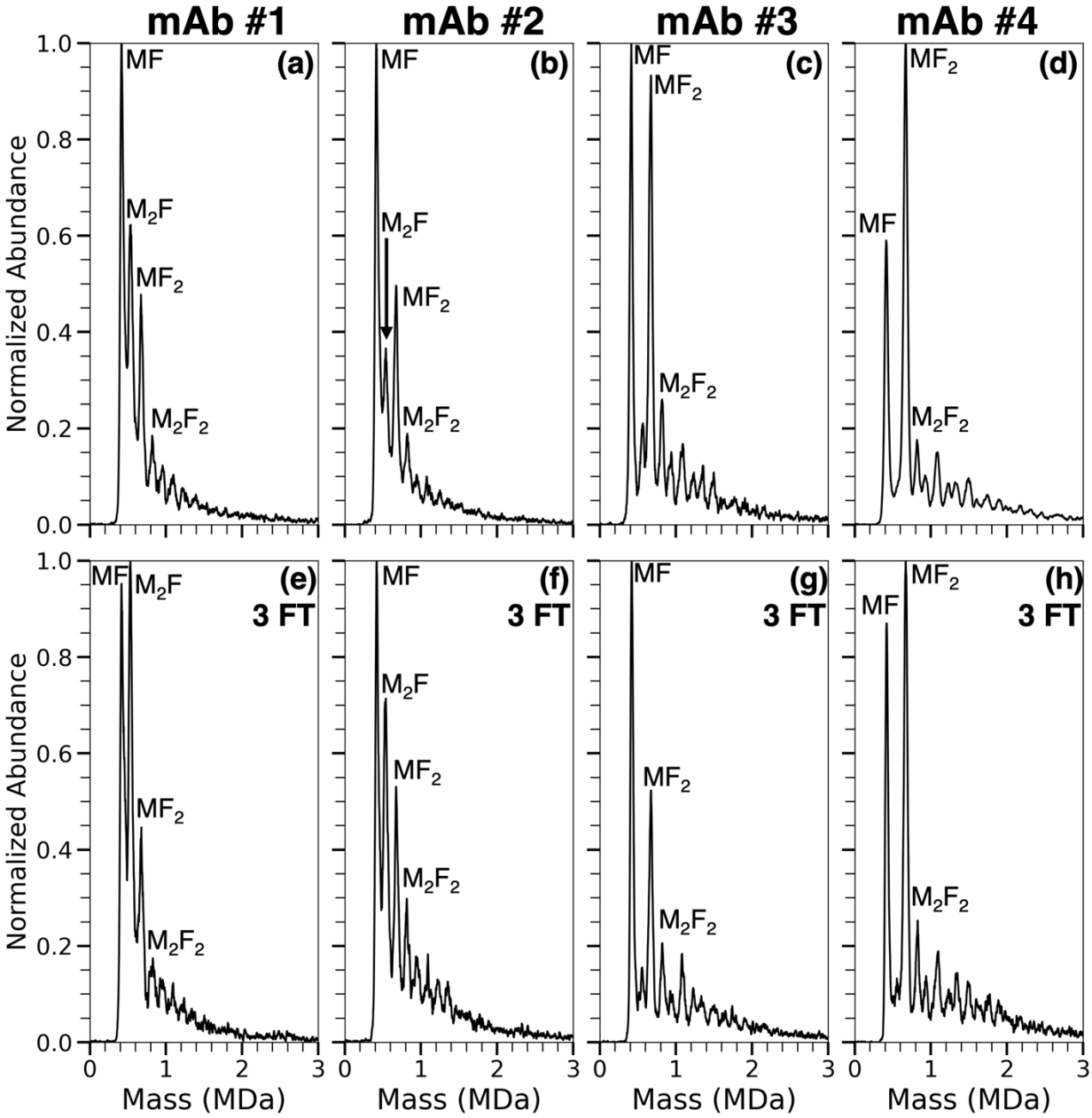

Figure 12.3. CDMS mass spectra acquired before (a, b, c, d) and after (e, f, g, h) 3 FT cycles of PE-mAbs #1 (a, e), #2 (b, f), #3 (c, g) and #4 (d, h).

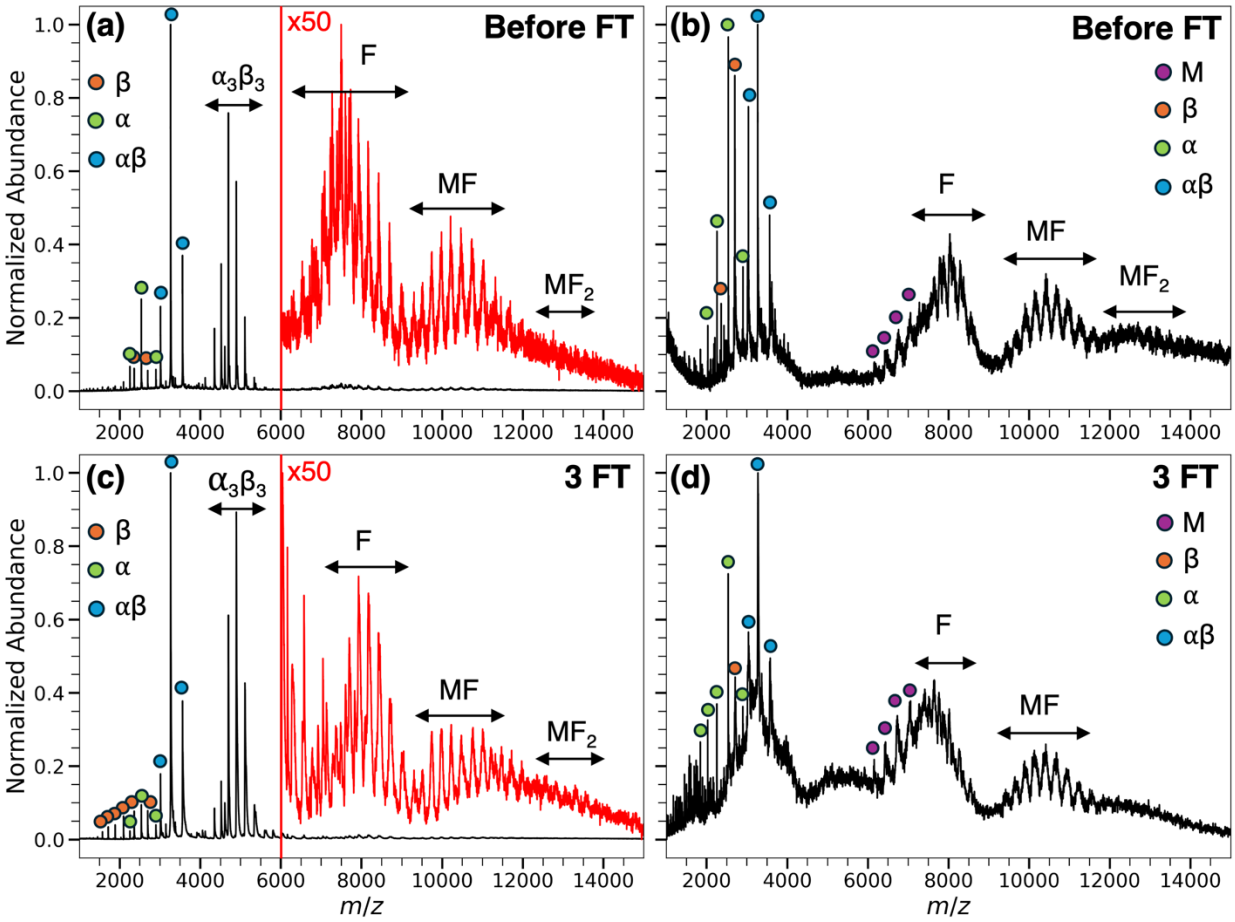

Figure 12.4. QTOF mass spectra acquired before (a) and after (b) 3 FT cycles of PE-mAbs (a,c) #1 and (b,d) #3.

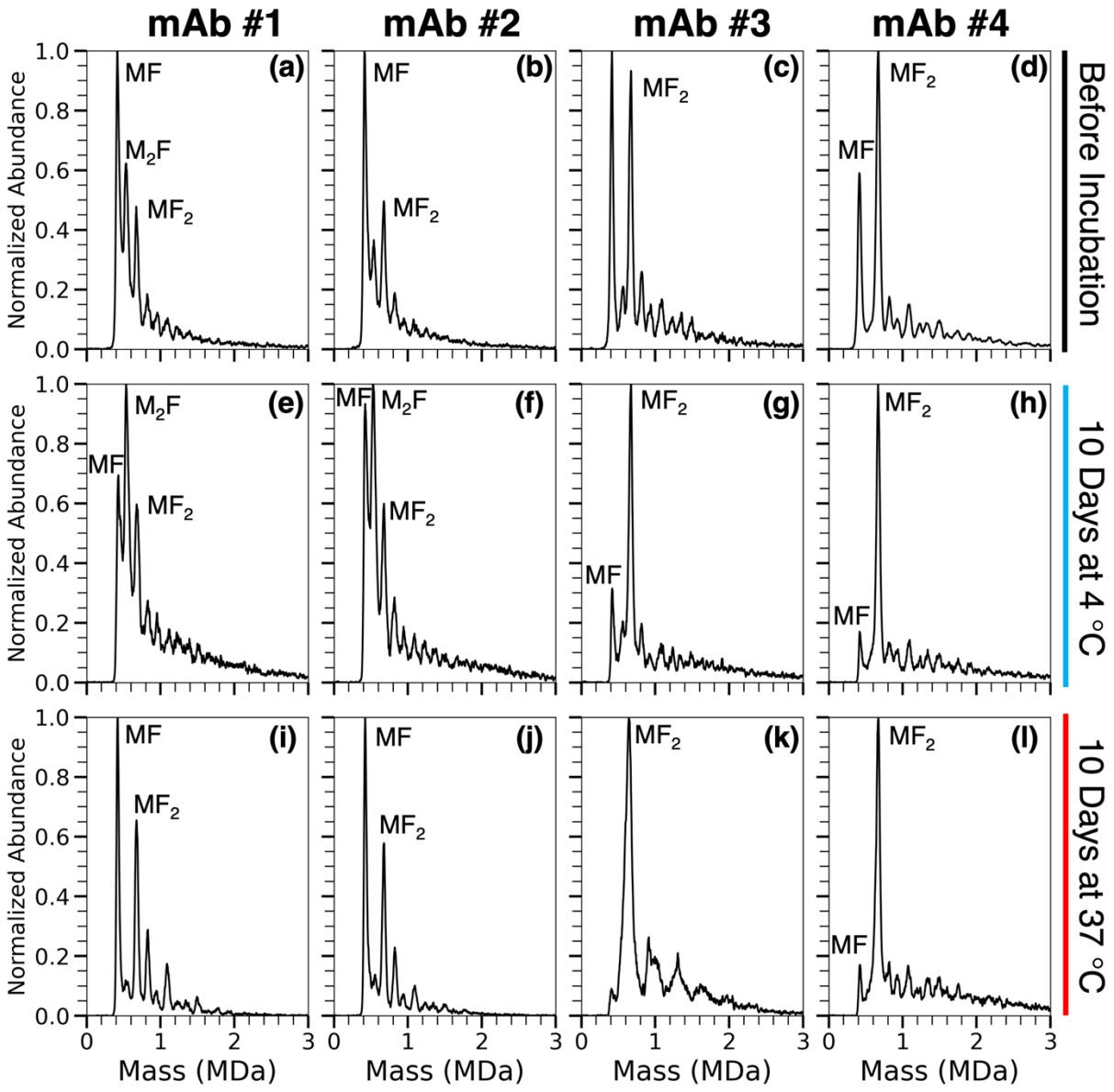

Figure 12.5. CDMS mass spectra of mAbs #1 (a,e,i), #2 (b,f,j), #3 (c,g,k), and #4 (d,h,l) acquired before incubation (a-d), after incubation at 4 °C (e-h), and after incubation at 37 °C for 10 days.

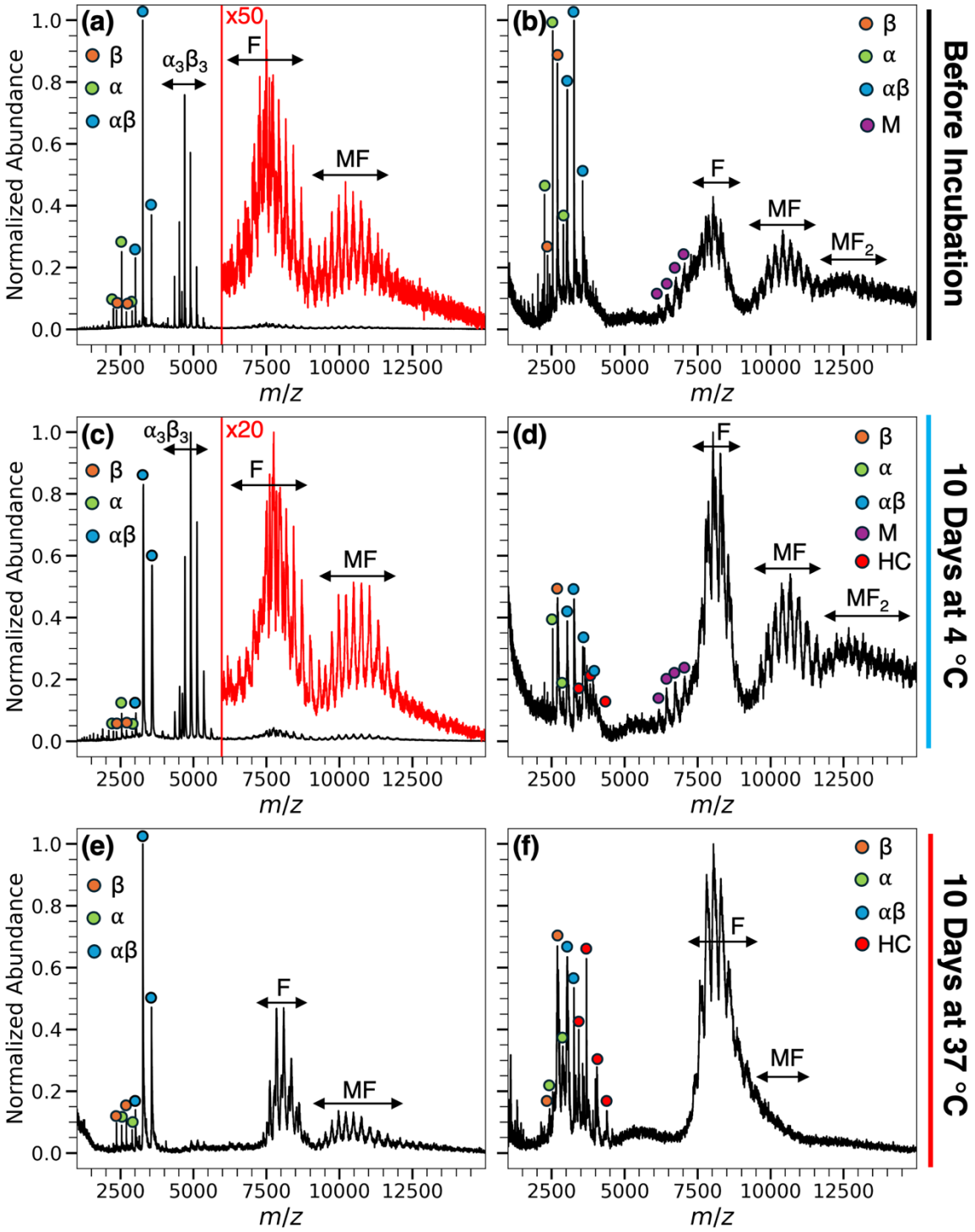

Figure 12.6. QTOF mass spectra of PE-mAbs (a,c,e) #1 and (b,d,f) #3 acquired before (a,b) and after incubation at (c,d) 4 °C and (e,f) 37 °C for 10 days.

12.8 Supplemental Information

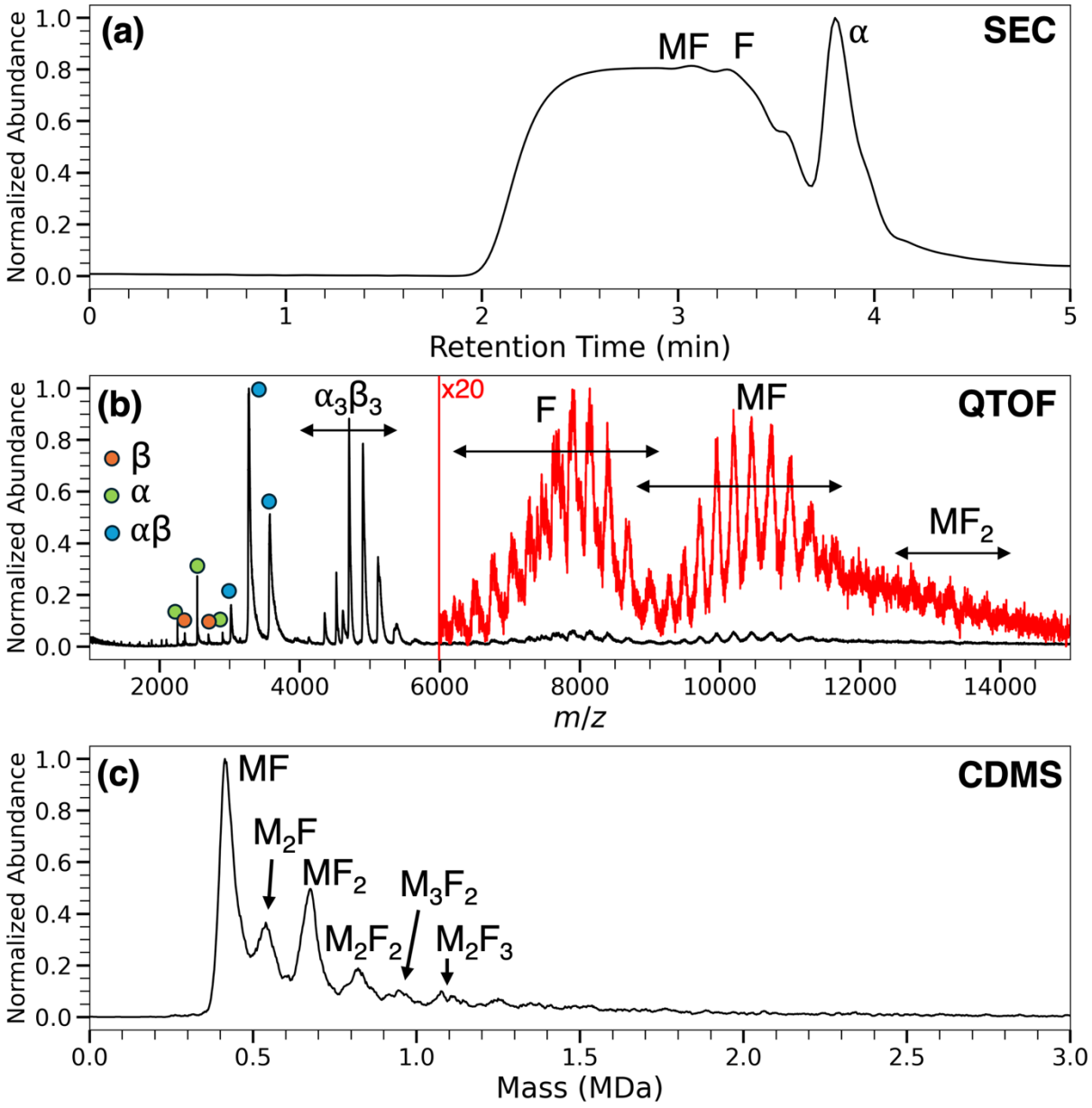

Supplemental Figure 12.1. Data for PE-conjugate mAb #2 obtained using (a) SEC, (b) QTOF MS, and (c) CDMS.

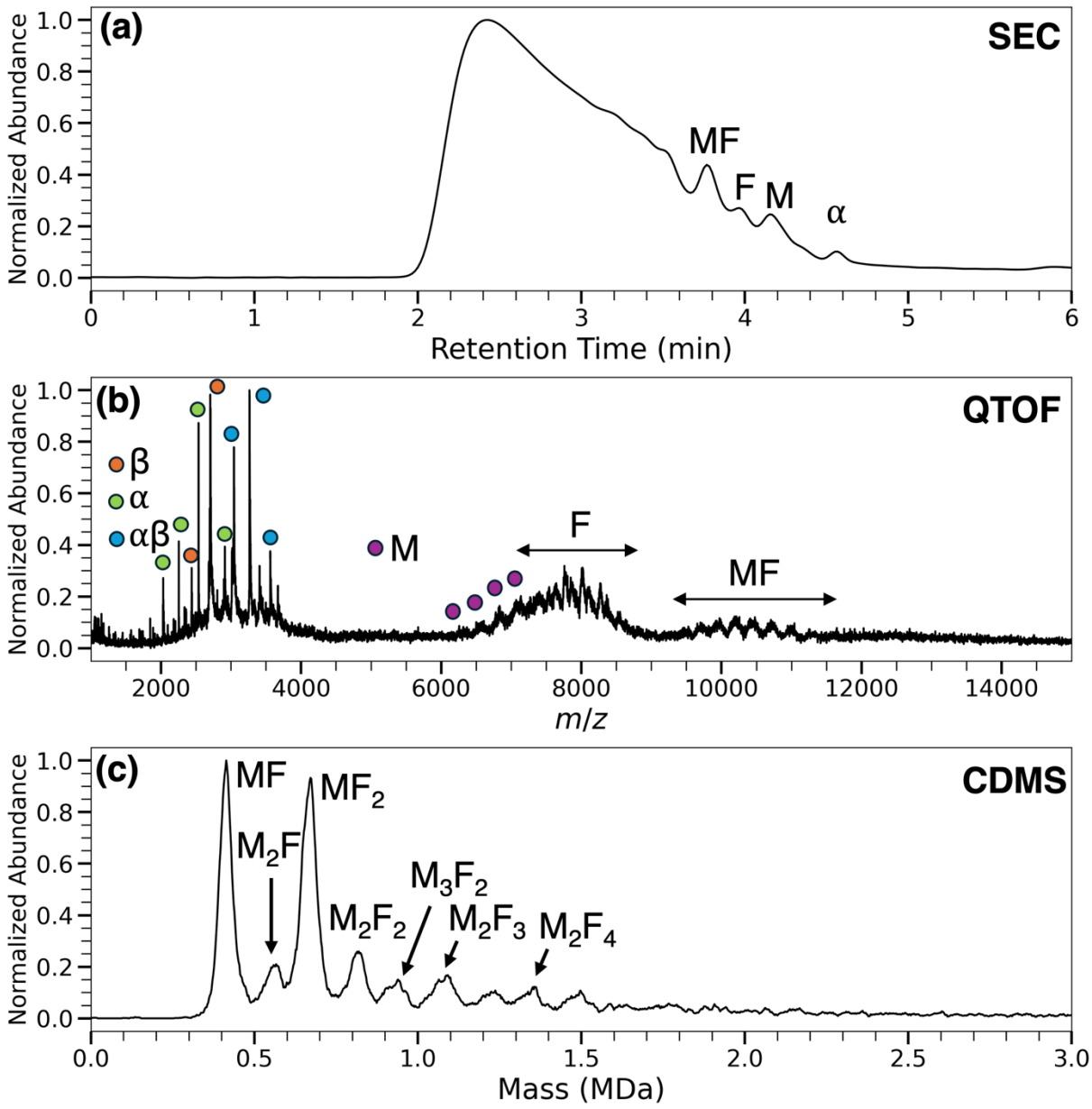

Supplemental Figure 12.2. Data for PE-conjugate mAb #4 obtained using (a) SEC, (b) QTOF MS, and (c) CDMS.

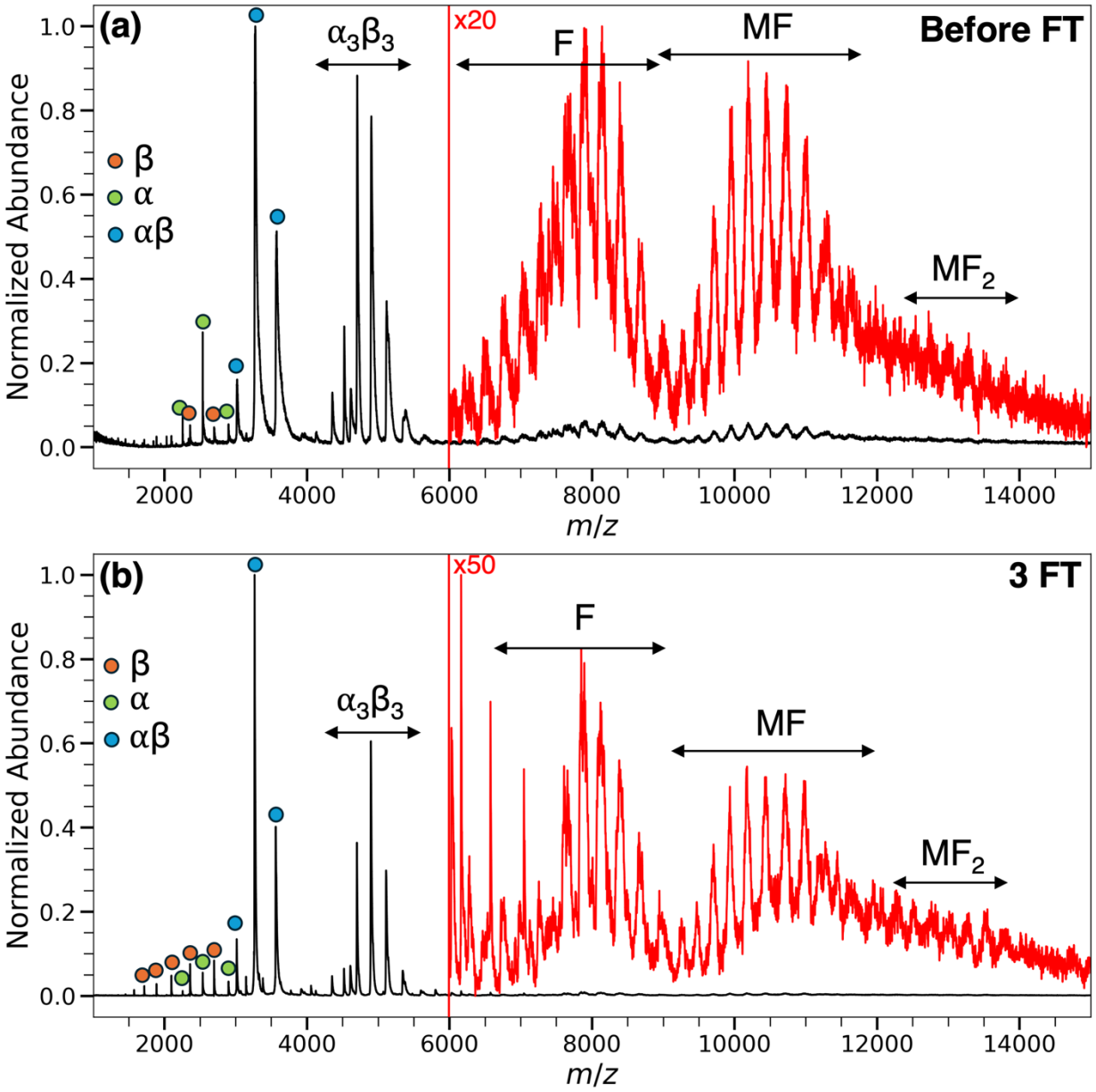

Supplemental Figure 12.3. QTOF mass spectra acquired before (a) and after (b) 3 FT cycles of PE-mAb #2.

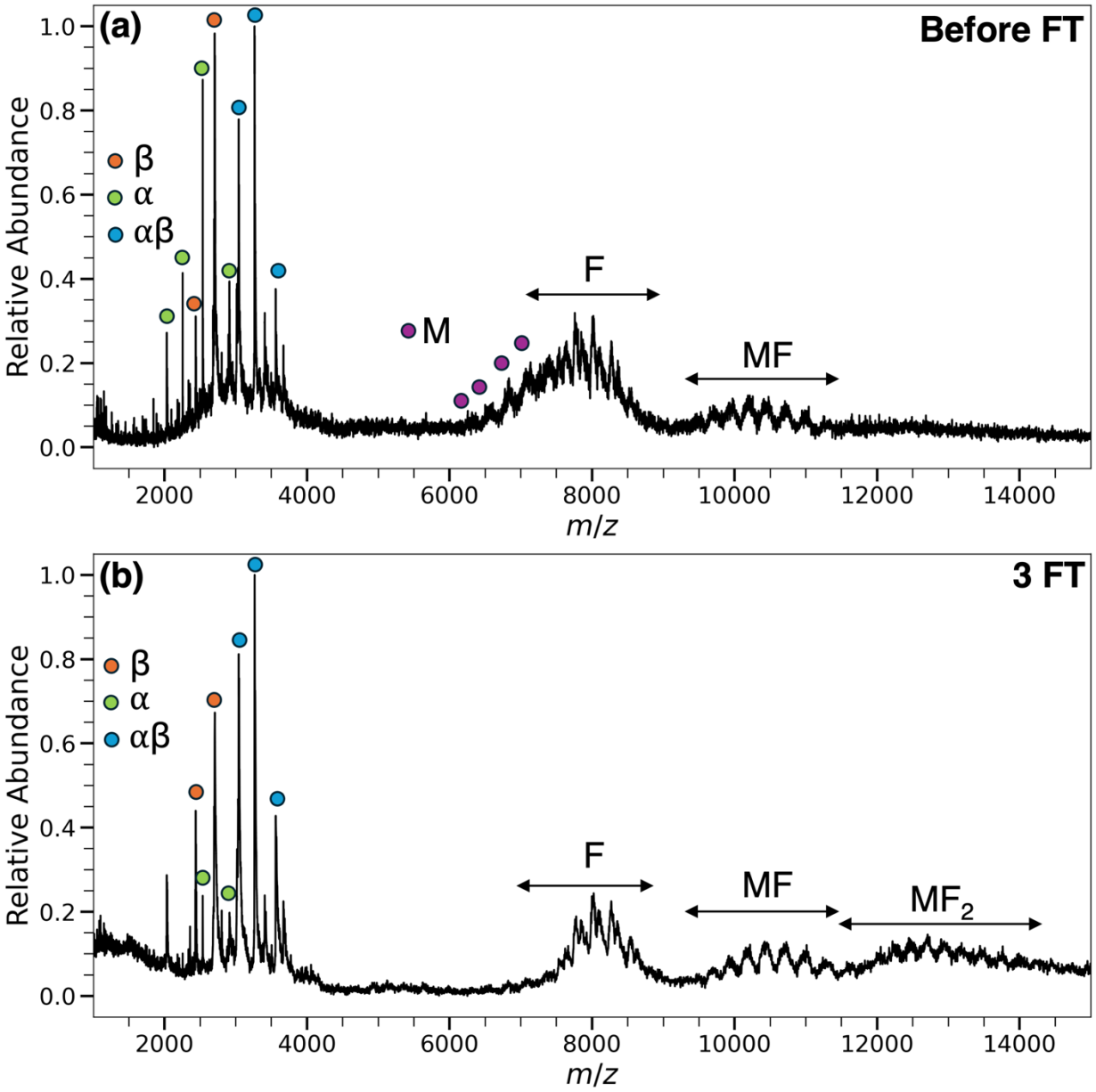

Supplemental Figure 12.4. QTOF mass spectra acquired before (a) and after (b) 3 FT cycles of PE-mAb #4.

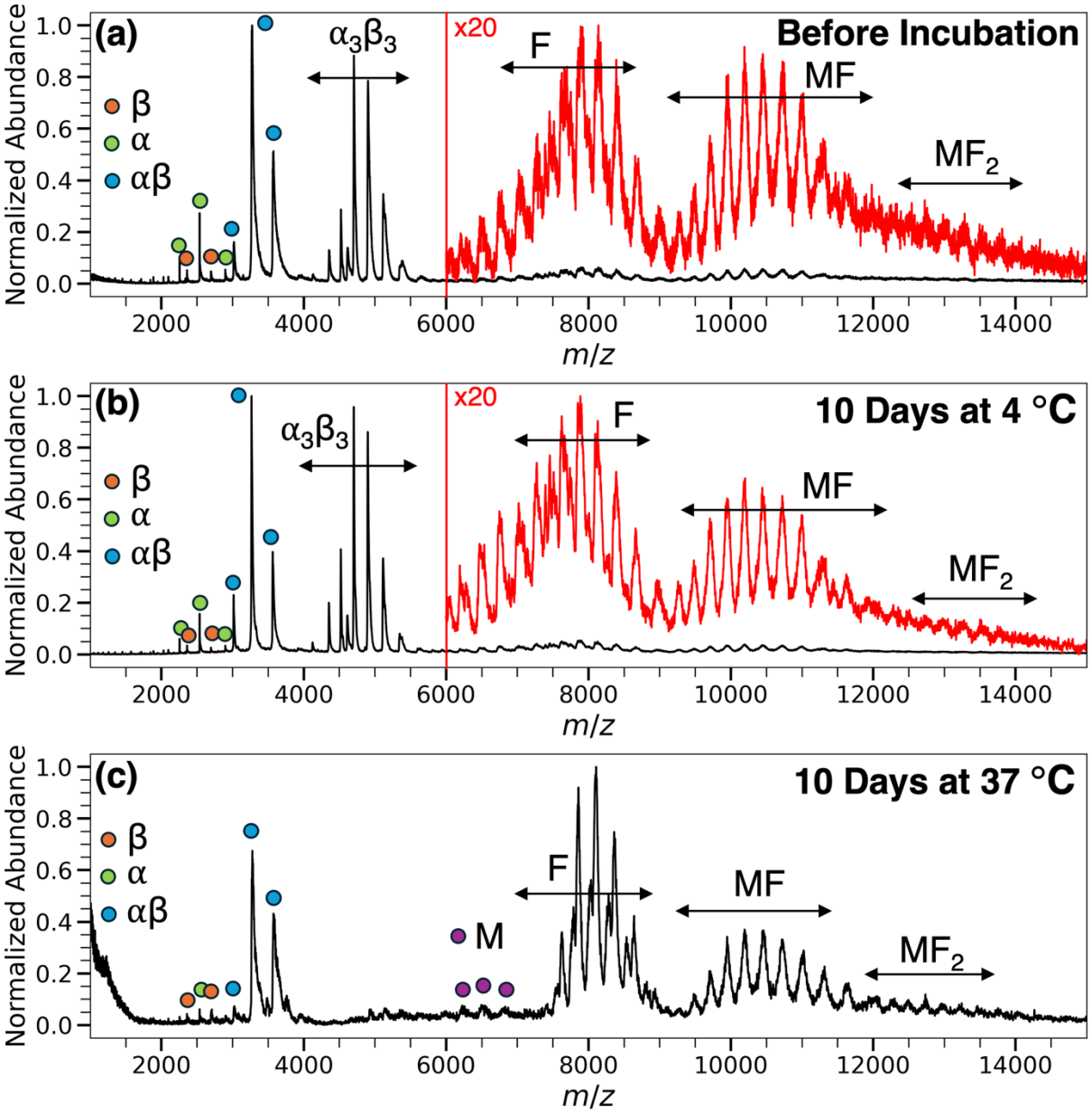

Supplemental Figure 12.5. QTOF mass spectra of PE-mAb #2 acquired after 10 days of incubation at (a) 4 °C and (b) 37 °C.

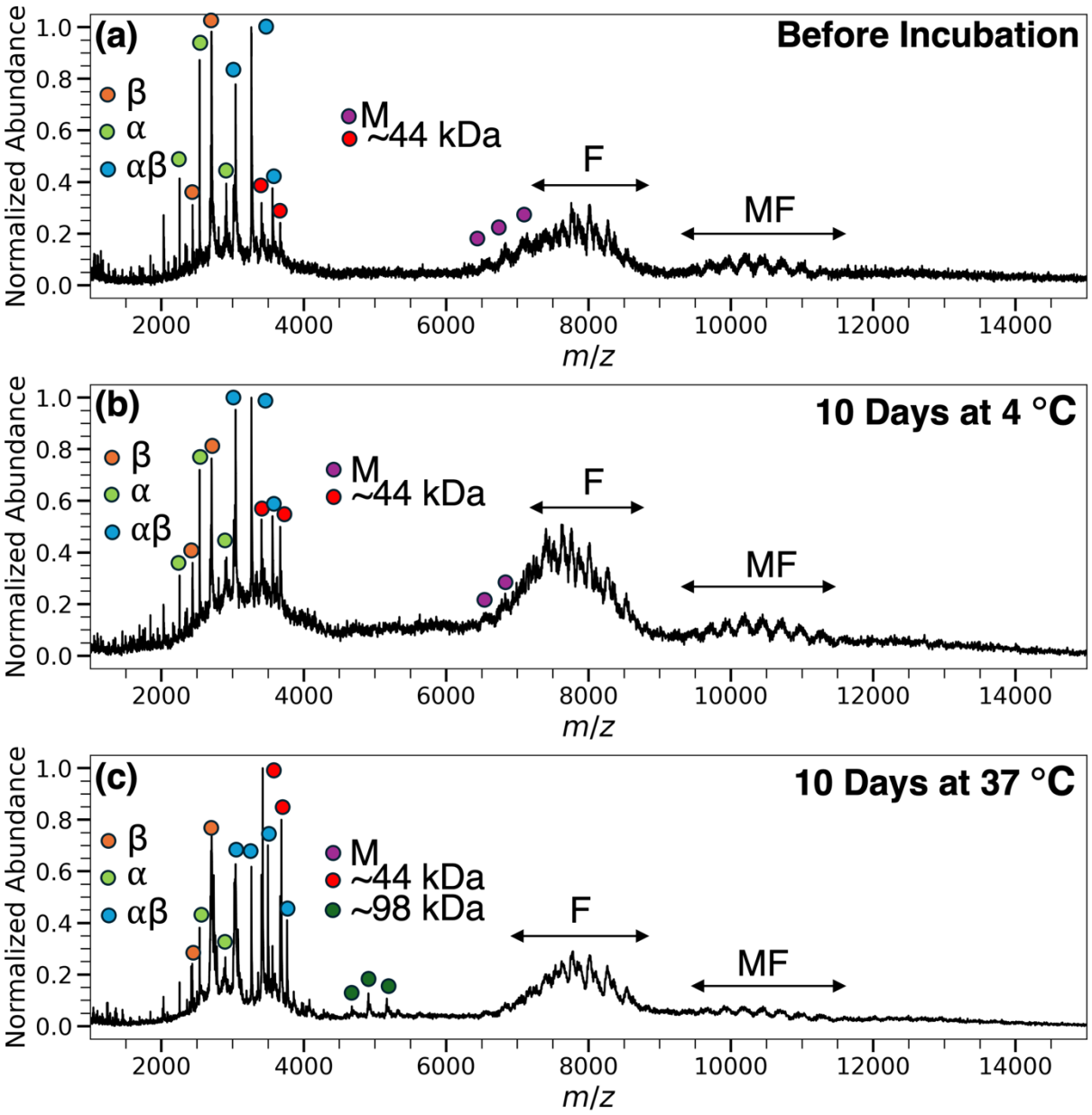

Supplemental Figure 12.6. QTOF mass spectra of PE-mAb #4 acquired after 10 days of incubation at (a) 4 °C and (b) 37 °C.

Chapter 13

Summary and Future Directions

The work in this dissertation focuses on the development of high-throughput methods for characterizing the biophysical properties of amino acid clusters, proteins, protein complexes, and biomolecular aggregates. These developments are achieved by modifying (1) the electrospray ionization source (Chapters 2 – 9) or (2) the method of detecting ions (Chapters 10 – 12). Modifications to the electrospray ion source include the use of submicron diameter electrospray emitters, which provide a clearer picture of the small molecule clusters, protein conformations, and protein complex stoichiometries that exist in solution without the influence of nonspecific aggregation, and the use of various heating methods to acquire mass spectra at elevated temperatures, which enables the acquisition of protein melting curves in <45 seconds and the observation of diverse conformational rearrangements that model proteins can undergo at temperatures near the thermal denaturation temperature. The fast heating enabled by laser-heated electrospray ionization allows for melting curves to be acquired for proteins and protein-ligand complexes prone to aggregation, extending MS-based measurements of thermal stability to a much broader class of biomolecules that also includes monoclonal antibodies involved in biopharmaceutical treatments. The protein aggregation process is difficult to study using conventional MS instrumentation due to the high mass species that are formed and *m/z* overlap that prevents the resolution of individual protein charge states and thus any information from being obtained. These challenges can be overcome using charge detection mass spectrometry (CDMS), which measures the *m/z* and *z* of individual ions separately. The wide mass range, high sensitivity, and ability to distinguish protein and oligomer conformations based on different extents of charging provides detailed insight into the protein aggregation process and products for both small proteins and large biotherapeutics that are challenging to characterize by any other analytical method.

The work performed in Chapters 2 – 6 rely on the use of submicron diameter electrospray emitters to study biomolecular complexes in the absence of nonspecific aggregation and in the presence of high concentrations of nonvolatile salts. In combination with vT-ESI sources, like those used in Chapters 7 and 9, submicron nESI emitters could be used to characterize the thermochemistry of the formation of small amino acid clusters in solution. Using submicron diameter emitters, it is possible to produce droplets that have an estimated diameter similar to the hydrodynamic radius of proteins. It would be interesting to investigate the biophysical properties of proteins under these confined conditions. Finally, by varying the emitter diameter and electrospray voltage conditions, these tips could be used to investigate fundamental aspects of the electrospray ionization process, including investigating how the size of electrospray droplets depends on emitter diameter or spray voltage. As described in Chapter 6, the unique ionization phenomena that are sometimes observed from these emitters can also provide insight into how different analytes are transferred from solution to the gas-phase.

Extending the vT-ESI measurements performed in Chapters 7 – 9 to proteins in different buffer conditions could provide insight into how the Hofmeister effect influences the melting temperature and thermochemical properties of proteins in the presence of different salts. It would also be interesting to assay the heat-induced conformational changes of other model proteins with catalytic activity to investigate whether the compaction observed for cyt *c* is a mechanism for

retaining catalytic activity at high temperatures or an evolutionary mechanism for preventing irreversible aggregation.

The laser heated ESI method established in Chapters 7 and 8 show significant promise as a method for the high-throughput characterization of protein melting temperatures. Performing these melting measurements on mixtures of monoclonal antibodies and other biotherapeutics that are difficult to characterize using conventional biophysical methods could be a useful tool for identifying optimal candidates for further development of biopharmaceuticals. LH-ESI in combination with submicron diameter emitters could be used to investigate how nonvolatile buffers affect the protein melting behavior for monoclonal antibodies and other proteins that aggregate too quickly to be characterized using vT-ESI. The time that proteins are exposed to direct heating in LH-ESI can be readily adjusted between ~100 ms – 1 min by varying the length of the emitter exposed to the laser beam or the flow rate. By sampling these different time points during ESI of aggregation-prone proteins like mAbs and those involved in neurodegenerative disease, LH-ESI could capture "snapshots" of the species involved in the fastest steps of the aggregation process, providing information about the kinetics of aggregation and interconversion between fast forming protein oligomers. Combining laser-heating with bulk heating (e.g. in a dry bath incubator) and measuring the resulting oligomers by CDMS has the potential to establish a comprehensive view of the aggregation process in both mass (monomer to multi-MDa oligomers) and temporal (~100 ms - days) space. Connecting LH-ESI with solution-phase separations would enable the high-throughput characterization of protein T_m values from complex mixtures like proteome extracts. Proteins bound to ligands often exhibit shifts in their T_m value and LH-ESI could prove useful as a screening tool for identifying protein-drug interactions on the proteome wide scale.

The use of CDMS for characterizing the mass and shape of intermediate-sized oligomers of proteins and antibodies was established in Chapters 10, 11, and 12 and opens the door for a number of interesting studies to be performed. In this work, protein oligomers generated by heat stress, freeze-thaw cycling, and during purification were characterized, but CDMS analysis of protein aggregates is equally applicable to oligomers generated by other stressors relevant to biopharmaceuticals, including pH changes, agitation, or light exposure. Through the use of submicron diameter emitters to desalt protein ions during measurement, CDMS can also be used to rapidly investigate the effect of different buffer conditions on the overall size and shape of oligomers formed during stress. These experiments could prove very useful for accelerating the development of formulation buffers to prevent aggregation during the storage and shipping of biotherapeutics without the need to wait long periods of time for light-scattering particles to form. Similar experiments characterizing aggregates formed in the presence of inhibitory compounds aimed at preventing the oligomerization process implicated in neurodegenerative disease could prove useful as a high-throughput screening tool for drug candidates. Finally, given recent advances in the acquisition speed of multiplexed CDMS instruments, it may be possible to acquire all of this information in a high-throughput fashion through the use of autosampling instrumentation.

This dissertation establishes methods for reducing experimental artifacts associated with ESI and for the high-throughput characterization of protein T_m values, thermochemistry, and oligomers formed from various types of stress. Future advancements on the methods established in this work could prove useful towards accelerating biopharmaceutical development pipelines and for understanding the fundamental processes and critical factors driving toxic oligomer formation in a wide variety of diseases.